ACTUAL DESIGN SPACE METHODOLOGY FOR HIGH-PERFORMANCE SWITCHED RELUCTANCE MACHINES DESIGN

Author: Roberto Rocca

Supervisors: Prof. Michael Galea, Prof. Chris Gerada, Dr. Savvas Papadopoulos and Dr. Mohamed Rashed

Thesis submitted to the University of Nottingham
for the degree of Doctor of Philosophy

January 2020

University of Nottingham
UK | CHINA | MALAYSIA

'Let us put our minds together and see what life we can make for our children'

Sitting Bull

'Mettiamo assieme le nostre menti e vediamo quale vita possiamo costruire per i nostri figli'

Toro Seduto

'Juntemos nuestras mentes y veamos qué vida podemos construir para nuestros hijos'

Toro Sentado

ABSTRACT

In the design of modern, high-performance Switched Reluctance machines, designers are challenged to face highly restrictive sets of constraints and requirements, which frequently tend to clash with each other. As a result, chances to find a feasible solution to the design problem reduce dramatically, in case a solution is at all available. Traditional design approaches, i.e. heuristic and optimisation-based, proved not to cope effectively with this kind of design problem, mainly because of their inherent impossibility to consider the interactions between the '*physics*' involved in the design from the very early stages.

A possible solution is therefore to change the way high-performance designs are approached. To this end, this thesis proposes a new approach to the design of high-performance Switched Reluctance machines, that is based on the introduction of an analytical stage prior to the Finite Elements stage, where the 'Actual Design Space' (ADS) is determined, i.e. the *'space wherein the final design can be found'*.

The process to determine the ADS begins by the rigorous count of the number of independent design variables. Subsequently, constraints and requirements are introduced one by one, in order to discard all of the unfeasible candidates. At the end of this process, the ADS is attained, whose main characteristic is to be populated only by feasible candidates. As it can be noted, this approach is inherently multiphysics, since thermal, mechanical and electromagnetic constraints are all handled together.

Following from the way the ADS is determined, the designer can benefit from a good insight of the design problem and hence is in the position to: 1) ensure that the design problem is feasible (ADS non-empty), and 2) once the feasibility has been proved, select the most convenient strategy to finalise the design via Finite Elements.

The design case study of a 5.5kW Switched Reluctance machine for a mild hybrid automotive drive train concludes this thesis with a practical implementation of the proposed ADS methodology, showing its effectiveness in coping with a restrictive set of constraints and requirements.

SOMMARIO

La progettazione di macchine *Switched Reluctance* moderne, dove vengono richieste prestazioni elevate, comporta il dover soddisfare un insieme di vincoli e requisisti normalmente molto stringenti, nonché spesso in conflitto tra loro. Il risultato è che il problema di progetto ammette normalmente un numero molto limitato di soluzioni, ammesso che ne ammetta. Gli approcci tradizionali alla progettazione, lo 'storico' approccio euristico, nonché il più moderno uso di algoritmi di ottimizzazione, stanno dimostrando di non essere all'altezza del compito, prevalentemente a causa della loro intrinseca impossibilità di considerare, già dalle fasi iniziali, tutte le 'fisiche' coinvolte nella progettazione.

Una possibile soluzione al problema è sicuramente un cambio di approccio. A riguardo, questa Tesi propone un nuovo approccio alla progettazione di macchine *Switched Reluctance* ad elevate prestazioni, basato sull'introduzione di uno step analitico, da effettuarsi prima di intraprendere la fase di simulazione agli Elementi Finiti, durante il quale viene determinato lo 'Spazio Effettivo di Progetto ' (in inglese *Actual Design Space*, ADS).

Il processo di determinazione dell'ADS inizia dalla conta rigorosa del numero di variabili di progetto indipendenti. Successivamente vincoli e requisisti vengono introdotti uno alla volta in modo da eliminare tutti i candidati non fattibili (*unfeasible*). Il risultato di tale scrematura è proprio l'ADS, cui principale caratteristica è di essere composto da soli candidati fattibili. Da notare che il metodo proposto è per sua natura multifisico, in quanto i vincoli elettromagnetici, termici e meccanici vengono considerati tutti insieme.

Considerato il modo in cui l'ADS viene definito, a seguito della sua determinazione il progettista possiede una visione completa del problema di progetto, ed è dunque in condizione di assicurare la fattibilità del progetto (ADS non vuoto), e, in caso di assicurata fattibilità, selezionare la strategia più efficace per completare la progettazione per mezzo di simulazioni agli Elementi Finiti.

Il progetto di una *Switched Reluctance* da 5.5kW per il *power train* di un veicolo ibrido conclude la Tesi con un esempio pratico dell'implementazione del metodo proposto e ne mostra l'efficacia nell'affrontare progetti con vincoli e requisiti molto stringenti.

RESUMEN

El diseño de máquinas *Switched Reluctance* modernas, que requieren prestaciones elevadas, obliga a los proyectistas a enfrentarse a conjuntos de vínculos y requisitos normalmente muy estrictos, que además suelen limitarse entre sí. Por consiguiente, el problema de diseño admite un número muy limitado de soluciones, si es que existe alguna. Los métodos tradicionales de diseño, el histórico método heurístico, junto a la aplicación de los algoritmos de optimización más modernos, están mostrando sus considerables limitaciones al enfrentarse a diseños de complejidad tan elevada. Causa principal de dichas limitaciones es la natural incapacidad de estos métodos para considerar, desde el principio, todas las 'físicas' implicadas en el diseño.

Una posible solución para el problema sería cambiar la manera de enfrentarse al diseño. Esta Tesis desarrolla un nuevo método de diseño de máquinas *Switched Reluctance* de elevadas prestaciones, basado en la introducción de un proceso analítico, que debe llevarse a cabo antes que la simulaciones con Elementos Finitos, y durante el cual se determina el 'Espacio Exacto de Diseño' (en inglés *Actual Design Space*, ADS).

El proceso de construcción del ADS empieza con la cuenta exacta del número de variables de diseño independientes. Posteriormente, los vínculos y requisitos son introducidos uno por uno, de manera que todos los candidatos que no son factibles sean descartados. El resultado de tal proceso es el mismo ADS, cuya principal propiedad es la de contener únicamente candidatos factibles. Otro aspecto muy relevante es que el método ADS es intrínsecamente multifisico, ya que los vínculos electromagnéticos, térmicos y mecánicos son introducidos simultáneamente.

Al considerar la manera en que el ADS se determina, y gracias a la información que se puede obtener de este, el proyectista está facilitado al asegurar la factibilidad del proyecto (ADS no vacío), y, si dicha factibilidad es asegurada, elegir la estrategia más conveniente de completar el proyecto a través de los Elementos Finitos.

El diseño de una *Switched Reluctance* de 5.5kW para el *power train* de un vehículo híbrido concluye la Tesis con un ejemplo práctico de la implementación del método ADS y comprueba su utilidad y eficacia al enfrentarse a diseños con vínculos y requisitos muy estrictos.

LIST OF PUBLISHED AND SUBMITTED PAPERS

R. Rocca, F. G. Capponi, G. D. Donato, M. Rashed, S. Papadopoulos, and M. Galea, "Analytical Approach for the Identification of an Optimal Design Space for Switched Reluctance Machines," in *2018 XIII International Conference on Electrical Machines (ICEM)*, Alexandropouli, 2018, pp. 569-575.

R. Rocca, F. Giulii Capponi, S. Papadopoulos, G. De Donato, M. Rashed, and M. Galea, "Optimal Advance Angle for Torque Maximisation in High-Speed, Single-Pulse Operated, Switched Reluctance Machines," in *2019 IEEE International Electric Machines & Drives Conference (IEMDC)*, San Diego, CA, 2019, pp. 80-85.

R. Rocca, F. Giulii Capponi, G. De Donato, S. Papadopoulos, M. Rashed and M. Galea, " Actual Design Space Methodology for Preliminary Design Analysis of Switched Reluctance Machines," under review at *IEEE Transactions on Industry Applications*

R. Rocca, F. Giulii Capponi, S. Papadopoulos, G. De Donato, M. Rashed, and M. Galea, " Optimal Advance Angle for Aided Maximum-Speed-Node Design of Switched Reluctance Machines," accepted, awaiting for publication on *IEEE Transactions on Energy Conversion*

UNPUBLISHED PAPER *

R. Rocca, S. Papadopoulos, M. Rashed, G. Prassinos, and M. Galea, "Design Considerations on a Switched Reluctance Machine for a High Inertia, High Speed Ratio Application," Conference Proceeding Paper, 2017.

*The paper was accepted for the 2017 WEMDCD but subsequently withdrawn due to a non-disclosure agreement between the University of Nottingham and OXTO Energy. Its text is attached at the end of this document.

ACKNOWLEDGMENTS

In this few lines, I would like to express my gratitude to all people that accompanied me during these four years and helped me to write an unforgettable page of my life. I have decided to acknowledge each person in his/her mother tongue, so that the text below is dedicated to the 'English speakers'.

First of all, I would like to thank my '*lead*' supervisor Mikiel, for his wise guidance that allowed me to overcome all of the challenges found along the way to the Ph.D. I'd like to thank my co-supervisor Chris for giving me the chance to undertake this incredible adventure. This successful outcome would have not been possible without the help of my co-supervisor, and friend, Dr. Savvas Papadopoulos, whose patience has been precious, especially in the lab days. A big thank you goes also to Dr. Mohamed for his precious advice.

I would like to thank my '*predecessor*' Dr. James B. Bartolo, for his help during my master thesis. I wish to thank also our senior technicians John and Kevin for their help in setting up our foolish SRFly test rig, nightmare of the whole High Power Area; I owe them more than one beer.

Finally, I have no words to thank all of my friends from the PEMC group, whom to me have been much more than a research group, it has been my family. Thank you all guys!

There could have been no better place for my Ph.D. to end but here, in the *Aeropuerto del Prat* in Barcelona. From here, thousands of new routes and new adventures can begin.

LET'S GO !

RINGRAZIAMENTI

Vorrei in queste poche righe ringraziare tutti coloro che mi hanno accompagnato durante questi quattro anni, contribuendo a scrivere una pagina indimenticabile della mia vita. Ho deciso di rivolgermi ad ognuno nella sua lingua materna, di seguito mi rivolgo a tutti gli italiani.

Il mio primo ringraziamento va alla mia famiglia, a Papà, Mamma Ale e Nonna, sempre al mio fianco, giorno dopo giorno, incondizionatamente. Senza di loro tutto questo non sarebbe mai stato possibile.

Altri due architetti di questa avventura, cui devo molto del mio sapere tecnico, e non solo, sono i Professori Fabio e Giulio della Sapienza, che mi hanno accolto come *visitor* per sette mesi e lavorato da supervisori aggiunti per più di due anni.

Altri compagni di avventura, ormai da una vita intera, sono i miei *amichielli* di Roma, sempre qui, sempre uguali, sempre gli stessi, per me, altri familiari aggiunti: Alessandro, Riccardo, Andrea R., Andrea B., Dario e Giorgio, anche se non con lui non ci vediamo più così spesso.

Un ringraziamento speciale vorrei ancora una volta dedicarlo a tutti i miei amici del PEMC, che oltre ad amici sono stati la mia famiglia, grazie a tutti ragazzi!

Davide, Luca R., Giorgio, Alberto, Giacomo, Albino, Francesco T., Alessandro M., Alessandro C., Stefano, Massimo, Mattia, Cosimo, Vincenzo, Francesco, Paolino, Sara, Gaetano, Mauro, Michele, Alberto, Andrea F., Perla, Andrea S.

Vorrei ringraziare anche i miei amici della Sapienza, Abdu, Federico, Alessandro, Tommaso (anche se studia a Nottingham), Hossein e Mostafa, per tutte le splendide giornate passate e che passeremo in dipartimento.

Un ringraziamento e un abbraccio anche al mio amico Stefano, unico 'superstite' dei tempi dell'università, che come me ricerca un modo di fare ricerca.

L'ultimo pensiero va al '*primo di tutti*', a colui che mi ha trasmesso l'amore per la conoscenza e per il sapere, e insegnato che la curiosità è un dono che va coltivato tutti i giorni, il Maestro Paolo della Scuola Elementare Statale A. Bertolotti (Roma).

Non poteva esserci posto migliore per finire il dottorato se non qui, nell' *Aeropuerto del Prat* a Barcellona, da dove migliaia di nuove vie e nuove avventure possono iniziare. Ovunque si vada,

AVANTI!

AGRADECIMIENTOS

En estas pocas líneas me gustaría agradecer a todos aquellos que me han acompañado durante estos cuatro años contribuyendo en la escritura de esta página inolvidable de mi vida. He elegido dar las gracias a cada persona en su lengua materna, así que ahora me dirigiré a los hispanohablantes. Esta es, con toda honestidad, una increíble sorpresa, pues hace cuatro años nunca habría imaginado haber podido aprender español (y sin ir a clase).

La arquitecta es mi novia Marta, con quien comparto todos los días de mi vida; y nada más podría pedir. No hay palabras que puedan describir mi infinita felicidad y gratitud por tenerla a mi lado, por apoyarme en aquellos (pocos) días duros a que me enfrenté, así como por las risas, las bromas y todo el cariño y el amor de cada día. También le agradezco haberme dado la oportunidad de conocer y poder vivir en España y Eslovaquia. "No sé cómo pude vivir los 25 años anteriores sin haber conocido estos lugares".

Quiero mandarles un abrazo enorme a mis dos amigos españoles de Nottingham: David, con el que he compartido tardes encantadoras en las cafeterías de la ciudad, y Carlos, el único hispanohablante del PEMC, ambos compañeros de cervezas echadas viendo el fútbol.

Otro abrazo se lo mando a Con y Luca (que es romano como yo, por supuesto), jefes de la movida de nuestro grupo de amigos en Nott's.

No existe mejor lugar para acabar mi doctorado que este, el Aeropuerto del Prat en Barcelona, desde donde miles de nuevos caminos y nuevas aventuras pueden empezar.

Vaya donde vaya el camino,

ADELANTE

Barcelona 12 / 01 / 2020

LIST OF CONTENTS

LIST OF FIGURES

LIST OF TABLES

LIST OF MAIN SYMBOLS

A

A_{ss}	Stator Slot Area

B

b	Coefficient of Cubical Expansion
B	Flux Density
B_g	Mid-Airgap Average Magnetic Flux Density
B_{rt}	Rotor Tooth Average Magnetic Flux Density
b_{ry}	Rotor Yoke Thickness
B_{ry}	Rotor Yoke Average Magnetic Flux Density
B_{st}	Stator Tooth Average Magnetic Flux Density
b_{sy}	Stator Yoke Thickness
B_{sy}	Stator Yoke Average Magnetic Flux Density

C

cs	Specific Heat

D

d_{duct}	Cooling Duct Diameter
D_r	Rotor Outer Diameter
D_s	Stator Bore Diameter
D_{sha}	Shaft Diameter

E

e	Electro-Motive Force
E	Young's Modulus

F

$\boldsymbol{F}$	Magnetic Force
$\mathcal{F}$	Magnetomotive Force
f_{CU}	Copper Slot Fill Factor
f_i	Current Form Factor
$f_{rot,1}$	Rotor Flux Density Waveform Fundamental Frequency
$f_{sta,1}$	Stator Flux Density Waveform Fundamental Frequency

G

g	Acceleration of Gravity

H

h_{rt}	Rotor Tooth Height
h_{st}	Stator Tooth Height

I

i	Electric Current
i_{ph}	Phase Current
i_{pk}	Peak Phase Current

J

J_{ss}	Stator Slot Current Density

K

k	Number of Internal Relationships

L

L	Phase Inductance
L_a	Aligned Inductance
l_g	Air Gap
l_{ry}	Rotor Yoke Average Path Length
l_{sy}	Stator Yoke Average Path Length
L_{sha}	Shaft Length
L_{stk}	Axial Stack Length
L_u	Unaligned Inductance

M

m	Number of Phases

N

N	Series-Connected Turns Per Phase
n	Number of Design Variables
N_s	Stator Teeth Number
N_{st}	Series-Connected Turns Around a Stator Tooth
N_r	Rotor Teeth Number

O

OD	Outer Diameter

P

P	Number of Repetitions
$\mathcal{P}$	Magnetic Permeance
P_{CU}	Copper Losses
P_{ew}	End-Winding Copper Losses
P_{FE}	Iron Losses
P_{rated}	Rated Power
P_{rt}	Rotor Teeth Iron Losses
P_{ry}	Rotor Yoke Iron Losses
P_{ss}	Stator Slot Copper Losses
P_{st}	Stator Tooth Iron Losses
P_{sy}	Stator Yoke Iron Losses

Q

q	Number of External Relationships

R

r	Number of Independent Design Variables
R	Phase Resistance
$\mathcal{R}$	Reluctance
R	Thermal Resistance
R_{ew}	End-winding Copper Resistance
R_{ss}	Stator Slots Copper Resistance

T

t	Time
T	Output Torque
T_{AVG}	Average Output Torque
T_{rated}	Rated Toque
T_{RIP}	Torque Ripple

U

u_{FEry}	Rotor Back-Iron Utilization Factor
u_{FEsy}	Stator Back-Iron Utilization Factor

V

V_{DC}	DC-Bus Voltage
v_{ph}	Phase Voltage

W

W_e	Electrical Input Energy
W_f	Magnetic-Field Energy
W_f'	Magnetic-Field Co-Energy
W_m	Mechanical Work

β

β_{rt}	Rotor Tooth Angle
β_{ss}	Stator Slot Angle
β_{st}	Stator Tooth Angle
$\beta_{st\_self\_start}$	Self-Starting Stator Tooth Angle

ε

ε	Electric Permittivity

ζ

ζ_r	Rotor Pitch Angle
ζ_s	Stator Pole Angle

θ

θ	Rotor
θ_a	Aligned Position
θ_{AD}	Turn-on Advance Angle
Θ_{amb}	Ambient Temperature
Θ_{dwell}	Dwell Period
$\Theta_{d\varphi}$	'De-Fluxing' Period
θ_E	Phase Current Extinction Rotor Position
Θ_{lim}	Maximum Allowed Temperature
θ_{ON}	Turn-on Rotor Position
θ_{OFF}	Turn-off Rotor Position
Θ_{rt}	Rotor Teeth Mean Temperature
Θ_{ry}	Rotor Yoke Mean Temperature
Θ_{ss}	Stator Slot Mean Temperature

Θ_{st}	Stator Tooth Mean Temperature
Θ_{sy}	Stator Yoke Mean Temperature
θ_u	Unaligned Position

λ

λ	Thermal Conductivity

μ

μ	Magnetic Permeability

ξ

ξ	Dynamic Viscosity

ρ

ρ	Density

ς

ς	Electrical Resistivity

σ

$\sigma_{\_lim}$	Maximum Tensile Strength

υ

υ	Poisson's Ratio

φ

φ	Magnetic Flux
φ_{pole}	Stator Pole Flux

ψ

Ψ_{ph}	Phase Flux Linkage

ω

ω	Rotational Speed
ω_b	Base Speed
ω_{max}	Maximum Speed

1 INTRODUCTION

1.1 A NEW GENERATION OF HIGH-PERFORMANCE SWITCHED RELUCTANCE MACHINES IS ON THE RISE

In recent years, the Switched Reluctance (SR) machine has gained renewed attention in both the academic and the industrial world. Its main advantages include a rugged and robust nature, as well as independence from Permanent-Magnets, [1-5]. Moreover, the SR machine is well-known for its capability to cover wide constant-power speed ranges, [6], and suitability to work in harsh environments, [7]. Indeed, further to the improvements in power electronics achieved in the last decade, all of these qualities have led the SR machine to be considered a valuable alternative for many applications where AC-machines have historically been dominant, such as in the aerospace, automotive, industrial (especially with harsh environments) and energy storage fields.

Nowadays, electrical machine technology is pushing towards more and more efficient, compact and lightweight solutions. Recent developments are looking at various machines aspects, e.g. new materials, cooling systems, etc. In particular, low-loss ferromagnetic materials are constantly helping to improve the machines' efficiency. Silicon-Carbide and Gallium-Nitride-based semiconductor devices are rising the fundamental switching frequency well above one kHz. Novel and more advanced cooling systems are pushing the power density limitations. Finally, high-strength ferromagnetic and structural materials, along with novel mechanical arrangements allow ever-increasing speeds.

The scenario described above clearly indicates that a new generation of high-performance electrical machines is on the rise, and the SR machine has an important role to play.

1.2 PRESENT AND FUTURE CHALLENGES IN SWITCHED RELUCTANCE MACHINE DESIGN

To satisfy these high-performance requirements, SR machines designers are now challenged to tackle a big range of widely varying requirements, which often clash with each other. These may include high power/torque densities, high efficiencies, power quality, mechanical robustness, operation in wide constant power speed ranges, etc.

The greatest challenge lies in the fact that with a so great number of restrictions, the mutual influence between electromagnetic, thermal and mechanical aspects must be necessarily addressed from the very initial design stage. Indeed, these strong interactions lead to difficult design problems, where very few, or even no, possible solutions are available.

The 'traditional' SR machine design methodology is based on a fully heuristic process, mainly based on the designer's experience and skills. When a design is approached with this methodology, the various design '*physics*' are traditionally addressed separately and most of the design efforts are put on the electromagnetic design, whereas thermal and mechanical aspects are often considered as a posteriori 'safety checks'. This approach has historically been demonstrated to achieve satisfying results for relatively simple design problems, where the small set of requirements allowed for a wide set of potential solutions. However, apart from the obvious challenge with 'overengineering' and 'safety factors', another difficulty is that as the set of requirements grows bigger, the fully heuristic methodology is proving to be quite ineffective, since it takes too many design iterations to identify one of the few possible solutions.

In the last decade, the so called 'multiphysics' approach has become very popular among SR machine designers, thanks to a greater availability of computational resources. In fact, this methodology relies on a strongly automated design routine based on several Finite Element Analysis (FEA) models, usually one per each '*physics*' involved, and driven by an optimization algorithm, [8]. So far, this methodology has been proven to cope excellently with design problems where the main challenge is the selection of the 'best' candidate among a large pool of possibilities; however, this is obtained at the price of a high computation time. On the other hand, as the number of potential solutions grows smaller, e.g. below 1000, this methodology might not remain as effective as it normally is in the conditions described above. In fact, one of the inherent challenges with the FEA-based 'multiphysics' approach is that, due to the high level of automation, the process cannot really account for any unforeseen inconsistencies. Consequently, if the design problem is not stated 'perfectly', a huge computational power might be spent to produce an unfeasible or inconsistent SR machine.

The previous discussion shows that neither of the two design approaches currently used can deal effectively with the design of the new generation of high-performance SR machines. The key point is that none of the aforesaid methods is capable of considering properly the interactions between the different '*physics*' from the very beginning of the design process.

A possible solution is therefore a change in the way these kinds of design problems are approached. To this end, this thesis proposes a new design methodology. The idea is to introduce an analytical stage prior to the FE stage, where the 'Actual Design Space'

(ADS) is determined, i.e. the *'space wherein the final design can be found'*. Then, once the ADS is available, designers can effectively select the most convenient strategy to finalise the design via FEA. A brief description of the ADS methodology is provided in the next Subsection.

1.3 THE 'ACTUAL DESIGN SPACE' METHODOLOGY

Rather than 'trying to jump' to the final solution, the proposed idea is to introduce a preliminary step aimed at the identification of a convenient 'neighbourhood', i.e. a 'space' wherein the final solution is expected to be found. This 'space' is referred to as the ACTUAL DESIGN SPACE (ADS). The term '*Design Space*' indicates the whereabouts that the designer shall investigate to attain the final solution, under the assumption that the solution is contained within this space. The adjective '*Actual'* denotes the fact that the ADS is built up by progressively eliminating all of the unfeasible candidates, so that it is populated only by SR machines that satisfy the entire set of constraints and requirements.

In addition to the way the ADS is made up, its determination prior to the FEA finalising iterations, leads to the following advantages:

1) It offers the possibility of verifying that the given specifications are consistent. In other terms, it is possible to verify that the design is feasible (ADS not empty), even from the initial design stage. In this way, if an 'impossible' design is found, the designer can immediately focus on how to 'relax' the design constraints (or quit the design if convenient).
2) Once the design feasibility has been proven, the ADS itself gives the possibility of selecting the most effective FE finalisation strategy. In fact, based on the size and the 'shape' of the ADS, the designer can benefit from a better insight into the design problem. For example, if the ADS is populated by a small number of candidates, it might be convenient to include all of them in the FEA stage. Conversely, if a large number of candidates populate the ADS, it might be convenient to implement an optimisation algorithm. However, once the ADS is available, the optimisation can be run with 'lower concerns than usual'. In fact, the optimiser can be set to move only inside the ADS. In this way, as almost all the candidates processed have been already proved feasible, successful convergence is likely to be achieved even at the first attempt.

1.4 MAIN THESIS OBJECTIVES

Further to the brief description of the ADS given in the subsection above, the main objectives of this thesis can be summarised as follows:

OBJ. 1) Clear and rigorous statement of the methodology to follow to define the ADS and subsequently finalise the design.

OBJ. 2) Rigorous count of the number of independent design variables offered by the SR machine design problem, independently of any specific application, which is necessary to conduct the design process correctly.

OBJ. 3) Development of a set of simple yet computationally cheap analytical models that predict the performance of any SR machine at both high-speed and low-speed conditions. These are needed to predict the performance of any SR machine candidate and thus verify it compliance with the requirements.

OBJ. 4) Development of an analytical model that caters for the unsaturated inductance values directly from the geometry of any possible SR machine. Indeed, this model is the input of OBJ. 3 above and is therefore necessary for a fully analytical ADS generation process.

1.5 Scientific Contribution

With this thesis, the Author wishes to provide his original contribution to the modelling, design, design optimisation and analysis of 'modern' SR machines. The main contributions given to the state of the art are described below:

A. The proposal and validation of a novel design approach based on the concept of the Actual Design Space. The Author perceives this as the main contribution and believes that it can lead to a broader diffusion of multiphysics design, making it 'affordable' also for research groups and organisations with limitations in time and/or in computational resources.

B. The development of a set of novel, analytical or ultra-fast numerical models devoted to the sizing and to the performance prediction at high-speed of the SR machine. In particular, a relevant contribution is provided by the closed-form expression of the optimal advance angle for operation at high speeds.

C. The proposal and validation of a novel approach to determine the unsaturated inductance profile of SR machines, capable of adapting to widely varying geometries. A particular remark is that the non-overlapping inductances are calculated through elliptical-shaped flux tubes.

1.6 Thesis Outline

This thesis is structured as follows.

Chapter 2 describes most of the salient works presented in the field of the SR machine design and design optimisation. The literature review is aimed at highlighting the limitations of the design methodologies that are currently used and the consequent necessity to introduce novel design approaches.

Chapter 3 begins by providing a purely theoretical description of the ADS methodology. In its second part the implementation of the ADS methodology in the case of an SR machine is shown.

Chapter 4 illustrates and discusses the two physical SR prototypes (named SRMyld and SRFly) that are considered in the course of this thesis, along with their electromagnetic and thermal FEA models. Then, FEA models are validated against experimental results, to ensure that they provide a solid ground to validate the analytical models developed in Chapters 5, 6 and 7.

Chapter 5 discusses in detail and validates the analytical electromagnetic models developed to define the ADS of an SR machine. Models proposed allow the prediction of the machines' performance, such as Torque, Torque Ripple, Copper and Iron Losses and Efficiency with very good accuracy and a relatively low computation time.

Chapter 6 proposes and validates an analytical model aimed at the determination of the unsaturated SR machine inductance values, which are necessary to implement the models developed in Chapter 5 and thus make the ADS derivation a fully analytical process.

Chapter 7 is devoted to the multiphysics extension of the proposed ADS methodology. Indeed, thermal aspects are introduced by means of a Lumped Parameters Thermal Network (LPTN).

Chapter 8 concludes this thesis with a practical design case study, where the ADS methodology is implemented to tackle the design of a $5.5kW$ SR machine for a mild hybrid automotive drive train.

Appendix 1 provides a more in-detail description of the test-rig facility set up for the SRFly prototype.

Appendix 2 completes the work done in Chapter 3, by gathering the equations of the thermal resistances that compose the LPTN. A Discussion about the resistances' derivation is also provided.

2 LITERATURE REVIEW

2.1 SR MACHINES: FROM THE EARLY TO THE PRESENT DAYS

The Switched Reluctance (SR) machine is a singly excited, doubly salient electric machine in which the electromagnetic-to-mechanical energy conversion is in discrete cycles, due to the interaction of the rotor and stator teeth in the presence of a linking field. Due to this effect, the SR machine is sometimes classified as a special member of the Synchronous Machine family. The first usage of the term 'Switched' is attributed to S.A. Nasar in 1969, [9], who described the importance of the correct timing of the machine's phases commutation in order not to produce a negative torque. This contribution was issued more than fifty years after the first patent describing what resembles a transverse flux, doubly salient machine by the Scottish engineer C.L. Walker in 1920, [10].

The first recorded radial flux machine with a doubly salient geometry was reported in 1927 for use on warships. It exhibited the same structure as a modern 6/4 SR machine, even though its phases were wired to a brush+drum system for manual phase commutation, [10]. Due to the inherent requirement for an independent commutation system, industrial interest soon faded, bringing this first era of the SR machine to an end.

With the advent of semiconductors, in particular the thyristor technology, the phase-commutation barrier started being overcome and industrial interest in this machine class bloomed again. Pioneering studies were mostly conducted by UK universities, i.e. Universities of Leeds, Nottingham, Glasgow and Newcastle, [11-14]. Due to the great work done in the decades from the 1960s to the late 1980's-early 1990's, this period is sometimes referred to as the 'Golden Age' of the SR machine.

In the early '90s, the burgeoning Permanent Magnets (PMs) market drove the electrical machine industry into the 'PM' era, where PM machines covered almost all the market demand of high-performance machines. However, in 2011–2012, the price of Dysprosium and Neodymium increased by almost an order of magnitude, due to the geopolitical concerns related to the security of supply, [15]. This crisis, along with concerns over the environmental sustainability of these materials, encouraged the

electrical machine industry to start looking again towards alternative solutions. Reduced PM designs, as well as PM-less solutions began to be investigated, or 'rediscovered. In particular, PM-less solutions sparked the beginning of the third age of the SR machine, which was fuelled by two main factors:

1) The remarkable improvements in the power converter technology, which overcame the commutation issues that had limited the growth of the SR drives over the previous decades,
2) The availability of more powerful computational resources that paved the way to Finite Element Analysis (FEA) methods, which soon became an indispensable design tool.

The long wave of the investigation started in the previous decade still keeps the interest in the SR machine well alive, with hundreds of scientific papers being published every year and several industrial applications implementing SR drives. Now, it is time for designers to look towards the challenges of the upcoming decade 2020-2030.

2.2 Design of Modern SR Machines: an Inherent Multiphysics Problem

By looking at the past, it is not difficult to guess what the future holds. In fact, development of the SR machine is inherently bonded to the developments in the power electronics. Nowadays, the semiconductor industry is experiencing the blooming of two wide-bandgap materials, i.e. the Silicon Carbide (SiC) and Gallium Nitrate (GaN). Many pieces of research demonstrate the suitability of SiC and GaN to operate continuously at much higher frequencies compared to the traditional Si-based devices, [16, 17]. Hence, similarly to the past, power electronics is expected to pave the way to a new era of SR machines.

In [18], C. Liu thoroughly identifies the most significant features that a modern electrical machine needs to possess. Considering the main strengths of the SR machines, along with its main fields of application, the most significant performance expected to characterise the next generation of SR machines are the following:

1) High Speed,
2) Extended Constant-Power Speed Range,
3) High Power Density and Efficiency.
4) Low Acoustic Noise.

The four points are thoroughly analysed in the Subsections below. Past works are gathered and analysed in order to provide an insightful viewpoint to acknowledge the main design challenges that each of the four aforementioned performance presents.

2.2.1 HIGH SPEED

In general, an electric machine's output power increases linearly with the speed of rotation, [19]. Therefore, increasing the speed of rotation is undoubtedly one of the most effective ways to reduce the machine's size for a given power rating, [20]. To this cause, high-speed technology is gaining an ever-increasing interest in the electrical machines' world.

Due to its simple and rugged, one-component rotor structure, the SR machine is by nature one of the most suitable candidates for high rotational speeds. Indeed, the absence of rotor features such as barriers or PMs, allows a well-designed SR machine rotor to reach the same rotational speed of a cylinder having the same rotor diameter.

For this reason, designers of aircraft starter generators started to look at the SR machine already in the 90's, [3, 21]. Then, the trend continued in the modern days for a wide range of applications, [1, 2, 5, 22-24], arriving to SR machine designed for going beyond one million rpm, [25, 26].

Operation at high speeds requires overcoming a variety of challenges. In [1, 2, 24], rotor teeth have been optimally shaped to improve the torque development at high speed, which is counteracted by huge back-emf levels. [5, 25] deal with the mechanical design of a low-mass two-pole rotor. Thorough mechanical assessment is necessary in both cases to safely operate at high speeds.

An important point to note is that both electromagnetic-oriented and mechanical-oriented works mentioned above show that the machine's performance is considerably sensitive to the same geometrical parameters. However, none of them provides a multiphysics overview of the design, meaning that mechanical robustness is not checked after the electromagnetic optimisation in [2], as well as electromagnetic performance are not evaluated in [25, 26]. In fact, as demonstrated in [24], several design iterations are usually required to satisfy both mechanical and electromagnetic constraints and requirements.

A final consideration concerned with high-speed electric machinery is that the B(H) characteristics of several electrical steels change considerably at different tensile strengths, [27]. Due to the doubly salient geometry, this phenomenon is particularly enhanced in SR machines. Even though past works normally neglected this change in magnetic properties, the high electric and magnetic loadings foreseen for the next-generation SR machines will force designers to take this aspect into account.

2.2.2 WIDE CONSTANT POWER SPEED RANGE

The SR machine is considered as one of the best machine classes in applications where the rated power must be developed across a wide constant power speed range (CPSR), [6], due to the absence of a physical back-emf generated by the rotor. However,

the CPSR is proportional to the ratio of the converter's VA rating and the machine's rated power.

In grid-connected applications, if voltage is rectified from a low-voltage line, DC-bus voltages available for the SR drive are in the range of 650-750V. Therefore, low and mid-power applications can easily extend their CPSR above six times the base speed, [28-30].

The scenario dramatically changes in mobile or stand-alone applications, where the DC-bus voltage level is dictated by a battery pack. To overcome this issue, in the last decade, various research groups attempted the development of a more advanced high-speed control strategy, named Continuous Conduction Mode (CCM). The idea is to control the switching pattern at high speeds in such a way that the phase current does not decay to zero at the end of each cycle, [31]. In this way, the magnetic core is kept constantly saturated, so that the lower inductance reduces the current rise and fall times, allowing for a better phase torque build up. As a result, the CPSR can be considerably enhanced, [32]. Following from that, considerable efforts have been put to integrate the CCM with the low-speed control strategies, [33, 34].

In terms of design, CCM-based SR machines have been widely explored, [35-38]. Unfortunately, to the best of the Author's knowledge, research on CCM has been interrupted around ten years ago. The reason was that the advantages provided by a CCM operation could not counterbalance its inherent disadvantages. One of them is the huge increase of copper and iron losses, [39]. Thus, even if from an electromagnetic point of view the CCM resulted extremely convenient, limitations imposed by the maximum temperature of operation blocked the development of this control strategy.

2.2.3 HIGH POWER DENSITY

Demand for high-power-density electrical machines, and hence SR machines, derives from the ever-increasing demand for portable applications. The two best examples are the automotive and aerospace fields.

As already observed, increasing the rotating speed is always an effective strategy to reduce the machine's size for a given power rating. On the other hand, high power density comes at the price of higher electric and magnetic loadings. This translates into highly saturated magnetic cores, [40], as well as high current densities. When losses come into play, both iron, [41], and AC copper losses, [42], are proportional to the fundamental frequency squared. Hence, if specific 'countermeasures' are not taken, possible drawbacks are the reduction of the efficiency and a difficult heat extraction, due to a higher amount of losses to be removed from a small surface.

Several solutions to enhance the heat extraction have been recently proposed, [42, 43], with particular attention paid to automotive applications, where water jackets seem to be the most convenient solution. Conversely, forced oil cooling is preferred in aircraft

applications, [1], where heat extracted from the electric machine is used to heat up the jet engine's fuel, [44]. In both cases, the critical aspect in the design of a high-power-density machine is to find the optimum share of the available volume between active and inactive parts.

Loss reduction is also addressed through the employment of high-performance materials. In recent years, novel solutions with lamination thicknesses below $0.1mm$ have been presented, [45]. However, the main drawback of low-loss materials is an abrupt decay in the mechanical robustness, which prevents them from reaching high rotational speeds, [46].

A possible solution to increase the power density in an SR machine is to use a fully-pitched winding arrangement, since it exploits the mutual coupling between phases, [47, 48]. As a rule of thumb, it can be said that for the same phase current, mutual inductance with fully pitched windings is around 1.5 times the self-inductance, the latter being responsible for the torque production in the conventional topology. However, the increase of a factor 1.5 in output power is the price to be paid. Fully pitched windings require the same end-winding configuration as AC machines, which results in an increased copper weight, higher copper losses and, for a given overall length, a reduced space for the lamination stack. As a consequence, fully pitched winding convenience must be investigated application by application.

A second solution proposed to increase the power density of the SR machine are the segmented rotors, [49-51]. With this rotor topology, rotor laminations are made up of segments, which resemble the rotor teeth, embedded or retained onto a structural-steel-made disc. However, this alternative arrangement requires a fully-pitched winding arrangement, [52, 53], whose pros and cons have already been discussed.

Segmented rotors are best in automotive applications, [54-57], due to the relatively reduced speed of rotation. In fact, the use of rotor segments for high-speed scenarios has not been yet completely verified, even though provisions for this to happen have been detailed in [58]. It is to note that the segment iron-loss, in view of very high number of strokes per revolution still has not been fully investigated. This scenario is only mentioned in [59].

2.2.4 Low Acoustic Noise

The doubly salient structure causes the SR machine to produced higher acoustic noise levels compared to AC machines. When a stator pole is supplied, it starts to attract the closest rotor pole. The tangential component of this attractive force generates the magnetic torque, while its radial component attracts the stator and rotor teeth towards each other, causing the stator to deform. Then, when the stator tooth is de-energised, the system returns to its relaxed configuration. This deformation /

relaxation cycle originates the stator vibrations which, in turn, are responsible for the machine's acoustic noise signature, [60, 61].

As the attractive force is directly driven by the phase current waveform, current shaping solutions are under investigation to mitigate the acoustic noise issues, as the reduction of the available torque is the main drawback, [62]. As observed, vibrational issues provide a further example of an interrelation and 'inter-limitation' between the '*physics*' involved in the SR machine.

2.2.5 DISCUSSION

The description around the four key design features of modern SR machines highlighted that any time an attempt to push the boundaries of the SR machine is made, at least two different physical phenomena interact with each other, with the effect of limiting the machine performance. Table 2-I provides a general overview of the phenomena involved in each design requirement. Following from this, the next Subsection analyses the most common design methodologies.

Table 2-I Physical phenomena interactions for each main design feature of modern SR machines.

	Electromagnetic	**Converter + Control**	**Thermal**	**Mechanical**
High Speed	X			X
Wide CPSR	X	X	X	
High Power Density	X		X	
Low Acoustic Noise	X	X		

2.3 DESIGN METHODOLOGIES FOR MODERN SR MACHINES

This Subsection analyses the different approaches that are currently used to tackle SR machine design. The intention is to understand their capabilities, limitations and thus acknowledge their suitability to satisfy the necessities of the next generation of SR machines.

Almost all design processes begin by attaining an initial 'sketch' design, by means of a sizing algorithm, [63-66]. This is usually a simple equation in the "Essen's" form: torque proportional to the bore diameter square. In this way, a first design of the magnetic core, airgap and the number of turns in normally achieved.

Then, it is common practice to devote the early design stages to a trade-off study, where several pole configurations and winding arrangements are compared, in a bid to identify the most appropriate solution. At this early design stage, only the heuristic method is used.

After the selection of an initial 'start-up' design candidate, the process enters the finalisation stage, in which the final design shall be determined in order to satisfy the entire set of constraints and requirements. Design finalisation can be carried out with two different approaches. With the first, the designer decides to carry on the design following a heuristic method, relying on his/her expertise and with the aid of FEA simulations. With the second, designers choose to be aided by an optimisation algorithm. These two finalisation strategies are discussed more in detail below.

2.3.1 TRADITIONAL HEURISTIC APPROACH

The heuristic approach has been probably used since humankind began to solve engineering-related problems. A definition of heuristic is as follows: "*Encouraging a person to learn, discover, understand, or solve problems on his or her own, by experimenting, evaluating possible answers or solutions, or by trial and error*".

In practical terms, if a designer follows the heuristic approach, the design is iteratively improved. At each iteration, usually no more than three design variables are modified. Then, the variation of the machine performance is acknowledged, and the next move is chosen accordingly. Most of the publications mentioned in Subsection 2.2 above adopt this kind of approach. The key point to note in almost all of them is that the modification of a design variable is chosen only in accordance with the electromagnetic performance. Subsequently, once a satisfactory electromagnetic design is achieved, designers move to the thermal and/or mechanical side to check that the design is feasible.

This practice has been proven to work quite well for relatively simple designs, where due to the weak interrelations between the '*physics*' involved in the design, it is perfectly reasonable to focus most of the efforts on the electromagnetic design. However, Subsection 2.2 pointed out that SR machines are going exactly in the opposite way, as the main challenge is exactly the tight bonding between all of the '*physics*' involved. Thus, the thinking pattern that drives a change in any of the design variables can no longer focus on the electromagnetic aspect only, since it might severely influence any of the other '*physics*'. Hence, the risk is that an unsustainable number of design iterations might be necessary to satisfy the full set of constraints and requirements to finalise the design, making this design approach highly ineffective.

2.3.2 OPTIMISATION-BASED APPROACH

In the last decade, the excellent improvements in the available computational resources paved the way to another solution to finalise the design, i.e. the computer-based optimisation algorithms, [67]. In this case, starting from the 'start-up' design candidate, the problem formulation begins. The first step is parametrisation. Usually, between two and eleven prime design variables are selected. For each of them, an upper

and a lower bound are chosen, defining the domain wherein the optimisation algorithm will move. A good overview of the optimisation algorithms found in the literature is given in [68]. The majority of these contributions employ stochastic algorithms to search for the optimal design, which requires the evaluation of a huge number of potential candidates. Each candidate is generated via a recombination of the aforementioned prime design variables. Thus, the machine geometry of each candidate is defined, and various performance indices are evaluated. This evaluation may be performed by: 1) FEA models,[69-78], 2) surrogate models, such as kriging, [76], or 3) analytical models, which may be based either on a Magnetic Equivalent Circuit, [79], or on the Maxwell's equations, [80]. Subsequently, the performance indices are assessed, and the stochastic algorithm recombines the prime design variables accordingly, in order to generate the next generation of candidates. The most common algorithms are the Genetic Algorithm (GA), [72, 73, 77], Particle Swarm Optimization (PSO), [75, 76, 79, 80], and the Differential Evolution (DE), [74], [78]. Optimal design is finally found by repeating the process described above for a predefined number of iterations.

The description above provides a clear picture of the design finalisation through optimisation algorithms. The designer's expertise is required only to formulate the optimisation problem, i.e. identify the prime design variables and their bounds. After that, a strongly automated process is started with no chance to step into it. Successful convergence of this kind of algorithm depends on two factors. The first, is the correct formulation. In fact, a PC does not possess the capability to detect inconsistencies or unfeasible aspects of each candidate. Hence, an incorrect problem formulation can be found only at the end of the process, with a huge waste of computation time. The second, is the random generation of the candidates, which might produce different final results for the same formulation. Hence, in cases where a relatively low number of feasible solutions is expected, it might be necessary to run the same optimisation several times to find the final solution just to understand whether the formulation is correct or not. Both factors do not represent a great issue if optimisation algorithms are used for the purpose they have been created for, i.e. select the best candidate among a population of almost all feasible ones. However, the scenario depicted in Subsection 2.2 points out that SR machines are going towards a direction where the number of feasible solutions drastically reduces, along with the chances of a successful optimiser's convergence. To this cause, an unsustainable number of attempts might be necessary before attaining a feasible finalised design (if any).

2.4 SR Machine Basics

In this Subsection, an elementary SR machine is analysed in order to highlight its salient geometrical, operating and electromechanical energy-conversion aspects.

2.4.1 PRINCIPLE OF OPERATION

The SR machine is generally referred to as a 'doubly salient' machine, due to the saliencies present in both rotor and stator. The basic operating principle of the SR machine derives from the merge of three different electric machines classes, i.e. Synchronous Machines, DC-Machines and Stepper Motors.

In conventional, rotating ac-machines, the electromechanical energy conversion process undergoes thanks to a rotating magnetic field, which is produced within the machine's airgap [81]. Conversely, in the SR machine, a quasi-rotating magnetic field is produced by supplying the stator coils in a rotor-position-based sequence, by means of a DC/DC converter. Figure 2-1 shows the basic geometry of an SR machine with 6 stator poles and 4 rotor poles. At the first instant of time, when the rotor is out of alignment with respect of the stator pole pair A-A' (Figure 2-1(a)), the latter is energized. Further to the current supply, a magnetic flux is generated through the aforementioned stator poles pair, as well as through the rotor pole pair R_2-R_2', causing these last to spontaneously align (Figure 2-1(b)). At this point, the situation described above repeats for the stator poles pair B-B' and the rotor poles pair R_1-R_1'. Thus, current is supplied to B-B' and the rotor moves again. With the poles' configuration at hand, it takes a sequence of three energisations to obtain a 90° rotation. In other words, one complete revolution is attained by supplying each stator pole pair as many times as the number of rotor poles, i.e. 4.

All the above, shows that the rotor velocity is imposed by the frequency at which the stator pole pairs are energised. Due to this behaviour, some pieces of literature classify the SR machine as a special kind of Synchronous Machine, [82]. Nevertheless, the sequence of the stator pole pairs energisations is in the opposite direction than the rotor movement, i.e. the clockwise energisation A-B-C corresponds to a counterclockwise rotor movement, which is typical of the Stepper Motors.

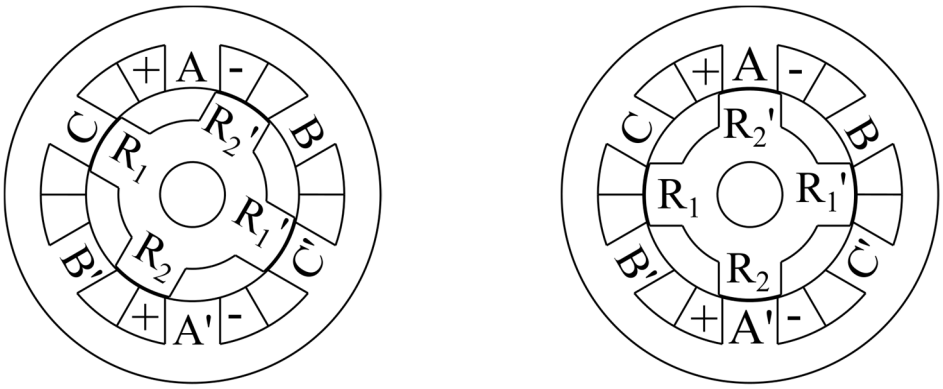

Figure 2-1 Basic geometry of a 6/4 SR machines.

2.4.2 ENERGY CONVERSION PROCESS

The torque production in the SR machine can be explained by applying the principle of electromechanical energy conversion in the elementary geometry shown in Figure 2-2(a). A solenoid made up of N turns is wound around a C-shaped iron yoke, which is fastened to a support that impedes its movement. Then, the iron-made armature is free to move and stands at a gap x. When the coil is energised with a current i, a magnetic flux φ is generated. In response to φ, a force $\boldsymbol{F}$ creates that moves the armature towards the yoke. Qualitatively, it is well-known that $\boldsymbol{F}$ grows in magnitude for higher coil currents and gaps. However, its exact evaluation is a non-trivial operation. Due to the absence of active components inside the rotor, the so called 'indirect approach' is used to evaluate this force, which is based on the Virtual Work Principle (VWP), [83].

The application of the VWP begins by assuming that the system being studied is lossless. Further to this hypothesis, it is possible to write the energy balance equation as in (2-1), which states that a variation in the electrical input energy dW_e is equal to the sum of the variations in energy stored into the magnetic field dW_f and the mechanical work dW_m.

$$dW_e = dW_f + dW_m . \tag{2-1}$$

dW_e is then expressed in terms of the induced electromotive force (emf) e, N, i and φ, as shown in (2-2).

$$dW_e = ei\ dt = Ni\frac{d\varphi}{\cancel{dt}}\cancel{dt} = Ni\ d\varphi . \tag{2-2}$$

Given that the armature moves only along the x direction, dW_m is by definition:

$$dW_m = F\,dx . \tag{2-3}$$

Thus, the variation in the field energy can be expressed by combining (2-1) to (2-3):

$$dW_f = dW_e - dW_m = Ni\ d\varphi - F\,dx . \tag{2-4}$$

Due to the hypothesis of absence of losses, the system at hand is *conservative*. Consequently, the value of W_f depends only by the values of φ and x and is the same

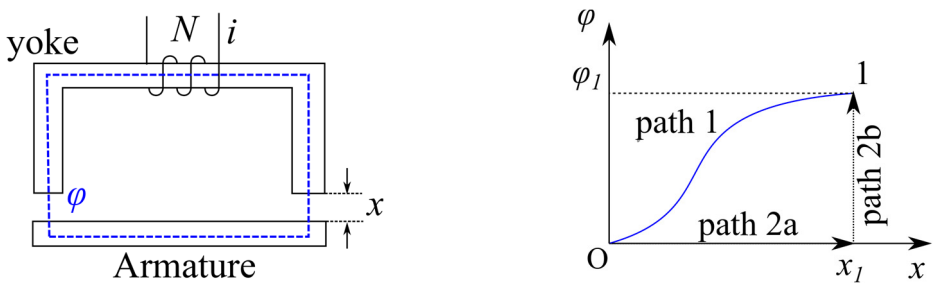

(a) (b)

Figure 2-2 Elementary geometrical scheme: (a) C-shaped yoke and armature outlook; (b) mmf vs. flux characteristics.

regardless of the path followed to arrive to any specific state. φ and x are therefore referred to as *state variables*.

Figure 2-2(b) is now considered. To attain the field energy of the system at point 1 W_f, infinite integration paths for (2-4) could be chosen. Path 1 represents the general case, which is impossible to integrate unless i and F are known functions of φ and x. However, path 2 is a valid option as well, which gives:

$$W_f(\varphi,x) = \int_{path\ 2a} dW_f + \int_{path\ 2b} dW_f \,. \tag{2-5}$$

Then, it can be noted that: 1) path 2a is flux-less, i.e. no magnetic energy is stored within the system $W_f=0$, and 2) path 2b is motionless, i.e. dx=0. In this way, (2-5) turns into (2-6), which expresses the field energy in terms of φ and i.

$$W_f(\varphi,x) = \int_0^{\varphi} Ni(\varphi,x)\,d\phi \,. \tag{2-6}$$

For practical reasons, the field energy W_f is commonly substituted with its complement, which is named co-energy W_f'. The idea is to manipulate the mathematical expressions developed above, in order to use i as state variable rather than φ:

$$dW_f' = d(Ni\varphi) - dW_f = Ni\,d\varphi + N\varphi\,di - dW_f \,. \tag{2-7}$$

By substituting (2-4) into (2-7), the energy balance expression is now rearranged in terms of co-energy, i and x.

$$dW_f'(i,x) = N\varphi\,di + F\,dx \,. \tag{2-8}$$

Thanks to the state functions properties, (2-8) can be rearranged as a sum of partial derivatives:

$$dW_f'(i,x) = \left.\frac{\partial W_f'(i,x)}{\partial i}\right|_x di + \left.\frac{\partial W_f'(i,x)}{\partial x}\right|_i dx \,. \tag{2-9}$$

At this point, since i and x are independent variables, φ and F can be evaluated by equating (2-8) and (2-9) term by term:

$$\begin{cases} \varphi = \dfrac{1}{N}\left.\dfrac{\partial W_f'(i,x)}{\partial i}\right|_x \\ F = \left.\dfrac{\partial W_f'(i,x)}{\partial x}\right|_i \end{cases} . \tag{2-10}$$

By analogy with (2-6), W_f' can be expressed in terms of i and x as shown in (2-11), being Ψ the coil's flux linkages:

$$W_f'(i,x) = \int_0^i \underbrace{N\varphi}_{\Psi}(i,x)\,di = \int_0^i \Psi(i,x)\,di \,, \tag{2-11}$$

which finally yields the expression of F in terms of i and x:

$$F(i,x)=\frac{\partial}{\partial x}\left(\int_0^i \Psi(i,x)\,di\right)\Bigg|_i . \tag{2-12}$$

By observing (2-8), (2-11) and (2-12), the physical meaning of the Virtual Work Principle can be acknowledged. (2-11) refers to a 'static' condition, where the armature does not move and a constant current flows through the coil. Hence, both terms in (2-8) are zero. The only physical way to maintain the condition above uninterruptedly is by applying a (virtual) force to the armature, in such a way as to prevent its movement. This retaining force is exactly the force $F(i,x)$ expressed by (2-12).

All the above provides the very general background of the energy-conversion principle of the SR machine. The more realistic case of a rotating SR machine is discussed in Chapter 5.

2.5 CONCLUSION

In the first part of this Chapter, the key feature for the design of the next-generation SR machines have been individuated: 1) High Speed, 2) Extended Constant-Power Speed Range, 3) High Power Density and Efficiency and 4) Low Acoustic Noise.

For each of them the most significant design contributions have been analysed. Result of the analysis is that the trend is going towards a direction where '*physics*' involved in the SR machine design are all tightly bonded, with the result of a high-complexity design with few expected solutions.

In the Second part, the most common design approaches have been analysed, i.e. heuristic and optimisation-based. Both approaches have been analysed and the result is that none of them, in its actual state, can provide an effective tool to cope with the highly-complex design problems of modern SR machines.

The conclusion is that a different design approach is required in order to address effectively the design of the SR machines over the upcoming decade 2020-2030. As a response, this thesis proposes a novel design approach based on the definition of the Actual Design Space (ADS), which is described in Chapter 3.

3 THE ACTUAL DESIGN SPACE METHODOLOGY: GENERAL DESCRIPTION AND IMPLEMENTATION TO THE SR MACHINE

3.1 INTRODUCTION

This Chapter is concerned with the description and the discussion of the Actual Design Space (ADS) methodology, along with its implementation for an SR machine. To the best of the Author's knowledge, this methodology has never been proposed before, not only in the electrical machines' field but in any other engineering field. For this reason, this Chapter is aimed at introducing and thoroughly describe the ADS. In the first part, the general statement of the ADS from a very general perspective, even though some specific remarks about electric machines designs are made. In the second part, the method is applied to the specific case of the SR machine, discussing both the 'Internal' and 'External' Stages that compose the methodology.

3.2 MATHEMATICAL FORMULATION OF THE DESIGN PROBLEM

This Section is devoted to the mathematical formulation of the design problem. Even though the latter is already well-know, the main objective is to provide a rigorous nomenclature of the most defining aspects of the design problem. This is essential to achieve a clear understanding of the proposed ADS method and avoid any confusion that may arise because of the different terminologies adopted across the literature.

The design process is generally defined as the process by which a problem is identified, understood, and addressed through design. From an engineering perspective, the problem is characterised by a specific number of Design Variables n: x_1, x_2,., x_n, which are defined as follows:

Design Variable (DV): *'quantity that the designer can deliberately choose to manipulate to achieve the final solution, and which is free to vary within a set of feasible values named Domain'.*

Picking one value from the domain of each DV, then this combination can be easily interpreted as an *n*-dimensional vector $\mathbf{X}^n$ where each DV corresponds to a vector's component:

$$\mathbf{X}^n = (x_1, x_2, \ldots, x_n), \quad being\ n \in \mathbb{Z}.$$

Then, if the set of all possible vectors $\boldsymbol{X}^n$ is considered, an n-dimensional space is generated. Considering the way it has been defined, this space contains every possible candidate to the final solution. Hence, it is the space wherein the designer will move to solve the design problem and thus is referred to as the Design Space:

Design Space (DS): *'space containing every possible candidate to the final solution, and thus the space wherein the designer moves to achieve it.*

The *n* DVs are not independent from each other. Indeed, they are interrelated by a set of *k* equations, named Internal Relationships (IRs):

$$\begin{cases} IR_1(x_1, x_2, \ldots, x_n) = a_1 \\ IR_2(x_1, x_2, \ldots, x_n) = a_2 \\ \vdots \\ IR_k(x_1, x_2, \ldots, x_n) = a_k \quad being \quad a_1, a_2, \ldots, a_k \in \mathbb{R} \end{cases},$$

Internal Relationship (IR): *'equation that relates two or more Design Variables to each other'.*

The term 'Internal' denotes the fact that these equations are given only by the characteristics of the device itself (e.g. by the specific class of electric machine). In other words, they are not at all related to the specific application, nor to the nameplate data.

When the specific application is taken into account, constraints and requirements come into play. Due to the fact that the two terms are sometimes confused with each other, this thesis follows the two definitions below:

Constraint (Cnt): *'Limitation to the feasible values of one Design Variable, or a combination of Design Variables, that arises from any sort of physical limitation'*,

Requirement (Rqm): *'Limitation to the feasible values of one Design Variable, or a combination of Design Variables, that arises from any sort of demanded performance'.*

If the design of an electric machine is considered, examples of Cnts are the maximum temperature allowed by the insulating materials, the maximum tensile strength of a structural material, etc. On the other hand, examples of Rqms are the demanded torque, the peak power, the maximum speed of rotation, etc.

In their most general form, Cnts and Rqms are both expressed by q inequations, named External Relationships (ERs), even though there exist cases where a Cnt and/or a Rqm is so strict that its related ER turns into an equation:

$$\begin{cases} ER_1(x_1,x_2,\ldots,x_n) \geq b_1 \\ ER_2(x_1,x_2,\ldots,x_n) = b_2 \\ \vdots \\ ER_m(x_1,x_2,\ldots,x_n) \geq b_m \quad being \quad b_1,b_2,\ldots,b_m \in \mathbb{R} \end{cases},$$

External Relationship (ER): *'inequation that limits or equation that fixes the feasible values of one or more Design Variable, due to either a Constraint or a Requirement'.*

The term 'External' denotes the fact that this set of inequalities depends on 'external' factors, i.e. the specific applications. Therefore, the q ERs have to be redefined any time a new design is undertaken.

Once the n DVs, the k IRs and the q ERs have been defined, the solution to the design problem can be found. The solution(s), if available, consists in one (or more) n-dimensional vector $\mathbf{X}^{n\_sol}$ that obeys to the entire set of k IRs and q ERs.

3.3 ADS Method Overview

Section 3.2 rigorously stated the design problem from a mathematical perspective. As said in the Introduction, this thesis addresses designs where the ERs dramatically reduce the number of possible $\mathbf{X}^{n\_sol}$.

For the particular case of the electric machines design, the ERs derive from the three '*physics*' involved, i.e. electromagnetic, thermal and mechanical, which are well-known for requiring long and computationally expensive FEA processes. For this reason, rather than 'jumping' to the final solution via FEA, the proposed idea is to introduce a preliminary stage ahead of the FEA stage. In this preliminary stage, a 'convenient' neighbourhood of the set of final solutions is identified basing on the IRs and ERs, i.e. the ACTUAL DESIGN SPACE (ADS). Figure 3-1 schematically represents the idea.

Following from the above, once the ADS has been defined, its outer edge encloses the

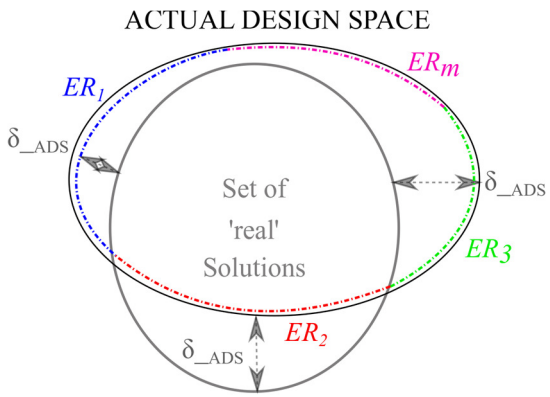

Figure 3-1 Graphic representation of the Actual Design Space.

portion of space populated by the potential solutions of the design problem. The outer edge determination constitutes the greatest challenge of the ADS method, since it comes from the evaluation of the ERs. Assuming that FEA solutions are 'perfect', if the q ERs were evaluated via FEA, the ADS would match with the set of 'real' solutions and the design problem would be already solved. However, an FEA evaluation of the ADS would give absolutely no advantages compared to the other design methodologies. To this end, the ERs shall be evaluated by means of analytical models, so that the computation time to determine the ADS remains negligible compared to any FEA process. On the other hand, analytical models introduce a discrepancy (error) compared against their FEA counterparts. As a result, the discrepancies introduced by the analytical models result in a 'clearance' δ_{ADS} between the outer edge of the analytically-determined ADS and the outer edge of the set of real solutions, as Figure 3-1 illustrates.

The existence of δ_{ADS} remarks the fact that the ADS method is not aimed at solving the design problem. Indeed, the method's goal is to find a 'convenient' space wherein to move to solve the design problem at a second stage. With different terms, the ADS can be defined as a particular DS, which is generated by maximising the probability that each of its members is a solution.

Actual Design Space (ADS): *'Design Space determined with the intention of maximising the probability that each of its members is a solution of the design problem'.*

To build up the ADS, a two-stage process must be followed. These steps are named in this thesis 'Internal Stage' and 'External Stage' and are described in Subsections 3.3.1 and 3.3.2 below.

3.3.1 INTERNAL STAGE

In the Internal Stage, the relationship between the DVs and the IRs is considered. In particular, the process begins with the rigorous count of the n DVs, along with the k IRs that relate them to each other. At this point, it is easy to observe that only a certain number of DVs are independent. The number of Independent Design Variables (IDVs), indicated with r, is given by the difference between the total number of DVs and the number of IRs, as expressed in (3-1):

$$IDVs \triangleq DVs - IRs \;\rightarrow\; r = n - k\,. \tag{3-1}$$

In different words, r defines the correct dimension of the ADS, meaning that the ADS is populated by r-dimensional vectors $\mathbf{X}_{ADS}{}^{r}$:

$$\mathbf{X}_{ADS}{}^{r} = (x_1, x_2, \ldots, x_r) \quad being\ r \le n,\ r, n \in \mathbb{Z}\,.$$

The Internal Stage concludes with the selection of r DVs to be used as independent, out of the n available. This task cannot be addressed with an automated process but is entirely driven by the designer's expertise.

Table 3-I Example of 'Rectangular' DS represented in a Table.

IDV	Upper Bound	Lower Bound	Discr. Step
x_1	x_{1_max}	x_{1_min}	Δ_1
x_2	x_{2_max}	x_{2_min}	Δ_2
⋮	⋮	⋮	⋮
x_r	x_{r_max}	x_{r_min}	Δ_r

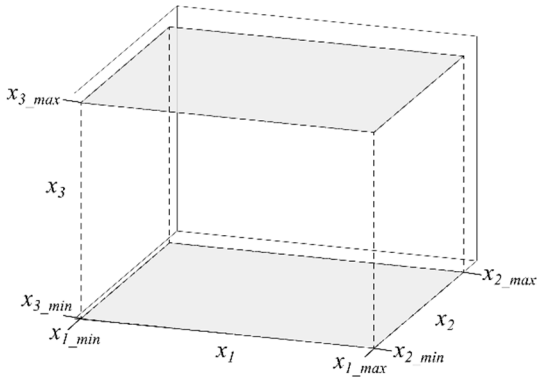

Figure 3-2 Parallelepiped representing a 3D 'rectangular' DS in the 3D case.

3.3.2 External Stage

In the External Stage, the domains of the r IDVs chosen at the end of the Internal Stage are considered.

At the very beginning, the ERs that provide an explicit upper or lower bound to one IDV are considered, such as in the following example:

$$ER_i: \; x_i \geq a \;\; being \; i \in \mathbb{Z}, \; a \in \mathbb{R},$$

These ERs are used to determine the minimum and maximum values for each of the r IDVs. Typical examples are the maximum machine's outer diameter or maximum axial length. Conversely, for those upper and/or lower bounds that cannot be found through the ERs, good engineering judgement shall be used. In addition, if discretised variables are used, then the step of discretisation must also be chosen. At the end of this process, the initial DS is attained. Due to the fact that the upper and lower bounds of the IDVs are not related to each other, this initial DS is referred to as '*rectangular*'. In most cases found across the literature, rectangular DSs are represented in the form of a table, as shown in Table 3-I. Figure 3-2 gives a graphic illustration of a rectangular DS in 3D, which is a parallelepiped.

After the determination of the initial DS, the remaining ERs are taken into account. One aspect that rectangular DSs do not take into account is that the domains of the IDVs are not constants. In fact, most of the ERs involve more than one IDV. Consequently, the maximum and minimum values of each IDVs are functions of other

IDVs. To explain this concept, the following simple design problem is considered. Three ERs define a two-dimensional DS; x_1 and x_2 are the IDVs, and it results:

$$\begin{cases} ER_1 : x_1 > x_2 \\ ER_2 : x_2 > a_2 \\ ER_3 : x_2 < -b_2 x_1 + c_2 \quad being \ a_2, b_2, c_2 \in \mathbb{R} \end{cases}.$$

Figure 3-3 provides the graphic representation of the resulting DS. The plot shows that the domain of x_1 is a function of x_2 and vice versa. In particular, it is observed that the domain of x_1, i.e. $x_1 \in \left(x_{1\_min}(x_2),\ x_{1\_max}(x_2)\right)$, progressively decreases as x_2 increases. Eventually, for x_2=x_{2_max}, only one feasible value of x_1 remains. The rectangular DS defined by the points (x_{1_min}, x_{2_min}), (x_{1_min}, x_{2_max}), (x_{1_max}, x_{2_max}) and (x_{1_max}, x_{2_min}) and the triangular DS marked in blue are now considered. From simple geometric considerations, one observes that the triangle area is half the rectangle area. In other words, the passage from the rectangular DS to the triangular DS alowed a reduction of 50% in the number of potential candidates to the solution of this simple design problem.

The example above demonstrates the importance of considering the ERs when embarking on a design process and thus the importance of finding the outer edge of the DS.

Generally speaking, the outer edge of the ADS is given by the overlapping of the limitations given by each of the q ERs. To generate the outer edge of the ADS, the ERs are considered one by one. For each ER, the associated equation is solved in the r-dimensional space. Then, the solution identifies an r-dimensional surface, which separates the portion of space populated by the candidates that comply with the Cnt or Rqm at hand, from those which do not.

Hence, starting from the initial rectangular DS, the progressive introduction of the ERs corresponds to a progressive reduction of volume of the DS. Once the q^{th} ER has been introduced, the space left, if any, identifies the ADS. In addition, the composition of the outer edges provided by each of the ERs identifies the ADS outer edge.

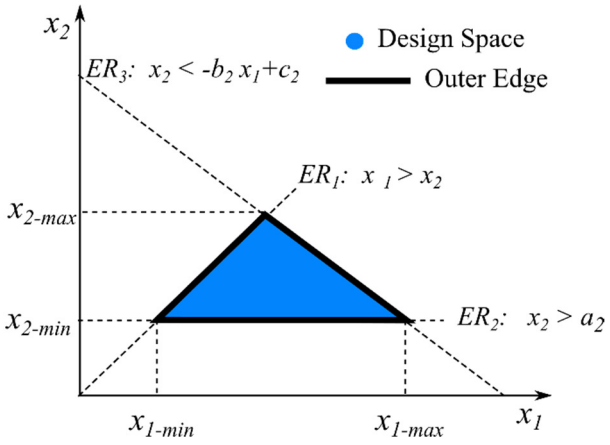

Figure 3-3 Example of non-rectangular DS.

An example of the process to achieve the ADS is shown in Figure 3-4. The initial rectangular DS is that illustrated in Figure 3-4. This example is taken from the Author's own work [84], for the design of an SR Starter/Generator. As one can observe, the introduction of the i^{th} ER corresponds to the i^{th} DS, indicated with DS^i. At the end of the process, the ADS is attained.

In the example above, the relevant fact is that the evaluation of the ADS allowed the reduction of the initial rectangular DS volume, i.e. the number of potential solutions, of more than the 99%.

All the above illustrated the two stages to determine the ADS. Subsection 3.3.3 provides a further discussion about the ADS representation.

3.3.3 ADS REPRESENTATION

The different approaches that can be followed to represent the ADS are now analysed more in detail.

The Author wishes to highlight that the ideas proposed in this Subsection are at a very early stage of development. The implementation of more sophisticated multidimensional representations is therefore a critical aspect of the future work.

In accordance with the specific design case, two possible representations of the ADS are proposed:

1. **Representation by Surface** The representation by surface is that adopted to

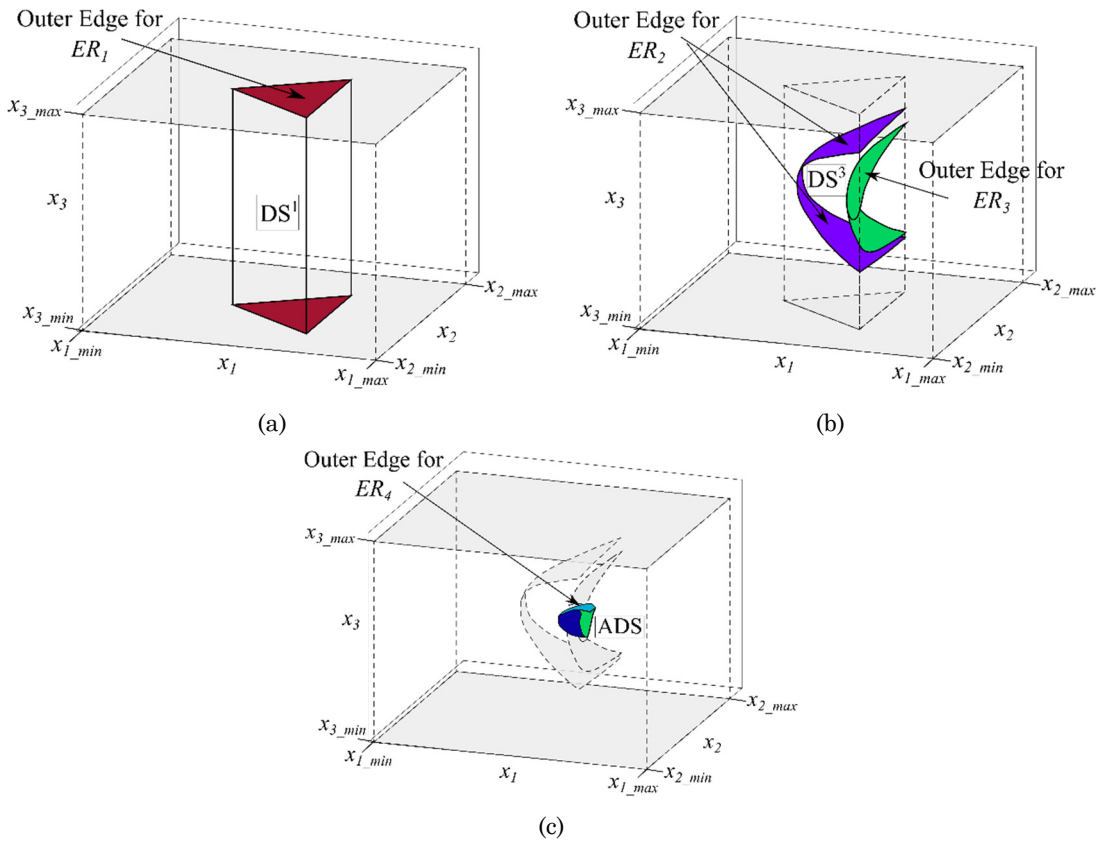

Figure 3-4 Example of ADS determination from a rectangular DS.

illustrate the ADS in Figure 3-4. In this case, the outer edge of the ADS is represented via a composition of surfaces, where each surface is expressed by an analytical or numerical equation. This representation is particularly suitable when the ERs can be easily expressed mathematically. Moreover, this representation is also preferred when a low number of continuous IDVs is considered, i.e. two or three. A representation by surface is also possible with discretised IDVs. In this case, a meshing algorithm may be used to joint all of the discrete surface points. Figure 3-5 illustrates the simple example of a 3-D triangular mesh.

2. **Representation by Cluster**. This kind of representation can be used when the IDVs are discretised variables. In this case, the initial rectangular space is divided into a finite number of points as shown in Figure 3-6 (a). Then, each point is considered individually all the way through the ADS generation. When the 1st ER (ER_1) is introduced, the inequality is verified at each point inside the rectangular DS. Then, those points where the ER_1 is satisfied compose the cluster of points defining the DS^1. The process repeats for all the other ER, as that the cluster of points progressively reduces. Finally, the cluster left at the end of the process defines the ADS. Figure 3-6 illustrates the same process to achieve the ADS represented in Figure 3-4, this time with a cluster representation. In particular, points that comply with the ER under consideration are marked in blue. Conversely, those that are discarded are marked in cyan. Figure 3-6 (b) shows the introduction of ER_1, Figure 3-6 (c) the introduction of ER_2 and ER_3 and finally, Figure 3-6 (d) depicts the introduction of ER_4 and the ADS.

Once the ADS has been properly represented, the designer is in the position to begin with the design finalisation via FEA. Different solutions to complete the process are discussed in Subsection 3.3.4 below.

3.3.4 DESIGN FINALISATION

As stated in the Subsections above, one of the main advantages of the ADS methodology is that its definition aids the designer in the identification of the most effective strategy to finalise the design.

A first observation is that since the ADS definition is run entirely by computationally cheap algorithms, no relevant drawbacks are incurred if the proposed methodology is adopted. On the other hand, significant advantages are provided. The first, is that it is possible to verify if the specifications are consistent, even from this initial design stage. In other terms, it is possible to verify that the design is feasible.

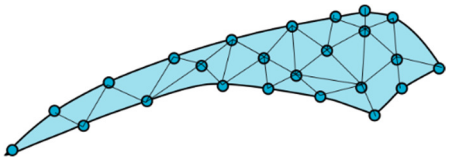

Figure 3-5 Example of triangular mesh of a portion of outer edge.

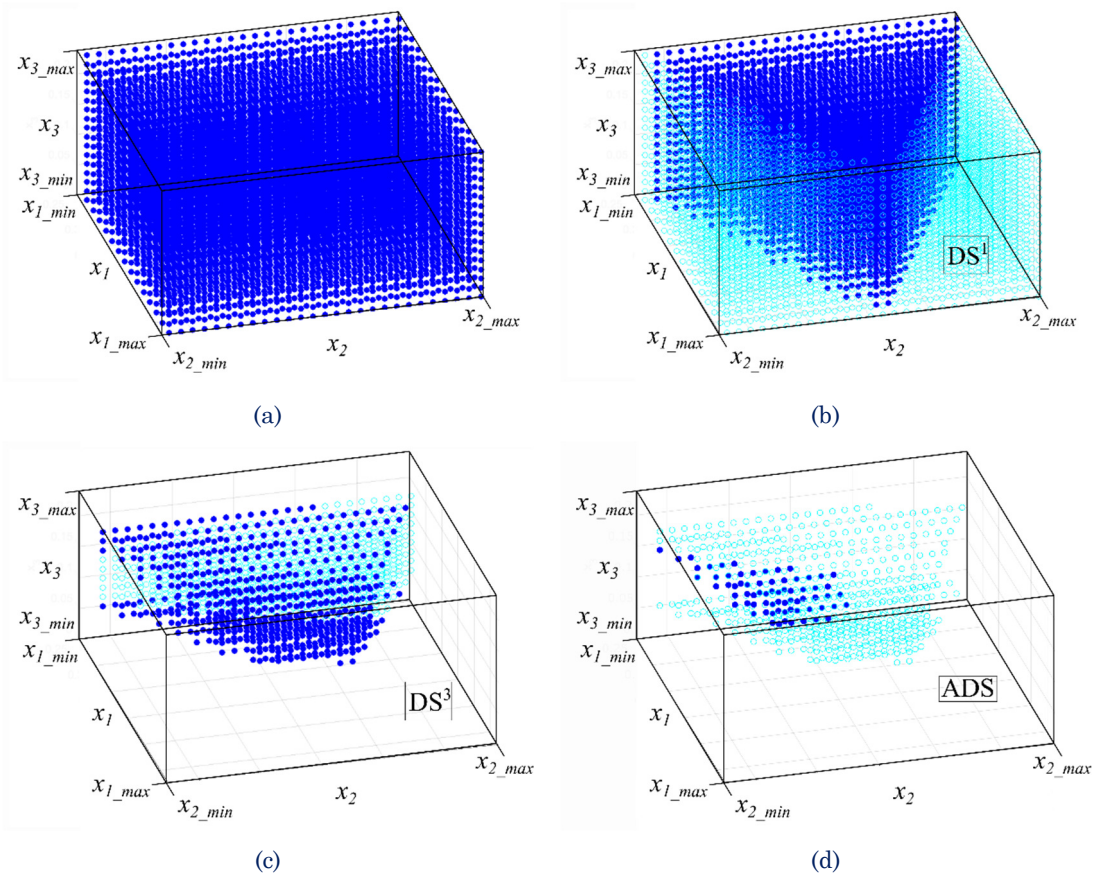

Figure 3-6 Cluster representation of the ADS proposed in [84] and represented in Figure 3-4.

Indeed, in case an empty ADS is found, designer is prevented from spending precious time and effort on the solution of an impossible problem and immediately reconsider the

set of Cnts and Rqms. Conversely, if a non-empty ADS is found, the designer can select the best strategy to complete the design. Some examples are given below:

1. If the ADS found has a small population, and the computational cost is reasonable, the designer can take into consideration the idea of evaluating through FEA the entire ADS, or conduct the rest of the design process in an heuristic manner.
2. If the ADS found has a conspicuous population, an optimization algorithm may be used. In this case, one opportunity could be to explore the ADS, following a grid-partitioning approach. Another possibility could be the implementation of an evolutionary algorithm. However, as the ADS is generated by discarding all of the unfeasible candidates, the evolutionary algorithm can be constrained to move within the ADS. In this way, the formulation of the optimisation problem is drastically reduced and successful convergence is likely to be achieved even at the first attempt.

3.3.5 ADS CLEARANCE

This Subsection provides some final comments about the effects that the analytical models used to generate the ADS.

Firstly, the kind of mathematical models used strongly affects the computational time required to generate the ADS. As previously stated in this Chapter, it would be desirable that the time required to generate the ADS is negligible compared to any further FEA process. As a rule of thumb, the Author proposes that the computation time to derive the ADS shall be smaller or equal than the time required by one FEA iteration, i.e. below two hours.

Secondly, mathematical models affect the clearance δ_{ADS} between the ADS and the set of 'real' solutions (see Figure 3-7). Clearance depends on the fact that the mathematical model underestimates or overestimates a physical quantity. Hence, since different portions of outer edge are the results of different models, δ_{ADS} is likely to vary across the entire outer edge. In particular, the sign of δ_{ADS} can be used to describe the way the ADS and the outer edge of the 'real' solutions intersect with each other. In this regard, the Author proposes the following convention, which is also illustrated in Figure 3-7:

- Case $\delta_{ADS} > 0$, indicates that the ADS outer edge contains the outer edge of the 'real' solutions. This fact means that the portion of ADS being considered contains some members that do not comply with the ER under consideration.
- Case $\delta_{ADS} < 0$, indicates that the outer edge of the ADS is contained inside the outer edge of the set of 'real' solutions. In this case, the error made by the mathematical model excludes from the ADS some candidates that would actually comply with the ER at hand.

All the above indicates that the underestimation or the overestimation of a physical quantity might affect the probability to arrive to the final solution. This aspect is particularly relevant for designs where the ADS is expected to have a very small volume (small number of potential candidates). Therefore, apart from quantifying the error introduced by each model, it is important to acknowledge the clearance sign as well.

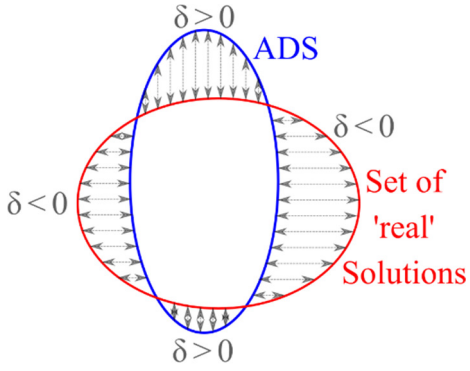

Figure 3-7 Example of triangular mesh of a portion of outer edge.

3.4 ADS OF AN SR MACHINE: INTERNAL STAGE

This Section is devoted to the description of the Internal Stage of an SR machine ADS determination. The main objective is the enumeration of the DVs that define the design of an SR machine, along with the IRs that link them to each other. The analysis considers the SR machine geometry, electromagnetic and thermal aspects, which are discussed respectively in Subsections 3.4.2, 3.4.3 and 3.4.4. Finally, Subsection 3.4.6 provides the final count of the electromagnetic+thermal IDVs.

3.4.1 MATERIALS

The design of an SR machine requires the selection of the following materials: 1) ferromagnetic material of the stator and rotor laminations, 2) materials for the winding and insulation and 3) high-strength steel for the structural components, e.g. the rotor shaft. Each material is potentially one IDV. However, materials' properties cannot absolutely be considered likewise standard design variables, since they cannot vary at will. The only way to account for different materials combinations, is to start a completely new design for each possible combination and subsequently compare the results. In the case of the proposed methodology, one ADS should be determined for any desired materials combinations and subsequently sum all of them up. Further to that, one materials' combination is sufficient to develop and discuss the ADS methodology. Therefore, in the course of this thesis, materials' combination is taken as an already made choice, so that all of the material-related quantities are considered to be known. In case a material property is a function of one or more IDV, such as the magnetic permeability, extreme care should be paid during the modelling process.

Finally, it is observed that the slot fill factor f_{CU} acts exactly as if it were a material. In fact, f_{CU} depends on the manufacturing process and designers can only opt between one winding technology or another. Therefore, in the rest of this thesis, f_{CU} is assumed as a known quantity.

3.4.2 GEOMETRIC DESIGN VARIABLES

This Section analyses the geometry of a standard SR machine. The term standard denotes that the machine has straight stator teeth and that there are not special features, such as chamfers, fillets, etc., neither in the stator nor in the rotor.

3.4.2.1 STATOR GEOMETRY

Figure 3-8(a) provides an illustration of the stator of an SR machine. The stator geometry counts nine DVs, which are reported in Table 3-II. The nine stator DVs are linked to each other through the four IRs given by (3-2) to (3-4). Hence, according to (3-1), the stator geometry provides five IDVs.

The stator slot angle β_{ss} is defined as the angle between two adjacent teeth. Then, the slot can either be filled with two different phases, if the traditional concentrated

winding is adopted, or with only one phase, if the distributed windings is used, [52]. Figure 3-10 illustrates the two winding typologies.

$$\zeta_s = \frac{2\pi}{N_s}, \tag{3-2}$$

$$OD = D_s + 2\left(h_{st} + b_{sy}\right), \tag{3-3}$$

$$\beta_{ss} = \zeta_s - \beta_{st}. \tag{3-4}$$

For the slot area expression A_{ss}, the slot geometry is zoomed in in Figure 3-8(b). A simplified yet accurate analytical expression of A_{ss} is found by approximating the length of the top stator slot arc l_{top_arc} and of the bottom slot arc l_{top_arc} by (3-5) and (3-6) respectively. Therefore, the slot area can be accurately approximated by (3-7).

$$l_{top\_arc} \cong \left(\frac{D_s}{2} + h_{st}\right)\zeta_s - \frac{D_s}{2}\beta_{st} = \frac{D_s}{2}\beta_{ss} + h_{st}\zeta_s, \tag{3-5}$$

Table 3-II Stator DVs.

	DV	Symbol
1	Stator Slot Area	A_{ss}
2	Stator Yoke Thickness	b_{sy}
3	Stator Bore Diameter	D_s
4	Stator Tooth Height	h_{st}
5	Stator Teeth Number	N_s
6	Outer Diameter	OD
7	Stator Tooth Angle	β_{st}
8	Stator Slot Angle	β_{ss}
9	Stator Pitch Angle	ζ_s

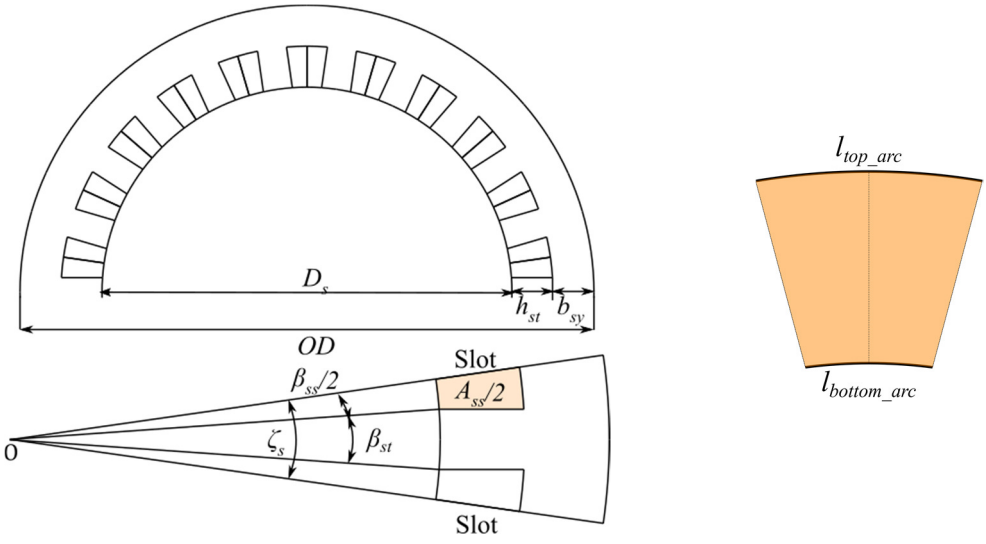

(a) (b)

Figure 3-8 a) Illustration of the stator geometry DVs; b) stator slot geometry.

$$l_{bottom\_arc} = \frac{D_s}{2}\beta_{ss}, \tag{3-6}$$

$$A_{ss} = \frac{h_{st}}{2}\left(D_s\beta_{ss} + h_{st}\zeta_s\right), \tag{3-7}$$

3.4.2.2 ROTOR GEOMETRY

Figure 3-9 shows that eight DVs characterize the SR rotor, as reported in Table 3-III. The DVs of the rotor geometry are related to each other by (3-8) and (3-9). Hence, the number of rotor IDVs is six.

$$\zeta_r = \frac{2\pi}{N_r}, \tag{3-8}$$

$$D_r = D_{sha} + 2\left(h_{rt} + b_{ry}\right). \tag{3-9}$$

3.4.2.3 FULL ASSEMBLY

Five further DVs belong to the full machine assembly. These are listed in Table 3-IV. An illustration of the front-view of the full assembly is given in Figure 3-10 (top), whilst the axial view is depicted in Figure 3-10 (bottom). Finally, (3-10) to (3-13)

Table 3-III Rotor DVs.

	DV	Symbol
10	Rotor Yoke Thickness	b_{ry}
11	Rotor Outer Diameter	D_r
12	Rotor Shaft Diameter	D_{sha}
13	Rotor Tooth Height	h_{rt}
14	Rotor Teeth Number	N_r
15	Rotor Tooth Angle	β_{rt}
16	Rotor Pitch Angle	ζ_r
17	Rotor Tooth Tilt Angle	γ_{rt}

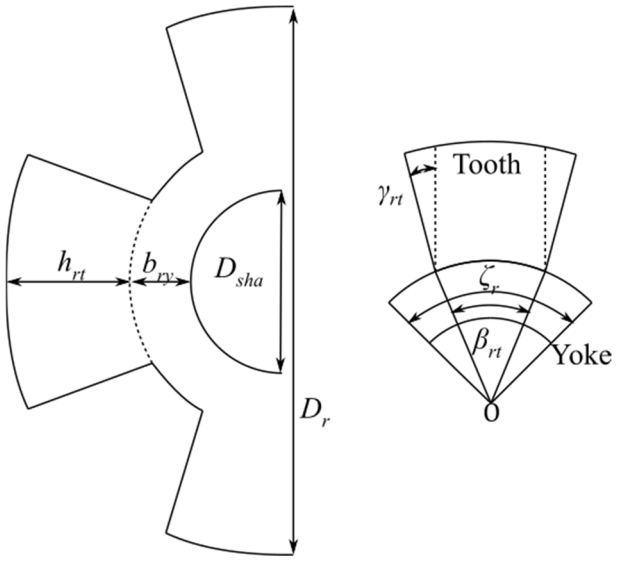

Figure 3-9 Illustration of the rotor geometry DVs.

interlink the full assembly DVs, so that two further IDVs are provided. Figure 3-10 includes also the shaft length L_{sha}. However, it is common practice to set L_{sha} at the minimum possible value, based on rotor dynamics limitations and the fitting of bearings. Therefore, for the analysis being conducted, it possible to consider L_{sha}. This last can be expressed as the sum of the stack length L_{stk} and an axial over length ΔL_{ax}, which usually depends on several factors such as the bearings housings, the end-windings' overhang lengths, etc. As a first initial approximation, all of these factors can be considered as material-dependent, so that ΔL_{ax} can be assumed as a known quantity as well; therefore, ΔL_{ax} can be excluded from the count.

$$l_g = \frac{D_s - D_r}{2}, \tag{3-10}$$

$$N_s = 2Pm, \tag{3-11}$$

$$m = \frac{lcm(N_s, N_r)}{N_r}. \tag{3-12}$$

Table 3-IV Full-Assembly DVs.

	DV	Symbol
18	Air Gap	l_g
19	Axial Stack Length	L_{stk}
20	Number of Phases	m
21	Number of Repetitions	P
22	Shaft Length	L_{sha}

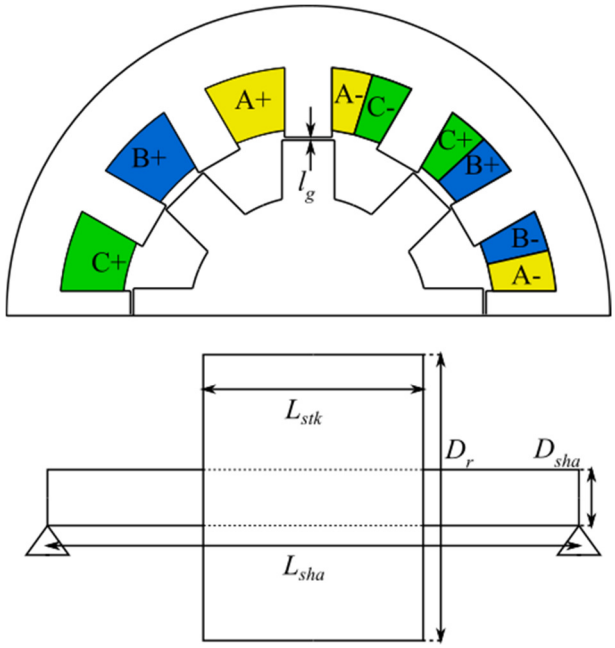

Figure 3-10 Top) Representation of a three-phase, two-repetition SR Machine; the right-hand side shows a conventional, concentrated winding configuration, whilst the left-hand side an example of the fully-pitched. Bottom) axial scheme of the full assembly of an SR machine.

$$L_{sha} = L_{stk} + \Delta L_{ax} \tag{3-13}$$

3.4.3 ELECTRIC AND MAGNETIC DESIGN VARIABLES

This Section defines and counts the electric and magnetic DVs and IRs. The enumeration is based on the magnetic circuit considered at the fully aligned position and in conditions of deep saturation, [40], as represented in Figure 3-11.

3.4.3.1 MAGNETIC CIRCUIT

The magnetic circuit defines six electric and magnetic DVs. They include the stator slot current density J_{ss} and the magnetic flux density B in each of the five sections of the magnetic circuit. Two more geometric DVs, i.e. the stator and rotor yoke average path lengths l_{sy}, and l_{ry}, are needed to fully define the path of the flux lines, which are expressed by (3-14) and (3-15):

$$l_{sy} = m\left(\zeta_s - \beta_{st}\right)\left(\frac{D_s}{2} + h_{st} + \frac{b_{sy}}{2}\right), \tag{3-14}$$

$$l_{ry} = \frac{N_r}{2P}\left(\zeta_r - \beta_{rt}\right)\left(\frac{D_r}{2} - h_{rt} - \frac{b_{ry}}{2}\right). \tag{3-15}$$

The full set of DVs is reported in Table 3-V. In addition, the IRs are given by Ampere's and Gauss' equations.

Ampere's equation is given by (3-16), where:

$$J_{ss}A_{ss}f_{CU} = 2\frac{B_{st}}{\mu_{st}}h_{st} + 2\frac{B_g}{\mu_0}l_g + 2\frac{B_{rt}}{\mu_{rt}}h_{rt} + \frac{B_{sy}}{\mu_{sy}}l_{sy} + \frac{B_{ry}}{\mu_{ry}}l_{ry}, \tag{3-16}$$

f_{CU} is the copper fill factor,

μ_{st} the stator tooth average magnetic permeability,

μ_{rt} the rotor tooth average magnetic permeability,

μ_{sy} the stator yoke average magnetic permeability,

μ_{ry} the rotor yoke average magnetic permeability.

It is observed that a simplification is made in (3-16). In fact, flux tubes that leave a stator tooth follow a curvilinear path when they enter the back-iron and are far from being parallel. As a result, flux density within the back-iron region is not constant. In order to take this aspect into account and keep the analytical expressions at their simplest, only the yoke portion comprised between the edges of two stator teeth is considered in (3-16), which is marked in grey in Figure 3-11, wherein flux density is constant and equal to its maximum. Results provided in the next chapters prove the validity of this assumption.

As discussed, all the permeabilities above are known material-dependent parameters. Similarly, l_{sy} and l_{ry} are functions of previously defined geometric quantities, which are expressed by (3-14) and (3-15).

Gauss' equations states that the flux passing through one pole φ_{pole} is constant. Then, by expressing φ_{pole} as a function of the stator pole geometry and flux density:

Table 3-V Electric and Magnetic DVs.

	DV	Symbol
23	Stator Slot Current Density	J_{ss}
24	Stator Yoke Average Magnetic Flux Density	B_{sy}
25	Stator Tooth Average Magnetic Flux Density	B_{st}
26	Mid-Airgap Average Magnetic Flux Density	B_g
27	Rotor Tooth Average Magnetic Flux Density	B_{rt}
28	Rotor Yoke Average Magnetic Flux Density	B_{ry}
29	stator yoke average path length	l_{sy}
30	rotor yoke average path length	l_{ry}

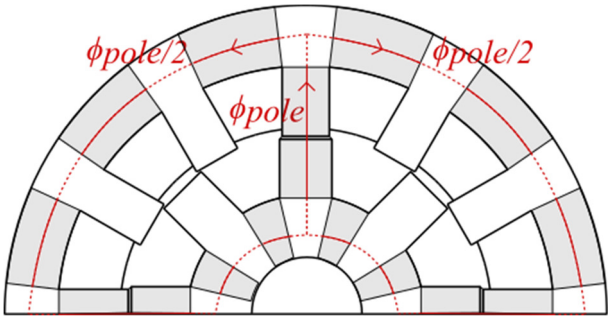

Figure 3-11 Representative flux line of the aligned, saturated magnetic circuit of the 12/8 machine represented in Figure 3-10.

$$\phi_{pole} = \left(B_{st} D_s \beta_{st} L_{stk}\right) / 2$$

(3-17), (3-18) and (3-19) express the magnetic flux density inside the rotor tooth, and the stator and rotor yoke respectively.

$$B_{rt} = \frac{\left(\beta_{st} D_s\right)}{\left(D_r \beta_{rt}\right)} B_{st}\,, \tag{3-17}$$

$$B_{sy} = \frac{\left(\beta_{st} D_s\right)}{\left(4 b_{sy}\right)} B_{st}\,, \tag{3-18}$$

$$B_{ry} = \frac{\left(\beta_{st} D_s\right)}{\left(4 b_{ry}\right)} B_{st}\,. \tag{3-19}$$

By assuming that the airgap cross section is equal to the average between the stator teeth and rotor teeth cross sections, [85] Gauss' equation for the airgap yields (3-20).

$$B_g = \frac{\left(2\beta_{st}\right)}{\left(\beta_{st} + \beta_{rt}\right)} B_{st}\,. \tag{3-20}$$

From all the above, this Subsection concludes that the magnetic circuit defines eight DVs and seven IRs, which result in one 'electromagnetic' IDV.

3.4.3.2 WINDING AND CONVERTER

This Subsection analyses the relationship that exists between the converter VA rating of an SR machine and the DVs defined by the machine's winding. Following from the winding arrangements used for the two prototypes considered, only the concentrated

winding configuration is considered in this thesis. In the case of distributed windings, the number of IDVs remains the same, even though their equations would be slightly different from those derived below.

From the converter side, the design of an SR machine allows for two DVs, namely the DC-bus voltage V_{DC} and the peak phase current i_{pk}. From the winding point of view, the number of series-connected turns per phase N is the DV introduced. However, as each phase is wound around multiple stator teeth, it is convenient to define also the number of series-connected turns wound around one tooth N_{st}. N and N_{st} are related to each other through (3-21). The full set of converter+winding DVs is contained in Table 3-VI.

$$N = 2PN_{st} \,. \tag{3-21}$$

Winding DVs are now to be connected to the stator slot DVs. This can be done through the equation of the total slot rms-current (3-22). Here, the equation left-hand side is expressed in terms of i_{pk}, while the right-hand side in terms of J_{ss}. The term f_i is a 'current form factor', which takes the non-rectangular shape into account. Values of f_i depend on the dynamic behaviour of the SR machine, which, in turn, stems from V_{DC} and the control strategy, so that its estimation requires very good engineering judgement. Based on the Author's experience, typical values for an SR machine range between 0.5 and 0.707.

$$N_{st} i_{pk} f_i = J_{ss} \frac{A_{ss}}{2} f_{CU} \,. \tag{3-22}$$

For the sake of completeness, it is observed that V_{DC} is not contained in any of the equations above. In this regard, apart from the insulation thickness that is accounted for with f_{CU}, effects of V_{DC} must counteract the effects of the machine pseudo back-emf. This aspect is discussed in Subsection 5.3.3 of Chapter 5.

3.4.4 ELECTROMAGNETIC IDVS

Following from the above, it is now possible to apply (3-1) to calculate the number of IDVs related to the electromagnetic design. Geometrical and electromagnetic aspects count 30 DVs interlinked by 17 IRs, which results in 13 IDVs. The converter-winding aspects add 2 more IDVs. Therefore, the electromagnetic design of an SR machine is characterised by 15 IDVs. The count is finally summarised in Table 3-VII. It is important to highlight that the 15 IDVs that derive from the electromagnetic and

Table 3-VI Converter-winding DVs.

	DV	Symbol
31	DC-bus voltage	V_{DC}
32	Peak phase current	i_{pk}
33	Number of series-connected turns per phase	N
34	Number of series-connected turns per stator tooth	N_{st}

geometric aspects are the only ones involved in the energy conversion process. In fact, even though thermal aspects introduce more IDVs, these last are related only to the inactive parts.

3.4.5 THERMAL DESIGN VARIABLES

After careful consideration of the electromagnetic design aspects, this Subsection is devoted to the definition of DVs, IRs and hence the IDVs related to the thermal design of an SR machine.

For this kind of analysis, a Lumped Parameter Thermal Network (LPTN) is chosen from amongst the thermal models commonly implemented. In fact, bearing in mind that the aim is the ADS determination, LPTNs have historically proven to provide sufficiently accurate results in return for a small implementation effort and reasonable computation time. Moreover, thermal resistances that compose the network can be simply related to the machine geometrical parameters and thus allow for a simple identification of the thermal DVs.

3.4.5.1 PRELIMINARY CONSIDERATIONS

Before embarking on the definition of the LPTN, some preliminary considerations are given below.

1. For a clear distinction between an electrical and a thermal resistances, the latter is indicated with the Andalusian font R;
2. Mean temperature of the active components are taken as DVs, since a maximum temperature constraint is imposed by the conductors' insulation, [86], and by the laminations' coating, [87];
3. Losses produced in the active parts must be considered as DVs as well, since they are involved in the machine efficiency constraint. In addition, iron and copper losses derive from the interaction between geometrical and electromagnetic quantities. Therefore, apart from considering them as DVs, iron and copper losses count also as IRs. Due to the fact that losses closed-form analytical expressions would be almost impossible to achieve, the generic form below is used:

$$P = P\left(geometry,\ operating\ conditions\right);$$

4. The common practice to set the ambient temperature Θ_{amb} at 40°C is followed in this thesis. Obviously, different values can be chosen when designing for harsher

Table 3-VII Independent Design Variables for SR machines Electromagnetic Design.

	STATOR GEOMETRY	ROTOR GEOMETRY	FULL ASSEMBLY	MAGNETIC CIRCUIT	CONVERTER-WINDING	TOT.
DVs	9	8	5	8	4	34
IRs	4	2	4	7	2	19
IDVs	5	6	1	1	2	15

environments;

5. Considering that the LPTN is solved through a nodal analysis, the analysis of the entire network is necessary to evaluate the number of thermal IDVs.
6. Elements with internal heat generation are represented with the well-known T-shaped thermal subnetwork, [88].
7. Thermal modelling requires the definition of four more material-dependent quantities:
    a. Conductors varnish thermal conductivity λ_{VN};
    b. Slot liner thermal conductivity λ_{IS};
    c. Slot liner thickness b_{IS};
    d. Structural steel thermal conductivity λ_{IR}.

Consistently with the approach used in this thesis, the four parameters above are considered as known quantities and hence do not provide any additional DVs.

Finally, Table 3-VIII defines the nomenclature adopted for temperatures and thermal resistances.

3.4.5.2 SR MACHINE LPTN

To construct the LPTN, the SR machine may be divided into ten thermal subdomains, that are:

1. Housing or Frame;
2. Stator Yoke;
3. Stator Teeth;
4. Stator Slots;
5. End-windings;
6. Airgap;
7. End-Caps air;
8. Rotor Teeth;
9. Rotor Yoke;
10. Shaft.

For each subdomain an equivalent subnetwork is defined following the guidelines provided by [89]. Then, all of the subnetworks are connected together to compose the

Table 3-VIII Temperatures and Resistances Nomenclature.

SYMBOL	DESCRIPTION
Θ_{xx}	Component *xx* average temperature
Θ_{xx_yy}	Components *xx* and *yy* interface temperature
R_{xx_yy}	Components *xx* and *yy* contact resistance
$R_{xx,r,o}$	Component *xx* thermal resistance towards radial, outward direction
$R_{xx,r,i}$	Component *xx* thermal resistance towards radial, inward direction
$R_{xx,r,a}$	Component *xx* thermal resistance towards axial direction

LPTN . Given that the LPTN as a whole is necessary to identify the thermal IDVs, it has been preferred to focus now on the resulting LPTN, which is shown in Figure 3-12. The derivation of the single subnetworks is thoroughly described Appendix 2.

As already mentioned in the preliminary considerations, thermal DVs are given by the mean temperatures and the losses belonging to the active components, i.e. stator yoke, stator teeth, stator slots, end-windings, rotor teeth and rotor yoke. The entire list is provided in Table 3-IX.

The analysis is now moved towards the single thermal resistances, with the intention to identify the potential parameters that can be deliberately modified during a design process. By observing the entire network, it can be noted that the frame-to-ambient thermal resistance R_{amb}, as well as the end-caps-to-stator/end-windings resistance $R_{ec,N/F}$, depends on the kind of heat transfer undergoing within the region. In

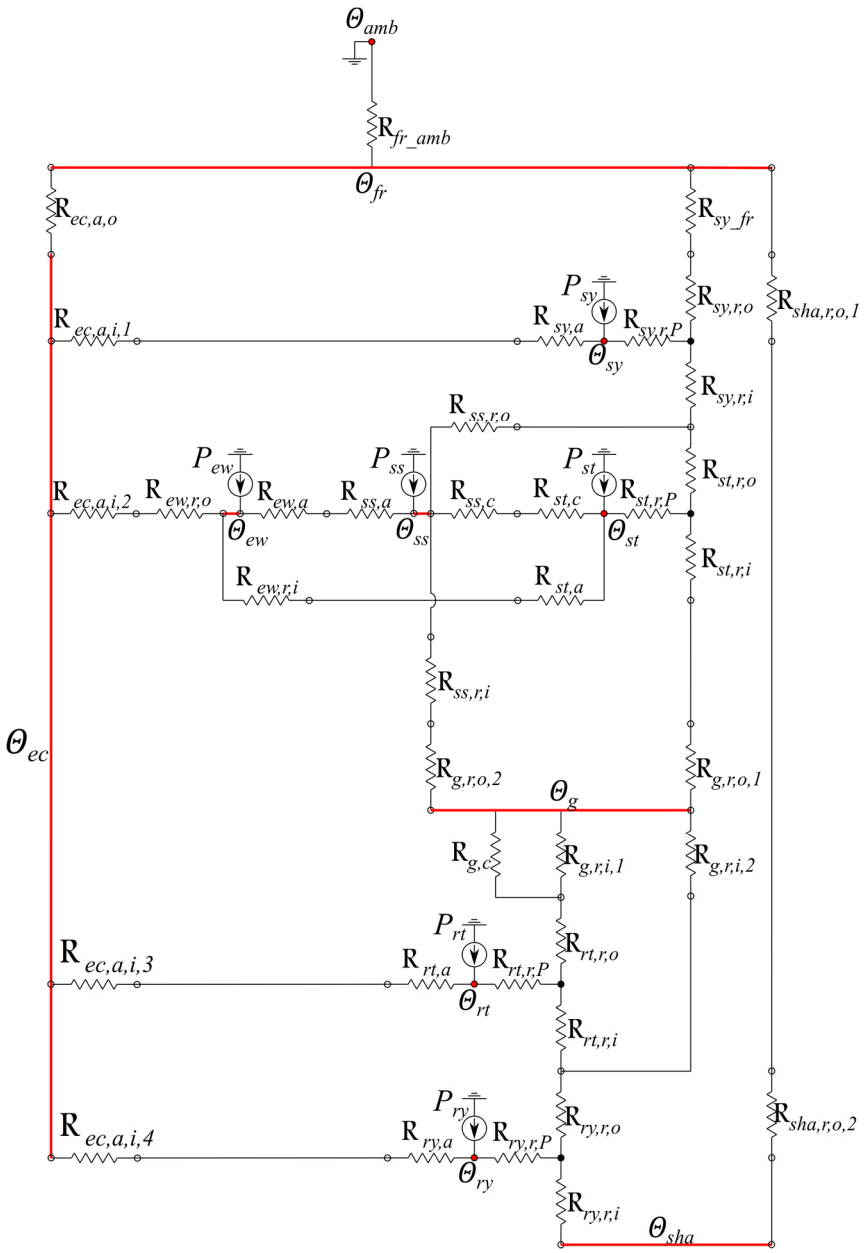

Figure 3-12 Resulting 15-node LPTN of an SR machine.

Table 3-IX Thermal DVs.

	DV	Symbol
35	Stator Yoke Mean Temperature	Θ_{sy}
36	Stator Yoke Iron Losses	P_{sy}
37	Stator Teeth Mean Temperature	Θ_{st}
38	Stator Teeth Iron Losses	P_{st}
39	Stator Slots Mean Temperature	Θ_{ss}
40	Stator Slots Copper Losses	P_{ss}
41	End-Windings Copper Losses	P_{ew}
42	Rotor Teeth Mean Temperature	Θ_{rt}
43	Rotor Teeth Iron Losses	P_{rt}
44	Rotor Yoke Mean Temperature	Θ_{ry}
45	Rotor Yoke Iron Losses	P_{ry}
46	Frame-to-ambient convection factor (i.e. cooling system)	χ_{amb}
47	End-Caps-to-stator/end-winding convection factor (i.e. any fans or not)	$\chi_{ec,N/F}$

particular, R_{amb} is dictated by the cooling system, i.e. natural air, forced air, forced liquid, etc., and can be therefore chosen by the designer. Moreover, $R_{ec,N/F}$ depends on the air velocity throughout the end-caps air, which, in turn, is dictated by the presence or absence of any fanning feature. Since the installation of these last is a deliberate designer's choice, $R_{ec,N/F}$ is also chosen by the designer.

In other words, R_{amb} and $R_{ec,N/F}$ are results of the design choices. Consequently, their corresponding heat transfer coefficients, i.e. χ_{amb} and $\chi_{ec,N/F}$, are included within the thermal DVs.

3.4.5.3 FINAL COUNT OF THERMAL IDVS

Following from the LPTN introduced above, it is now possible to finalise the count of the IDVs offered by the thermal aspect of an SR machine. In the preliminary considerations made in Subsection 3.4.5.1, it is stated that the LPTN as a whole is necessary to calculate the final number of IDVs. Firstly, it is considered that the LPTN constitutes a linear system of equations, which is expressed by (3-23). $[\Delta\Theta]$ denotes the vector of the nodal temperature rises compared to the ambient temperature. $[C]$ is the nodal conductances matrix, being the latter the inverse of the resistances R. Finally, $[P]$ indicates the vector nodal losses injections, which are 'imported' from the electromagnetic operation.

$$[\Delta\Theta] = [C]^{-1}[P]. \tag{3-23}$$

Therefore, once $[C]$ and $[P]$ have been defined, none of the nodal temperatures can be independent. In other words, the LPTN provides as many IRs as the number of nodal temperatures considered as DVs. For the particular case of the LPTN described above, this number counts 5.

To recap, losses in the active components result in 6 DVs and, at the same time, in 6 IRs. Besides, active components mean temperatures give 5 DVs, whose corresponding 5 IRs are provided by the LPTN, i.e. (3-23). On the other hand, χ_{amb} and $\chi_{ec,N/F}$ provide two further DVs, which are not counterbalanced by any IRs. In conclusion, it is found that the thermal design of an SR machine provides two additional IDVs: 1) the main cooling system chosen, which is described more in-depth in Subsection 3.4.5.4, and 2) presence or absence of fanning features swirling the end-caps air. The final count of the number of DVs, IRs and IDVs provided by the thermal design aspects is given in Table 3-X.

Table 3-X Independent Design Variables for SR machines Thermal Design.

	Frame	End-Caps	Active Components Losses	Active Components Mean Temperatures	Tot.
DVs	1	1	6	5	13
IRs	0	0	6	5	11
IDVs	1	1	0	0	2

3.4.5.4 Frame-to-Ambient Thermal Resistance

This Subsection provides a deeper discussion about the frame-to-ambient thermal resistance R_{fr_amb}, since it is the only DV that includes the cooling system in the analysis proposed in this Chapter. Some considerations about the passive and active cooling systems are made below.

3.4.5.5 Passive

When passive cooling is used, heat is mainly moved from the heat sources to the outer housing by conduction. Then, heat is rejected by convection and radiation to the environment. In this case, the machine's outer surface can be either a smooth cylinder or, to increases the heat exchange rate, a finned surface. In the case of a passive cooling system, R_{amb} is expressed as in (3-24).

$$R_{amb} = \frac{1}{\chi_{amb,N} L_{sha} \pi OD}. \tag{3-24}$$

The natural convection coefficient $\chi_{amb,N}$ is expressed in (3-25) as a function of the nine parameters listed below, [90]:

b_{air} coefficient of air cubical expansion [1/K],

g acceleration of gravity,

ΔT difference between external air and surface temperature,

ρ_{air} air density,

ξ_{air} air dynamic viscosity,

cs_{air} air specific heat capacity,

$$\chi_{amb,N} = \chi_{amb,N}\left(b_{air}, g, \Delta T, \rho_{air}, L_{sha}, \xi_{air}, cs_{air}, \lambda_{air}, h_{fin}\right). \tag{3-25}$$

In particular, h_{fin} represents the presence or absence of cooling fins on the outer surface. Its interpretation is defined as follows:

- If cooling fins are installed, their number and height are always determined through an optimisation process. Then, h_{fin} is set to h_{fin_opt}, [91];
- If a smooth outer surface is chosen, h_{fin} is simply set to 0.

The analysis above confirms that if passive cooling between frame and ambient is used, R_{amb} provides one DV.

3.4.5.6 ACTIVE

If active cooling is adopted, external devices such as pumps, fans, nozzles or blowers force the coolant to flow through cooling channels, which can be placed either inside or outside, or both, of the motor, [91]. However, due to their extreme complexity, internal forced cooling systems are not considered in this thesis. R_{amb} can be expressed by (3-26). In this case, the convection factor $\chi_{amb,F}$ considers forced cooling, as shown in (3-27).

$$R_{fr\_amb} = \frac{4}{\chi_{amb,F} L_{sha} \pi OD^2}, \tag{3-26}$$

$$\chi_{amb,F} = \chi_{amb,F}\left(\rho_{cool}, L_{sha}, \xi_{cool}, cs_{cool}, \lambda_{cool}, d_{duct}, u_{cool}\right). \tag{3-27}$$

In (3-27), the mean coolant speed u_{cool} and the duct diameter d_{duct} appear. In order to complete the description of the forced cooling system, the fluid circuit equation (3-28) must be included, where f_{cool} is the coolant mass-flow rate, Π the pump's hydraulic head and R_{hy} the overall hydraulic resistance of the flow circuit.

$$f_{cool} = \frac{\rho_{cool} \pi d_{duct}^{\ 2}}{4} u_{cool} = \frac{\Pi}{R_{hy}}. \tag{3-28}$$

From (3-28), considering that Π and R_{hy} can be taken as known-parameters, it is observed that only one between u_{cool} and d_{duct} can be chosen deliberately. Therefore, it is confirmed that forced cooling systems provide only one DV.

3.4.6 INDEPENDENT DESIGN VARIABLES OF AN SR MACHINE

At this point, as both the electromagnetic and thermal DVs and IRs have been introduced, it is possible to provide a final count of the total number of IDVs that is offered by the electromagnetic+thermal design of an SR machine. The count is summarised in Table 3-XI and shows seventeen IDVs. In future works, the count will be

Table 3-XI Independent Design Variables for an SR machine.

	ELECTROMAGNETIC	THERMAL	TOTAL
DVs	34	13	47
IRs	19	11	30
IDVs	15	2	**17**

extended to comprise also the mechanical design aspect.

3.5 ADS OF AN SR MACHINE: EXTERNAL STAGE

Once the number of IDVs has been evaluated, the second stage to determine the ADS can be undertaken. To this end, the design Cnts and Rqms given by the specific application are introduced one by one. As it has been pointed out Subsection 3.3.2 of Chapter 3, Cnts and Rqms are expressed in terms of inequalities, and hence their effect is that of reducing the range of feasible values that each IDV can assume. This Subsection examines the most common Cnts and Rqms that characterise the design of a high-performance SR machine. It is important to bear in mind that not all of them may be simultaneously imposed.

3.5.1 GEOMETRICAL CONSTRAINTS

The first constraint to be satisfied is concerned with the geometrical quantities. As it is obvious, all geometrical DVs, as such, can only assume positive values.

3.5.2 OVERALL DIMENSIONS CONSTRAINTS

One of the most restrictive kinds of Rqm, which is typical of the high-power-density SR machines, is not to exceed a certain overall diameter and/or an overall length, including the inactive parts. In theory, the constrained DVs would be the shaft length L_{sha} and the overall outer diameter, being the latter equal to the sum of the outer stator laminations diameter OD and frame thickness b_{fr}. In practical terms, it is reasonable to assume as constrained DVs directly OD and L_{stk}, as given in (3-29)-(3-30).

$$OD \le OD_{-\max}, \tag{3-29}$$

$$L_{stk} \le L_{stk-\max}. \tag{3-30}$$

3.5.3 MANUFACTURING CONSTRAINT

Manufacturing processes may be highly imposing over some geometric DVs. For instance, machining laminations to reach airgaps smaller than $0.25mm$ is almost impossible, [92]. This constraint yields (3-31).

$$l_g \ge l_{g-\min}. \tag{3-31}$$

3.5.4 SWITCHED RELUCTANCE OPERATIONAL CONSTRAINTS

Modern SR machines are required to provide both self-starting and bidirectional rotation capability. As demonstrated in [85], this condition is to be set on m, β_{st} and β_{rt}, as shown in (3-32)-(3-33).

$$m>3, \tag{3-32}$$

$$\beta_{st} \ge \beta_{st\_self-start} = \frac{4\pi}{N_s N_r}. \tag{3-33}$$

Further criteria to effectively set β_{st} and β_{rt} are discussed in [14], which are as follows:

- manufacturing and performance constraints lead to the condition in (3-34),
- in order to exploit the full inductance gradient potentially available, condition in (3-35) must be respected.

$$\beta_{st} \leq \beta_{rt}\,, \tag{3-34}$$

$$\beta_{st} + \beta_{rt} = \zeta_r\,. \tag{3-35}$$

From the two expressions above, (3-36) and (3-37) can be defined, in order to summarise the range of feasible values for β_{st} and β_{rt}. Figure 3-13 provides the graphical representation of the so called 'Stephenson's Triangle'.

$$\frac{4\pi}{N_s N_r} \leq \beta_{st} \leq \frac{\zeta_r}{2}\,, \tag{3-36}$$

$$\frac{4\pi}{N_s N_r} \leq \beta_{rt} \leq \zeta_r - \frac{4\pi}{N_s N_r}\,. \tag{3-37}$$

3.5.5 Magnetic Circuit Constraint

In a well-designed SR machine, the stator tooth must be the most saturated point of the magnetic circuit. Low flux densities inside the stator and rotor yokes are not desirable, due to the poor utilization of the back-iron [85]-[92]. Following from the magnetic circuit equations given in Subsection 3.4.3, these constraints can be expressed through two back-iron utilization factors: u_{FEsy} and u_{FEry}, as given in (3-38)-(3-39). This aspect gains critical importance in situations where two or more phases conduct simultaneously, [93], since the magnetomotive force of different phases are exerted on the same yoke portions.

$$u_{FEsy} = \frac{B_{sy}}{B_{st}} \qquad 0.5 < u_{FEsy} < 1\,, \tag{3-38}$$

$$u_{FEry} = \frac{B_{ry}}{B_{st}} \qquad 0.5 < u_{FEry} < 1\,. \tag{3-39}$$

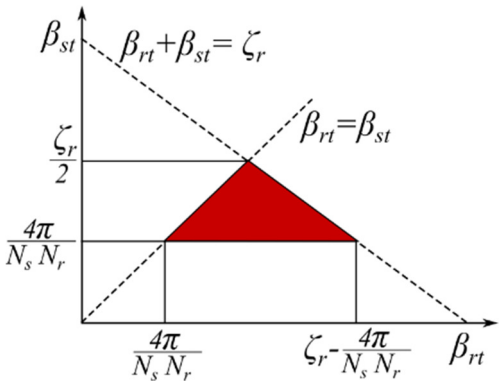

Figure 3-13 Representation of the constraints on the stator and rotor teeth arcs for SR machines, the 'Stephenson's Triangle'.

3.5.6 RATED TORQUE SPECIFICATION

The development of the rated torque T_{rated}, is probably the most critical Rqm to be satisfied. Indeed, the inequality expressed in (3-40) is the first one to be applied, since if no feasible candidates are left after its introduction, is literally useless to carry on with the design. In (3-40), ω_b indicates the 'base speed'.

$$T(\omega_b) > T_{rated} = \frac{P_{rated}}{\omega_b}. \tag{3-40}$$

3.5.7 HIGH-SPEED TORQUE SPECIFICATION

A further Rqm that might be imposed is the capability to develop the rated power from ω_b to the maximum speed ω_{max}. The capability to provide the rated power for a wide Constant Power Speed Range, i.e. for ω_{max} four times or more than ω_b is normally highly restrictive. Therefore, a wide CPRS is considered as a highly demanding performance. This requirement is mathematically expressed through (3-41).

$$T(\omega_{\max}) \geq \frac{P_{rated}}{\omega_{\max}}. \tag{3-41}$$

3.5.8 THERMAL CONSTRAINT

Thermal constraints are dictated by the maximum temperature allowed by either the conductors' insulation or the laminations' coating. In both cases temperature limitations are used to define specific classes. For instance, according to the historical IEC 60085:2007, thermal classes for electrical machines windings range from 'class A', for maximum-temperature allowance up to 105°C, to 'class H' for allowances up to 180°C, [86].

In terms of electrical steel, temperature limitations imposed are dictated by the insulation coating. Basing on the ASTM A976-97, coatings are classified from C-1 to C-6. Usually, maximum electrical steel temperatures are in the range of 200°C.

If a multiphysics design approach is used, temperatures are included into the process as DVs. Therefore, temperature limitations can be directly verified. On the other hand, the traditional electromagnetic design approach expresses this Cnt in terms of the maximum J_{ss} allowed by the cooling system. In this case, acceptable J_{ss} values for the different cooling systems are summarized in Table 3-XII, [92].

Table 3-XII Current Density Constraint Imposed by the Cooling System

CONSTRAINT ON J_{ss} (A_{rms}/mm^2)	COOLING SYSTEM
$4{,}7 < J_{ss} < 5{,}4$	Natural Convection
$7{,}8 < J_{ss} < 10{,}9$	Forced-Air Cooling on the Outer Surface
$14 < J_{ss} < 15{,}5$	Forced- Cooling with Ducts and/or Embedded Fans
$23.3 < J_{ss} < 31$	Liquid Cooling, either in Ducts or Sprays

3.5.9 EFFICIENCY CONSTRAINT

The vast majority of designs present a minimum efficiency Rqm. As the efficiency is concerned with losses, two approaches are available. In the multiphysics approach, losses are handled directly, since they are transferred from the electromagnetic to the thermal side. Conversely, in the purely electromagnetic design, iron losses may be associated to B_{st}, whilst copper losses to J_{ss}. Therefore, a minimum efficiency constraint yields an upper boundary to B_{st} and J_{ss}, as expressed by (3-42) and (3-43).

$$B_{st} \leq B_{st\_\max}, \tag{3-42}$$

$$J_{ss} \leq J_{ss\_\max}. \tag{3-43}$$

3.6 CONCLUSION

This Chapter has proposed a novel, valuable alternative to the traditional multiphysics design approaches. The latter has demonstrated that by adding a simple and fast-computing analytical step to the design process, prior to any FEA simulations, the identification of all potential solutions to the design problem is dramatically simplified, as well as an impossible design problem can be promptly identified. Thanks to these properties, it can be concluded that the ADS worth further investigation. In the future, all of the aspects concerned with the clearance δ_{ADS} shall be assessed thoroughly, as they drive the choice of the analytical models.

In the second part of this Chapter, the Internal Stage of an SR machine provided the rigorous count of the IDVs associated to the electromagnetic+thermal design, i.e. 15+2=17. This result can provide a useful guideline for the designers during any design optimisation problem, as it helps to understand how 'local' or 'global' an optimisation is.

The output of this Chapter has resulted in the conference paper [84], whose follow-up journal version is now under review.

4 DESCRIPTION OF PHYSICAL PROTOTYPES, FINITE ELEMENT MODELS AND EXPERIMENTAL VALIDATION

In this Chapter, two SR prototypes are presented along with their electromagnetic and thermal Finite Element Analysis (FEA) models. Then, FEA results are validated against the experimental data from the prototypes. In preparation for the analytical models developed in the next Chapters, the objective is now to prove that the experimentally-validated FEA models ensure a solid foundation for the validation of any possible analytical model.

4.1 PROTOTYPE 1: SRMYLD

The first prototype considered is a small SR machine that was already available at the University of Nottingham from a previous project. The prototype was conceived for a mild-hybrid electric vehicle. For this reason, the prototype is referred to as SRMyld, where 'y' is taken from the word 'hybrid'.

4.1.1 PHYSICAL PROTOTYPE DESCRIPTION

A picture of the physical prototype is shown in Figure 4-1. The main nameplate

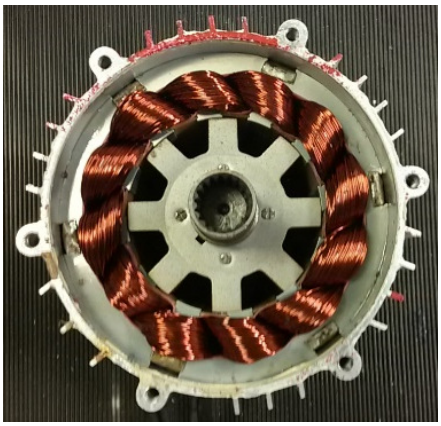

Figure 4-1 SRMyld prototype outlook.

data are provided in Table 4-I, while the geometrical parameters are given in Table 4-II. Due to the uncertainty on the rated rms-phase current, the value reported in Table 4-I has been obtained experimentally.

As it can be observed, the typical $36V$ of a battery pack are considered for the DC-bus voltage. Moreover, the CPSR is typical of an Internal Combustion Engine (ICE), i.e. between $1500rpm$ and $6000rpm$.

Table 4-I SRMyld prototype nameplate data.

Parameter	Measure Unit	Value
DC-bus Voltage	V	36
Rated rms Current	A_{rms}	38
Rated Power	kW	0.9
Base Speed	rpm	1500
Maximum Speed	rpm	6000

Table 4-II SRMyld prototype geometrical parameters.

Parameter	Measure Unit	Value
Stator Poles	-	12
Rotor Poles	-	8
Stator Outer Diameter	mm	137.8
Stator Yoke Thickness	mm	10
Stator Tooth Height	mm	15.8
Stator Tooth Width	mm	10.85
Airgap	mm	0.56
Rotor Tooth Height	mm	13.3
Rotor Tooth Width	mm	12.2
Rotor Yoke Thickness	mm	14.1
Number of Turns per Phase	-	4x12
Axial Stack Length	mm	60

4.1.2 FEA MODELS

This Subsection describes the development of the FEA models of SRMyld. As it is common occurrence in automotive designs, electromagnetic and thermal aspects have been thoroughly considered. On the other hand, due to the relatively low speed for the given rotor weight, it is reasonable to neglect mechanical stress analyses and rotor dynamics.

4.1.2.1 ELECTROMAGNETIC MODEL

The electromagnetic model is Author's own work, realised with the MagNet software package by Mentor (ex Infolytica). Figure 4-2 (a) shows the outlook of the solid FEA model and the 2D mesh, while subplot (b) provides a detailed image of the airgap mesh. As it can be noted, the stator is subdivided into twelve stator teeth and yoke segments.

Similarly, the rotor is split in eight teeth and yoke segments. In this way, local losses can be quantified and sent to the thermal model for a more accurate temperature estimation.

Based on the FEA model described above, machine performance is evaluated following the traditional lookup-table-based approach:

1. A set of static simulations is run in a bid of deriving the phase flux linkage lookup table Ψ_{ph} ([θ], [i_{ph}]), for discrete rotor positions and discrete values of the phase current.
2. From Ψ_{ph} ([θ], [i_{ph}]), the terminal voltage equation is numerically solved for i_{ph} following the algorithm presented in [94].
3. i_{ph} is shifted in order to produce the current waveforms of the remaining phases.
4. The set of phase currents is fed into a transient with motion simulation to finally derive the machine performance, namely output torque T, copper and iron losses.

FEA results of the SRMyld prototype are presented and discussed in Subsection 4.1.5, where they are validated against the experimental results.

4.1.2.2 THERMAL MODEL

The thermal model is also Author's own work, developed with the MotorCad by Motor Solve software package. The model's front and side views are shown in Figure 4-4 (a) and (b) respectively. As it can be observed from Figure 4-1 and Figure 4-4 (below), SRMyld prototype has a totally enclosed frame. Heat is rejected to the ambient through a set of twenty-eight axial cooling fins, which are $4.5mm$ tall and uniformly distributed

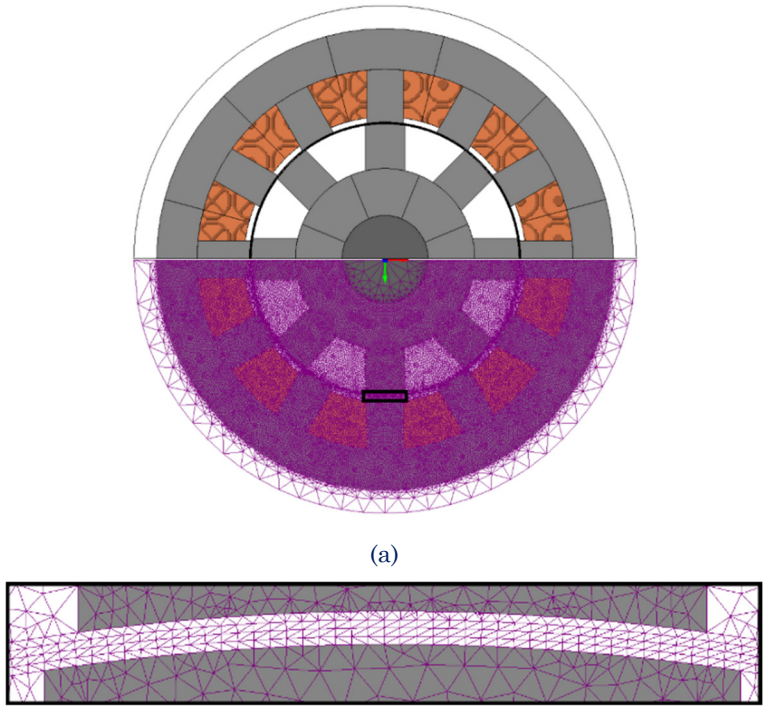

(a)

(b)

Figure 4-2 SRMyld FEA model: (a) solid model and 2D mesh, (b) detail on airgap mesh.

around the frame's surface.

A non-negligible amount of heat is also rejected through the coupling frame, which has been therefore included in the MotorCad model. Finally, a standard $0.03mm$ equivalent airgap has been consider to model the contact resistance between stator laminations and frame.

Results of the thermal analyses are presented in Subsection 4.1.5 and compared against the experimental testing results.

4.1.3 EXPERIMENTAL TESTING

This Subsection describes the experimental testing campaign conducted on the SRMyld prototype. To conduct the experimental campaign, a fully instrumented test bench has been set up in the University of Nottingham Laboratories.

The SRMyld prototype has been coupled to a high-speed Induction Machine (IM) through a Magtrol TM300 in-line torque transducer. The two machines coupled together are depicted in Figure 4-4 (a). Converter and control platform previously designed and developed by the University of Nottingham have been used to power and control SRMyld, [24]. The controller is realised on a DSP/FPGA control platform based on a Texas instruments C6713 floating point DSP. The latter has been developed by the PEMC group at the University of Nottingham over the past years. Consistently with the control platform specifications, a Tamagawa Smartsyn TS2620N1051E11 Brushless

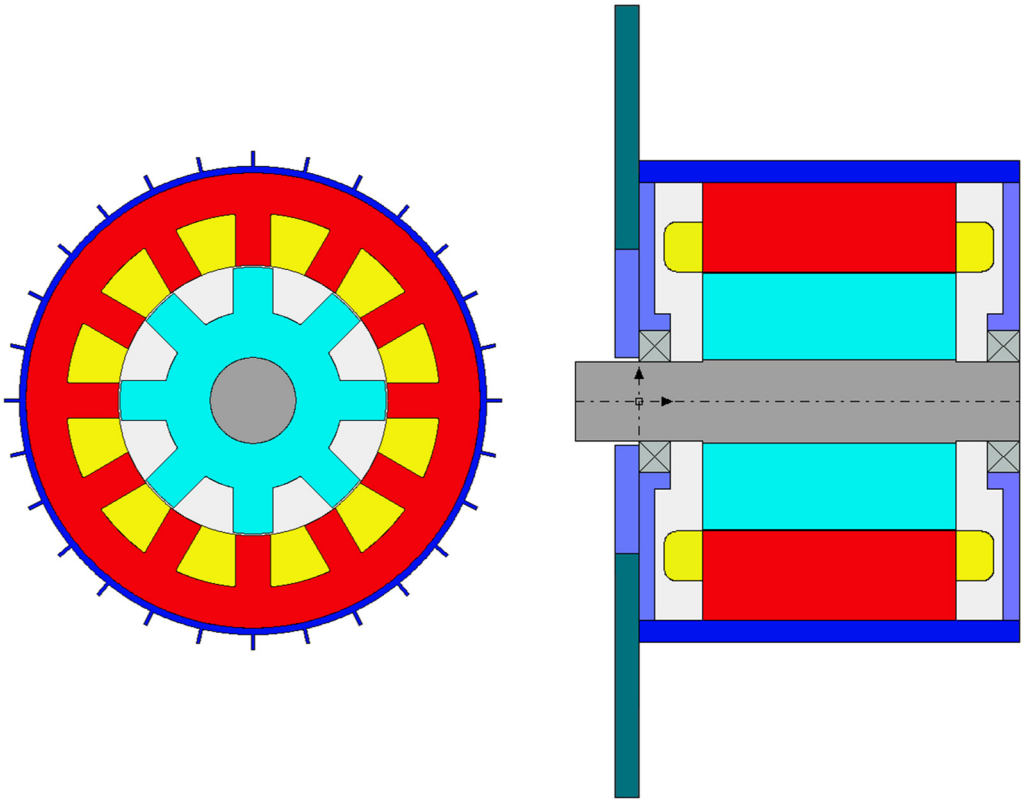

(a) (b)

Figure 4-3 SRMyld MotorCad model: (a) front view, (b) side view.

Pancake Resolver has been mounted.

For thermal testing, a set of six thermocouples has been installed in the following parts of the prototype:

- Housing outer surface,
- Cooling wing tip,
- End-winding,
- Stator tooth,
- Stator yoke,
- Housing inner surface.

Installation sites of the four internal thermocouples are shown in Figure 4-4 (b). Temperatures have been monitored and recorded through a laboratory PC by means of a PicoLogger interface.

4.1.4 FEA Model Validation

In this Subsection, FEA and experimental results are compared. The validation campaign is conducted in three different steps. In the first, the FEA and experimental

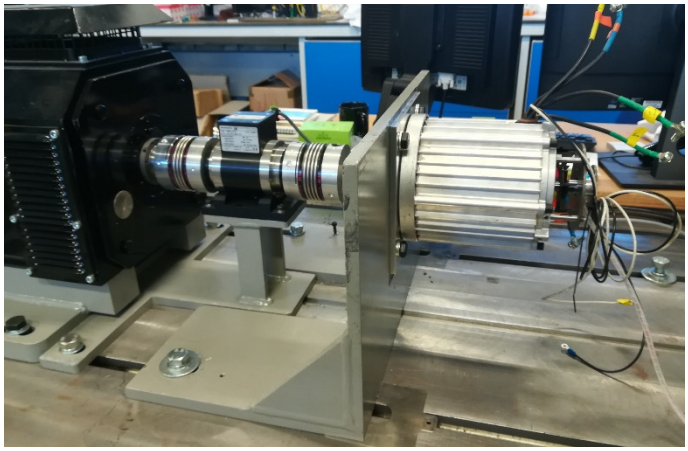

(a)

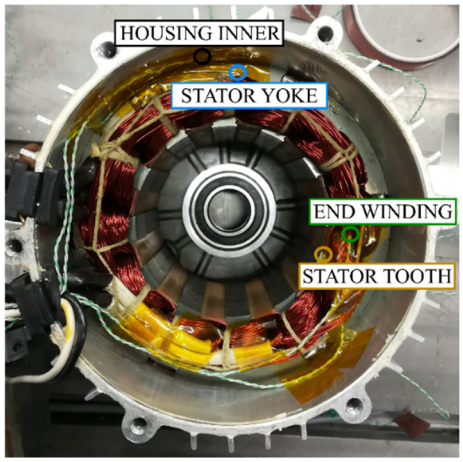

(b)

Figure 4-4 (a) SRMyld prototype under test coupled to a high-speed IM in the test rig, (b) thermocouples locations.

unsaturated inductance profiles are compared. In the second, the rated $0.9kW$ are developed at $6000rpm$. In the third, machine performance at the base-speed operating conditions, i.e. $0.9kW$ at $1500rpm$ are considered.

4.1.5 FEA MODEL VALIDATION

In this Subsection, FEA and experimental results are compared. The validation campaign is conducted in three different steps. In the first, the FEA and experimental unsaturated inductance profiles are compared. In the second, the rated $0.9kW$ are developed at $6000rpm$. In the third, machine performance at the base-speed operating conditions, i.e. $0.9kW$ at $1500rpm$ are considered.

4.1.5.1 UNSATURATED INDUCTANCE PROFILE VALIDATION

The first step to validate the FEA models is concerned with the SRMyld prototype inductance vs. rotor position profile, being the magnetic core out of saturation. Experimental inductances have been measured by an N4L-PSM1735-IAI impedance analyser set at approximately $50Hz$, with the rotor locked at every 1.25° (mech.). The FEA profile is compared against that obtained experimentally in Figure 4-5. Inductances at the maximum alignment L_a and maximum misalignment L_u are compared in Table 4-III. A good match over the whole range of rotor positions is observed, with a very small error for L_a and L_u. Discrepancy in the central profile part are mainly due to the end-effects that are not accounted for in the 2D FEA model.

Table 4-III SRMyld: FEA and experimental values of L_a and L_u.

	FEA	Experimental	Error (%)
L_a (mH)	1.527	1.540	-0.84
L_u (mH)	0.269	0.275	-2.18

4.1.5.2 HIGH-SPEED TESTS

For the high-speed test, the maximum power available at the maximum speed, i.e. $6000rpm$, is developed. In Figure 4-6 phase voltage and phase current waveforms are shown in subplots (a) and (b) respectively. Experimental waveforms are represented

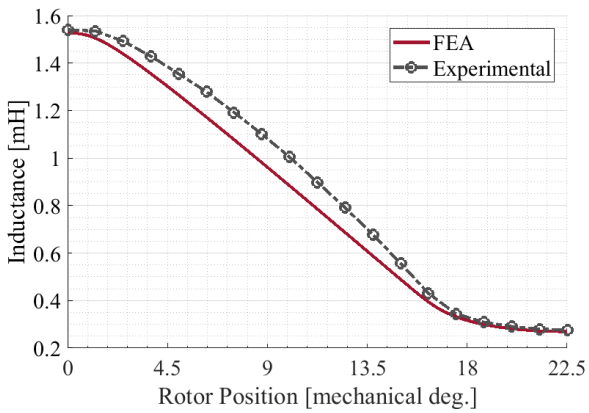

Figure 4-5 SRMyld FEA and experimental inductance profiles.

with the dash-dotted line. As it can be observed, the experimental voltage presents a constant $2.5V$ voltage drop, which is due to the resistive voltage drops caused by the converter. For this reason, two different FEA models have been considered. In the first, the full $36V$ are considered, while in the second the converter resistive voltage drop has been accounted for. FEA results achieved with the first method are plotted with the scarlet line. FEA results derived with the second are plotted with the yellow line. The phase current waveforms show that, if the converter voltage drop is not considered, the FEA model leads to a slight current overestimation. On the other hand, if the voltage drop is compensated, a much closer approximation is achieved. In this second case, the small differences are due to the differences between FEA and real inductance profile, as well as to the effects of the mutual inductances. On the other hand, waveforms discrepancy at around 300 electrical degrees is due to the capacitive effects, which do not allow the voltage dropping to zero instantaneously. However, this voltage transient evolves with a no current, so that no significant energy exchanges undergo and can therefore be neglected.

In Table 4-IV, the rms-phase current i_{ph_RMS} and the average torque T_{AVG} values are compared. For the sake of completeness, the average power P_{AVG} is also reported. Results demonstrate that if the converter voltage drop is not considered, errors around 8% and 10% are incurred. On the other hand, the voltage drop compensation allows for a perfect estimation of i_{ph_RMS} and a -6% error on T_{AVG}. The negative sign derives from

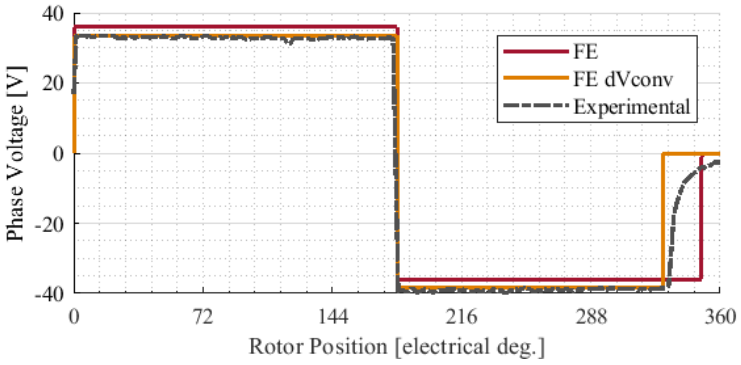

(a)

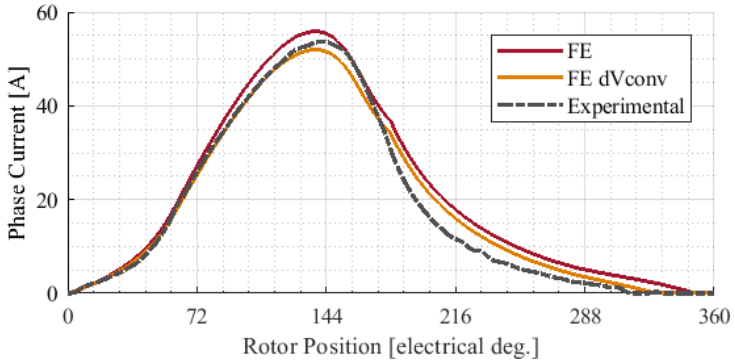

(b)

Figure 4-6 SRMyld FEA and experimental results at 6000rpm: (a) phase voltage vs. rotor position, (b) phase current vs. rotor position.

Table 4-IV SRMyld High-speed performance prediction, analytical vs. FEA results at 36V, 6000rpm

	Exp.	FEA	Error (%)	FEA_dV$_{conv}$	Error (%)
i_{ph_RMS} [A]	25.94	28.03	8.05	25.96	0.07
T_{AVG} [Nm]	1.48	1.63	10.13	1.39	-6.08
P_{AVG} [kW]	0.93	1.02	10.13	0.87	-6.08

the torque underestimation caused by the mutual inductance effects. Results of the experimental thermal test are shown in Figure 4-7.

Results from the MotorCad model are presented in Figure 4-8. Temperatures of housing, end-winding, stator tooth and stator yoke are reported in Table 4-V, along with the discrepancy between the simulation and experimental values. As observed, apart from the end-windings, errors are almost negligible. In the case of the end-windings, the small discrepancy arises because of the uncertainty on the copper loss estimation, as well as because the thermocouple has not been placed exactly at the hot-spot, whose exact position is usually unpredictable.

4.1.5.3 LOW-SPEED TESTS

For the low-speed test, the maximum power available at the base speed, i.e. 1500rpm, is developed. Figure 4-9 (a) shows the phase voltage, while Figure 4-9 (b) the phase current waveforms. As it can be observed, the experimental voltage presents a 2.5V voltage drop only when the negative DC-bus is applied (difference with the high-speed case is due to a loose connection in the setup, which has been fixed prior to the low-speed

Table 4-V SRMyld temperatures 6000rpm, MotorCad results and errors.

Component	Temperature [°C]	Error [%]
Frame	71.2	-1.11
End-winding	84.3	5.11
Stator Yoke	75.0	-
Stator Tooth	77.3	-2.15
Ambient	22	-

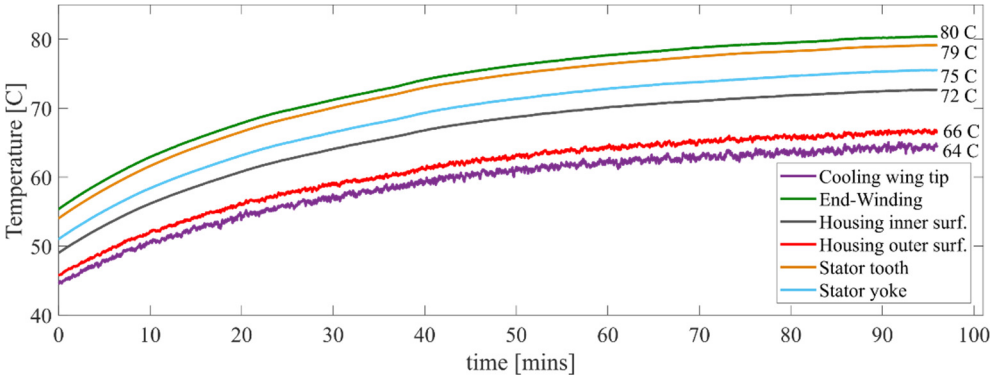

Figure 4-7 SRMyld thermal experimental results at 6000rpm.

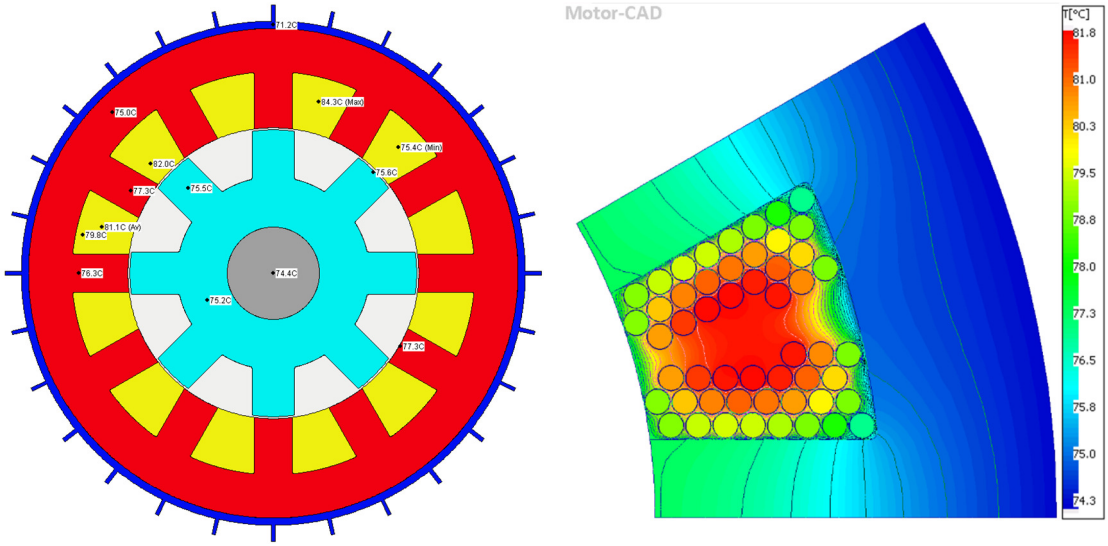

(a) (b)

Figure 4-8 SRMyld MotorCad results at 6000*rpm*: (a) components' temperatures, FEA slot temperature distribution.

testing). Hence, FEA model has been run with both the ideal voltage waveform and with compensated voltage drop.

Thermal experimental results for operation at 1500*rpm* are presented in Figure 4-10, while MotorCad results are reported in Figure 4-11. Housing, end-winding, stator tooth and stator yoke temperatures are reported in Table 4-VII along with the errors. Similarly to the high-speed case, errors range between 1% and 5%, showing that a very good agreement is reached in both operating conditions. The low ambient temperature is due to the fact that this experimental test has been conducted overnight. Another important point to note is that this test reached exactly the maximum end-winding temperature allowed by the insulating class, i.e. 150°*C*. Therefore, based on this test, the rated rms current has been empirically determined.

Because of the chopping regulation, the current waveform prediction is definitely more challenging than in single-pulse mode. As it can be observed from the FEA curves, in case the voltage drop is compensated, phase current is chopped only twice, and after the second chop, it rises and falls naturally without reaching the threshold value, similarly to the experimental case. Conversely, with the idealised voltage waveform, phase current is chopped thrice, but after the third chop, it immediately decreases.

Table 4-VI SRMyld High-speed performance prediction, analytical vs. FEA results at 36*V*, 70 ±10*A*, 1500*rpm*.

	Exp.	FEA	Error (%)	FEA_dV$_{conv}$	Error (%)
i_{ph_RMS} [A]	37.13	39.42	6.16	40.62	9.39
T_{AVG} [Nm]	6.01	5.2	-13.47	5.91	-1.66
P_{AVG} [kW]	0.95	0.82	-13.47	0.92	-1.66

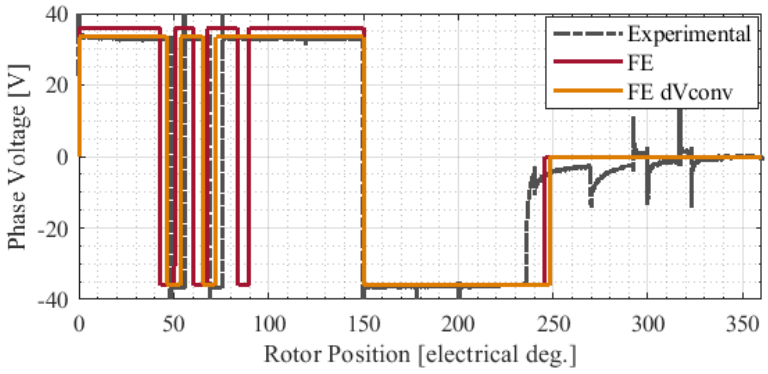

(a)

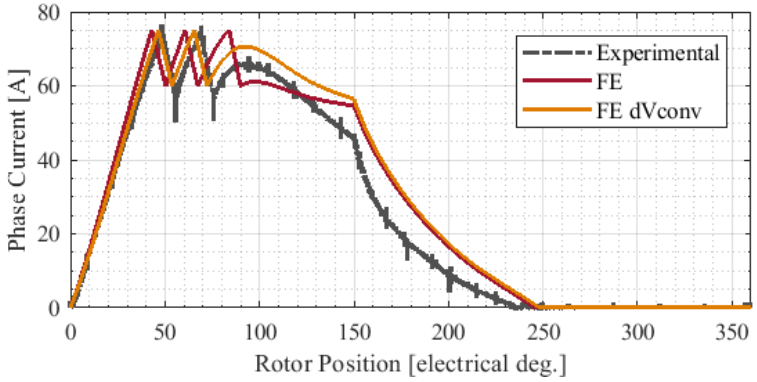

(b)

Figure 4-9 SRMyld FEA and experimental results at 1500rpm: (a) phase voltage vs. rotor position, (b) phase current vs. rotor position.

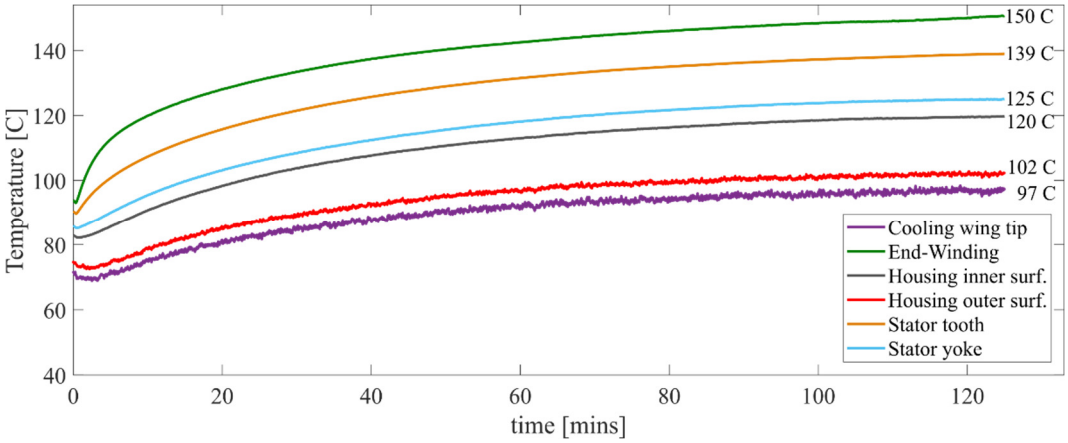

Figure 4-10 SRMyld thermal experimental results at 1500*rpm*.

Table 4-VII SRMyld temperatures at 1500*rpm*, MotorCad results and errors.

Component	Temperature [°C]	Error [%]
Frame	120.5	0.41
End-winding	154.8	2.66
Stator Yoke	130	4.00
Stator Tooth	136	-2.15
Ambient	18	-

Thus, the idealised case results in a lower rms current, as shown by Table 4-VI. Therefore, given the inherent difficulty of predicting the phase current waveform in chopping mode, FEA proved an excellent accuracy. As shown in Table 4-VI, FEA torque and power estimation with compensated converter voltage drop incurred in an error smaller than the 2%.

4.2 PROTOTYPE 2: SRFLY

The second design case study is a large-scale SR machine to be used for a flywheel-based energy storage system. The main difference with the traditional flywheel units is that the rotor of this SR machine itself serves as unique source of inertia for the entire storage system. For this reason, the prototype is named SRFly.

4.2.1 APPLICATION OVERVIEW

The idea of an integrated-flywheel SR machine has been developed at the University of Nottingham in collaboration with the industrial partner OXTO Energy [95], in response to the challenges of the flywheel units that are currently used, related to the massive outer containments needed to handle the highly destructive forces that arise in case of faults.

4.2.2 PHYSICAL PROTOTYPE DESIGN

The prototype's design is Author's own work, as he served as the machine designer during the project. The design has been developed following the traditional heuristic approach, with the aid of simple preliminary sizing equations and several FEA iterative refinements. In the initial trade-off study, the 6/4, 12/10 and 16/14 configurations with either an inner or outer rotor topology have been investigated, [29]. The trade-off study led to the choice of the inner-rotor, 16/14 topology, due to its highest suitability to extend

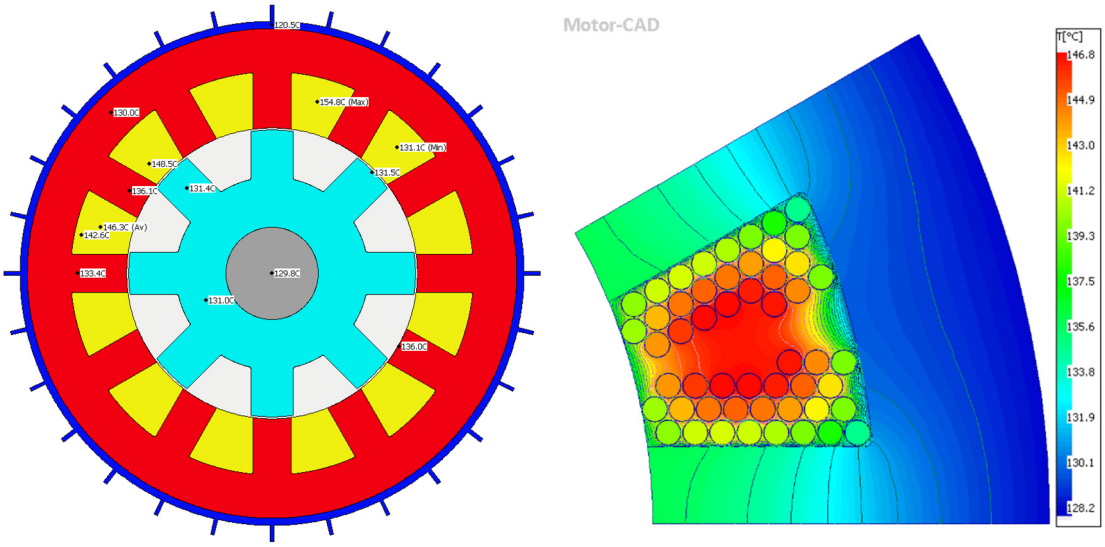

(a) (b)

Figure 4-11 SRMyld MotorCad results at 1500*rpm*: (a) components' temperatures, FEA slot temperature distribution.

Table 4-VIII SRFly prototype geometrical parameters.

Parameter	Measure Unit	Value
Rated Power	kW	45
Stator Poles	-	16
Rotor Poles	-	14
Stator Outer Diameter	mm	959
Stator Yoke Thickness	mm	50
Stator Tooth Height	mm	27
Stator Tooth Angle	°	11.57
Airgap	mm	2.6
Rotor Tooth Height	mm	61
Rotor Tooth Angle	mm	12.72
Rotor Yoke Thickness	mm	61
Number of Turns per Phase	-	2X17
Axial Stack Length	mm	165
Rotor Material	-	M270-35A

the CPSR.

The geometrical parameters of the SRFly prototype are reported in Table 4-VIII. A picture of the physical prototype is shown in Figure 4-12 In Appendix 1, a more in-depth description about the SRFly prototype manufacturing and testing facility setup is provided.

4.2.3 FEA MODELS

This Subsection describes the development of the SRFly electromagnetic FEA model.

4.2.3.1 ELECTROMAGNETIC MODEL

The electromagnetic model realised using the MagNet software is shown in Figure 4-13. Solid FEA model and the 2D mesh are represented in subplot (a), the airgap mesh is zoomed in in subplot (b). Stator and rotor components are split respectively into

Figure 4-12 SRFly prototype outlook.

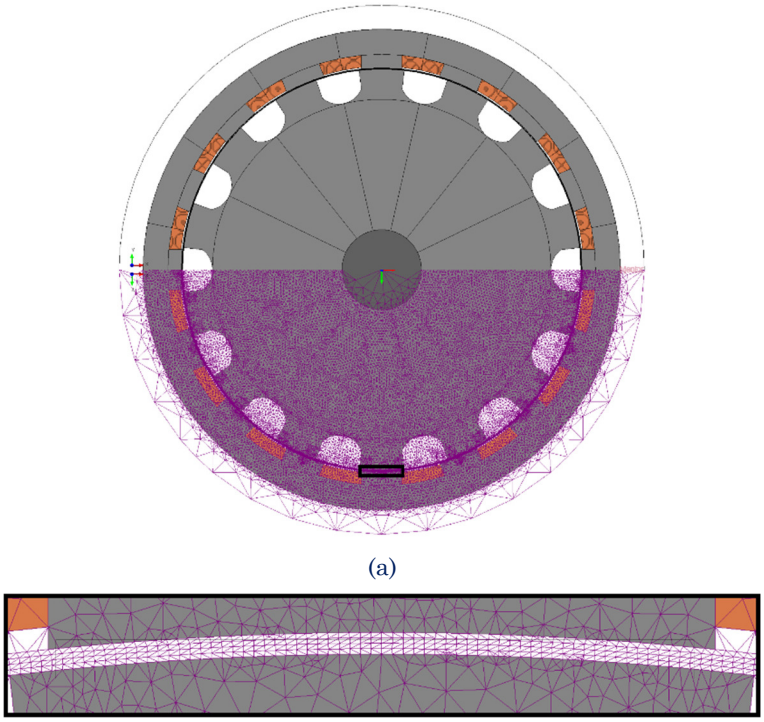

(a)

(b)

Figure 4-13 SRFly FEA model: (a) solid model and 2D mesh, (b) detail on airgap mesh.

sixteen and fourteen segments, in order to attain a local estimation for the iron losses.

FEA results are shown and compared against the experimental values directly in Subsection 4.2.5.

4.2.4 Experimental Testing

To conduct the experimental campaign, a fully instrumented test bench has been set up in the University of Nottingham Laboratories. In particular, due to the high risks related to the flywheel testing, a special segregated room within the University of Nottingham Tower Building has been used as 'bunker' to set up the experimental rig. More in-depth information about the testing facility is provided in Appendix 1.

Similarly to the previous prototype setup, the controller is realised on a DSP/FPGA control platform based on a Texas instruments C6713 floating point DSP, [28]. On the other hand, this time an encoder-based position acquisition system has been chosen. Due to the special kind of application, an incremental rotary encoder MNI40N from Pepperl+Fuchs, with a custom-made magnetic wheel, has been chosen.

4.2.5 FEA Model Validation

This Subsection compares FEA and experimental results obtained from the SRFly prototype. Once again, the first step of the validation is the comparison between FEA and experimental inductance profiles. In the second, a low-speed operating condition is considered to compare the FEA and experimental waveforms of phase current and phase voltage.

4.2.5.1 UNSATURATED INDUCTANCE PROFILE VALIDATION

Due to the application itself, no mechanical coupling is present on the SRFly prototype, so that it is not possible to lock the rotor at a desired position. For this reason, experimental inductances have been measured at the only five rotor positions where it is possible to lock the rotor by injecting current in one of the eight phases. Measurements have been taken by an N4L-PSM1735-IAI impedance analyser. The FEA profile is compared versus the experimental one in Figure 4-14. Inductances at maximum alignment L_a and maximum misalignment L_u are reported in Table 4-IX. Similarly to the previous prototype, an excellent similarity is obtained.

4.2.5.2 LOW-SPEED TESTS

The low-speed test has been conducted with the following operating conditions: $350V$ DC-bus voltage, current regulator set at $50\pm10A$ and $1000rpm$. The phase voltage vs. rotor positions and phase current vs. rotor positions characteristics are shown in Figure 4-15.

In this case, no significant DC-bus voltage drops are observed. Likewise the previous prototype, an excellent similarity is obtained for both phase voltage and phase current waveforms.

4.3 CONCLUSION

In this Chapter, the reliability and robustness of the FEA models developed in this thesis has been demonstrated by validating the FEA results against the experimental values attained from two physical prototypes. In order to ensure the FEA models' capability to adapt to different geometric characteristics and poles configurations, a 3-phase, 12/8 machine and an 8-phase, 16/14 machine prototypes have been used.

Robust FEA models, capable to adapt to widely varying SR machines are critical for

Table 4-IX SRFly: FEA and experimental values of L_a and L_u.

	FEA	Experimental	Error (%)
L_a (mH)	3.970	3.923	1.19
L_u (mH)	0.757	0.770	-1.68

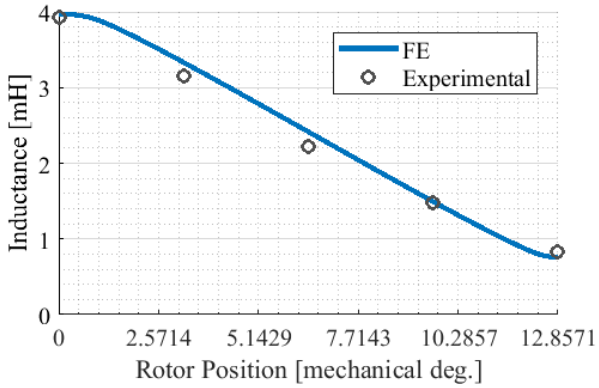

Figure 4-14 SRMyld FEA and experimental inductance profiles.

the rest of this thesis. In fact, FEA models are now necessary to validate the set of analytical models, through which the ADS is defined.

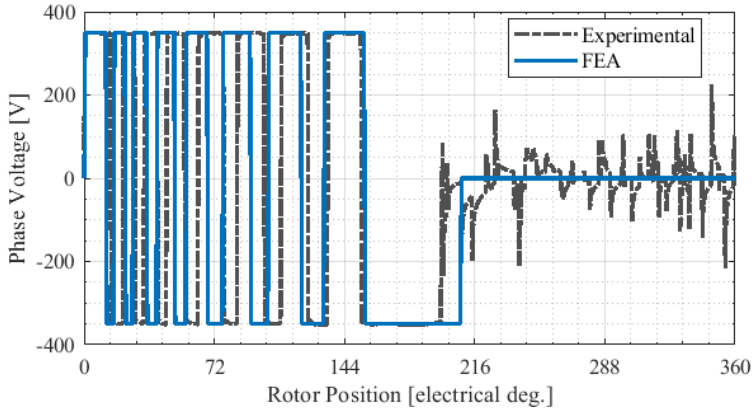

(a)

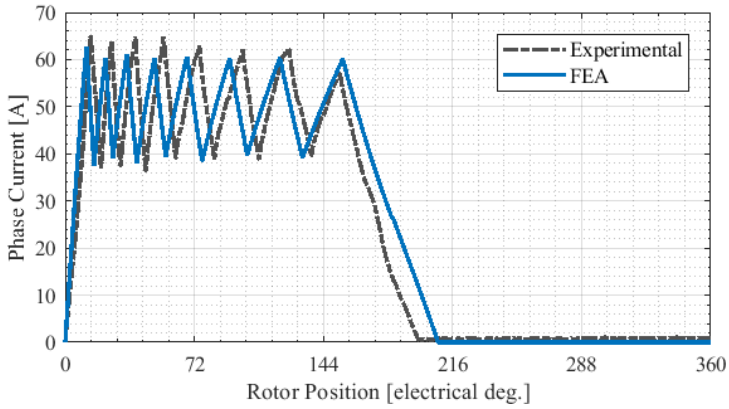

(b)

Figure 4-15 SRFly FEA and experimental results at 1000rpm: (a) phase voltage vs. rotor position, (b) phase current vs. rotor position.

5 ANALYTICAL ELECTROMAGNETIC MODELLING OF THE SR MACHINE FOR ADS DETERMINATION

Analytical models developed in this thesis are aimed at the determination of the ADS and therefore are required to predict the performance of any of its possible members, i.e. any possible SR machine design candidate. To this end, an extreme flexibility, as well as the capability to adapt to a wide variety of geometries and poles configurations is absolutely necessary. To ensure that the proposed comply with this *diktat*, it has been preferred to proceed as follows:

1. Begin with the development of the FEA models, based on two physical SR prototypes widely different in their geometry and poles configuration (their description is provided in Chapter 4);
2. Validate the FEA models reliability and flexibility against the experimental results from the two prototypes;
3. Develop the analytical models and validate their results against experimentally-validated FEA models.

This Chapter is devoted to the description of the electromagnetic modelling.

5.1 ANALYTICAL FORMULATION AND NUMERICAL RESOLUTION

In Chapter 3, it has been pointed out that the ADS generation process should be computationally negligible compared to any FEA process. Therefore, the kind of mathematical models used to generate the ADS must be chosen accordingly. Further to that, all of the analytical models proposed are based on an analytical formulation, meaning that all of the equations are expressed through an explicit analytical formula. Consequently, the need for computationally cheap mathematical models yields the exclusion of all of the high-complexity models, such as Finite Differences or Conformal Mapping. In the future, the implementation of these more advance modelling techniques for the generation of the ADS will be investigated.

In terms of resolution, it is well known that any nonlinear equation, or set of equations, can be either solved analytically (not always), or numerically. In this thesis, in cases where analytical solutions became cumbersome and/or too long to handle, numerical, non-iterative solution have been preferred.

5.2 SR MACHINE OPERATING PRINCIPLE

This Section is a follow-up of the background provided in Section 2.4 about the energy conversion principle that the SR machine uses. In particular, this Section introduces the effects of the applied control strategy and the resulting operating mode on the SR machine performance.

5.2.1 TORQUE-PRODUCING MECHANISM

Figure 5-1 illustrates the geometry of a pole pair of an m-phase SR machine. The energy exchange between an m-phase SR machine and an external supply circuit is now considered. Recalling the basics discussed in Chapter 2, (2-12) is now extended to a rotating machine. Then, the output torque T is evaluated as the variation of co-energy W_f' during an infinitesimal rotary displacement $d\theta$. T and W_f' are expressed by (5-1) and (5-2) respectively. In (5-1), i represents the total amount of current flowing through the SR machine and θ the rotor position. In (5-2), Ψ_{ph_k} and i_{ph_k} indicate the flux linkage and current of the k^{th} phase.

$$T(i,\theta)=\frac{\partial W_f'(\theta,i)}{\partial\theta}, \tag{5-1}$$

$$W_f'(\theta,i)=\sum_{k=1}^{m}\int \Psi_{ph\_k}\left(\theta,i_{ph\_k}\right)di_{ph\_k}. \tag{5-2}$$

Given that the mutual inductances in the SR machine are negligible (unless specific winding configurations are used, [52]), (5-2) yields (5-3), where L represents the self-inductance of the k^{th} phase.

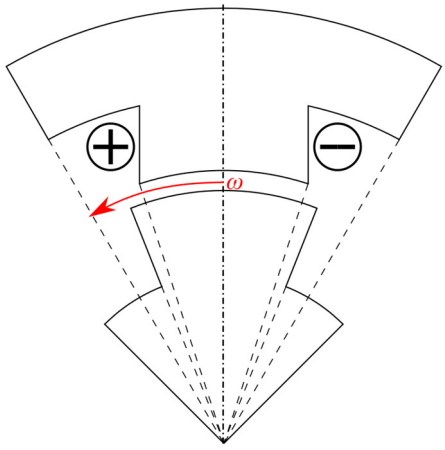

Figure 5-1 A pole-pair of a generic m-phase SR machine

$$T(\theta,i)=\sum_{k=1}^{m}\frac{1}{2}i_{ph\_k}(\theta)^2\frac{\partial L_{\_k}(\theta,i_{ph\_k})}{\partial\theta}. \tag{5-3}$$

Eq. (5-3) shows the well-known fact that the output torque is proportional to the inductance gradient. Consequently, a positive torque, i.e. a motoring mode of operation, is produced when the phase current flows in conjunction with a positive self-inductance gradient. Conversely, a negative torque, or generating mode of operation, is developed if the phase winding is excited under a negative self-inductance gradient. A deeper insight about the inductance vs. rotor position profile of the SR machine is given in Subsection 5.3.1. In the course of this thesis, only the motoring mode is considered, as it is common practice for design purposes.

Apart from the inductance gradient, (5-3) shows that torque production is also proportional to the phase current square. The latter derives from the response of the magnetic circuit to the supplied phase voltage. This response is strongly dependent on the speed of rotation, as discussed in Subsection 5.2.2 below.

5.2.2 PHASE VOLTAGE EQUATION AND EQUIVALENT CIRCUIT

SR drives belong to the voltage-driven type. Hence, the phase-current stems from the response of the magnetic circuit to the voltage applied across the phase winding. Several converter architectures for SR machines have been investigated [96]. However, the majority of SR drives opt for the unidirectional H-bridge, [12]. The topology of one converter phase is shown in Figure 5-2.

The 'energizing', or 'dwell' period Θ_{dwell} starts at the rotor position θ_{ON}. As soon as the switches T1 and T2 are turned-on, the current rise is driven by the phase voltage v_{ph} (see Figure 5-2 (a)). Then, the 'de-energizing', or 'de-fluxing' period $\Theta_{d\varphi}$ starts at the position θ_{OFF}. Hence, both T1 and T2 are turned off and the phase voltage is reversed due to the freewheeling diodes D1 and D2, as Figure 5-2 (b) shows. At this point, i_{ph} decays until it reaches the 'extinction' point θ_E. Finally, v_{ph} and i_{ph} remain at zero until a new cycle begins.

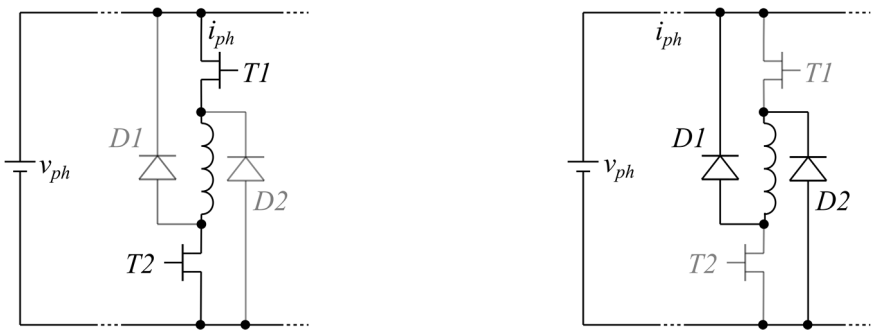

(a) energization current flow. (b) de-energization current flow.

Figure 5-2 The k^{th} phase of a unidirectional H-Bridge Topology

For a constant speed of rotation ω, the phase current waveform can be found from the terminal voltage equation (5-4), [1], being v_{ph} the applied phase voltage, L and R the phase inductance and phase resistance respectively.

$$v_{ph} = Ri_{ph} + L\left(\theta, i_{ph}\right)\frac{di_{ph}}{dt} + i_{ph}\frac{\partial L(\theta, i_{ph})}{\partial \theta}\omega\,. \tag{5-4}$$

The first two terms in (5-4) represent the resistive and inductive voltage drops. The third term is known as the pseudo machine back-emf e_{ph}, since it is proportional to the machine speed. Eq. (5-4) corresponds to the elementary equivalent circuit represented in Figure 5-3.

Based on the impact of the pseudo machine back-emf over the other two terms at the right-hand side of (5-4), it is possible to define the high-speed and low-speed operating conditions:

1. Operation at low speed is characterised by ω being so low that the 'pseudo' back-emf is negligible compared to the other voltage drops, as shown in (5-5):

$$i_{ph}\frac{\partial L(\theta, i_{ph})}{\partial \theta}\omega \ll Ri_{ph} + L\left(\theta, i_{ph}\right)\frac{di_{ph}}{dt}\,. \tag{5-5}$$

2. The high-speed operation is defined for ω sufficiently high that the 'pseudo' back-emf dominates over the other voltage drops and becomes comparable to the phase voltage, as shown in (5-6):

$$i_{ph}\frac{\partial L(\theta, i_{ph})}{\partial \theta}\omega \gg Ri_{ph} + L\left(\theta, i_{ph}\right)\frac{di_{ph}}{dt}\,. \tag{5-6}$$

The phase current waveforms that results from the low-speed and high-speed operating are described in Subsections 5.2.3 and 5.2.4 below.

5.2.3 The Low-Speed Chopping Mode Operation

In the operating conditions described by (5-5), the phase current tends to rise with relatively high rates. As a consequence, the control system engages to limit its peak value through an hysteresis controller.

Figure 5-4 and Figure 5-5 illustrate the typical waveforms of the phase voltage and phase current vs. the rotor position θ over one electric period, along with a real inductance profile. As said above, once it is engaged, the hysteresis controller conditions the opening and closing of T1 and T2 in order to keep the phase current within the hysteresis band Δi. This operating mode is named 'chopping'.

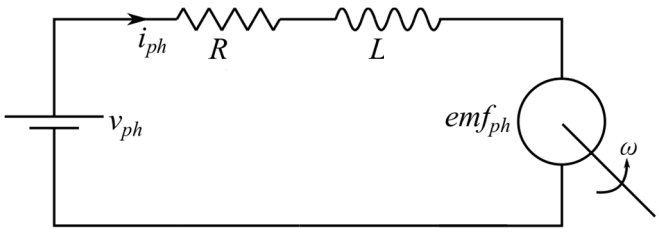

Figure 5-3 Equivalent circuit of an SR machine

As it is also illustrated in Figure 5-4 and Figure 5-5, the turn-on instant is advanced by a relatively small angle θ_{AD} with respect of the ideal turn-on position, i.e. the point of minimum inductance. This advance is aimed at compensating for the current rise time so that i_{pk} is reached nearby the position where the inductance gradient begins to grow with a significant rate. Similarly, the OFF signal is given near the position where the inductance gradient begins to approach zero. In this way, the phase current discharges with no torque production.

Basing on the opening and closing strategies of T1 and T2, two chopping modes are possible, namely hard and soft chopping. The hard-chopping mode is that represented in Figure 5-4. T1 and T2 are opened and closed synchronously, so that the full positive $+V_{DC}$ or full negative $-V_{DC}$ voltage is applied across the phase winding. The soft chopping mode is represented in Figure 5-5. In this case, as soon as the phase current reaches the threshold value i_{pk}, one of the two switches (usually T1) is left closed for the whole dwell period. Meanwhile, the other switch is opened and closed. As a result, the applied phase voltage alternates between $+V_{DC}$ and 0 during chopping.

The mathematical modelling aimed at the performance evaluation of the SR machine working in low-speed conditions is outlined in Subsection 5.4.

5.2.4 THE HIGH-SPEED SINGLE-PULSE OPERATION

When the condition expressed in (5-6) is entered, i_{ph} is limited by the pseudo back-emf itself. Hence, there is a need for conditioning the peak value through the inverter. The typical waveforms of the phase voltage and phase current vs. the rotor position θ over one electric period, in single-pulse mode, are illustrated in Figure 5-6. The inductance vs. rotor position profile is also illustrated. This operating mode is named 'single-pulse', due to the fact that each converter leg is switched on and off only once per

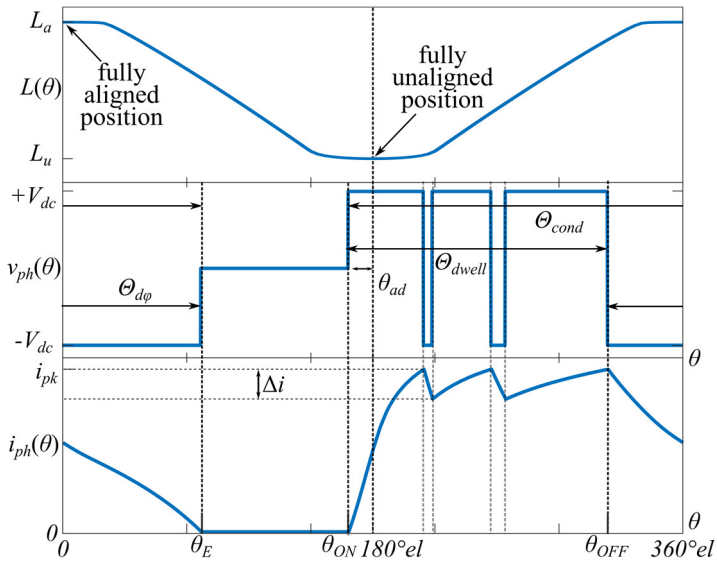

Figure 5-4 SR machine, hard chopping mode: inductance profile, voltage and current waveforms.

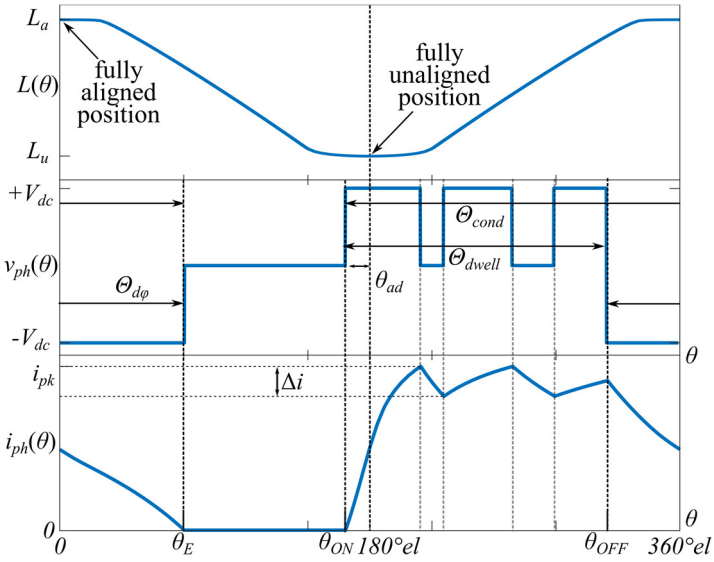

Figure 5-5 SR machine, soft chopping mode: inductance profile, voltage and current waveforms.

cycle.

When running at high speeds in single-pulse mode, θ_{ON} and θ_{OFF} are chosen with a very different criterion compared to the low-speed case. In fact, a considerable advance angle is required to reach the desired torque levels. Indeed, this early magnetization allows the phase current to rise to a sufficiently high level before the instantaneous back-emf becomes comparable to the instantaneous phase voltage. Moreover, wide dwell periods, in the range of 150°- 180° (elec.), are usually required to produce the desired torque. The mathematical modelling of the machine performance in high-speed, single-pulse mode is discussed in Subsection 5.3.

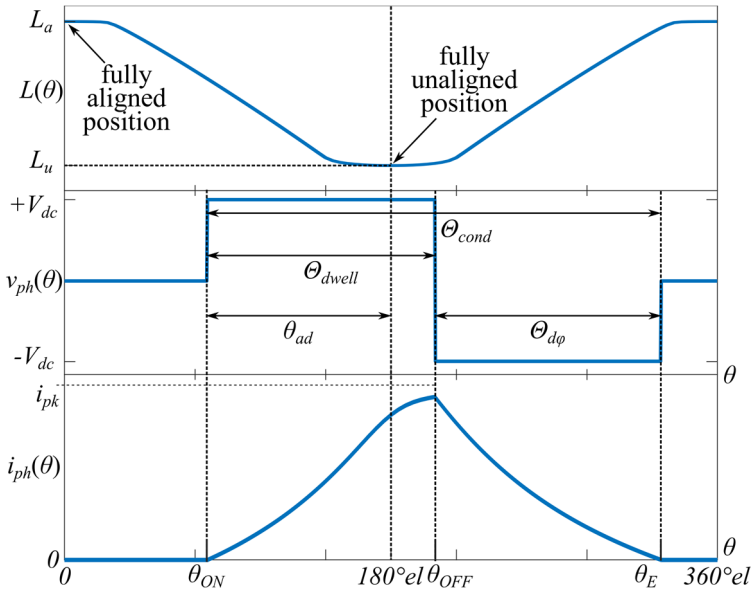

Figure 5-6 SR machine, single-pulse mode: inductance profile, voltage and current waveforms.

5.3 HIGH-SPEED ELECTROMAGNETIC PERFORMANCE PREDICTION

This Subsection describes the mathematical modelling of the SR machine operating in the conditions of high speed described by (5-6). Aim of the models is the determination of the main machine performance, namely the rms current value i_{ph_RMS} along with the slot current density J_{ss}, the average torque T_{AVG} and torque ripple T_{RIP}, as well as the iron and copper losses P_{FE} and P_{CU}.

From the current and voltage waveforms shown in Figure 5-6, it is possible to derive phase flux linkage Ψ_{ph} vs. phase current locus, which is depicted in Figure 5-7. This locus is also known as energy-conversion loop, [92]. In fact, in accordance with (5-3), its subtended area represents the amount of energy that each phase converts into mechanical work in one cycle.

From Figure 5-7, it can be seen that even though the phase current can reach a considerably high value, the highest values are reached when the inductance is around its lowest value. Consequently, Ψ_{ph} remains well below the saturation level of the magnetic core. This behaviour explains the widely accepted assumption that saturation is negligible in SR machines that run at high speeds [38]. The possibility to neglect the effects of the iron core saturation, allows us to consider the behaviour of the magnetic circuit independent of the phase current. This kind of model is referred to as 'linear', [97].

5.3.1 UNSATURATED INDUCTANCE VS. ROTOR POSITION PROFILE

As already discussed in Chapter 3, for determining the ADS analytical models are the most convenient option. For the unsaturated inductance profile, the model proposed in this thesis is based on a piecewise inductance vs. rotor position expression, since this representation has historically demonstrated to provide the best compromise between computational cost, simplicity and accuracy when used to predict the SR machine's unsaturated behaviour.

To this cause, inductance values are analytically determined at some specific rotor positions. Then, fitting curves are introduced to join the nodes. With regard to the

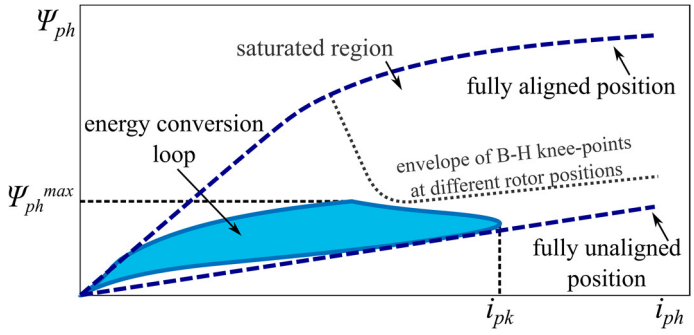

Figure 5-7 SR machine operation in single-pulse mode: current vs. flux linkage energy-conversion loop.

inductance evaluation at a given rotor position node, Subsection 5.3.1.2 provides an insightful discussion about the most suitable analytical approach to derive the ADS, whereas the analytical calculation of the inductance values is presented in Chapter 6.

5.3.1.1 FULL-OVERLAP, PARTIAL OVERLAP AND NON-OVERLAP REGIONS

This Subsection introduces the three regions that determine the SR machine inductance profile.

The initial rotor position, $\theta=0$ or θ_a, is considered at the full alignment between one stator and one rotor tooth, as shown in Fig. 5-8(a). As the rotor moves, the two facing poles remain fully overlapped until the position θ_1 is reached. Fig. 5-8(b) and Fig. 5-8(c) show respectively the full-overlap condition and the position θ_1. The expression for θ_1 is given in (5-7), where β_{st} and β_{rt} are the stator and rotor pole arcs respectively. As the rotation continues, the two facing poles overlap only partially, as in Fig. 5-8(d). This partial-overlap region terminates at the position θ_2, which is shown in Fig. 5-8(e) and whose equation is given by (5-8).

$$\theta_1 = \frac{\beta_{rt} - \beta_{st}}{2}, \tag{5-7}$$

$$\theta_2 = \frac{\beta_{rt} + \beta_{st}}{2}. \tag{5-8}$$

At θ_2, the non-overlap region commences, as shown in Fig. 5-8(f). Finally, the maximum misalignment condition occurs at $\theta=\pi/N_r$ or θ_u, represented in Fig. 5-8(g). Then, the profile symmetrically repeats.

5.3.1.2 FIELD-SOLUTION-BASED VS. FLUX-TUBE-BASED MODELS

For the determination of the inductance at a given rotor position, analytical models available can be classified into two families: 1) field-solution based and 2) flux-tubes based:

1. The field-solution-based models require the determination of the flux density distribution inside the areas of interest. The solution can be achieved either in the original physical system, [98], or through the Schwarz-Christoffel transformation,

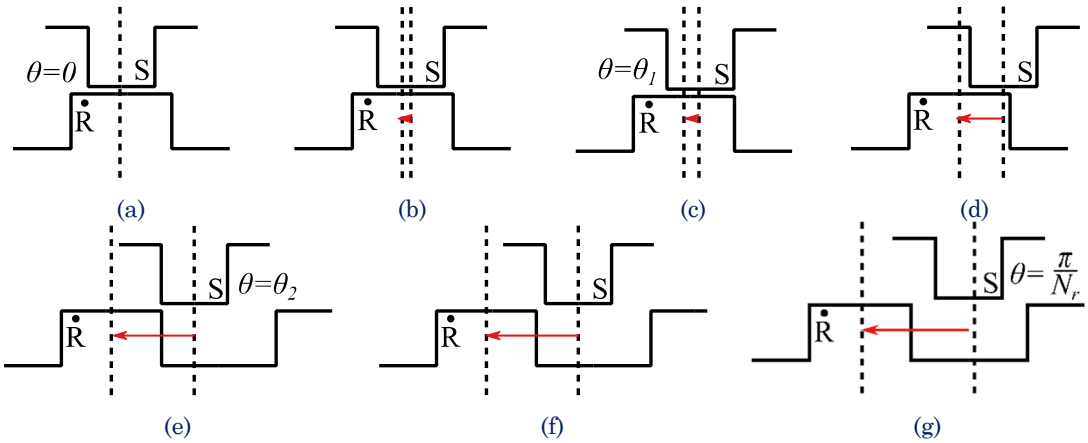

Fig. 5-8. Inductance Profile: (a) $\theta=0$, (b) full-overlap region, (c) $\theta=\theta_1$, (d) partial-overlap region, (e) $\theta=\theta_2$, (f) non-overlap region, (g) $\theta=\pi/N_r$.

[99], also known as conformal mapping, [100].

2. The flux-tubes-based models rely on a set of flux tubes that follow a predefined path. Then, flux tubes are used to define either a network of reluctances, [85], or a permeance function, [19], which yield the inductance.

Even though field-solution-based models proved to achieve levels of accuracy comparable to FEA models, they result highly time-consuming in terms of both implementation and computation. On the other hand, flux-tubes-based methods proved to reduce dramatically the computational cost, providing acceptable levels of accuracy. Hence, the flux-tubes-based methods represents the best option for the ADS determination.

Apart from the low computational cost, a further requirement for the analytical model is to adapt to widely different machine geometries, in order to guarantee accurate inductance estimates for every member of the ADS. In this regard, reluctance-network-based methods usually consider flux paths that are tailored on a specific machine geometry, e.g. fixed stator and rotor pole arcs, fixed rotor and stator tooth height, etc.. Consequently, accuracy tends to lower as long the machine under consideration differs from the reference machine, [101]. For example, the 60° angle shown in Figure 5-9 (a) is a valid approximation for geometries with high rotor teeth. As the rotor tooth height reduces, flux lines change their path and hence the angle value is no longer valid. A possible alternative could be to consider a multitude of reference machines, which would surely overcomplicate the method.

The permeance-function-based approach proved to adapt effectively to widely different geometries, with no extra implementation effort. In fact, as it can be seen in Figure 5-9 (b), [102], flux tubes paths are suitable for any machine geometry. For instance, a variation of the geometry in Figure 5-9 only results in a variation of the portions of airgap where tube families 1-4 are found.

To recap, the best option for the ADS determination is found to be the permeance-based model. The determination of the inductance values at the four inductance nodes

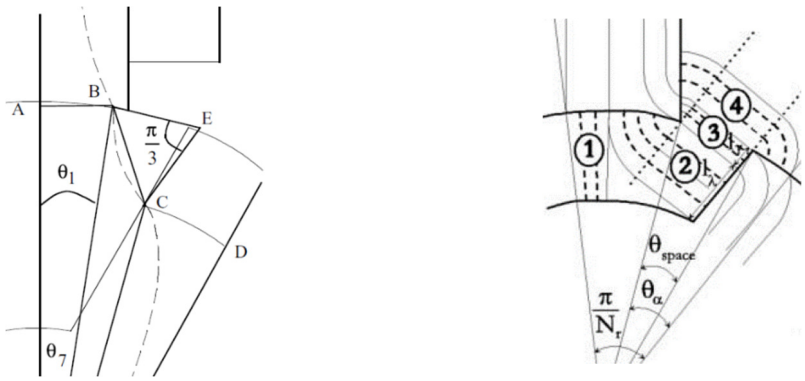

(a) (b)

Figure 5-9 Example of predetermined flux tube path for: a) reluctance network, [101]) and b) permeance function, [102].

indicated in Subsection 5.3.1.1, namely θ_a, θ_1, θ_2 and θ_u, is described later in this thesis in Chapter 6.

5.3.1.3 THREE-INDUCTANCE AND FOUR-INDUCTANCE LOCI

The simplest representation of the inductance vs. rotor position locus is the idealised trapezoidal profile, [85], which is based on the assumption of negligible fringing and rounding phenomena. In the full-overlap region, $0 \leq \theta \leq \theta_1$, the inductance is considered constant at its maximum L_a. In the partial-overlap region, $\theta_1 \leq \theta \leq \theta_2$, the profile descends linearly. Finally, in the non-overlap region, $\theta_2 \leq \theta \leq \pi/N_r$, the profile remains constantly at the minimum inductance L_u. Illustrations of the trapezoidal profile in the full-overlap and non-overlap regions are given in Figure 5-10.

As it can be observed, only two inductance values are required to define a trapezoidal locus. However, this representation is extremely simplified and hence cannot provide an accurate evaluation of the machine performance. The main reasons are the following:

1. Inaccurate representation of the non-overlapping region. As the FEA profile plotted in Figure 5-10 (b) shows, the trapezoidal profile underestimates the inductance in the non-overlap region. This inaccurate estimation might lead to inaccurate estimates of the phase current, of the inductance gradient and therefore of the output torque.
2. Discontinuous derivative. As shown by (5-3), the instantaneous torque value is proportional to the inductance gradient. In the trapezoidal profile, the two sharp variations of inductance at θ_1 and θ_2 might cause inaccurate torque ripple estimations.

To overcome the aforementioned issues, this thesis proposes two improved representations: a three-inductance profile and a four-inductance profile.

THREE-INDUCTANCE LOCUS

In order to avoid the issues caused by an inductance underestimation in the non-overlapping region, a Fröhlich-like expression is used instead of a constant inductance value, [103]. The proposed representation is plotted in Figure 5-10 (b), where a close match with the FEA locus is observed. On the other hand, the calculation of an additional inductance value is required, i.e. L_2 at the position θ_2.

The proposed three-inductance profile is defined as follows:

- In the full-overlap region, due to the low phase currents, it is reasonable to maintain the representation with the constant inductance value used in the trapezoidal locus (see Figure 5-10 (a));
- In the partial-overlap region, the inductance decays linearly until the point (θ_2, L_2). The slope s of the inductance in this region is given by (5-9).

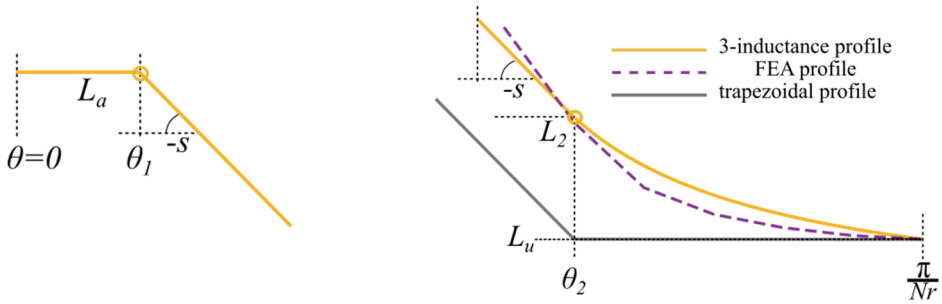

(a) (b)

Figure 5-10 Three-inductance profile: full-overlap and non-overlap regions.

$$s = \frac{L_a - L_2}{\theta_2 - \theta_1}, \tag{5-9}$$

- In the non-overlap region, the inductance descends from L_2 to L_u following the aforementioned Fröhlich-like trend, whose expression is in the form:

$$L_x + \frac{ab(\theta - \theta_x)}{b + (\theta - \theta_x)},$$

where L_x and θ_x represent one of the two region extremes and a and b are two coefficient to be determined by imposing two boundary conditions. The first condition sets the inductance value L_u at θ_2; the second sets the derivative value at θ_2 equal to s, [103]. The resulting expressions of a and b are expressed in (5-10).

$$\begin{cases} a = s \\ b = \dfrac{(L_2 - L_u)\left(\dfrac{\pi}{N_r} - \theta_2\right)}{s\left(\dfrac{\pi}{N_r} - \theta_2\right) - (L_2 - L_u)} \end{cases}. \tag{5-10}$$

Finally, the analytical expression of the three-inductance profile is given in (5-11), while its graphical representation is provided in Figure 5-11.

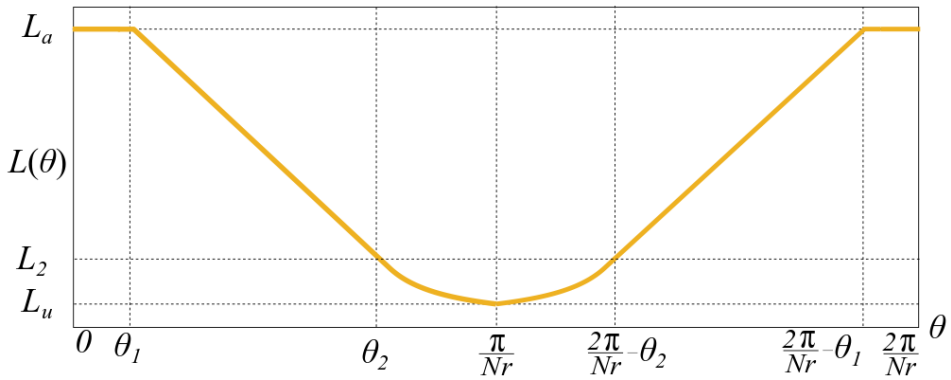

Figure 5-11 Three-Inductance profile.

$$L(\theta)=\begin{cases} L_a & 0\le\theta\le\theta_1 \\ L_a - s(\theta-\theta_1) & \theta_1\le\theta\le\theta_2 \\ L_2 - \dfrac{sb(\theta-\theta_2)}{b+(\theta-\theta_2)} & \theta_2\le\theta\le\dfrac{\pi}{N_r} \\ L_2 + \dfrac{sb\left(\theta+\theta_2-\dfrac{2\pi}{N_r}\right)}{b-\left(\theta+\theta_2-\dfrac{2\pi}{N_r}\right)} & \dfrac{\pi}{N_r}\le\theta\le\dfrac{2\pi}{N_r}-\theta_2 \\ L_a + s\left(\theta+\theta_1-\dfrac{2\pi}{N_r}\right) & \dfrac{2\pi}{N_r}-\theta_2\le\theta\le\dfrac{2\pi}{N_r}-\theta_1 \\ L_a & \dfrac{2\pi}{N_r}-\theta_1\le\theta\le\dfrac{2\pi}{N_r} \end{cases} \quad (5\text{-}11)$$

FOUR-INDUCTANCE LOCUS

The four-inductance locus is proposed as an improvement with respect of the three-inductance locus proposed above, even though at the price of a more complex mathematical expression. In particular, the four-inductance locus is built in order to guarantee the continuity of the profile derivative as well. The latter is achieved by adding two modifications to the trapezoidal profile:

1. The node (θ_1, L_1) is added to the profile expression.
2. The full-overlapping and non-overlapping regions are modelled with a slightly modified Fröhlich-like expression.

With regard to point 2 above, it is observed that the derivative of the Fröhlich-like expression used in the three-node profile is never equal to zero. Consequently, this representation does not allow setting to zero the profile's derivative at θ_a and θ_u. To overcome this issue, the 'quadratic' Fröhlich-like expression is proposed in this thesis:

$$\begin{cases} L(\theta) = L_x + \dfrac{ab(\theta-\theta_x)^2}{a+(\theta-\theta_x)} \\ \dfrac{dL(\theta)}{d\theta} = \dfrac{ab(\theta-\theta_x)\left(2a+(\theta-\theta_x)\right)}{\left(a+(\theta-\theta_x)\right)^2} \end{cases}.$$

L_x, θ_x, a and b are evaluated by imposing the following four boundary conditions: 1) function value at the left-hand-side node, 2) function value at the right-hand-side node, 3) derivative value at the left-hand-side node and 4) derivative value at the right-hand-side node.

Figure 5-12 (a) and (b) illustrate respectively the full-overlapping and non-overlapping regions of the proposed four-inductance locus. A close match with the FEA locus is observed, along with a smooth curve with no sharp nodes.

The proposed four-inductance locus is defined as follows:

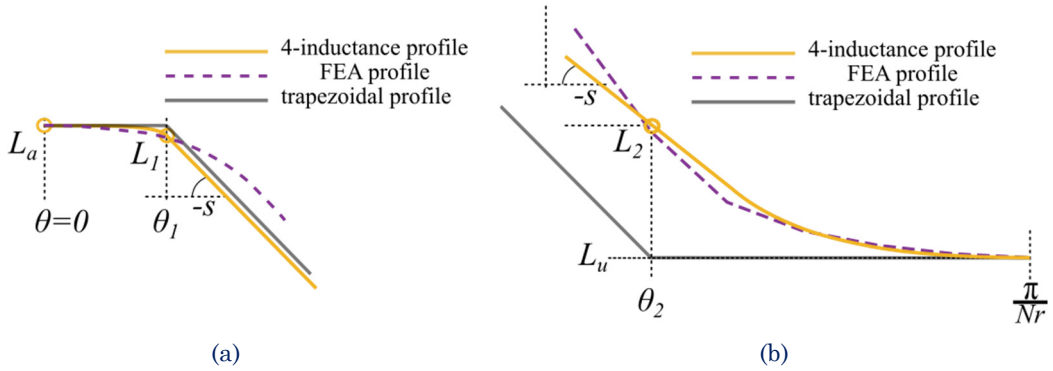

Figure 5-12 Three-inductance profile: full-overlap and non-overlap regions.

- The full-overlap region is represented by the 'quadratic' Fröhlich-like expression given above. Curve parameters L_{fo}, θ_{fo}, a_{fo} and b_{fo} are given below (to note that s is given by the partial-overlap region):

$$\begin{cases} L_{fo} = L_a \\ \theta_{fo} = 0 \\ a_{fo} = -\theta_1 \dfrac{s\theta_1 - L_a - L_1}{s\theta_1 - 2(L_a - L_1)} \\ b_{fo} = \left(\dfrac{L_a - L_1}{\theta_1}\right)\left(\dfrac{a_{fo} + \theta_1}{a_{fo}\theta_1}\right) \end{cases}, \tag{5-12}$$

- In the partial-overlap region, the inductance follows a linear trend between (θ_1, L_1) and (θ_2, L_2). The slope s is expressed by (5-13).

$$s = \frac{L_1 - L_2}{\theta_2 - \theta_1}, \tag{5-13}$$

- The non-overlap region is also represented with a 'quadratic' Fröhlich-like expression. Parameters L_{no}, θ_{no}, a_{no} and b_{no} are as follows:

$$\begin{cases} L_{no} = L_u \\ \theta_{no} = \theta_u \\ a_{no} = -(\theta_2 - \theta_u)\dfrac{s(\theta_2 - \theta_u) + (L_2 - L_u)}{s(\theta_2 - \theta_u) + 2(L_2 - L_u)} \\ b_{no} = \left(\dfrac{L_2 - L_u}{\theta_2 - \theta_u}\right)\left(\dfrac{a_{no} + \theta_2 - \theta_u}{a_{no}(\theta_2 - \theta_u)}\right) \end{cases}. \tag{5-14}$$

Eq. (5-15) provides the analytical expression of the four-inductance profile, while Figure 5-13 its graphical representation.

5.3.1.4 LOCI VALIDATION AND DISCUSSION

The three-inductance and the four-inductance profiles proposed above are now validated against the results from the experimentally-validated FEA models of the SRMyld and SRFLY prototypes. It is highlighted that the inductance values at the rotor positions θ_a, θ_1, θ_2 and θ_u used to produce the curves below have been determined analytically with the method is discussed in Chapter 6.

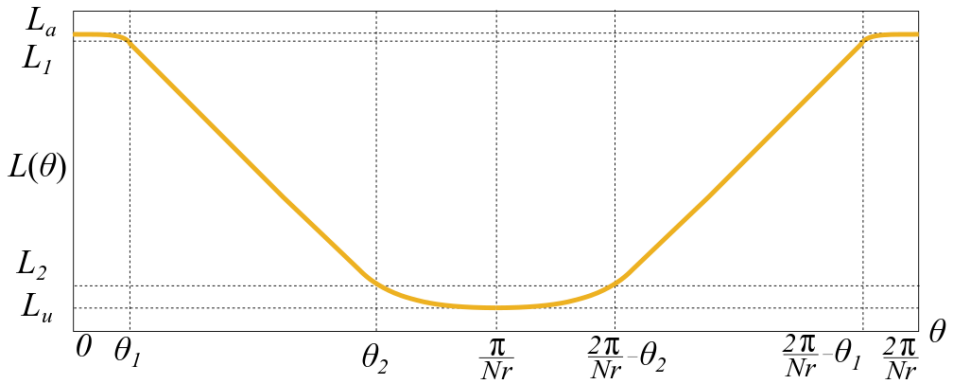

Figure 5-13 Four-Inductance profile.

$$L(\theta)=\begin{cases} L_a-\dfrac{a_{fo}b_{fo}(\theta)^2}{a+\theta} & 0\le\theta\le\theta_1 \\ L_1-s(\theta-\theta_1) & \theta_1\le\theta\le\theta_2 \\ L_u-\dfrac{a_{no}b_{no}(\theta-\theta_u)^2}{a_{no}+\theta-\theta_u} & \theta_2\le\theta\le\dfrac{\pi}{N_r} \\ L_u-\dfrac{a_{no}b_{no}(\theta_u-\theta)^2}{a_{no}+\theta_u-\theta} & \dfrac{\pi}{N_r}\le\theta\le\dfrac{2\pi}{N_r}-\theta_2 \\ L_1+s\left(\theta+\theta_1-\dfrac{2\pi}{N_r}\right) & \dfrac{2\pi}{N_r}-\theta_2\le\theta\le\dfrac{2\pi}{N_r}-\theta_1 \\ L_a-\dfrac{a_{fo}b_{fo}\left(\dfrac{2\pi}{N_r}-\theta\right)^2}{a+\dfrac{2\pi}{N_r}-\theta} & \dfrac{2\pi}{N_r}-\theta_1\le\theta\le\dfrac{2\pi}{N_r} \end{cases} \quad (5\text{-}15)$$

Validation against the SRMyld results is represented in Figure 5-14. Subplots (a) and (c) respectively compare the three-inductance and four-inductance profiles against the FEA and experimental results. As observed, in both cases the error drops from the -1% at θ_a to the -6% at θ_u. In the non-overlap region, the error introduced by the two profiles varies in a slightly different way because of the different analytical expressions being used. However, the maximum error remains below the 8%. Subplots (b) and (d) illustrate the inductance derivative with respect of the rotor position. Due to the non-derivable point at θ_u, the error in the three-inductance profile grows to infinite.

Figure 5-15 illustrates the comparison against the SRFLY FEA data. In this case, the error in the inductance estimation oscillates between the -11% and the +3%. Reasons for a higher discrepancies in the non-overlap conditions, compared to SRMyld, are thoroughly explained in Chapter 6. However, for the SRFly profile, errors above the 10% are incurred in a relatively short region of the profile, so that performance prediction is not strongly affected.

The two proposed profile representations are now compared. The following two points can be noted:

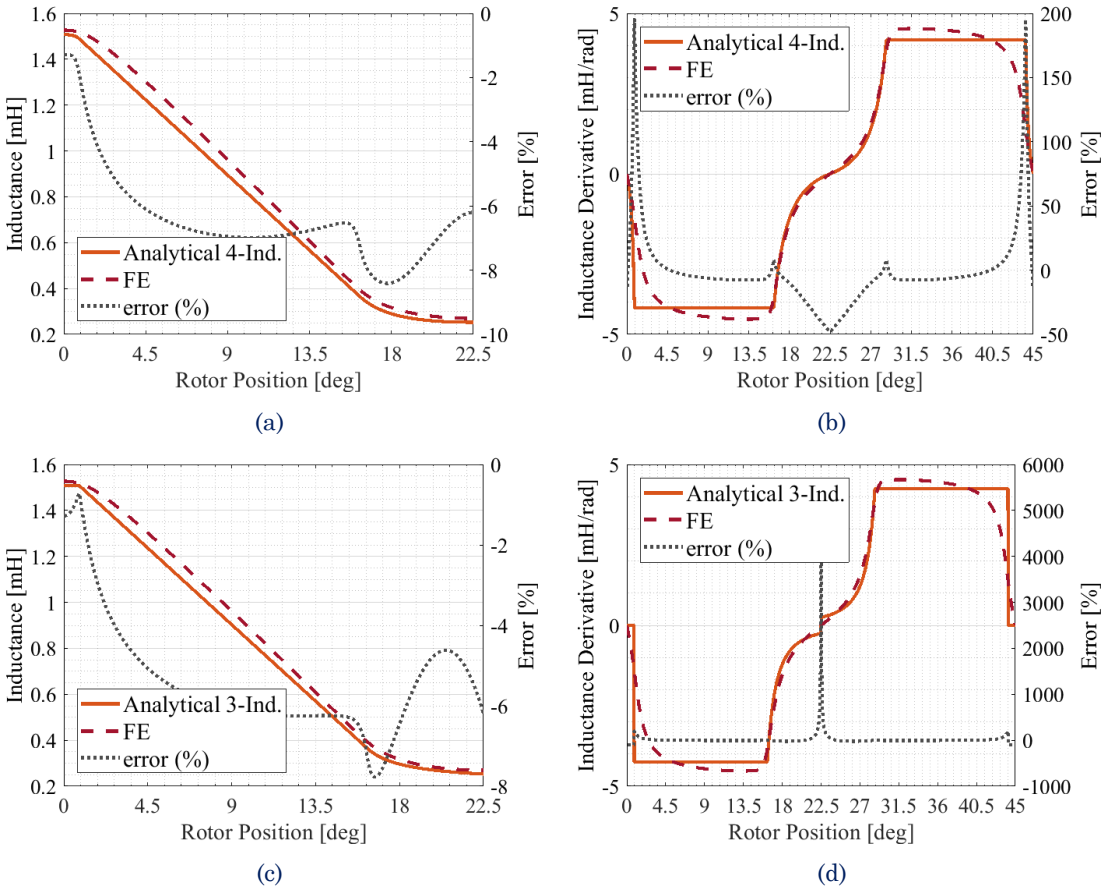

Figure 5-14 SRMyld unsaturated inductance profile validation: a) three-inductance locus, b) three-inductance locus derivative, c) four-inductance locus and d) c) four-inductance locus derivative.

1. both profiles can predict accurately the inductance vs. rotor position characteristics with errors that are below the 10%;
2. at the price of a more complicated mathematical expression, the four-inductance profile provides a finite-valued derivative at every rotor position.

Given that the computational cost required to calculate analytically one more inductance value is totally negligible, the main difference remains in the mathematical formulation complexity. The four-inductance representation may be preferred when a higher accuracy in the performance estimations is required. Indeed, it is used in Subsections 5.3.3 and 5.3.4 to determine the full set of SR machine performance. Conversely, the three-inductance locus may be preferred when a simple mathematical formulation is an absolute priority. In particular, this locus representation is used in Subsection 5.3.2 below to derive the optimal advance angle for operation at high speed directly in a closed-form analytical expression.

5.3.2 Torque-Maximising Advance Angle: Closed-Form Expression

When performance at the maximum speed is accounted for during the ADS determination, priority shall be given to the compliance with the power requirement.

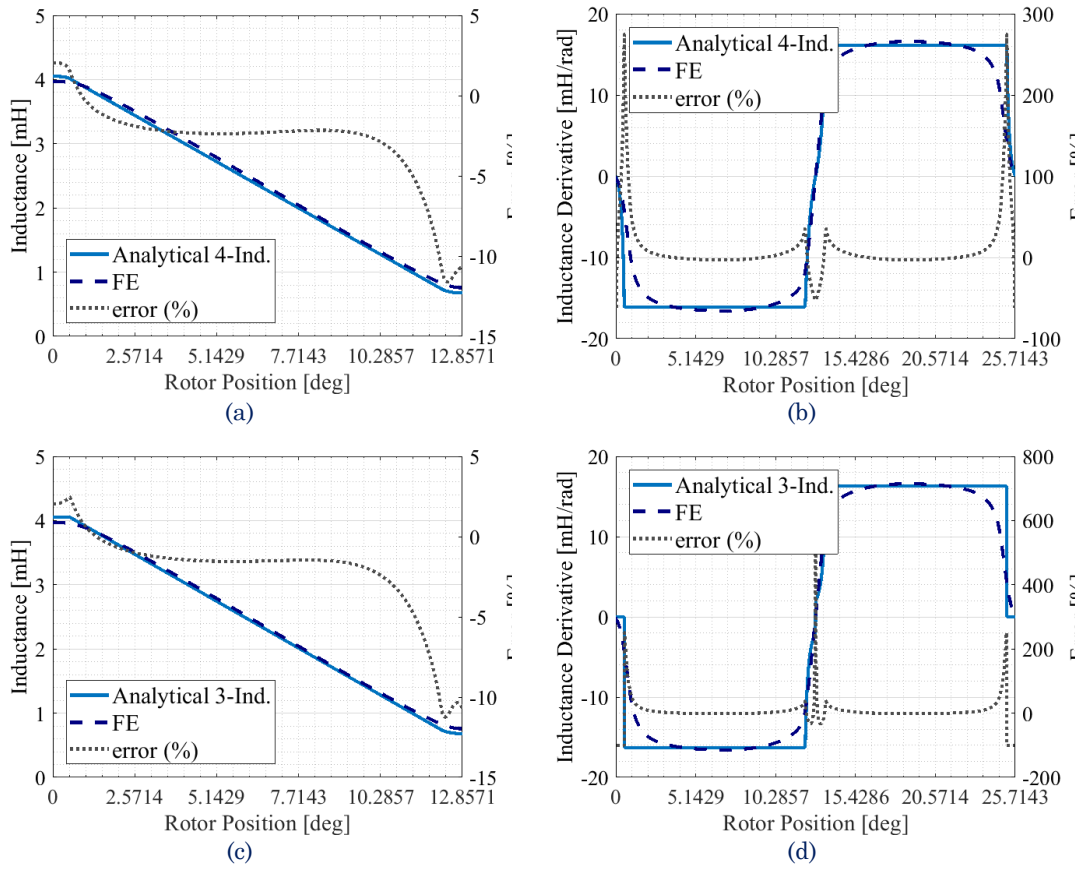

Figure 5-15 SRFLY unsaturated inductance profile validation: a) three-inductance locus, b) three-inductance locus derivative, c) four-inductance locus and d) c) four-inductance locus derivative.

Hence, candidates that provide a power that is equal or greater than the rated one 'survive', whereas those which do not are discarded. In SR machines, performance at high speed are strongly affected by the control parameters. Therefore, the application of this requirement needs the control parameters to be included into the process. As shown in Subsection 5.2.4, single-pulse operation offers three control variables, namely: DC-bus voltage V_{DC}, advance angle θ_{AD} and dwell period Θ_{dwell}. Then, the three parameters shall be set in order to develop the maximum output torque.

At first glance, one finds that there is usually no room for increasing V_{DC} further; therefore it is considered equal to its rated value.

For Θ_{dwell} and θ_{AD}, Figure 5-16 shows the typical trends of the average output torque T_{AVG} vs. θ_{AD}, for different Θ_{dwell}. As observed, the maximum average torque T_{AVG} occurs when Θ_{dwell} is maximized, i.e. it is equal to 180° (elec.). This is a well-known fact confirmed by several contributions available in the literature, [33, 34, 104-107]. This coincides with the standard dwell period limit, since greater values might not allow the phase current to decay to zero at the end of each cycle.

On the other hand, θ_{AD} is traditionally evaluated through iterative optimisation algorithms, such as the simplex method, [104], or search-grids, [107], due to its strong dependency on the machine geometry, winding configuration and, in some cases, to the

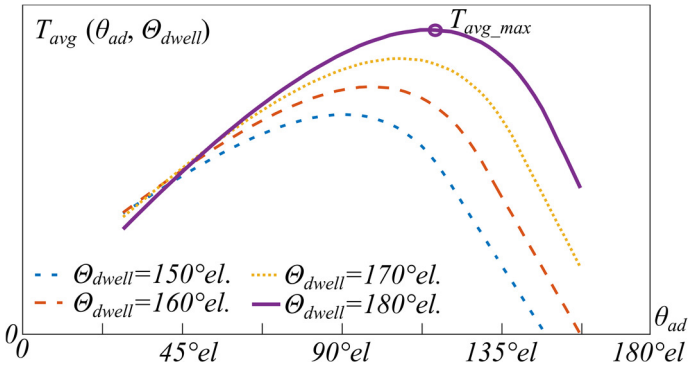

Figure 5-16 SR machine operation in single-pulse mode: average torque vs. advance angle for different dwell periods.

operating conditions. The main drawback of these methods is that they require the output torque to be computed approximately ten times per each member of the ADS. To solve this issue, and thus speed up the ADS generation process, this Subsection develops a closed-form analytical expression for the advance angle θ_{AD}^* that provides the maximum torque. In this way, a one-shot torque evaluation is sufficient to verify the compliance with the power requirement.

5.3.2.1 Model Assumptions

The analytical model developed to attain the aforesaid closed-form expression is now described. The model is based on the following assumptions:

1. According to the discussion in Subsection 5.3.1, magnetic saturation can be neglected due to the operation at high speeds,
2. the machine operates in steady-state conditions with a constant speed of rotation ω,
3. the mutual coupling between phases is negligible,
4. the resistive voltage drop is negligible,
5. the asymmetric H-bridge topology is considered for the VSI [96],
6. the machine operates in single-pulse mode, without any constraint on the peak or rms values of the phase current,
7. Θ_{dwell} is set to 180° (elec.), in order to maximize the output torque.

5.3.2.2 Voltage and Flux Linkage Waveforms

Starting from the assumptions above, phase voltage $v_{ph}(\theta, \theta_{AD})$ and phase flux linkages $\Psi_{ph}(\theta, \theta_{AD})$ can be expressed as functions of the rotor position θ for a given θ_{AD}. In single-pulse operating conditions, the full DC-voltage V_{DC} is applied across the phase between θ_{ON} and θ_{OFF}, which can be written as functions of θ_{AD} and Θ_{dwell}, as in (5-16) and (5-17).

$$\theta_{ON} = \frac{\pi}{P_r} - \theta_{AD}\,, \tag{5-16}$$

$$\theta_{OFF} = \theta_{ON} + \Theta_{dwell} = \frac{2\pi}{N_r} - \theta_{\mathrm{AD}} \tag{5-17}$$

Once the off signal is triggered, the DC-voltage is reversed. Then, since the resistive voltage drop is neglected, the energy conservation principle applies and thus the de-fluxing period has the same duration as the dwell. The resulting $v_{ph}(\theta, \theta_{AD})$ is a rectangular waveform, which is shown in Figure 5-17 (a) and expressed by (5-18).

$$v_{ph}(\theta,\theta_{ad}) = \begin{cases} -V_{DC} & 0 \le \theta \le \frac{\pi}{N_r} - \theta_{AD} \\ +V_{DC} & \frac{\pi}{N_r} - \theta_{AD} \le \theta \le \frac{2\pi}{N_r} - \theta_{AD} \\ -V_{DC} & \frac{2\pi}{N_r} - \theta_{AD} \le \theta \le \frac{2\pi}{N_r} \end{cases}. \tag{5-18}$$

Subsequently, since the resistive voltage drop is neglected, the phase voltage is equal to the variation in time of the phase flux linkage. Then, at a constant speed of rotation, $\Psi_{ph}(\theta, \theta_{AD})$ can be determined by simply integrating v_{ph}, as given in (5-19). To perform the integration, the boundary condition needs to express the full core demagnetization at the turn-on instant, i.e. $\Psi_{ph}(\pi/P_r - \theta_{ad})=0$. The result is a triangular waveform, as illustrated in Figure 5-17 (b).

$$\Psi_{ph}(\theta,\theta_{AD}) = \begin{cases} -\frac{V_{DC}}{\omega}\left(\theta + \theta_{AD} - \frac{\pi}{N_r}\right) & 0 \le \theta \le \frac{\pi}{N_r} - \theta_{AD} \\ \frac{V_{DC}}{\omega}\left(\theta + \theta_{AD} - \frac{\pi}{N_r}\right) & \frac{\pi}{N_r} - \theta_{AD} \le \theta \le \frac{2\pi}{N_r} - \theta_{AD} \\ -\frac{V_{DC}}{\omega}\left(\theta + \theta_{AD} - \frac{3\pi}{N_r}\right) & \frac{2\pi}{N_r} - \theta_{AD} \le \theta \le \frac{2\pi}{N_r} \end{cases} \tag{5-19}$$

.

5.3.2.3 PHASE CURRENT, PHASE TORQUE AND OUTPUT TORQUE

The expression of the phase current $i_{ph}(\theta, \theta_{AD})$ can be found as the ratio between the phase flux linkage $\Psi_{ph}(\theta, \theta_{AD})$:

$$i_{ph}(\theta,\theta_{AD}) = \frac{\Psi_{ph}(\theta,\theta_{AD})}{L(\theta)}. \tag{5-20}$$

As already discussed in Subsection 5.3.1.3, $L(\theta)$ is modelled through the three-inductance locus, due to its relatively simple analytical formula that allows for handy derivative and integral expressions.

From the expression of the phase current, it is then possible to obtain the torque per phase $T_{ph}(\theta, \theta_{AD})$, as in (5-21).

$$T_{ph}(\theta,\theta_{AD}) = \frac{1}{2} i_{ph}(\theta,\theta_{AD})^2 \frac{dL(\theta)}{d\theta} \tag{5-21}$$

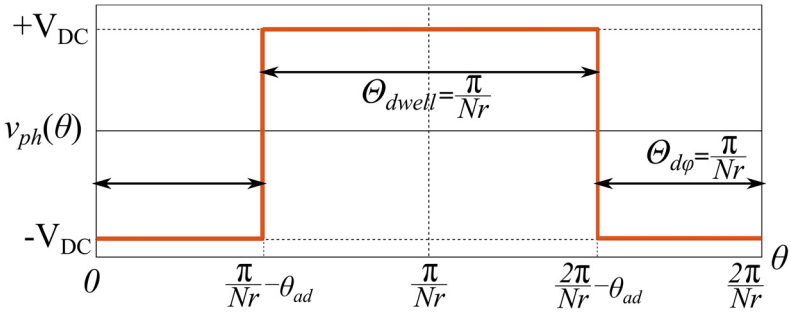

(a)

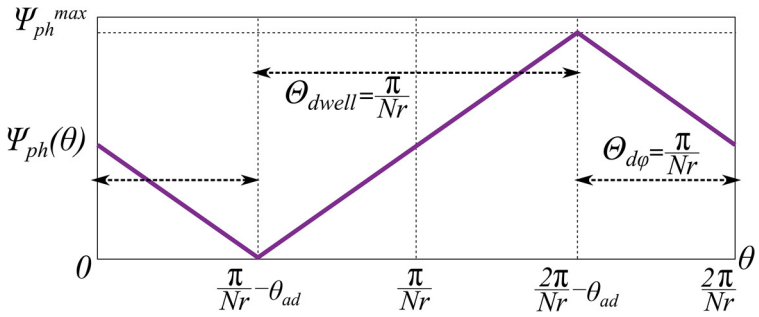

(b)

Figure 5-17 Single-pulse waveforms in output torque maximization mode: a) rectangular phase voltage, b) triangular flux linkage.

The average torque produced by one phase T_{ph_avg} (θ_{AD}), is expressed by (5-22). Finally, since the m phases are controlled with the same θ_{AD} and Θ_{dwell}, the average torque produced by each phase is the same. Therefore, the average overall torque T_{avg} (θ_{AD}), for a given θ_{AD}, is equal to m times T_{ph_avg} (θ_{AD}), as shown in (5-23). This expression is used in Subsection 5.3.2.4 to derive the advance angle that maximizes T_{avg} (θ_{AD}).

$$T_{ph\_AVG}(\theta_{AD}) = \frac{N_r}{2\pi}\int_0^{\frac{2\pi}{N_r}} T_{ph}(\theta, \theta_{AD})\, d\theta \tag{5-22}$$

$$\begin{aligned} T_{AVG}(\theta_{AD}) &= m T_{ph\_AVG}(\theta_{AD}) = m\frac{N_r}{2\pi}\int_0^{\frac{2\pi}{N_r}} T_{ph}(\theta, \theta_{AD})\, d\theta = \\ &= m\frac{N_r}{4\pi}\int_0^{\frac{2\pi}{N_r}} i_{ph}(\theta, \theta_{AD})^2 \frac{dL(\theta)}{d\theta} d\theta \end{aligned} \tag{5-23}$$

5.3.2.4 TORQUE-MAXIMISING ADVANCE ANGLE

The advance angle that maximises the output torque θ_{AD}^*, can be attained from (5-23) by setting equal to zero the derivative of T_{avg} (θ_{AD}) with respect to θ_{AD}:

$$\frac{dT_{AVG}(\theta_{AD})}{d\theta_{AD}} = 0 \tag{5-24}$$

Then, by substituting (5-20) and the derivative of (5-11) with respect of θ into (5-23), (5-25) is derived.

$$\frac{dT_{ph\_AVG}(\theta_{AD})}{d\theta_{AD}} = m\frac{N_r}{2\pi}\frac{{V_{DC}}^2}{\omega^2}\left[\frac{B\theta_{AD}+C}{D\theta_{AD}+E}+F\right]=0 \tag{5-25}$$

Terms B, C, D, E and F are expressed respectively by (5-27), (5-28), (5-29), (5-30) and (5-31). θ_{AD}^* is finally obtained by (5-26).

$$\theta_{AD}{}^* = -\frac{FE+C}{B+FD} \quad \theta_{AD}{}^* = -\frac{FE+C}{B+FD} \tag{5-26}$$

Considering B, C, D, E and F, it is observed that the torque-maximising angle is independent of V_{DC} and ω. In other words, θ_{AD}^* is only a function of the parameters that define the inductance vs. rotor position profile, i.e. the machine geometry and number of turns. At first glance, this fact might look surprising. However, its qualitative explanation is quite simple. Due to the hypothesis of negligible resistive voltage drop, the machine is supplied with a rectangular voltage waveform regardless of the speed. Then, the current waveform depends only on the inductance profile, which is assumed being independent of the current. Therefore, the shape of the current waveform and hence that of the output torque are maintained, regardless of the voltage level.

$$B=-4(L_a-L_2)\left[{L_a}^2\left(\frac{\pi}{N_r}-\theta_2\right)-L_2\theta_1-L_aL_2\left(\frac{\pi}{N_r}-\theta_1\left(1-\ln\left(\frac{L_a}{L_2}\right)\right)-\theta_2\left(1+\ln\left(\frac{L_a}{L_2}\right)\right)\right)\right] \tag{5-27}$$

$$\begin{aligned}C=&2\left[(L_a-L_2)\left(L_2\theta_1\left(L_a\theta_2-L_2\theta_1+\frac{\pi}{N_r}(L_a-L_2)\right)-L_a\theta_2\left(L_a\theta_2-L_2\theta_1-\frac{\pi}{N_r}(L_a-L_2)\right)\right)\right]+\\&+2\left[L_aL_2(L_a\theta_2-L_2\theta_1)\left(2\ln\left(\frac{L_a}{L_2}\right)(\theta_2-\theta_1)+\left(\frac{1}{L_a}-\frac{1}{L_2}\right)\left(L_a\theta_2-L_2\theta_1-\frac{\pi}{N_r}(L_a-L_2)\right)\right)\right]\end{aligned} \tag{5-28}$$

$$D=-L_aL_2N_r(L_a-L_2)(\theta_2-\theta_1) \tag{5-29}$$

$$E=L_aL_2N_r(L_a\theta_2-L_2\theta_1)(\theta_2-\theta_1) \tag{5-30}$$

$$F=\frac{4(L_a-L_2)sb}{(\theta_2-\theta_1)L_2\,(L_2-sb)^2}\left[(L_2-sb)\left(\frac{\pi}{N_r}-\theta_2\right)-bL_2\ln\left(\frac{L_2\left(\frac{\pi}{N_r}-\theta_2-b\right)-sb\left(\frac{\pi}{N_r}-\theta_2\right)}{bL_2}\right)\right] \tag{5-31}$$

5.3.2.5 VALIDATION

In this Subsection, the expression of θ_{AD}^* given in (5-26) is validated against FEA results attained from both SRMyld and SRFly prototypes.

Validation has been conducted as follows. The torque vs. advance angle profiles are obtained via FEA. In order to prove that the optimal angle is independent on speed and voltage, four different operating conditions have been considered for each prototype. Firstly, θ_{AD}^* is compared against the FEA-computed torque-maximising advance angle $\theta_{AD\_FEA}^*$. Subsequently, θ_{AD}^* is fed into a one-shot FEA simulation and the torque achieved $T(\theta_{AD}^*)$ is compared against the actual maximum torque T_{MAX_FEA}.

VALIDATION AGAINST SRMYLD

For SRMyld Prototype, the following combinations of DC-bus voltage and rotating speed have been considered:

a. 36V, 5000rpm;

b. 36V, 6000rpm;

c. 24V, 5000rpm;

d. 24V, 6000rpm.

Table 5-I SRMyld: Optimal Advance Angles Computed Analytically, θ_{AD}^*, and by FEA, $\theta_{AD\_FEA}^*$.

	θ_{AD}^* [°elec.]	$\Theta_{AD\_FEA}^*$ [°ELEC.]	Discrepancy $\Delta\theta_{AD}^*$ [%]
36V, 5000rpm	111.55	104.88	+6.30
36V, 6000rpm	111.55	107.92	+3.3
24V, 5000rpm	111.55	104.88	+6.30
24V, 6000rpm	111.55	107.92	+3.3

Table 5-II SRMyld: FEA-computed maximum Torque computed for θ_{AD}^* and $\theta_{AD\_FEA}^*$

	$T(\theta_{AD}^*)$ [Nm]	T_{MAX_FEA} [Nm]	Discrepancy ΔT [%]
36V, 5000rpm	2.206	2.214	-0.36
36V, 6000rpm	1.565	1.569	-0.25
24V, 5000rpm	0.981	0.984	-0.30
24V, 6000rpm	0.696	0.698	-0.28

The four torque vs. advance angle loci are represented in Figure 5-18. The torque-maximising advance angle found by (5-26) results of 111.49° (elec.). The analytical estimation is compared against the torque-maximising advance angles found by FEA in Table 5-I. As observed, the discrepancy oscillates between around 3% and 6%. This small difference is due to the effects of the resistive voltage drop, which is more pronounced at lower rotating speeds. In

Table 5-II, the four values of $T(\theta_{AD}^*)$ are compared versus the actual maximum

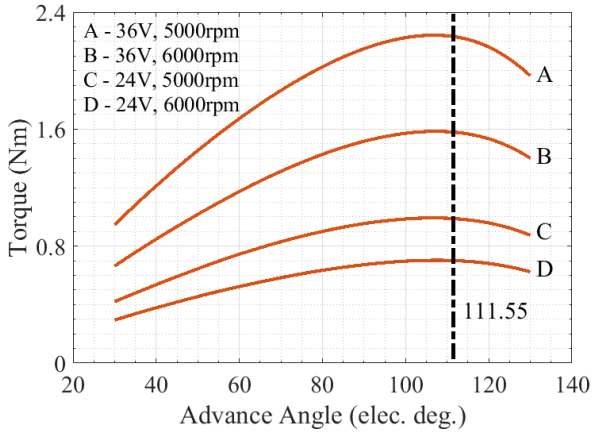

Figure 5-18 SRMyld Prototype FEA torque vs. advance angle loci and optimal advance angle.

torques. In this case, all discrepancies are well below 1%. This fact demonstrates that the error in the optimal angle estimation has very little impact on the evaluated maximum torque. This effect is due to the flat-topped shape that the torque vs. advance angle profile follows around its maximum point.

VALIDATION AGAINST SRFLY

For SRFly Prototype, the considered DC-bus voltages and rotating speeds are the following:

a. 550V, 13500rpm;
b. 500V, 16000rpm;
c. 400V, 13500rpm;
d. 400V, 16000rpm.

An important aspect to be born in mind is that this validation has been conducted only for electromagnetic purposes, with the intention to validate the proposed closed-form expression. Therefore, in order to be able to reach the single-pulse operating mode with the SRFly prototype, a much higher speed than the maximum allowed by the mechanical design has been considered.

Figure 5-19 shows the four FEA torque vs. advance angle profiles. The torque-maximising advance angle given by (5-26) is found of 117.54° (elec.), whilst its FEA-computed counterpart is of 115° (elec.) for the four operating conditions. Both values are compared in Table 5-III. In this case, due to the bigger machine size, the resistive voltage drop is entirely negligible. As a consequence, the torque-maximising advance angle is completely independent of the DC-bus voltage and rotating speed, as observed in Subsection 5.3.2.4. In Table 5-VI, the four values of T (θ_{AD}^*) are compared versus the actual maximum torques, showing highly negligible errors.

Table 5-III SRMyld: Optimal Advance Angles Computed Analytically, θ_{AD}^*, and by FEA, $\theta_{AD\_FEA}^*$.

	θ_{AD}^* [°elec.]	$\Theta_{AD\_FEA}^*$ [°ELEC.]	Discrepancy $\Delta\theta_{AD}^*$ [%]
500V, 16000rpm	117.54	114	+3.10
500V, 13500rpm	117.54	113	+4.01
400V, 16000rpm	117.54	114	+3.10
400V, 13500rpm	117.54	113	+4.01

Table 5-IV SRMyld: FEA-computed maximum Torque computed for θ_{AD}^* and $\theta_{AD\_FEA}^*$.

	T (θ_{AD}^*) [Nm]	T_{MAX_FEA} [Nm]	Discrepancy ΔT [%]
500V, 16000rpm	18.83	18.89	-0.31
500V, 13500rpm	26.24	26.34	-0.37
400V, 16000rpm	12.05	12.09	-0.33
400V, 13500rpm	16.79	16.85	-0.35

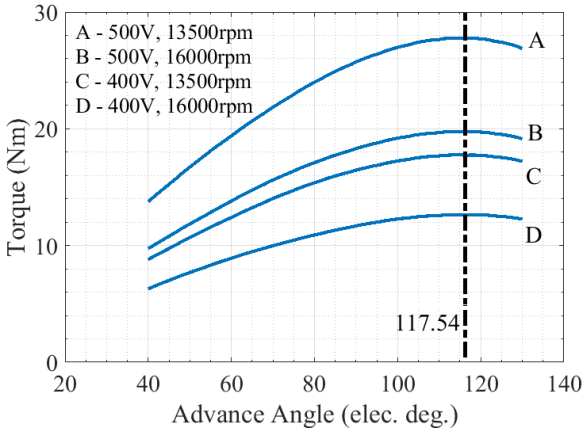

Figure 5-19 SRFly Prototype FEA torque vs. advance angle loci and optimal advance angle.

5.3.3 Current vs. Rotor Position and Torque vs. Rotor Position Profiles

This Subsection is devoted to the determination of the machine performance in the high-speed operating conditions. The objective is to verify the compliance of each member of the ADS with the following Cnts and Rqms considered at the maximum-speed:

1. rated power, or torque, T_{AVG};
2. torque ripple, T_{RIP};
3. RMS phase current, i_{ph_RMS}.

As opposed to the analytical model developed to determine the optimal advance angle, in this case it is necessary to account for the resistive voltage drop to guarantee a sufficiently high accuracy and consequently a relatively smaller clearance δ_{ADS} of the ADS outer edge. For the rest, the remaining six hypotheses proposed in 5.3.2.1 are still considered.

The model begins with the solution of the terminal voltage equation (5-4), which is rewritten in (5-32) to express the phase flux linkage Ψ_{ph} explicitly:

$$\begin{cases} v_{ph}(\theta) = \dfrac{R}{L(\theta)}\Psi_{ph}(\theta) + \omega\dfrac{d\Psi_{ph}(\theta)}{d\theta} \\ \Psi_{ph}(\theta) = L(\theta)\, i_{ph}(\theta) \end{cases} \tag{5-32}$$

As already discussed in Subsection 5.3.1.3, the inductance vs. rotor position profile is modelled through the four-inductance locus.

The fact that the resistive voltage drop is now not neglected requires a numerical solution. To this end, the rotor position θ is discretised. Discretised θ is indicated with square brackets $[\theta]$. $n\theta$ equally-spaced discrete rotor positions are taken, being $\Delta\theta$ the interval. Eq. (5-32) is expressed in its discretised form in (5-33) where the i^{th} element is highlighted. Expressions of the phase flux linkage $\Psi_{ph}([\theta])$ and phase current $i_{ph}([\theta])$ are provided.

At this point, the solution is started from the turn-on instant, since it is the only point where initial conditions can be expressed:

$$\begin{cases} v_{ph\_[1]} = +V_{DC} \\ \Psi_{ph\_[1]} = 0 \\ i_{ph\_[1]} = 0 \\ L_{[1]} = L(\theta_{ON}) \end{cases} \tag{5-34}$$

An important point to note is that, when the negative voltage is applied, current value must be checked. Indeed, if the current at the i[th] instant is approximately zero, voltage from the iteration i+1 onwards shall be set equal to zero and hence solving can be stopped.

$$if\left\{ i_{ph\_[i]} \cong 0 \quad \Leftrightarrow \quad v_{ph\_[k]} = 0\Big|_{k=i+1.....n\theta} \right\}.$$

From the phase current expression, the phase torque T_{ph_1} is found straightforwardly by, (5-35), where the derivative of the inductance is attained directly from (5-15). For convenience, the phase at hand is assumed to be phase 1.

$$T_{ph\_1\_[i]} = \frac{1}{2} i_{ph\_[i]}^{\,2} \left(\frac{dL_{ph}}{d\theta} \right)_{[i]}. \tag{5-35}$$

For the remaining phases, their torque is found by applying the phase-shift $\Delta\varphi$ to the discretised torque waveform attained through (5-35).

Phases are shifted of a mechanical angle $\Delta\varphi$, which depends on the number of poles as expressed in (5-36).

$$\Delta\varphi = 2\pi \left(\frac{1}{N_s} - \frac{1}{N_r} \right). \tag{5-36}$$

Reminding the m is the number of machine phases; the torque vs. rotor position of the k[th] phase is expressed by (5-37), where, $\Delta\varphi$ has to be converted into an integer:

$$T_{ph\_k\_[i]} = T_{ph\_1\_[i-(k-1)\Delta\varphi]}\Big|_{k=1...m}. \tag{5-37}$$

The model concludes with the determination of the overall torque vs. rotor position discretised profile $T([\theta])$, which is given in (5-38).

$$\begin{cases} v_{ph\_[i]} = \dfrac{R}{L_{[i]}} \Psi_{ph\_[i]} + \omega \left(\dfrac{\Psi_{ph\_[i]} - \Psi_{ph\_[i-1]}}{\Delta\theta} \right) \\ \Psi_{ph\_[i]} = L_{[i]} i_{ph\_[i]} \end{cases}\Bigg|_{i=2...n\theta}$$

$$\Updownarrow$$

$$\begin{cases} \Psi_{ph\_[i]} = \dfrac{v_{ph\_[i]} - \dfrac{\omega}{\Delta\theta} \Psi_{ph\_[i-1]}}{\dfrac{R}{L_{[i]}} + \dfrac{\omega}{\Delta\theta}} \\ i_{ph\_[i]} = \dfrac{\Psi_{ph\_[i]}}{L_{[i]}} \end{cases}\Bigg|_{i=2...n\theta} \tag{5-33}$$

$$T_{[i]} = \sum_{k=1}^{m} T_{ph\_k\_[i]} \,. \tag{5-38}$$

Finally, by observing (5-33) to (5-38), it can be seen that solution can be carried out point by point with no need for iterations. This aspect allows one to consider the computational time of the proposed numerical method comparable with that of a fully analytical method. As discussed in Chapter 3, this aspect is critical to keep the computational time of the ADS generation to a minimum.

5.3.3.1 VALIDATION

The proposed numerical solutions for the phase current $i_{ph}([\theta])$, phase flux linkage $\Psi_{ph}([\theta])$ and the overall torque $T([\theta])$ are now validated against FEA results of both prototypes considered in this thesis.

Validation is conducted by considering two operating conditions for each prototype. Initially, the following four waveforms derived numerically and via FEA are compared: $v_{ph}([\theta])$, $i_{ph}([\theta])$, $\Psi_{ph}([\theta])$ and $T([\theta])$. Subsequently, the values of RMS phase current, average torque and torque ripple are compared.

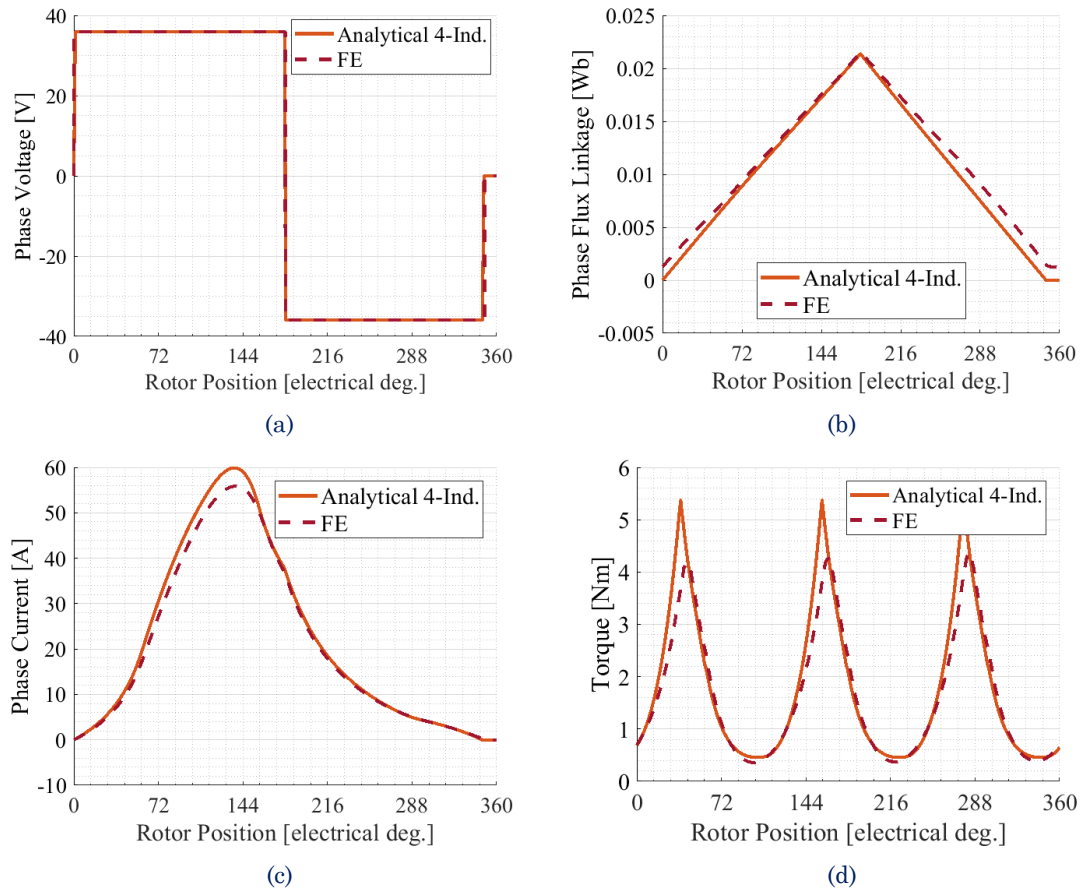

Figure 5-20 SRMyld high-speed single-pulse performance prediction at 36V, 6000rpm: a) phase voltage vs. rotor position, b) phase flux linkage vs. rotor position, c) phase current vs. rotor position, and d) c) output torque vs. rotor position.

VALIDATION AGAINST SRMYLD

The operating conditions considered for validating the analytical mode are reported below:

a. 36V, 5000rpm

b. 36V, 6000rpm

Recalling the discussion in 5.3.2, the dwell period and advance angle are selected in order to maximise the output torque: Θ_{dwell}=180°(elec.), θ_{AD}^{*}=111.55°(elec.). As observed, the optimal advance angle found analytically has been chosen.

Condition (a) represents the maximum-speed design node, i.e. rated power developed at the maximum speed. Figure 5-20 (a) illustrates the comparison between the phase voltage waveforms achieved numerically (solid orange line) and via FEA (dotted scarlet line). A perfect match between the two curves can be observed. In particular, phase voltage returns to zero at the same rotor position, which means that the resistive voltage drop is accounted for correctly. Subplot (b) compares the phase flux linkage waveforms. Both plots follow the expected triangular form, even though the FEA edges are above those of the numerical locus. This small extra amount of flux linkage is provided by the mutual coupling with the other two phases, which is neglected in the proposed analytical/numerical model.

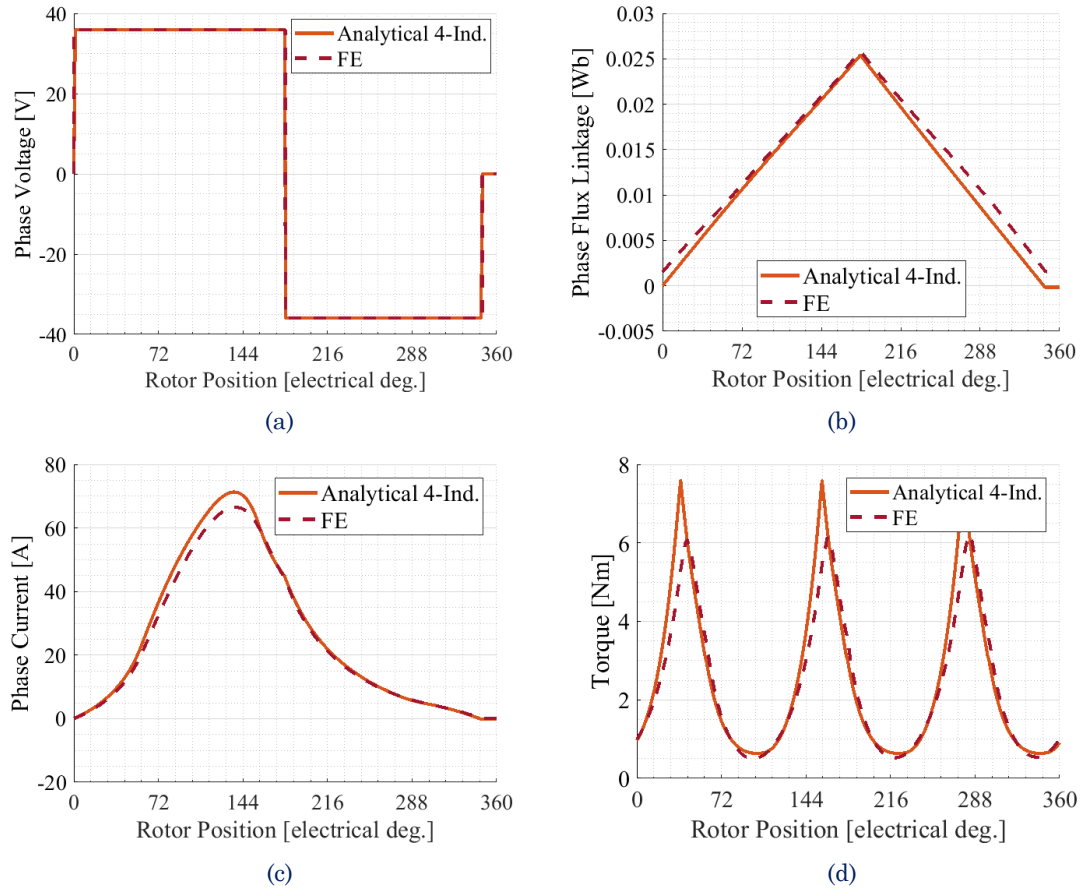

Figure 5-21 SRMyld high-speed single-pulse performance prediction at 36V, 5000rpm: a) phase voltage vs. rotor position, b) phase flux linkage vs. rotor position, c) phase current vs. rotor position, and d) c) output torque vs. rotor position.

Subplot (c) compares the phase currents. In this case, a small discrepancy (below the 5%) is observed between 70° (elec.) and 150°(elec.), which is mainly due to the error introduced by the analytical estimation of the inductances. Finally, subplot (d) represents the output torque waveforms. In this case, local saturation effects provide a further element of discrepancy.

However, a very good match between analytical and FEA loci is achieved. Table 5-V compares the numerical and FEA values of the RMS phase current i_{ph_RMS}, average torque T_{AVG} and torque ripple T_{RIP}. As observed, errors incurred in i_{ph_RMS} and T_{AVG} are well below 10%, whilst for T_{RIP} is around 13%.

To prove the robustness of the proposed method, operating condition (b) has been considered, where a lower speed allows for a higher phase current and hence output torque. Figure 5-21 illustrates the four waveforms considered in the previous operating condition. Very good agreement between FEA and numerical results is achieved once again. Table 5-VI compares the values of i_{ph_RMS}, T_{AVG} and T_{RIP} found with the two methods. Discrepancies achieved are comparable with the operating condition (a).

Table 5-V SRMyld High-speed performance prediction, analytical vs. FEA results at 36V, 6000rpm.

	Analytical 4-Ind.	**FEA (mH)**	**Error (%)**
i_{ph_RMS} **[A]**	29.69	28.03	5.93
T_{AVG} **[Nm]**	1.76	1.63	8.01
T_{RIP} **[%]**	277	245	13.35

Table 5-VI SRMyld High-speed performance prediction, analytical vs. FEA results at 36V, 5000rpm.

	Analytical 4-Ind.	**FEA (mH)**	**Error (%)**
i_{ph_RMS} **[A]**	35.35	33.47	5.61
T_{AVG} **[Nm]**	2.49	2.33	6.64
T_{RIP} **[%]**	279	244	14.24

VALIDATION AGAINST SRFLY

For the SRFly prototype, the following operating conditions have been considered:

a. 500V, 16000rpm

b. 500V, 13500rpm

with Θ_{dwell}=180°(elec.) and θ_{AD}^{*}=117.54°(elec.).

With regard to the rotating speed, the same considerations done to validate the optimal advance angle in Subsection 5.3.2.5 have been made for the validation below. Figure 5-22 compares the results achieved through the analytical model (solid cobalt lines) and via FEA (dashed blue lines).

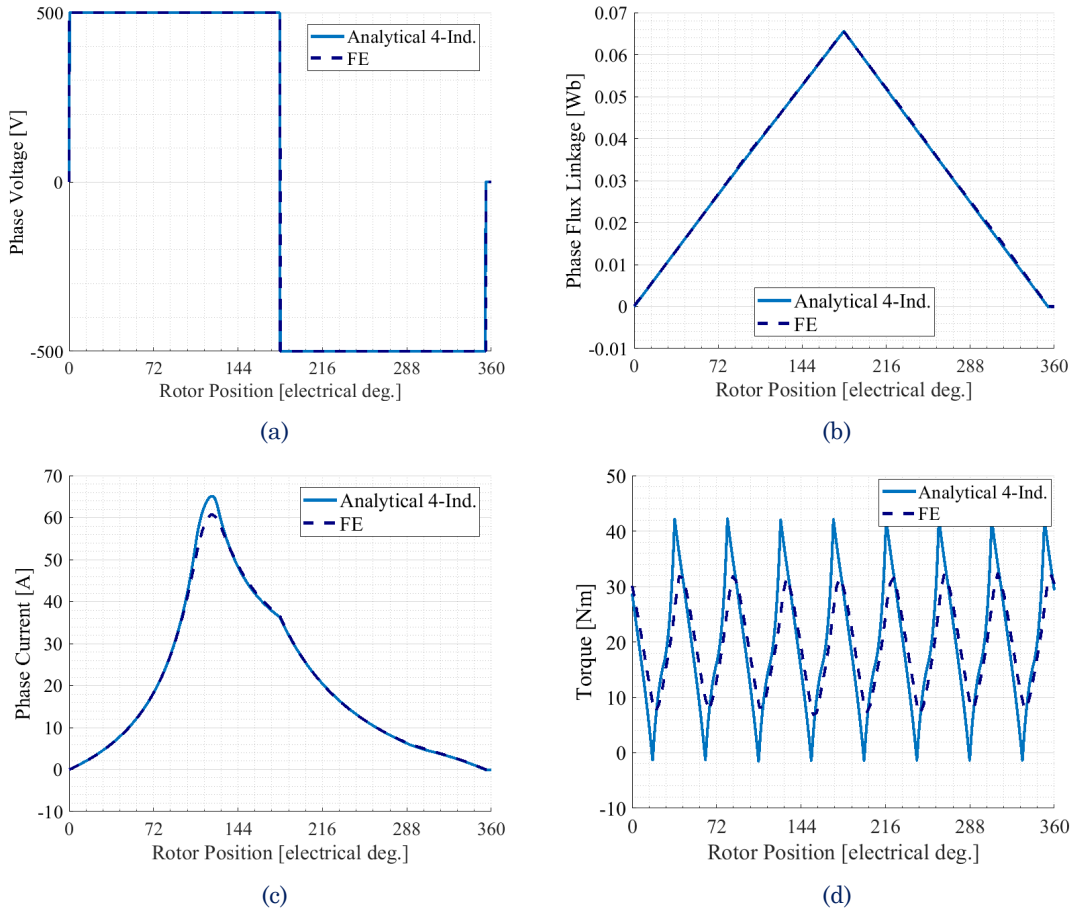

Figure 5-22 SRFly high-speed single-pulse performance prediction at 500V, 16000rpm: a) phase voltage vs. rotor position, b) phase flux linkage vs. rotor position, c) phase current vs. rotor position, and d) c) output torque vs. rotor position.

As observed, the phase voltage, phase flux linkages and phase current predicted by the proposed numerical model match almost perfectly with the FEA results. On the other hand, torque waveform shows a relevant discrepancy in terms of positive and negative peaks. This mismatch is caused by the fact that, at every instant of time, four phases are motoring simultaneously. Consequently, the errors introduced by the four phases sum up, so that the overall error is amplified. Table 5-VII reports the analytical and FEA values of i_{ph_RMS}, T_{AVG}, T_{RIP}. Similarly to the previous prototype, errors incurred in i_{ph_RMS} and T_{AVG} are well below the 5%. Unfortunately, the error in the torque ripple estimation is 70%.

In this regard, it is observed that torque ripple limitations are connected to vibrations and acoustic noise issues. Based on the Author's experience, in many applications, it is the operation in chopping mode at low speed to be the most imposing constraint. Therefore, even a 70% error might not affect the correct determination of the ADS.

For the operating condition (b), Figure 5-23 compares the phase voltage, phase flux linkage, phase current and output torque waveforms. Table 5-VIII contains the values

of i_{ph_RMS}, T_{AVG}, T_{RIP}. Despite the lower speed and hence higher current levels and torque, errors did not change compared to operating condition (a).

Table 5-VII SRFly High-speed performance prediction, analytical vs. FEA results at 500V, 16000rpm.

	Analytical 4-Ind.	**FEA**	**Error (%)**
i_{ph_RMS} **[A]**	27.49	26.94	2.04
T_{AVG} **[Nm]**	19.66	19.45	1.04
T_{RIP} **[%]**	222	130	70.29

Table 5-VIII SRFly High-speed performance prediction, analytical vs. FEA results at 500V, 13500rpm.

	Analytical 4-Ind.	**FEA (mH)**	**Error (%)**
i_{ph_RMS} **[A]**	32.49	31.84	2.03
T_{AVG} **[Nm]**	27.37	27.07	1.08
T_{RIP} **[%]**	223	130	71.43

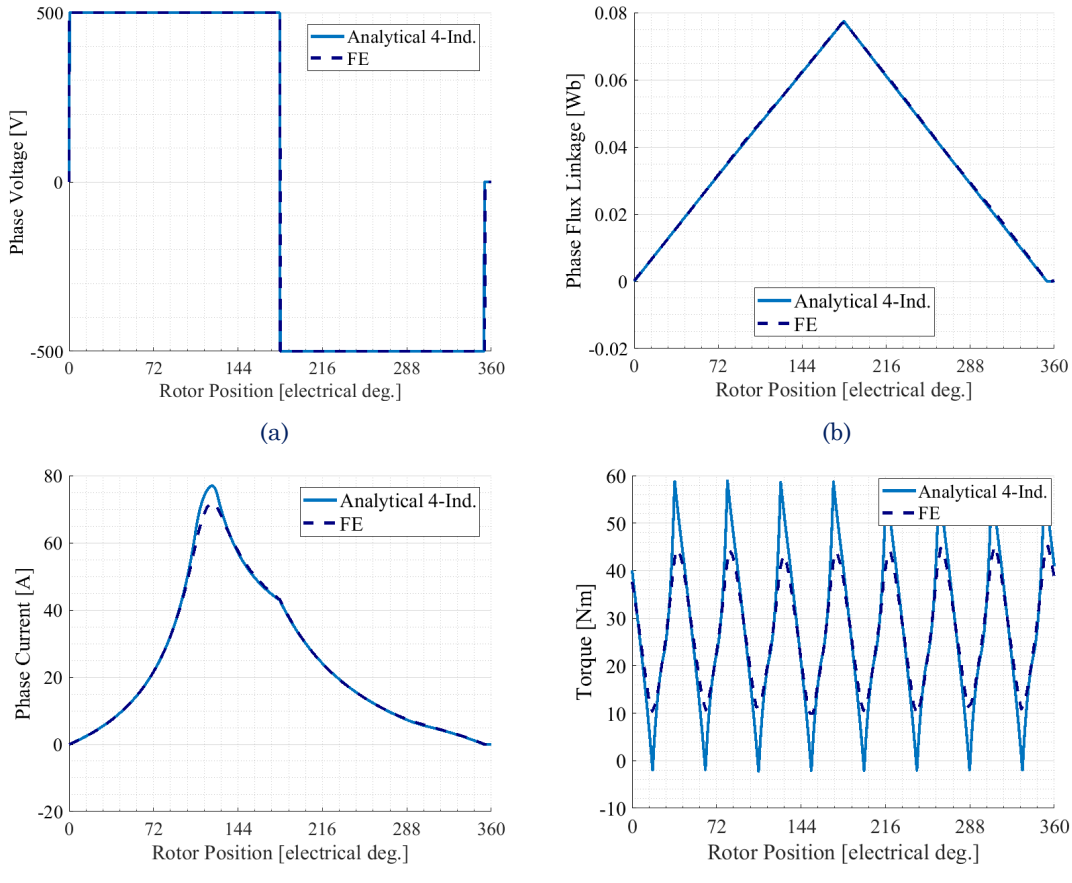

Figure 5-23 SRFly high-speed single-pulse performance prediction at 500V, 13500rpm: a) phase voltage vs. rotor position, b) phase flux linkage vs. rotor position, c) phase current vs. rotor position, and d) c) output torque vs. rotor position.

5.3.4 COPPER AND IRON LOSSES

This Subsection describes the analytical models developed to estimate copper and iron losses in high-speed, single-pulse operating mode. In terms of ADS determination, losses are needed for the introduction of the design constraint concerned with the maximum allowed temperatures and the design requirement expressing the efficiency at maximum speed.

It must be born in mind that the final objective of the analytical models is to determine the ADS and this task should require low computation time and implementation effort. Consequently, the models proposed below have been developed in a bid of providing the best compromise between accuracy, computational cost and implementation effort.

5.3.4.1 COPPER LOSSES

Following from the consideration above, copper losses P_{CU} are estimated considering only the DC resistance. Hence, P_{CU} is found through the well-known expression (5-60), where the RMS phase current i_{ph_RMS} is calculated directly from the phase current waveform $i_{ph}([\theta])$ and R is the DC resistance. The latter is determined from the geometrical parameters as described below.

$$P_{CU} = mRi_{ph\_RMS}^{2}. \tag{5-39}$$

DC RESISTANCE

This thesis considers the most common case where all of the stator-teeth coils belonging to the same phase are series-connected. Then, the DC resistance can be expressed as the combination of slot and end-winding resistances, as expressed in (5-40):

$$R = 4PR_{ss} + 4PR_{ew}. \tag{5-40}$$

R_{ss} is the resistance given by the active length of all series-connected conductors inside one slot as expressed by (5-41), where ς_{CU} is the copper electrical resistivity. In the entire SR machine, $4P$ slots are connected in series, P being the number of repetitions. An example of series connection between stator half-slots is shown in Figure 5-24. For future work, more accurate models such as those proposed in [108] and [109] can be implemented.

$$R_{ss} = \frac{2\varsigma_{CU} L_{stk} N_{tooth}^{2}}{A_{ss} f_{CU}}. \tag{5-41}$$

R_{ew} expresses the resistance given by one end-winding. The end-winding geometry and geometrical parameters are discusses in Appendix 2. R_{ew} results in (5-42), where

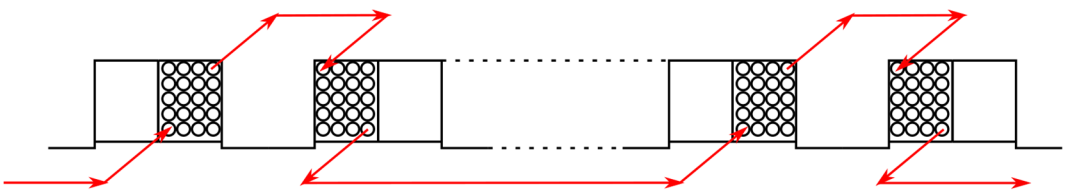

Figure 5-24 example of series-connected stator slots.

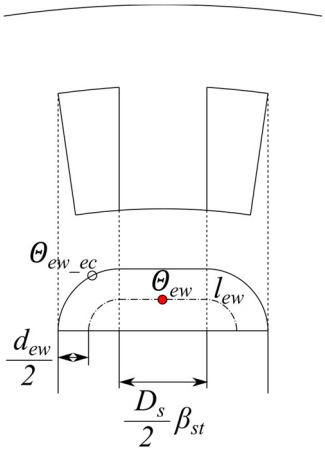

Figure 5-25 Schematic representation of the end winding geometry.

d_{ew} and l_{ew} are the end winding equivalent diameter and length respectively, as shown in Figure 5-25. Their expression are provided in (A2-18) and (A2-19) in Appendix 2. Likewise the stator slots, $4P$ end-windings are connected in series.

$$R_{ew} = \frac{4\varsigma_{CU} l_{ew} N_{tooth}^{\ 2}}{\pi d_{ew}^{\ 2} f_{CU}}. \tag{5-42}$$

5.3.4.2 IRON LOSSES

When it comes to the iron losses, it is well known that analytical models can provide only gross estimates, [85], due to the high complexity of the physical phenomenon.

Across the literature, several approaches to calculate the iron losses have been proposed. Generally, methods are classified into three different kinds, [110]: 1) the loss separation model, [111], the energy vector model, [112] and the Steinmetz model, [113]. From a qualitative analysis, it is soon noted that the loss separation model requires experimentally-determined coefficients, whilst the energy vector model needs the exact solution of the Maxwell's equations. Therefore, none of them possesses the characteristics to suit well the ADS generation process. On the other hand, Steinmetz-formula-based models undoubtedly offer the best compromise between accuracy, computational cost and implementation and are therefore considered for the ADS generation.

A further simplification of the model is that a 'global' flux density distribution is considered for each component of the magnetic core, as it is commonly done for gross iron losses estimate [14, 85]. In other words, 'local' information about the flux density distribution is neglected.

Steinmetz-formula-based model is expressed as follows. For a generic kth iron-made element, if a purely sinusoidal flux density waveform is considered, along with a uniform flux density distribution, iron losses P_{FE} are given by the sum of hysteresis and eddy currents contributions:

$$P_{FE,k} = m_k \left(\underbrace{k_{hy} B_k{}^{\alpha} f^{\beta}}_{hysteresis} + \underbrace{k_{ec} B_k{}^{2} f^{2}}_{eddy\ currents} \right);$$

m_k indicates the k[th] element mass, k_{hy}, k_{ec}, α and β are material-dependent constants, which are usually found via post processing of the manufacturer's data, and finally f and B_k are the sinusoid's frequency and amplitude respectively.

To take into account the fact that typical flux density waveforms of SR machines are non-sinusoidal, the flux density vs. time waveform can be expressed through its Fourier Series. Hence, iron losses are given by the summation of the losses produced harmonic by harmonic as expression in (5-42), where h represents the harmonic order and f_1 is the fundamental frequency.

$$P_{FE,k} = m_k \sum_{h=1}^{\infty} \left(k_{hy} B_{k,h}{}^{\alpha} \left(h f_{k,1} \right)^{\beta} + k_{ec} B_{k,h}{}^{2} \left(h f_{k,1} \right)^{2} \right). \tag{5-43}$$

In the case of the SR machine, four major components can be identified, namely stator tooth, stator yoke, rotor tooth and rotor yoke. Flux density vs. time waveforms and iron losses of the four components are discussed below.

Before embarking on the losses determination, it is remarked that stator and rotor components experience two different fundamental frequencies, respectively $f_{sta,1}$ and $f_{rot,1}$. Their expressions are provided in (5-44).

$$\begin{cases} f_{sta,1} = \dfrac{\omega N_r}{2\pi P} \\ f_{rot,1} = \dfrac{\omega}{2\pi P} \end{cases}. \tag{5-44}$$

STATOR TOOTH IRON LOSSES

The stator tooth average flux density B_{st_avg} can be found directly from the flux linkage vs. rotor position waveform $\Psi_{ph}([\theta])$, by substituting the electrical-degrees position with time and dividing by the number of turns per-phase and the cross section:

$$B_{st\_avg}\left([t]\right) = \frac{\Psi_{ph}\left([t]\right)}{N \dfrac{D_s}{2} \beta_{st} L_{stk}}. \tag{5-45}$$

Then, the iron losses produced in the stator teeth can be found by expressing B_{st_avg} its Fourier series and applying (5-43):

$$P_{FE,st} = \left(\rho_{FE} \frac{D_s}{2} \beta_{st} h_{st} L_{stk} \right) \sum_{h=1}^{\infty} \left(k_{hy} B_{st\_avg,h}{}^{\alpha} \left(h f_{sta,1} \right)^{\beta} + k_{ec} B_{st\_avg,h}{}^{2} \left(h f_{sta,1} \right)^{2} \right). \tag{5-46}$$

Starting from the expression of B_{st_avg} ([t]), the corresponding average flux φ_{st_avg} ([t]) can be determined:

$$\varphi_{st\_avg}\left([t]\right) = B_{st\_avg}\left([t]\right) N_{tooth} \frac{D_s}{2} \beta_{st} L_{stk}. \tag{5-47}$$

At this point, waveforms of the average flux densities inside the remaining three components: B_{sy_avg} ([t]), B_{rt_avg} ([t]) and B_{ry_avg} ([t]), can be reconstructed by means of the Gauss' law.

STATOR YOKE IRON LOSSES

Figure 5-26 represents the stator yoke flux contributions provided by the stator teeth of a generic m-phase SR machine. As observed, stator teeth are considered to be wound, so that an alternating polarity is achieved, i.e. N,S,N,S, etc. In the case a different winding polarity is used, the approach discussed below can still be used by changing the sign +/- associated to the polarity where necessary.

The portion of stator yoke between teeth A and B is now considered. As observed, both teeth A and B provide a clockwise flux contribution, whilst an alternate polarity is produced from tooth C onwards.

Following from the above and reminding that fluxes associated to adjacent teeth are space-shifted by $2\pi/N_s$, flux passing through a generic the stator yoke section φ_{sy_avg} ([t]) can be determined through (5-48), where $\angle$ indicates the phase shift and ω the rotating speed.

$$\varphi_{sy\_avg}\left([t]\right)=\frac{1}{2}\varphi_{st\_avg}\left([t]\right)+\sum_{i=2}^{m}\frac{1}{2}(-1)^{i}\left(\varphi_{st\_avg}\left([t]\right)\angle\frac{2\pi}{\omega N_s}(i-1)\right). \tag{5-48}$$

Subsequently, the average stator yoke flux density B_{sy_avg} ([t]) and the iron losses can be expressed as in (5-49) and (5-50).

$$B_{sy\_avg}\left([t]\right)=\frac{\varphi_{sy\_avg}\left([t]\right)}{b_{sy}L_{stk}}. \tag{5-49}$$

$$P_{FE,sy}=\left(\rho_{FE}\left(\frac{D_s+b_{sy}}{2}\right)\zeta_s b_{sy}L_{stk}\right)\sum_{h=1}^{\infty}\left(k_{hy}B_{sy\_avg,h}{}^{\alpha}\left(hf_{sta,1}\right)^{\beta}+k_{ec}B_{sy\_avg,h}{}^{2}\left(hf_{sta,1}\right)^{2}\right) \tag{5-50}$$

ROTOR TOOTH IRON LOSSES

The reconstruction of the rotor tooth flux density B_{rt_avg} ([t]) from the stator flux density is one of the most challenging tasks concerned with the iron losses determination. Indeed, if leakage flux is neglected, it can be noted that when the rotor stands at full alignment, the entire stator-tooth flux passes to the rotor tooth.

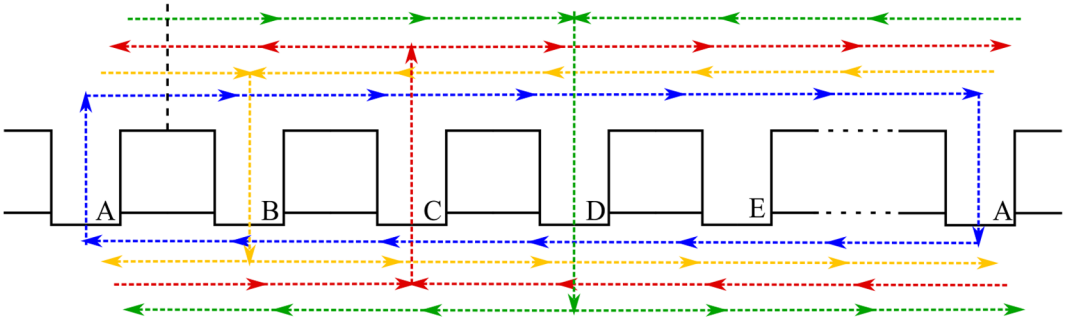

Figure 5-26 example of stator yoke flux contributions directions.

Conversely, at maximum misalignment, the stator-tooth flux is equally split between two rotor teeth.

In this regard, the Author wishes to highlight that, to the best of his knowledge, a rigorous methodology to accomplish this task has never been proposed. Therefore, this thesis proposes a simple first-attempt original approach. However, more work is required to improve this method. The idea is to define a stator/rotor mutual coupling coefficient $M_{s/r}$, expressing the ratio between φ_{rt_avg} and φ_{st_avg} as a function of the rotor position θ:

$$M_{s/r}(\theta) = \frac{\varphi_{rt\_avg}}{\varphi_{st\_avg}}(\theta). \tag{5-51}$$

The concept is schematically illustrated in Figure 5-27. The expression of $M_{s/r}$ (θ) must be defined across an entire rotor period, i.e. $2\pi/P$. The idea is based on the trapezoidal waveform that is commonly used to schematically describe the inductance vs. rotor position locus, with the difference that the concept of poles overlapping replaces that of teeth overlapping.

An example of the trapezoidal trend of $M_{s/r}$ (θ) is shown in Figure 5-27. From the full alignment condition until the position θ_M, where stator and rotor poles fully overlap, $M_{s/r}$ is equal to one, since the entire stator tooth flux passes to the rotor tooth. θ_M is expressed in (5-52) and is also represented in Figure 5-27.

$$\theta_M = \frac{\zeta_r - \zeta_s}{2}. \tag{5-52}$$

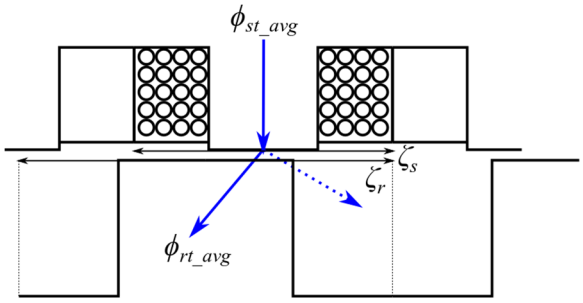

Figure 5-27 Illustration of stator/rotor mutual coupling coefficient $M_{s/r}$ at position θ_M

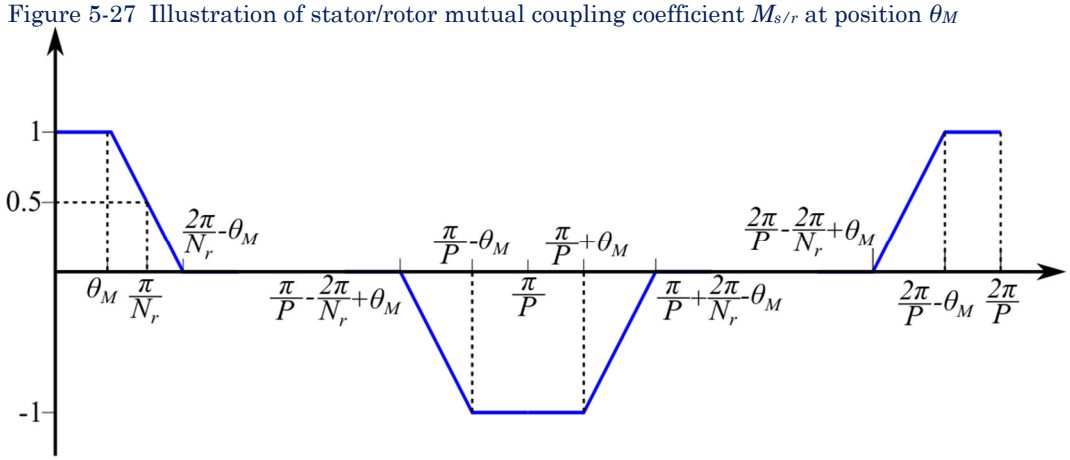

Figure 5-28 Trapezoidal waveform of $M_{s/r}(\theta)$.

Once θ becomes greater than θ_M, $M_{s/r}$ begins to decay linearly. The linear slope is defined by imposing that $M_{s/r}$ equals 0.5 at the maximum misalignment position π/N_r. Then, due to the geometric symmetry, the linear slope terminates at the position $2\pi/N_r$-θ_M, where $M_{s/r}$ is equal to 0, so that the first positive half pulse is completed. Subsequently, $M_{s/r}$ remains equal to 0 until the rotor tooth approaches the second stator tooth belonging to the same phase, with the new full alignment reached at π/P. Since the stator tooth polarity is inversed, $M_{s/r}$ produces a negative pulse. Finally, as the rotor approaches the third stator tooth, which possesses the same polarity as the first one, the remaining positive half pulse completes the entire period $2\pi/P$.

The zero position is defined at the full alignment with phase A. The rotor tooth contribution given by phase A is expressed below:

$$\varphi_{rt\_avg\_A}\left([t]\right) = \varphi_{st\_avg}\left([t]\right) M_{s/r}\left(\theta\left([t]\right)\right). \tag{5-53}$$

Therefore, reminding that contributions provided by the remaining m-1 phases are space-shifted by $2\pi/N_s$, the overall rotor tooth flux density can be attained by (5-54).

$$\varphi_{rt\_avg}\left([t]\right) = \sum_{i=1}^{m}\left(\varphi_{st\_avg}\left([t]\right)(-1)^{i-1} M_{s/r}\left(\theta\left([t]\right)\right)\right)\angle\frac{2\pi}{\omega N_s}(i-1). \tag{5-54}$$

From (5-54), the average rotor tooth flux density B_{rt_avg} ([t]) and the corresponding iron losses are found via (5-55) and (5-56).

$$B_{rt\_avg}\left([t]\right) = \frac{\varphi_{rt\_avg}\left([t]\right)}{\frac{D_r}{2}\beta_{rt} h_{rt} L_{stk}}. \tag{5-55}$$

$$P_{FE,rt} = \left(\rho_{FE}\frac{D_r}{2}\beta_{rt} h_{rt} L_{stk}\right)\sum_{h=1}^{\infty}\left(k_{hy} B_{rt\_avg,h}{}^{\alpha}\left(hf_{rot,1}\right)^{\beta} + k_{ec} B_{rt\_avg,h}{}^{2}\left(hf_{rot,1}\right)^{2}\right). \tag{5-56}$$

ROTOR YOKE FLUX DENSITY WAVEFORM

Rotor yoke flux is reconstructed directly from the B_{rt_avg} ([t]) by following the same approach that has been used to reconstruct the stator yoke flux. To do so, rotor teeth shall be grouped as if they were part of the same 'phase', where term 'phase' indicates the set of rotor poles that experience the same flux density distribution over one rotor period (regardless of the polarity). The number of rotor 'phases' derives directly from the number of repetitions P:

$$number\ rotor\ 'phases' = \frac{N_r}{2P}.$$

Reminding that rotor teeth fluxes are phase-shifted by an angle of $2\pi/N_r$, the reconstruction of the rotor yoke flux is performed by summing up the fluxes provided by one rotor tooth from each 'phase', as described in (5-57). An illustration of the rotor yoke flux contributions is provided in Figure 5-29.

$$\varphi_{ry\_avg}\left([t]\right)=\sum_{i=1}^{\frac{N_r}{2P}}\varphi_{rt\_avg}\left([t]\right)\angle\frac{2\pi}{\omega N_r}(i-1)\,. \tag{5-57}$$

An important point to note is that no negative terms appear in (5-57). In fact, as opposed to the case of the stator, rotor teeth experience a bidirectional magnetic flux, so that the information about the flux polarity is already contained in φ_{rt_avg} ([t]).

Average rotor yoke flux density B_{ry_avg} ([t]) and iron losses are expressed by (5-58) and (5-59).

$$B_{ry\_avg}\left([t]\right)=\frac{\phi_{ry\_avg}\left([t]\right)}{b_{ry}L_{stk}}\,. \tag{5-58}$$

$$P_{FE,ry}=\left(\rho_{FE}\left(\frac{D_{sha}+b_{ry}}{2}\right)\zeta_r b_{ry}L_{stk}\right)\sum_{h=1}^{\infty}\left(k_{hy}B_{ry\_avg,h}{}^{\alpha}\left(hf_{rot,1}\right)^{\beta}+k_{ec}B_{ry\_avg,h}{}^{2}\left(hf_{rot,1}\right)^{2}\right) \tag{5-59}$$

5.3.4.3 Validation and Discussion

In this Subsection, the proposed analytical model that predicts copper and iron losses is validated against FEA results of both prototypes.

Validation Against SRMyld

For the SRMyld prototype, the same operating conditions considered for validating the current and torque waveforms in Subsection 5.3.3.1 are used:

a. 36V, 5000rpm;

b. 36V, 6000rpm.

with Θ_{dwell}=180°(elec.) and θ_{AD}^{*}=111.55°(elec.).

Results for the operating conditions (a) are reported in Table 5-IX, while results for the operating conditions (b) in Table 5-X. As it can be observed, in the SRMyld prototype, copper losses are predominant against iron losses even at high-speed, i.e. 110W against 15W. As expected, a 12% error exists, as it is around the double of the 6% error incurred in the RMS current estimation (see Table 5-V and Table 5-VI); analytical and FEA results are calculated with practically the same DC resistance.

With regard to the rotor losses, the main source of error is the assumption of a uniform flux density distribution within each component. However, iron losses are proportional to powers ranging between 1.5 and 2, so that a strongly uneven flux density

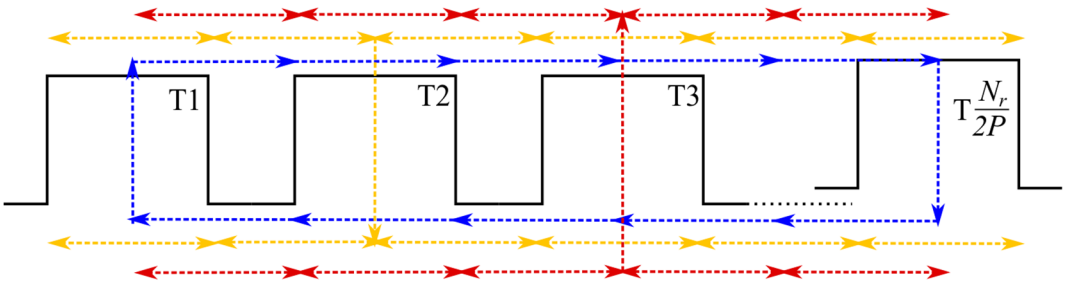

Figure 5-29 example of rotor yoke flux contributions directions.

spatial distribution may cause significant errors. This aspect is particularly significant in the rotor.

Just to give the idea, an extremely simple example is made. The condition illustrated in Figure 5-30 is considered. With the aim of only showing this concept, the rotor tooth is divided into four quarters. The top quarters have a 1.5 B_{AVG} flux density, whilst the lower quarters 0.5 B_{AVG}. Assuming that iron loss are proportional to B_{AVG}^2, comparison between 'global' and 'local' flux density distributions is as follows:

$$P_{FE}(global) \simeq k_{FE} B_{AVG}^{\ 2},$$

$$P_{FE}(local) \simeq \frac{1}{2} 2.25 k_{FE} B_{AVG}^{\ 2} + \frac{1}{2} 0.25 k_{FE} B_{AVG}^{\ 2} \simeq 1.25 k_{FE} B_{AVG}^{\ 2}.$$

Even a so simple example, shows the strong correlation between spatial flux density distribution and iron losses.

As said above, the proposed approach is just an initial attempt aimed at finding a gross loss estimate. In the future, more effort is necessary to improve the two following aspects:

a. consider the effects of the special flux density distribution,
b. derive a more accurate analytical determination of $M_{s/r}$ including flux leakages effects.

In terms of efficiency estimation, it is found that the analytical model overestimates both the mechanical output power (see Table 5-V and Table 5-VI) and the copper losses, whereas iron losses are far less relevant than copper losses. As a result, the combination of the three effects above yields an extremely accurate efficiency estimation.

VALIDATION AGAINST SRFLY

For the SRFly prototype, the operating conditions considered for validation of current and torque waveforms in Subsection 5.3.3.1 are once again considered:

a. 500V, 16000rpm
b. 500V, 13500rpm

with Θ_{dwell}=180°(elec.) and θ_{AD}^*=117.54°(elec.). Results are reported in Table 5-XI and Table 5-XII.

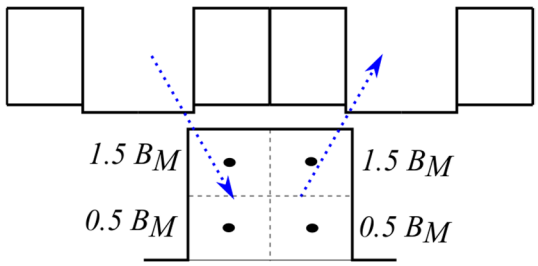

Figure 5-30 Example of local flux density distribution over iron loss estimation.

Table 5-IX SRMyld high-speed losses and efficiency prediction, analytical vs. FEA results at 36V, 6000rpm.

Copper Loss [W]		**ANA**	91.77
		FEA	81.77
		Err [%]	12.23
Iron Loss [W]	**Stator**	**ANA**	10.88
		FEA	10.23
		Err [%]	6.36
	Rotor	**ANA**	4.11
		FEA	5.21
		Err [%]	-21.00
Total Loss [W]		**ANA**	106.77
		FEA	97.21
		Err [%]	9.83
Efficiency [%]		**ANA**	91.19
		FEA	91.32
		Err	-0.13

Table 5-X SRMyld high-speed losses and efficiency prediction, analytical vs. FEA results at 36V, 5000rpm.

Copper Loss [W]		**ANA**	130.11
		FEA	116.59
		Err [%]	11.59
Iron Loss [W]	**Stator**	**ANA**	11.96
		FEA	11.91
		Err [%]	0.46
	Rotor	**ANA**	4.36
		FEA	5.21
		Err [%]	-16.24
Total Loss [W]		**ANA**	146.61
		FEA	135.13
		Err [%]	8.49
Efficiency [%]		**ANA**	89.89
		FEA	90.02
		Err	-0.13

As opposed to the previous prototype, the SRFly prototype shows a dramatic dominance of the stator iron losses over the copper losses. This behaviour results from the flywheel application itself, where the rotor outer diameter and stack length have been sized to comply with a moment of inertia requirement. In particular, the flywheel

application led to a hugely oversized rotor yoke, which is far away from any standard electrical machine. Therefore, it cannot provide a meaningful term of comparison for the model's validation, so that it is preferred not to include rotor iron losses in this validation.

In general, copper and iron losses errors are in line with the results achieved for SRMyld prototype. Copper losses overestimation is slightly smaller, due to the fact that the error stems from the error introduced by the RMS phase current, and this last has better estimation for this prototype. Stator iron losses error is comparable with that a incurred in the SRMyld rotor. This is due to the non-uniform flux density distribution, as described in the simple example above.

Efficiency estimation results higher of approximately 1%, since the mechanical power overestimation superimposes with the iron losses underestimation.

DISCUSSION

Results attained from the comparison above, lead to some useful considerations with regard to the ADS clearance δ_{ADS} attained when the efficiency constraint at high speed is introduced. In this regard, it is observed that:

1) The mechanical output power is overestimated;
2) Copper losses are always overestimated;
3) Iron losses are likely to be underestimated.

Consequently, based on this losses distribution, two scenarios are possible. In the case of SR machines where iron losses are dominant, efficiency is overestimated. This results in a positive clearance $\delta_{ADS}>0$, which indicates that some machine candidates with a high-speed efficiency that is lower than the required might be included. Conversely, in SR machine where iron losses are dominant a general law about the sign of δ_{ADS} cannot be found and therefore, clearance must be investigated application by application.

In any case, for both prototypes considered in this thesis, the error incurred in the efficiency estimate is lower or equal than 1%, which is much lower compared to the discrepancies that are usually found between FEA models and physical prototypes.

5.4 LOW-SPEED ELECTROMAGNETIC PERFORMANCE PREDICTION

This Subsection describes the analytical modelling that predicts the machine performance in the low-speed condition, i.e. the base-speed design node. As opposed to the operation at high speed, low-speed operation is characterized by high levels of magnetic saturation, as it is required to reach power densities competitive with that of AC machines, [40]. For this reason, determination of the current and flux linkage waveforms with an accuracy comparable with the high-speed model would require to consider local saturation effects. This analytical models are well known for being highly

Table 5-XI SRFly high-speed losses and efficiency prediction, analytical vs. FEA results at 500V, 16000rpm.

Copper Loss [W]		**ANA**	92.92
		FEA	87.88
		Err [%]	5.73
Iron Loss [W]	**Stator**	**ANA**	1686
		FEA	2053
		Err [%]	-17.87
	Rotor	**ANA**	n.a.
		FEA	n.a.
		Err [%]	n.a.
Total Loss [W]		**ANA**	1780
		FEA	2141
		Err [%]	-16.90
Efficiency [%]		**ANA**	94.87
		FEA	93.83
		Err	1.04

Table 5-XII SRFly high-speed losses and efficiency prediction, analytical vs. FEA results at 500V, 13500rpm.

Copper Loss [W]		**ANA**	130.49
		FEA	122.76
		Err [%]	6.29
Iron Loss [W]	**Stator**	**ANA**	1754
		FEA	2058
		Err [%]	-14.78
	Rotor	**ANA**	n.a.
		FEA	n.a.
		Err [%]	n.a.
Total Loss [W]		**ANA**	1884
		FEA	2180
		Err [%]	-13.59
Efficiency [%]		**ANA**	95.43
		FEA	94.60
		Err	0.82

complex and usually not so accurate within a wide range of machine geometries, as in the case of an ADS.

Therefore, due to the relatively limited timeframe available, this thesis considers only the low-speed average output torque model, since it allows a relatively simple formulation without the necessity to consider local saturation effects. For the future, more work is obviously necessary to develop a simple yet effective analytical model that accurately predicts phase current, phase flux linkage and instantaneous torque waveforms, as well as iron and copper losses. The proposed model is built in Subsection 5.4.1.

5.4.1 AVERAGE LOW-SPEED OUTPUT TORQUE

The analytical model to predict the low-speed torque proposed in this thesis is based on the standard SR machine sizing approach, [66, 85, 101]. The conventional sizing equations for SR machines is based on the torque-coenergy expression (5-1). In (5-60), the expression is rearranged in a discretised form, where m is the number of phases, N_r the number of rotor poles and ΔW_f' the variation of coenergy of one phase during a stroke.

$$T_{AVG} = m\frac{\Delta W_f'}{2\pi}N_r\,. \tag{5-60}$$

To determine ΔW_f', the Ψ_{ph} vs. i_{ph} energy-conversion loop of an idealised low-speed cycle is considered. The idealised cycle is composed of four 'transformations', as illustrated in Figure 5-31:

1) OA: at the minimum inductance point, the phase winding is switched on and i_{ph} instantaneously reaches its peak value i_{pk};

2) AB: the rotor moves from the unaligned to the aligned position with constant current i_{pk};

3-4) BO: with the rotor at the fully aligned position, the phase winding is instantaneously discharged, with the magnetic core being saturated until point C (segment BC), and then unsaturated until fully discharged (segment CO).

To relate the quantities that define the Ψ_{ph} vs. i_{ph} loop with the DVs defined in

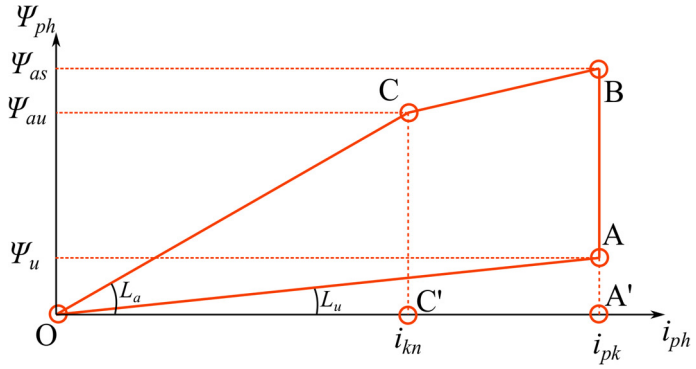

Figure 5-31 Ψ_{ph} vs. i_{ph} energy-conversion loop of an idealised low-speed cycle.

Chapter 3, the peak phase current i_{pk} reached during the cycle is related to the other slot quantities through (5-61).

$$i_{pk} = \frac{J_{ss} A_{ss} f_{CU} P}{f_i N}. \tag{5-61}$$

Then, it is well-known that the phase coenergy variation ΔW_f' is equal to the area enclosed by the Ψ_{ph} vs. i_{ph} loop:

$$\Delta W_f' = A_{OC'CO} + A_{C'A'BCC'} - A_{OA'AO} = \frac{1}{2}\left(\left(i_{pk} - i_{kn}\right)\left(\Psi_{as} + \Psi_{au}\right) - \left(i_{pk}\Psi_u\right)\right). \tag{5-62}$$

To calculate the phase coenergy variation, the three points that define the Ψ_{ph} vs. i_{ph} loop are defined below.

POINT A

Point A is related to the DVs by means of the unaligned inductance L_u, which is given by (6-123) in Chapter 6. Subsequently, the unaligned flux linkage Ψ_u is given by (5-63).

$$\Psi_u = L_u i_{pk}. \tag{5-63}$$

POINT B

Point B coincides with the fully aligned condition with deep magnetic core saturation. The latter has been already discussed in Subsection 3.4.3. Hence, recalling what has been said in Chapter 3, the system of equations (3-16) to (3-20) is solved for the stator tooth flux density B_{st}. Then, B_{st} is used to attain the aligned saturated flux linkage Ψ_{as} by (5-64).

$$\Psi_{as} = N\left(B_{st}\frac{D_s}{2}\beta_{st}L_{stk}\right). \tag{5-64}$$

POINT C

Point C represents the knee-point of the Ψ_{ph} vs. i_{ph} loop, where the magnetic core enters the unsaturated region. Hence, the iron core magnetic behaviour is described by the aligned inductance L_a, whose expression as a function of the geometrical DVs is given by (6-37) in Chapter 6. Initially, the knee-value B_{kn} of the selected material is picked up from the $B(H)$ curve (or datasheet). Then, the aligned unsaturated flux linkage Ψ_{au} is found straightforwardly:

$$\Psi_{au} = N\left(B_{kn}\frac{D_s}{2}\beta_{st}L_{stk}\right). \tag{5-65}$$

Finally, to fully define point C, the knee-current i_{kn} is calculated from Ψ_{au} and L_a via (5-66).

$$i_{kn} = \frac{\Psi_{au}}{L_a}. \tag{5-66}$$

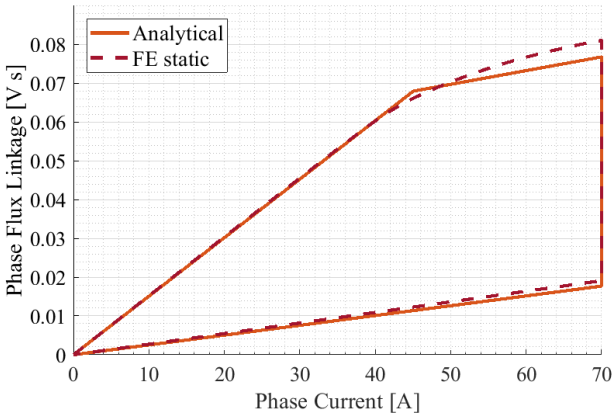

Figure 5-32 SRMyld Prototype analytical and FEA Ψ_{ph} vs. i_{ph} energy-conversion loop.

At this point, all members of (5-62) have been defined and T_{AVG} can be calculated. The proposed analytical model is validated against FEA results from both SRMyld and SRFly prototypes in Subsection 5.4.1.1 below.

5.4.1.1 VALIDATION

The validation is conducted by comparing the analytical and FEA Ψ_{ph} vs. i_{ph} loops from both prototypes discussed in Chapter 4. The loops are attained in 'static' conditions, where an almost zero speed and perfect chopping are considered.

VALIDATION AGAINST SRMYLD

For the SRMyld prototype, peak phase current i_{pk} is set to 70A. The knee-point for the magnetic core is set at 1.6T. Analytical and FEA loops are compared in Figure 5-32. As it can be observed, the FEA and analytical loops match almost perfectly. A slight difference occurs at the aligned saturated flux linkages Ψ_{as}, i.e. point B, which is due to the overestimation of the aligned saturated reluctance attained by solving the saturated aligned magnetic circuit by means of (3-16) to (3-20). Table 5-XIII compares the low-speed torque values achieved by the two methods. As expected, a negligible error is incurred.

Table 5-XIII SRMyld prototype, analytical and FEA T_{AVG} at low-speed.

	Analytical	FEA (mH)	Error (%)
T_{AVG} [Nm]	10.37	10.37	-0.06

VALIDATION AGAINST SRFLY

For the SRFly prototype the peak phase current is set at 100A. Analytical and FEA Ψ_{ph} vs. i_{ph} loci are illustrated in Figure 5-33. An extremely close match is once again achieved. As observed, this time the Ψ_{ph} vs. i_{ph} loop has a pseudo-triangular shape, as opposed to the usual pseudo-trapezoidal one. In fact, due to the large airgap, the SRFly magnetic core cannot reach the knee-point of the material's $B(H)$ curve.

For this reason, the expression of $\Delta W'$ can be simplified as shown below:

$$\Delta W' = \frac{1}{2} i_{pk} \left(\Psi_{as} - \Psi_u \right) = \frac{1}{2} {i_{pk}}^2 \left(L_a - L_u \right). \tag{5-67}$$

Table 5-XIV reports the low-speed torque predicted by the analytical model and by the FEA results. A 5.2% discrepancy is attained. This time, the only source of error lies in the analytical estimation of L_a and L_u.

Table 5-XIV SRFly prototype, analytical and FEA TAVG at low-speed.

	Analytical	**FEA (mH)**	**Error (%)**
TAVG [Nm]	300.75	285.85	5.21

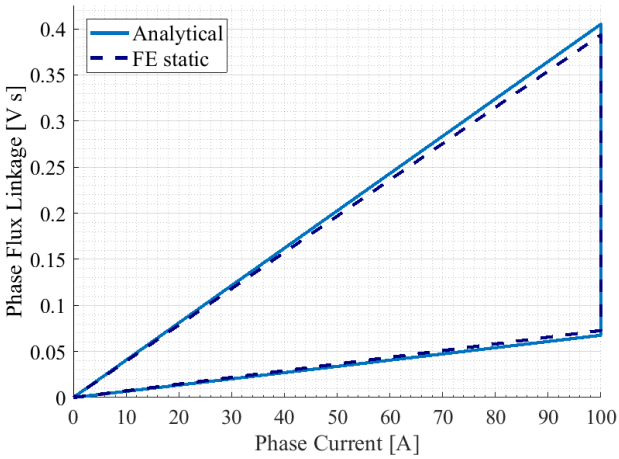

Figure 5-33 SRFly Prototype analytical and FEA Ψ_{ph} vs. i_{ph} energy-conversion loop.

DISCUSSION

The main limitation of the model described above is that an ideal Ψ_{ph} vs. i_{ph} loop is considered, as it is common occurrence for SR machine sizing purposes. In particular, the idealised loop assumes an 'infinite' high DC-bus voltage, so that the phase current rise and fall times, t_{rise} and t_{fall}, are neglected. However, when the real behaviour at the base speed is considered, the DC-bus voltage might be relatively low and t_{rise} and t_{fall} are no longer negligible. In this case, the torque output might be smaller compared to ideal, infinite-voltage case.

In terms of ADS determination, it is important to highlight that this potential discrepancy generates a positive clearance at the outer edge, i.e. $\delta_{ADS}>0$. In simple words, when the proposed model is applied to introduce the low-speed torque requirement, the cut out process excludes only candidates that do not comply with the power requirement independently of V_{DC}. In the future, more accurate low-speed models will be developed, so that this aspect can be improved and a more accurate ADS generation process achieved.

5.5 CONCLUSION

The entire set of analytical models presented in this Chapter is critical to ensure a fast and reliable determination of the ADS for any possible SR machine's design candidate, ranging from widely different sizes to different poles configurations.

The main point to note is that the inductance vs. rotor position is the 'main pillar' of all models, since all performance determination relies on it. Further to that, the determination of the unsaturated inductances, required for a fully analytical definition of the inductance profile, is undertaken in Chapter 6.

Finally, apart from the models' improvements, an important piece of the future work will be focusing on a cost/benefit analysis aimed at finding the best compromise between the models' accuracy and the implementation effort, in return for the necessary δ_{ADS}.

The analytical closed-form analytical expression of the torque maximising advance angle discussed in Subsection 5.3.2 has resulted in the conference publication [114], whose follow-up journal version is now under review. In addition, the analytical models built up to estimate the torque at both base- and maximum-speed nodes will be the subject of a future publication(s), where a novel two-node sizing methodology will be proposed.

6 ANALYTICAL MODELS FOR UNSATURATED INDUCTANCES DETERMINATION

This Chapter completes the work presented in Subsection 5.3.1 by providing the analytical derivation of the inductance at the four nodes θ_a, θ_1, θ_2 and θ_u. The four profile nodes are represented in Figure 6-1.

As already discussed in Subsection 5.3.1.2, the proposed model is based on the construction of a permeance function from predefined flux tubes paths, from which the inductance value is achieved. The choice of a permeance-based model derives from the requirements of low computational cost and capability to maintain high levels of accuracy for widely different SR machines geometries, in order to accurately predict the performance any potential SR machine design candidate.

6.1 PERMEANCE FUNCTION AND INDUCTANCE

The concept of permeance $\mathcal{P}$ derives from the Hopkinson's law that describes the magnetic circuits. In particular, this Chapter considers only magnetic circuits where iron magneto-motive force drops are negligible.

The case of an SR machine at the aligned position is considered, which is represented in Figure 6-2. For convenience, the geometry has been linearized and the linearised horizontal coordinate κ is introduced. The flux tubes crossing the mid-airgap surface between points κ_1 and κ_2 are now considered. As their length varies with κ, the

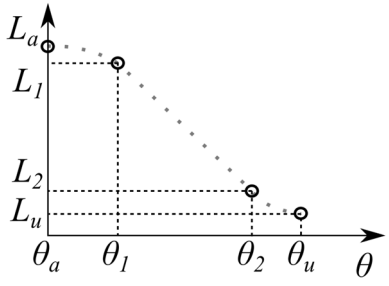

Figure 6-1 Schematic representation of the four nodes defining the inductance profile.

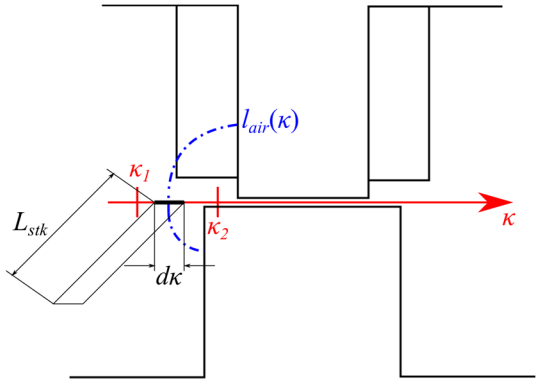

Figure 6-2 Linearized SR machine geometry at aligned position.

tube's length is expressed by $l(\kappa)$. Assuming that the flux tube links perfectly all of the coil turns, Ampere's equation is expressed as follows:

$$\oint H dl(\kappa) = Ni_{ph} ,$$

where H is the magnetic field intensity, $d\kappa$ an infinitesimal portion of mid-airgap surface and Ni_{ph} the total Magneto Motive Force (*MMF*) $\mathcal{F}$ exerted on the flux tube, as N indicates the number of series-connected turns interlinked by the flux tubes.

To keep this example simple yet realistic, the following hypotheses are introduced:

- Iron components have infinite permeability, $\mu_{FE}=\infty$.
- All flux tubes interlink the same MMF, equal to Ni_{ph};
- A pair of adjacent flux lines, which form a tube, are all parallel to each other, meaning that each tube has a constant cross section $dA = d\kappa\, L_{stk}$.

Then, Ampere's law yields:

$$\int_{l_{FE}} \frac{B_{FE}}{\mu_{FE}} dl + \int_{l_{air}} \frac{B_{air}(\kappa)}{\mu_0} dl(\kappa) = Ni_{ph} .$$

Gauss' law is now applied to a flux tube of infinitesimal cross section dA:

$$\oiint B_{air} dA = \oiint B_{air}(\kappa) L_{stk} d\kappa = const .$$

Given that flux tubes have a constant cross section along the flux tube length, the product $L_{stk}\, d\kappa$, and consequently $B_{air}(\kappa)$, are not a function of l. Therefore, Ampere's law can be simplified as follows:

$$\frac{B_{air}(\kappa)}{\mu_0} l_{air}(\kappa) = Ni_{ph} .$$

The infinitesimal flux $d\varphi$ passing through dA defines the infinitesimal permeance $d\mathcal{P}$:

$$d\varphi(\kappa) = B_{air}(\kappa) L_{stk} d\kappa = \underbrace{\left(\frac{\mu_0 L_{stk}}{l_{air}(\kappa)} d\kappa \right)}_{d\mathcal{P}} Ni_{ph} .$$

Finally, the total flux φ_{12} crossing the mid-airgap surface between κ_1 and κ_2, expressed in the familiar Hopkinson's law form, defines the permeance $\mathcal{P}_{12}$:

$$\phi_{12} = \left(\mathcal{P}_{12}\right) N i_{ph}$$

$$\mathcal{P}_{12} = \int_{\kappa_1}^{\kappa_2} \frac{\mu_0 L_{stk}}{l_{air}(\kappa)} d\kappa .$$

Due to the hypothesis that all flux lines between κ_1 and κ_2 interlink all the coil turns, the inductance value L_{12} related to $\mathcal{P}_{12}$ is found straightforwardly:

$$\Psi_{12} = N\varphi_{12} = L_{12} i_{ph}$$
$$\Updownarrow$$
$$L_{12} = N^2 \mathcal{P}_{12}$$

6.2 PERMEANCE FUNCTION APPROACH FOR THE SR MACHINE

The permeance approach described in the previous Subsection is based on the summation, i.e. integration, of flux linkage contributions provided by parallel flux tubes with an infinitesimal cross section. The same approach is adopted in this Subsection to develop an analytical model that caters for the inductance at a specific rotor position.

The model is based on the following assumptions:

1. Iron core has infinite permeability ($\mu_{FE}=\infty$), with flux lines entering the iron surfaces perpendicularly,
2. Conductors are uniformly distributed over the coil cross-section,
3. Current density J_{ss} is constant over the coil cross-section.

As shown in Subsection 6.1 above, $\mu_{FE}=\infty$ yields the inductance by summing up flux linkages contributions provided by a series of air flux tubes parallel to each other. The model being proposed applies this concept by defining the flux tubes entering/leaving the outer surface of a stator tooth and subsequently summing up their flux linkages contributions.

Tubes can be classified into two groups: 1) leakage tubes, which do not enter/leave the rotor body and 2) magnetising tubes, which do enter/leave the rotor body. Leakage flux lines enter/leave the stator tooth only from the right and left edges, whereas magnetising lines do so from both the front and side surfaces. The concept is illustrated in Figure 6-3.

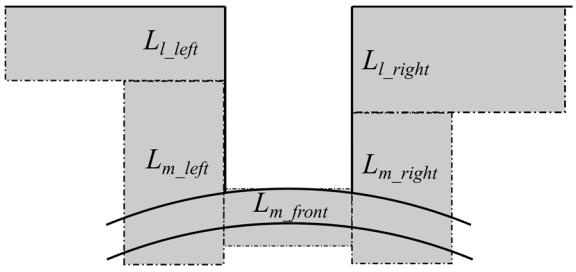

Figure 6-3 Five tubes families contributing to the inductance value.

Hence, the inductance $L(\theta)$ can be expressed as the sum of five contributions, as shown in (6-1), where Ψ denotes the flux linkages and:

L_{l_left} is the contribution from the left-side leakage tubes,

L_{m_left} is the contribution from the left-side magnetisation tubes,

L_{m_front} is the contribution from the front magnetisation tubes,

L_{m_right} is the contribution from the right-side magnetisation tubes and

L_{l_right} is the contribution from the right-side leakage tubes.

$$L(\theta) = \frac{1}{i_{ph}}\left(\Psi_{l\_left} + \Psi_{m\_left} + \Psi_{m\_front} + \Psi_{m\_right} + \Psi_{l\_right}\right) = \\ = L_{l\_left} + L_{m\_left} + L_{m\_front} + L_{m\_right} + L_{l\_right} \quad (6\text{-}1)$$

It shall be noted that (6-1) does not represent an equivalent magnetic circuit with series-connected inductances. Indeed, it represents a mere summation of flux linkage contributions.

Leakage flux tubes are modelled in Subsection 6.2.1, whereas the magnetising tubes are introduced for the four rotor positions under consideration, namely θ_a, θ_1, θ_2 and θ_u, respectively in Subsections 6.2.2, 6.2.3, 6.2.5 and 6.2.6.

6.2.1 LEAKAGE FLUX TUBES

Leakage flux tubes usually follow two kind of paths, which are schematically represented in Figure 6-4:

- path l_I: from the tooth side surface to the yoke inner surface,
- path l_{II}: from the tooth side surface to the adjacent tooth side.

For the sake of completeness, it is observed that these paths are typical of machines where the tooth height is equal or greater than the average slot width, such as the SRMyld prototype (see Figure 6-25 to Figure 6-27).

On the other hand, in machines similar to the SRFly prototype, where the tooth height is much smaller than the average slot width, leakage tubes can also lead from the stator yoke directly to the rotor (see Figure 6-25 to Figure 6-27). However, the following considerations can be made:

- leakage paths link small MMFs compared to the magnetizing regions,
- leakage paths length increases as the linked MMF increases.

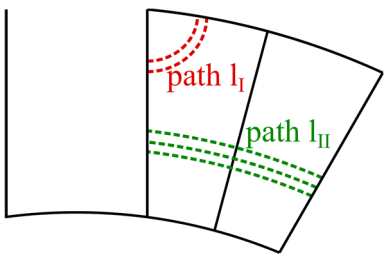

Figure 6-4 Leakage tubes paths l_I and l_{II}.

The two points above explain the well-known fact that leakage tubes provide a small inductance contribution compared to the magnetising paths. Therefore, the assumption of modelling the leakage tubes through the shapes of l_I and l_{II}, regardless of the toot-height/slot-width ratio, can be justified. A second reasonable assumption introduced with regard to the leakage tubes is that their shape does not change at different rotor positions, as it can be observed in Figure 6-25 to Figure 6-27. Hence, geometry of paths l_I and l_{II} can be maintained at the four positions being considered.

A final observation is that the linked MMF changes drastically with the tubes length. Consequently, leakage paths are dealt with as partly linked and therefore the permeance approach discussed in Subsection 6.2.1 cannot be applied. Contributions provided by paths l_I and l_{II} are described respectively in Subsections 6.2.1.1 and 6.2.1.2.

6.2.1.1 LEAKAGE TUBES l_I

Figure 6-5 shows a leakage tube of the l_I type. The tube is modelled by means of an elliptic arc, which subtends an arc of $\pi/2-\delta_{sy}$ and whose semi-axes are Γ_x and Γ_y. The stator yoke angle δ_{sy} can be expressed by the approximated formula (6-2).

$$\delta_{sy} = \frac{\left(\frac{D_s}{2}+h_{st}\right)\left(1-\cos\left(\frac{\zeta_s}{2}\right)\right)}{\frac{D_s}{2}\sin\left(\frac{\zeta_s-\beta_{st}}{2}\right)-h_{st}\sin\left(\frac{\zeta_s}{2}\right)}. \tag{6-2}$$

Due to its elliptical shape, the tube cross section is not constant along the full path. Consequently, a mathematical formulation with two independent variables is necessary. The first variable chosen is the vertical abscissa y_{side}, being the latter positive as it points downwards. The second is a curvilinear abscissa l that follows the average tube path. The chosen coordinates are represented in Figure 6-5.

Given that the MMF drop along the iron path is negligible, and that for the flux tubes properties the magnetic field intensity vector H directs along l, Ampere's law gives (6-3), where A_{encl} expresses the conductors' area linked by a flux tube and f_{CU} the slot fill factor.

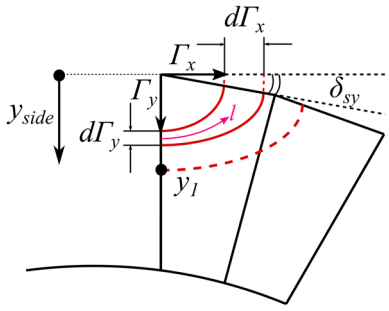

Figure 6-5 Leakage tube l_I.

$$\int_{l_{lI}(y_{side})} \frac{B_{air}(y_{side},l)}{\mu_0} dl = Ni_{ph} = J_{ss} A_{encl}(y_{side}) f_{CU} \,. \tag{6-3}$$

Eq. (6-3) points out that the overall tube length l_{lI} and the linked MMF are functions of y_{side}.

The ellipses semi-axes are now defined. Γ_y is obviously equal to y_{side}. Γ_x is defined through the parameter e_{lI}, as shown in (6-4). e_{lI} is used in replacement of the ellipses eccentricity, in order to allow for a simpler analytical expression.

$$\begin{cases} \Gamma_y = y_{side} \\ \Gamma_x = e_{lI}\Gamma_y = e_{lI} y_{side} \end{cases}. \tag{6-4}$$

As observed in the SRMyld field lines distribution, tube eccentricity increases along with the lines length. However, reminding that the field lines contribution to the overall inductance is normally much smaller than that of the magnetising lines, a big overall error is not incurred if an average value of e_{lI} is taken. Hence, e_{lI} is considered here as a constant value, which depends on the slot geometry. This dependency is expressed by the two following dimensionless parameters: the ratio between the tooth height and the bore diameter h_{st}/D_s and the slot angle β_{ss}. The relationship is provided in (6-5).

$$e_{lI} = \frac{1}{c_{lI}} \left(a_{lI} \beta_{ss} - b_{lI} \frac{h_{st}}{D_s} + d_{lI} \right). \tag{6-5}$$

The coefficients a_{lI}, b_{lI}, c_{lI} and d_{lI} have been determined via the FEA-based procedure shown in Appendix 3. Their values are as follows:

$$\begin{cases} a_{lI} = 4.83 \\ b_{lI} = 0.607 \\ c_{lI} = 6.75 \\ d_{lI} = 6.93 \end{cases}.$$

A further simplification introduced to keep a handy analytical formulation without incurring in a great error, is that even in case a portion of enclosed area exceeds the coil surface (likewise the dashed line in Figure 6-5); the resulting small empty space is considered as filled with conductors.

From (6-4), the tube length l_{air} and cross section dA are found. The length of an ellipse is a well-known mathematical problem, which does not allow for a closed-form analytical expression, [115]. To this cause, several approximated formulae have been proposed. This thesis opts for the expression (6-6).

$$l_{lI}(y_{side}) \cong \left(\frac{\pi}{2} - \delta_{sy} \right) \frac{(\Gamma_x + \Gamma_y)}{2} \Leftrightarrow \left(\frac{\pi}{2} - \delta_{sy} \right) \frac{(1 + e_{lI})}{2} y_{side} \,. \tag{6-6}$$

For the elliptical-shaped tubes at hand, it is reasonable to assume that the cross section varies linearly as one moves from the y-semi-axis towards the x-semi-axis:

$$dA(y_{side},l)=L_{stk}\left(1+\frac{4(e_{lI}-1)}{\pi(1+e_{lI})y_{side}}l\right)dy_{side}\,. \tag{6-7}$$

Finally, A_{encl} is simply expressed by (6-8).

$$A_{encl}(y\_side)=\left(\frac{\pi}{2}-\delta_{sy}\right)\frac{\Gamma_x\Gamma_y}{2}=\left(\frac{\pi}{2}-\delta_{sy}\right)\frac{e_{lI}}{2}{y_{side}}^2\,. \tag{6-8}$$

The first step to attain the flux linkages contributions of the tubes l_I is the derivation of the magnetic flux $d\varphi$ of an infinitesimal flux tube entering/leaving a portion of the tooth surface equal to $d\Gamma_y L_{stk}$. $d\varphi$ can be found by combining the Ampere's and Gauss' equations, and reminding that, due to the flux tubes properties, $d\varphi$ does not change along the path length. The expression is derived in (6-9), which yields (6-10).

$$\begin{cases} B(y_{side},l)=\dfrac{d\varphi(y_{side})}{dA(y_{side},l)} \\ \displaystyle\int_0^{l_{air}(y_{side})}\frac{B_{air}(y_{side},l)}{\mu_0}dl \Leftrightarrow d\varphi(y_{side})=\frac{\mu_0 J_{ss} f_{CU}\left(\frac{\pi}{2}-\delta_{sy}\right)\frac{e_{lI}}{2}{y_{side}}^2}{\displaystyle\int_0^{l_{air}(y_{side})}\frac{1}{dA(y_{side},l)}dl}\,. \end{cases} \tag{6-9}$$

$$d\varphi(y_{side})=\frac{\mu_0 J_{ss} L_{stk} e_{lI}(e_{lI}-1)}{(1+e_{lI})\ln\left(1+(e_{lI}-1)\left(1-\frac{2\delta_{sy}}{\pi}\right)\right)}\left(1-\frac{2\delta_{sy}}{\pi}\right)y_{side}\,dy_{side}\,. \tag{6-10}$$

The second step is the derivation of the infinitesimal flux linkage contribution $d\Psi$ provided by $d\varphi$. This contribution is calculated by multiplying $d\varphi$ for the number of conductors n_{cond} the tube links. Due to the hypothesis of a homogeneous conductors distribution across the coil surface, $d\Psi$ can be expressed by (6-11).

$$d\Psi(y\_side)=d\varphi(y_{side})n_{cond}(y_{side})=d\varphi(y_{side})\frac{2N}{A_{ss}}A_{encl}(y\_side)\,. \tag{6-11}$$

The third and final step is the integration of (6-11) along the tooth surface entered/left by tubes l_I, as expressed by (6-12). To complete the integral, the upper bound y_1 is required. The latter depends of the field lines distribution along the entire tooth surface. Its determination is discussed in Subsection 6.2.1.3.

$$\Psi_{lI}=\int_0^{y_1}d\Psi(y_{side})\,. \tag{6-12}$$

6.2.1.2 LEAKAGE TUBES L_{II}

Figure 6-6 shows a leakage tube of the l_{II} type. The tube is modelled by means of two concentric circular arcs, whose centre is the actual machine centre. Leakage tubes are dealt with as partially linked.

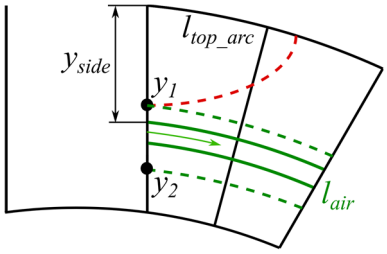

Figure 6-6 Leakage tube l_{II}.

By following the same approach used to derive the top arc length expression (3-5), the tube's air-path length $l_{air}(y_{side})$ can be expressed as in (6-13).

$$l_{lII}\left(y_{side}\right) \cong \frac{D_s}{2}\beta_{ss} + \left(h_{st} - y_{side}\right)\zeta_s \,. \tag{6-13}$$

The enclosed conductors' area A_{encl} is found by assuming a trapezoidal shape, whose bases are half of l_{air} and l_{top_arc}, and the leg y_{side}. The formula is provided in (6-14).

$$A_{encl}\left(y_{side}\right) = \frac{y_{side}}{4}\left(l_{air}\left(y_{side}\right) + l_{top\_arc}\right) = \frac{y_{side}}{4}\left(D_s\beta_{ss} + \left(2h_{st} - y_{side}\right)\zeta_s\right). \tag{6-14}$$

As a flux tube is composed of two concentric arcs, its cross section remains constant across its full length. Therefore, in Ampere's equation, B_{air} is constant and thus can be taken out of the integral.

$$\int_{l_{lII}(y_{side})} \frac{B_{air}(y_{side},l)}{\mu_0}\,dl = \frac{B_{air}(y_{side},l)}{\mu_0}\,l_{lII}\left(y_{side}\right) = J_{ss}A_{encl}(y_{side})f_{CU}\,. \tag{6-15}$$

The magnetic flux $d\varphi$ of an infinitesimal flux tube entering/leaving a portion of the tooth surface equal to dy_{side} L_{stk} can be expressed by combining (6-13), (6-14) and (6-15). The final expression is given in (6-16).

$$d\varphi = \frac{\mu_0 J_{ss} f_{CU} L_{stk} y_{side}\left(D_s\beta_{ss} + \left(2h_{st} - y_{side}\right)\zeta_s\right)}{2D_s\beta_{ss} + 4\left(h_{st} - y_{side}\right)\zeta_s}\,dy_{side}\,. \tag{6-16}$$

The derivation of the infinitesimal flux linkage contribution $d\Psi$ provided by $d\varphi$ is now addressed. Similarly to the case of flux tubes lI, this contribution is given by $d\varphi$ times the number of conductors n_{cond} linked by the tube. $d\Psi$ is expressed by (6-17).

$$d\Psi(y\_{side}) = d\varphi\left(y_{side}\right)n_{cond}\left(y_{side}\right) = d\varphi\left(y_{side}\right)\frac{2N}{A_{ss}}A_{encl}(y\_{side})\,. \tag{6-17}$$

The final step is the integration of $d\Psi$ along the tooth surface entered/left by tubes l_{II}, as given in (6-18). The upper and lower bounds y_1 and y_2 depend on the field lines distribution along the entire tooth surface. Their derivation is discussed in Subsection 6.2.1.3.

$$\Psi_{lII} = \int_{y_1}^{y_2} d\Psi\left(y_{side}\right). \tag{6-18}$$

6.2.1.3 RIGHT AND LEFT LEAKAGE INDUCTANCES L_{l_left} AND L_{l_right}

This Subsection describes the determination of y_1 and y_2, which are necessary to determine the leakage contributions to the overall inductance. As said above, this task requires the knowledge of the complete tubes distribution alongside the tooth surface. To this end, it is critical to take into account the flux tubes of the regions L_{m_right} and L_{m_left}, which may have different shapes at different rotor positions.

Ref [116] identifies the point where flux tube paths change by equalling the ratio of the tube-length over its enclosed area, which, in other terms, is the imposition of the continuity of B alongside the tooth's side surface. However, even though this would be the most rigorous approach, it might lead to an unreasonably overcomplicated analytical formulation. The fact that the leakage contribution is usually much smaller than the magnetising contribution, justifies the simplification that the point where flux tubes change path is identified by equalling the paths lengths.

Firstly, the point y_{lI_lII} where flux tubes change from l_I to l_{II} is found. As leakage flux lines follow the same shape regardless of the rotor position, y_{lI_lII} is found straightforwardly by equalling (6-6) and (6-13):

$$y_{lI\_lII} = \frac{D_s\beta_{ss} + 2h_{st}\zeta_s}{2\zeta_s + \left(\frac{\pi}{2} - \delta_{sy}\right)\left(1 + e_{II}\right)}. \tag{6-19}$$

Secondly, the point y_{lI_mI} where the length of the leakage tubes l_I equals that of the magnetising lines m_{side}, along with the point y_{lII_m} where tubes l_{II} and m_{side} equal each other in length, are determined. It is observed that magnetising lines may change their shape as the rotor position changes, as can be seen in Figure 6-25 to Figure 6-27. Therefore, different values of y_{lI_m} and y_{lII_m} may be found on either tooth side: $y_{lI\_m\_right}$, $y_{lI\_m\_left}$, $y_{lII\_m\_right}$ and $y_{lII\_m\_left}$.

For convenience, the general case with symbols y_{lI_m} and y_{lII_m} is now discussed. Results can then be easily applied to either tooth side. At a given rotor position, as the tooth height h_{st} changes, two different scenarios can be encountered, i.e. 'short stator tooth' and 'tall stator tooth'.

SHORT STATOR TOOTH

An example of short tooth is illustrated in Figure 6-7 (a). As observed, leakage tubes l_{II} do not exist. This scenario occurs in two different situations.

The first is when lengths l_I and l_{II} and/or lengths l_{II} and m_I do not equal each other in any point of the side surface. Mathematically, (6-20) describes this case:

$$\begin{cases} y_{lI\_lII} \notin (0, h_{st}) \\ and\,/\,or \\ y_{lII\_m} \notin (0, h_{st}) \end{cases}. \tag{6-20}$$

The second, when y_{lI_lII} is simply major than y_{lI_m} as given in (6-21):

$$\begin{cases} y_{lI\_lII} \in (0, h_{st}) \\ and \\ y_{lI\_m} \le y_{lI\_lII} \end{cases}. \tag{6-21}$$

In this scenario, to represent the fact that paths l_{II} do not exist, y_1 and y_2 are set equal to each other:

$$y_1 = y_2 . \tag{6-22}$$

TALL STATOR TOOTH

A tall stator tooth is depicted in Figure 6-7 (b). This time, leakage tubes l_{II} do exist. This scenario occurs when (6-23) is verified.

$$\begin{cases} y_{lI\_lII} \in (0, h_{st}) \\ and \\ y_{lI\_m} \ge y_{lI\_lII} \end{cases}. \tag{6-23}$$

Then, y_1 and y_2 are defined as follows:

$$\begin{cases} y_1 = y_{lI\_lII} \\ y_2 = y_{lII\_m} \end{cases}. \tag{6-24}$$

Observation: Terms short and tall have been used here relatively to a specific side, and at a given rotor positions. In absolute terms, the Author wishes to propose the following definitions:

- Short-toothed stator, whence lines l_{II} do not exist in any rotor position, neither on the right, nor on the left side. The SRFly prototype belongs to this kind.
- Mid-toothed stator, when lines l_{II} exist in only some rotor position, not necessarily on either side.
- Tall-toothed stator, when lines l_{II} exist in any rotor position and on both sides. SRMyld prototype belongs to this case.

6.2.2 θ_A

The magnetising tubes in the condition of full alignment are discussed in this Subsection. Figure 6-8 provides a schematic representation of the flux tubes

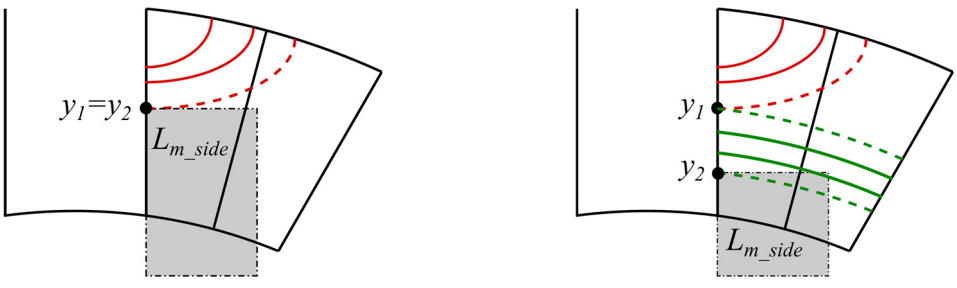

(a) (b)

Figure 6-7 Examples of short-toothed stator (a) and tall-toothed stator (b).

distribution. Due to the geometrical symmetry, flux tubes are equal on either tooth side. Hence, the subscript 'side' is intended as both right and left. Tubes are modelled with three different paths:

- m_{side_I}: are the outermost lines (cyan). Lines are composed of three pieces: a circular leading from the stator tooth side to the airgap, a straight line crossing the airgap and a final arc closing on the rotor tooth side.
- m_{side_II}: are composed of the same circular arc leading from the stator tooth side to the airgap and a straight line crossing the airgap and entering/leaving the rotor front surface.
- m_{front}: made by a straight line crossing the airgap and connecting the stator and rotor front surfaces facing each other.

Since most of the flux is provided by the front lines, the best compromise between model's complexity and accuracy is attained by representing the side flux tubes as compositions of straight lines and circular arcs [102],[48, 116, 117]. The three paths are analysed one by one in the Subsections below.

6.2.2.1 MAGNETISING TUBES M_{SIDE_I}

As the greatest inductance contribution at the aligned position is given by the front tubes, it is convenient to simplify the modelling of the side flux tubes by linearizing the pole pair geometry as shown in Figure 6-9.

The tube air-path length $l_{m\_side\_I\_\theta a}$ (y_{side}) can be expressed as in (6-25), with $\Delta R_{\theta a}$ being defined in the approximated expression (6-26).

As the tubes length is known, the first step is the determination of $y_{1\_\theta a}$ and $y_{2\_\theta a}$ to complete the evaluation of the leakage inductance. To this end, points $y_{II\_m\_\theta a}$ and $y_{III\_m\_\theta a}$ are determined by equalling (6-25) to respectively (6-6) and (6-13). The resulting expressions are given in (6-27) and (6-28).

$$\begin{aligned} l_{m\_side\_I\_\theta a}(y_{side}) &= \frac{\pi}{2}R_{s\_mI} + l_g + \left(\frac{\pi}{2}+\gamma_{rt}\right)R_{r\_mI} = \\ &= \frac{\pi}{2}(h_{st}-y_{side}) + l_g + \left(\frac{\pi}{2}+\gamma_{rt}\right)(h_{st}-y_{side}-\Delta R_{\theta a}) \end{aligned}. \tag{6-25}$$

$$\Delta R_{\theta a} \cong \frac{D_r}{4}(\beta_{rt}-\beta_{st}). \tag{6-26}$$

$$y_{lI\_m\_\theta a} = \frac{l_g + \frac{\pi}{2}h_{st} + \left(\frac{\pi}{2}+\gamma_{rt}\right)(h_{st}-\Delta R_{\theta a})}{\gamma_{rt}+\pi+\left(\frac{\pi}{2}-\delta_{sy}\right)(1+e_{lI})}. \tag{6-27}$$

$$y_{lII\_m\_\theta a} = \frac{l_g + \frac{\pi}{2}h_{st} - \frac{D_s}{2}(\zeta_s-\beta_{st}) - \zeta_s h_{st} + \left(\frac{\pi}{2}+\gamma_{rt}\right)(h_{st}-\Delta R_{\theta a})}{\gamma_{rt}+\pi-\zeta_s}. \tag{6-28}$$

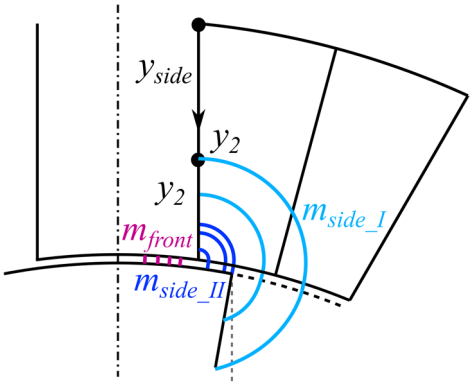

Figure 6-8 Magnetising tubes at θ_a.

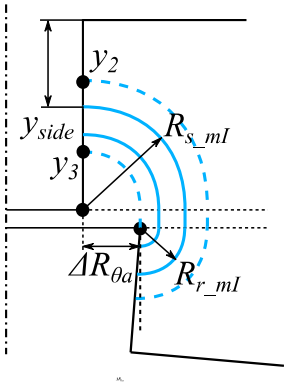

Figure 6-9 Linearized geometry at θ_a, tube paths m_{side_I}.

At this point, conditions (6-20) and (6-21) can be checked, so that $y_{1\_\theta a}$ and $y_{2\_\theta a}$ are finally attained. Then, leakage contributions $\Psi_{lI\_side\_\theta a}$ and $\Psi_{lII\_side\_\theta a}$ are determined through (6-12) and (6-18), resulting in (6-29).

$$\begin{aligned}\Psi_{lI\_side\_\theta a} &= \int_0^{y_{1\_\theta a}} d\Psi_{lI}\left(y_{side}\right) \\ \Psi_{lII\_side\_\theta a} &= \int_{y_{1\_\theta a}}^{y_{2\_\theta a}} d\Psi_{lII}\left(y_{side}\right)\end{aligned} \quad . \tag{6-29}$$

With regard to the inductance contribution $L_{m\_side\_I\_\theta a}$ provided by the magnetising paths m_{side_I}, the following considerations can be done:

- lines are assumed to completely link the full MMF,
- adjacent flux paths are parallel to each other, meaning that the tube cross section is constant along the entire length.

Therefore, $L_{m\_side\_I\_\theta a}$ can be simply determined through the definition of permeance P given in Subsection 6.2. The permeance is expressed by (6-31), where, for convenience the difference h_{st}-y_{side} has been substituted with κ. It is observed that the point y_3 where magnetising lines change their shape corresponds to h_{st}-$\Delta R_{\theta a}$.

$$L_{m\_right\_I\_\theta a} = L_{m\_left\_I\_\theta a} = L_{m\_side\_I\_\theta a} = N^2 \mathcal{P}_{m\_side\_I\_\theta a} \quad . \tag{6-30}$$

6.2.2.2 MAGNETISING TUBES M_{SIDE_II}

The tube air-path length $l_{m\_side\_II\_\theta a}(y_{side})$ is easily derived from (6-25) by removing the third piece leading from the airgap surface to the rotor side edge, as shown in (6-32). Tubes path is illustrated in Figure 6-10.

$$\begin{aligned}\mathfrak{P}_{m\_side\_I\_\theta a} &= \mu_0 L_{stk}\int_{\Delta R_{\theta a}}^{h_{st}-y_{2\_\theta a}} \frac{1}{l_{m\_side\_I\_\theta a}(\kappa)}d\kappa \\ &= \mu_0 L_{stk}\int_{\Delta R_{\theta a}}^{h_{st}-y_{2\_\theta a}} \frac{1}{l_g+\frac{\pi}{2}\kappa+\left(\frac{\pi}{2}+\gamma_{rt}\right)\left(\kappa+\Delta R_{\theta a}\right)}d\kappa \\ &= \frac{\mu_0 L_{stk}}{\pi+\gamma_{rt}}\ln\left[8l_g+8\kappa\left(\pi+\gamma_{rt}\right)+D_s\left(2\gamma_{rt}+\pi\right)\left(\beta_{rt}+\beta_{st}\right)\right]\Big|_{\Delta R}^{h_{st}-y_{2\_\theta a}}\end{aligned}. \tag{6-31}$$

$$l_{m\_side\_II\_\theta a}(y_{side}) = \frac{\pi}{2}R_{s\_mI}+l_g = \frac{\pi}{2}\left(h_{st}-y_{side}\right)+l_g\,. \tag{6-32}$$

Furthermore, as the same hypotheses made for tubes m_{side_I} are valid, inductance contribution $L_{m\_side\_II\_\theta a}$ can be found via permeance function.

$$L_{m\_right\_II\_\theta a} = L_{m\_left\_II\_\theta a} = L_{m\_side\_II\_\theta a} = N^2\mathfrak{P}_{m\_side\_II\_\theta a}\,. \tag{6-33}$$

$$\mathfrak{P}_{m\_side\_II\_\theta a} = \mu_0 L_{stk}\int_0^{\Delta R_{\theta a}} \frac{1}{l_{m\_side\_II\_\theta a}(\kappa)}d\kappa = \frac{2\mu_0 L_{stk}}{\pi}\ln\left[1+\frac{\pi\,\Delta R_{\theta a}}{2l_g}\right]. \tag{6-34}$$

6.2.2.3 MAGNETISING TUBES M_{FRONT}

In the case of magnetising tubes m_{front}, since the tubes length is constant and equal to l_g, then permeance derivation is straightforward. The final expression is given in (6-35)-(6-36).

$$L_{front\_\theta a} = N^2\mathfrak{P}_{front\_\theta a}\,. \tag{6-35}$$

$$\mathfrak{P}_{front\_\theta a} = \frac{\mu_0 L_{stk} D_s \beta_{st}}{l_g}\,. \tag{6-36}$$

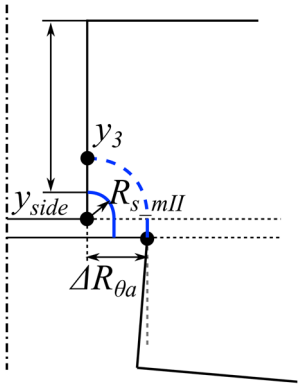

Figure 6-10 Linearized geometry at θ_a, tube paths m_{side_II}.

6.2.2.4 ALIGNED INDUCTANCE L_A

From the equations derived in Subsections 6.2.2.1 to 6.2.2.3, it is possible to derive the final value of the aligned inductance L_a by applying (6-1).

Leakage contributions are given by (6-29), as shown below. For convenience, the rated phase current i_{ph} is set equal 1A, assuming that this value is low enough to avoid saturation.

$$L_{l\_left\_\theta a} = L_{l\_right\_\theta a} = \left(\frac{\Psi_{lI\_side\_\theta a}}{i_{ph}} + \frac{\Psi_{lII\_side\_\theta a}}{i_{ph}} \right)\Bigg|_{i_{ph}=1}.$$

Side magnetising contributions are expressed by (6-30) and (6-33).

$$L_{m\_left\_\theta a} = L_{m\_right\_\theta a} = N^2 \left(\wp_{m\_right\_I\_\theta a} + \wp_{m\_right\_II\_\theta a} \right).$$

Front magnetising contribution is given in (6-35):

$$L_{front\_\theta a} = N^2 \left(\wp_{front\_\theta a} \right).$$

$$L(\theta_a) = L_a = L_{l\_left\_\theta a} + L_{m\_left\_\theta a} + L_{front\_\theta a} + L_{m\_right\_\theta a} + L_{l\_right\_\theta a}. \quad (6\text{-}37)$$

6.2.3 θ_1

The magnetising tubes as the rotor stands at θ_1 are the topic of this Subsection. Figure 6-11 provides a schematic representation of the flux tubes distribution. Similarly to the position θ_a, most of the flux is provided by the front lines and hence flux tubes are represented by a compositions of straight lines and circular arcs.

On the other hand, the geometrical configuration is now asymmetrical and therefore the right and left side edges are different. In order to keep a concise notation, sometimes the subscript 'r' is used in replacement of 'right'. This time, four tube patterns appear:

- m_{right}: are the only pattern appearing at the right edge. Lines are composed of a circular arc leading from the stator tooth side to the airgap, a straight line crossing the airgap and a final arc closing on the rotor tooth side.
- m_{front}: made by a straight line crossing the airgap and connecting the front surfaces of stator and rotor.
- m_{left_II}: occur only at the left stator side and are composed of the same circular arc leading from the stator tooth side to the airgap and the straight line crossing the airgap.
- m_{left_I}: are the outermost left lines. The path followed is the same as in m_{right} except for the radius of the lines leading from the airgap to the rotor side edge.

The four paths are modelled in the following Subsections.

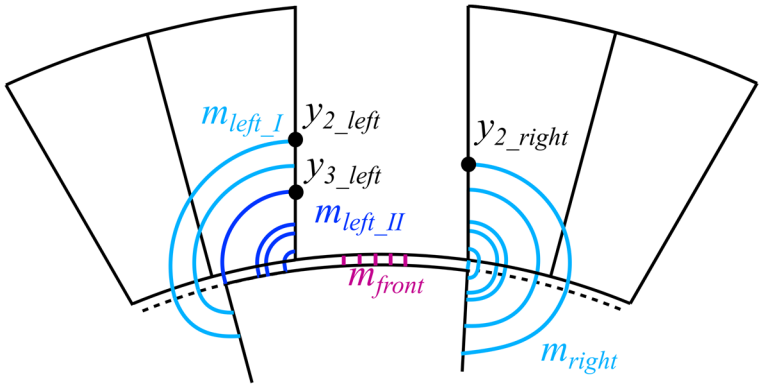

Figure 6-11 Magnetising tubes at θ_1.

6.2.3.1 MAGNETISING TUBES M_{RIGHT}

Similarly to the aligned position, the greatest inductance contribution is given by the front tubes. Hence, the linearized pole pair geometry is kept, as can be seen in Figure 6-12.

The tube air-path length $l_{m\_right\_\theta1}(y_{side})$ is derived in (6-38).

$$l_{m\_right\_\theta1}(y_{side}) = (\pi + \gamma_{rt})(h_{st} - y_{side}) + l_g \quad T(\omega_b) > T_{rated} = \frac{P_{rated}}{\omega_b}. \tag{6-38}$$

As a first step, the leakage inductance is determined. To this end, $y_{1\_right\_\theta1}$ and $y_{2\_right\_\theta1}$ must be found. Points $y_{lI\_m\_right\_\theta1}$ and $y_{lII\_m\_right\_\theta1}$, where flux tubes equal each other in length, are expressed in (6-39) and (6-40).

$$y_{lI\_m\_right\_\theta1} = \frac{l_g + h_{st}(\pi + \gamma_{rt})}{\gamma_{rt} + \pi + \left(\frac{\pi}{2} - \delta_{sy}\right)(1 + e_{lI})}. \tag{6-39}$$

$$y_{lII\_m\_right\_\theta1} = \frac{l_g - \frac{D_s}{2}(\zeta_s - \beta_{st}) - \zeta_s h_{st} + h_{st}(\pi + \gamma_{rt})}{\gamma_{rt} + \pi - \zeta_s}. \tag{6-40}$$

Then, by checking conditions (6-20) and (6-21), $y_{1\_right\_\theta1}$ and $y_{2\_right\_\theta1}$ are found straightforwardly. In a bid of deriving the leakage contributions given by the leakages tubes l_I and l_{II} $\Psi_{lI\_right\_\theta1}$ and $\Psi_{lII\_right\_\theta1}$, (6-12) and (6-18) are applied:

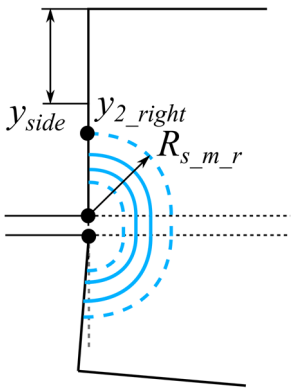

Figure 6-12 Linearized geometry at θ_1, tube paths m_{right}.

$$\Psi_{lI\_right\_\theta_1} = \int_0^{y_{1\_right\_\theta1}} d\Psi_{lI}\left(y_{side}\right)$$
$$\Psi_{lII\_right\_\theta_1} = \int_{y_{1\_right\_\theta1}}^{y_{2\_right\_\theta1}} d\Psi_{lII}\left(y_{side}\right) \quad . \tag{6-41}$$

Finally, the inductance contributions given by the magnetising lines of the region at hand is calculated from the permeance definition, as shown in (6-42).

$$L_{m\_right\_\theta1} = N^2 \mathfrak{P}_{m\_right\_\theta1} \, . \tag{6-42}$$

$$\mathfrak{P}_{m\_right\_\theta1} = \mu_0 L_{stk} \int_0^{h_{st}-y_{2\_right\_\theta1}} \frac{1}{l_{m\_right\_\theta1}(\kappa)} d\kappa$$
$$= \mu_0 L_{stk} \int_0^{h_{st}-y_{2\_right\_\theta1}} \frac{1}{l_g + \kappa(\pi+\gamma_{rt})} d\kappa = \frac{\mu_0 L_{stk}}{\pi+\gamma_{rt}} \ln\left[l_g + \kappa(\pi+\gamma_{rt})\right]\Big|_0^{h_{st}-y_{2\_right\_\theta1}} \, . \tag{6-43}$$

6.2.3.2 MAGNETISING TUBES M_{FRONT}

For the front region, the same configuration found at full alignment remains the unvaried. Hence, the front inductance contribution is derived straightforwardly from (6-44).

$$L_{front\_\theta1} = N^2 \mathfrak{P}_{front\_\theta1} \, . \tag{6-44}$$

$$\mathfrak{P}_{front\_\theta1} = \frac{\mu_0 L_{stk} D_s \beta_{st}}{l_g} \, . \tag{6-45}$$

6.2.3.3 MAGNETISING TUBES M_{LEFT_II}

As it can be observed from Figure 6-13, tubes m_{left_II} are exactly equal to paths m_{side_II} at full alignment. Therefore, tubes length is already given in (6-32) and thus that same inductance expression can be used. The only difference lies in the integral upper bound $\Delta R_{\theta 1}$, which is shown in Figure 6-13, and whose approximated expression is shown in (6-46).

$$\Delta R_{\theta1} \cong \frac{D_r}{4}\left(\beta_{rt} - \beta_{st} + \theta_1\right) . \tag{6-46}$$

$$L_{m\_left\_II\_\theta1} = N^2 \mathfrak{P}_{m\_right\_II\_\theta1} \, . \tag{6-47}$$

$$\mathfrak{P}_{m\_right\_II\_\theta1} = \mu_0 L_{stk} \int_0^{\Delta R_{\theta1}} \frac{1}{l_{m\_side\_II\_\theta a}(\kappa)} d\kappa = \frac{2\mu_0 L_{stk}}{\pi} \ln\left[1 + \frac{\pi \Delta R_{\theta1}}{2 l_g}\right] . \tag{6-48}$$

6.2.3.4 MAGNETISING TUBES M_{LEFT_I}

Tubes m_{left_I} are represented in Figure 6-13. As observed, tubes follow exactly the same path followed at the fully aligned position by tubes m_{side_I}, with the exception of the

different rotor radius $\Delta R_{\theta 1}$. Therefore, results for this region are found straightforwardly by simply replacing $\Delta R_{\theta 1}$ in the equations derived in Subsection 6.2.2.1.

For the sake of completeness, final expressions are given below.

$$\begin{aligned}\Psi_{lI\_left\_\theta 1} &= \int_{0}^{y_{1\_left\_\theta 1}} d\Psi_{lI}\left(y_{side}\right) \\ \Psi_{lII\_left\_\theta 1} &= \int_{y_{1\_left\_\theta a}}^{y_{2\_left\_\theta 1}} d\Psi_{lII}\left(y_{side}\right)\end{aligned} \quad . \tag{6-49}$$

$$L_{m\_left\_I\_\theta 1} = N^2 \mathrm{P}_{m\_left\_I\_\theta 1} \quad . \tag{6-50}$$

$$\begin{aligned}\mathfrak{P}_{m\_left\_I\_\theta 1} &= \mu_0 L_{stk} \int_{\Delta R_{\theta 1}}^{h_{st}-y_{2\_left\_\theta 1}} \frac{1}{l_{m\_left\_I\_\theta 1}\left(\kappa\right)} d\kappa \\ &= \mu_0 L_{stk} \int_{\Delta R_{\theta 1}}^{h_{st}-y_{2\_left\_\theta 1}} \frac{1}{l_g + \frac{\pi}{2}\kappa + \left(\frac{\pi}{2}+\gamma_{rt}\right)\left(\kappa + \Delta R_{\theta a}\right)} d\kappa \\ &= \frac{\mu_0 L_{stk}}{\pi+\gamma_{rt}} \ln\left[8l_g + 8\kappa\left(\pi+\gamma_{rt}\right) + D_s\left(2\gamma_{rt}+\pi\right)\left(\beta_{rt}+\beta_{st}\right)\right]\Big|_{\Delta R_{\theta 1}}^{h_{st}-y_{2\_left\_\theta 1}}\end{aligned} \tag{6-51}$$

6.2.3.5 INDUCTANCE L_1

Eq. (6-1) is now applied and all the contributions of the inductance L_1 are summed up. Leakage contributions are given by (6-42) and (6-49), respectively for the right and left side. The phase current i_{ph} is set to $1A$, assuming that with this value core saturation does not occur.

$$\begin{aligned}L_{l\_right\_\theta 1} &= \left(\frac{\Psi_{lI\_right\_\theta 1}}{i_{ph}} + \frac{\Psi_{lII\_right\_\theta 1}}{i_{ph}}\right)\Big|_{i_{ph}=1} \\ L_{l\_left\_\theta 1} &= \left(\frac{\Psi_{lI\_left\_\theta 1}}{i_{ph}} + \frac{\Psi_{lII\_left\_\theta 1}}{i_{ph}}\right)\Big|_{i_{ph}=1}\end{aligned} \quad .$$

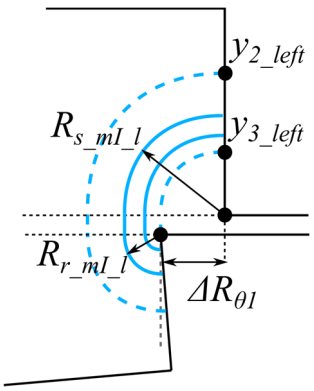

Figure 6-13 Linearized geometry at θ_1, tube paths m_{left_I}.

Side magnetising contributions are expressed by (6-42), (6-47) and (6-50).

$$L_{m\_right\_\theta 1} = N^2\left(\mathfrak{P}_{m\_right\_\theta 1}\right)$$
$$L_{m\_left\_\theta 1} = N^2\left(\mathfrak{P}_{m\_right\_I\_\theta 1} + \mathfrak{P}_{m\_right\_II\_\theta 1}\right).$$

Front magnetising contribution is given in (6-44):

$$L_{front\_\theta 1} = N^2\left(\mathfrak{P}_{front\_\theta 1}\right).$$

$$L(\theta_1) = L_1 = L_{l\_left\_\theta 1} + L_{m\_left\_\theta 1} + L_{front\_\theta 1} + L_{m\_right\_\theta 1} + L_{l\_right\_\theta 1}. \tag{6-52}$$

6.2.4 PRELIMINARY DISCUSSION ABOUT THE NON-OVERLAP CONDITION: ELLIPTICAL-SHAPED FLUX TUBES

When the rotor stands at the position θ_2 and θ_u, the stator and rotor teeth no longer overlap. In this condition, as the air paths length becomes considerably larger than the airgap, the simplified representation of the flux tubes through straight lines and circular arcs might result highly inaccurate. In particular, the error in the inductance estimation grows higher as the average air path length increases.

A visual representation of the critical conditions for the inductance determination is given by the position that the SR machine at hand occupies inside its Stephenson's triangle (see Subsection 3.5.4). Figure 6-14 shows the Stephenson's triangles defined by the SRMyld (a) and SRFly (b) prototypes. For ease of representation, both x and y-axes have been normalised with respect to their maximum value. As discussed in Subsection 3.5.4, a Stephenson's triangle defines the region of feasible values for β_{st} and β_{rt} for a given poles combination. Its right edge corresponds to the limit condition where θ_2 equals θ_u, and thus the stator tooth corners face exactly two rotor teeth corners (see Figure 6-14). This condition represents the best-case scenario for the non-overlap inductance determination ($L_2 = L_u$), since it provides the shortest air paths. Then, the further the machine lies from the triangle's right edge, the harder is the determination of L_2 and L_u.

As a demonstration, Table 6-I shows the values of L_u for both SR prototypes, calculated with the 'historical' method proposed in [116]. It is found that accuracy is

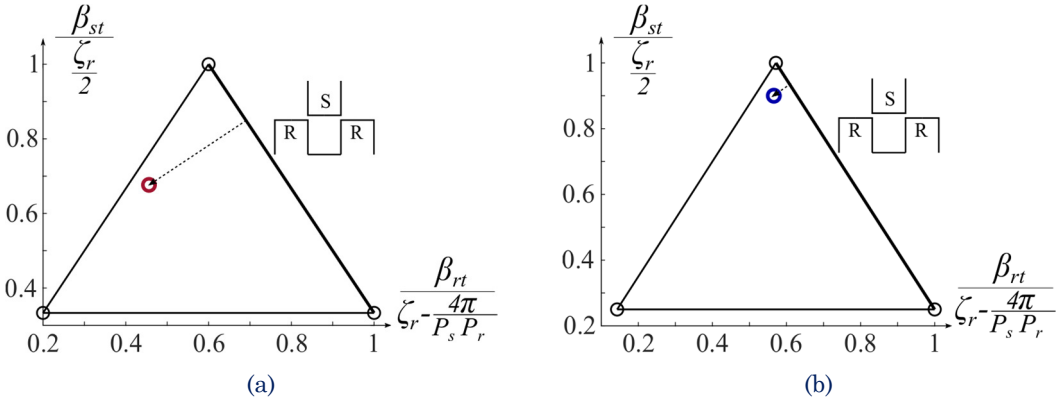

Figure 6-14 Stephenson's triangles: (a) SRMyld prototype and (b) SRFly prototype

more than acceptable for the SRFly prototype, where air paths are relatively short. Conversely, accuracy dramatically lowers in the case of the SRMyld prototype, as air flux paths are longer.

Hence, it is concluded that flux lines representation through straight segments and circular arcs cannot guarantee a sufficiently high accuracy for any potential member of the ADS, when it comes to the non-overlap condition. To overcome this issue, this thesis aims to give a little contribution by proposing the determination of L_2 and L_u by means of elliptical arcs in replacement of the circular arcs.

Elliptical lines have been firstly proposed by Takemoto *et al.* in [118] to overcome the issues caused by the traditional circular-arc-based representation in the development of a bearingless SR motor. However, it was the form of the analytical equation, rather than the low level of accuracy, to push Takemoto *et al.* towards this new idea. Indeed, [118] does not provides any accuracy comparison between the elliptical and the circular representation. Moreover, [118] considered only flux lines leading directly from the rotor front surface to the stator side surface, only in conditions of partial overlap, for an linearised geometry. Non-overlap conditions are not accounted for. This thesis extends and adjusts the elliptical representation proposed in [118] to the non-overlap conditions and considers a non-linearised geometry.

In particular, to extend the elliptical representation to the non-overlap condition, all flux tubes are considered as a composition of a stator stretch and a rotor stretch. Stretches intersect with each other on the mid-airgap surface, being both of them perpendicular to the surface. For convenience, the mid-airgap surface is represented as a straight horizontal surface passing through the midpoint between the stator and rotor corners. Figure 6-15 illustrates the concept.

In terms of solving strategy, as the stator and rotor stretches are considered separately, contribution are calculated individually and subsequently summed up. Consistently with the positions θ_a and θ_1, all magnetising lines are considered to link the entire MMF and therefore the permeance approach can be adopted. In this case, stator and rotor permeances, namely P_{sta} and P_{rot}, are parallel connected, and hence are simply summed up.

Observation: the fact that flux tubes cross the mid-airgap surface perpendicularly is undoubtedly a gross simplification. However, when stator and rotor do not overlap, flux lines are far from being parallel and therefore any other path that considers parallel flux lines would also be a simplification. In conclusion, this thesis shows that representing flux lines perpendicular to the mid-airgap surface is a necessary simplification to attain the best compromise between model's accuracy and complexity.

Table 6-I L_2 and L_u values of the SR prototypes found by the method proposed in [116].

	Analytical [116] (mH)	FEA (mH)	Error (%)
SRMyld	**0.232**	0.269	-13.75
SRFly	**0.619**	0.757	-18.23

6.2.4.1 ELLIPTICAL-SHAPED TUBES MATHEMATICAL FORMULATION

Based on the elliptical representation proposed in [118] ellipses eccentricity changes along with their length. Likewise the leakage lines l_l, the ratio between the ellipse's semi-axes Γ_x and Γ_y is preferred to the actual eccentricity, in a bid of keeping the mathematical formulation at its simplest. The relation between Γ_x and Γ_y is expressed by the function $e_m(\Gamma_x)$ (the subscript m stands for magnetising) shown in (6-53) below:

$$\begin{cases} \Gamma_y = e_m(\Gamma_x)\Gamma_x + l_g \\ e_m(\Gamma_x) = \dfrac{\Gamma_x / l_g}{\varepsilon_m + \Gamma_x / l_g} = \dfrac{\Gamma_x}{l_g \varepsilon_m + \Gamma_x} \end{cases}. \tag{6-53}$$

As observed, Γ_y is expressed as a function of Γ_x. The parameter ε_m is a constant and has been determined in [118] via FEA simulation. Its value is given below:

$$\varepsilon_m = 1.18.$$

Finally, it is observed that for the positions θ_2 and θ_u, the horizontal coordinate x is preferred to the vertical y_{side} to represent the flux tubes, even though a change of reference variable will be necessary in few occasions.

6.2.5 θ_2

When the rotor stands at the position θ_2, magnetising tubes are schematically represented in Figure 6-15. Tubes geometry is described as follows:

- m_{left}: as previously discussed, flux lines are modelled through elliptical paths. In this case, path is composed of a stator stretch, leading from the tooth side to the mid-airgap surface, and of a rotor stretch from the mid-airgap to the rotor front.
- m_{front_I}: made by a stator straight line, leading from the stator front surface to the mid-airgap, and by an elliptic rotor line closing up to the rotor left side surface.
- m_{front_II}: made by a straight line crossing the airgap and connecting the stator front surface to the rotor yoke.
- m_{front_III}: have the same shape has lines m_{front_I} but close up to the rotor's right tooth side.
- m_{right_I}: made by a stator elliptic line leading from the stator side surface to the mid-airgap, and the rotor elliptic line closing up to the rotor's right tooth side.
- m_{right_II}: likewise the m_{left}.

The six paths are analysed one by one in the Subsections below.

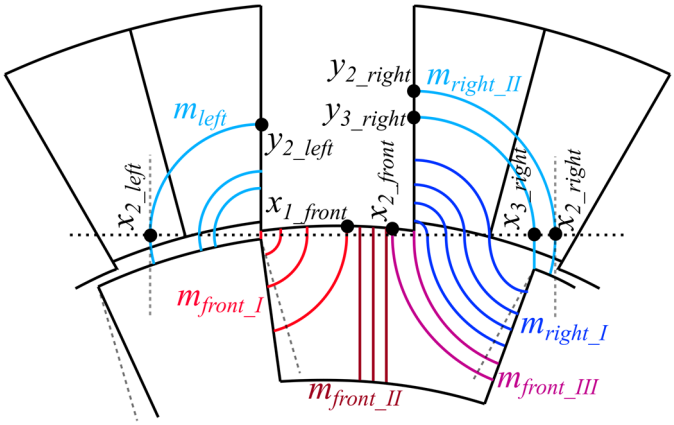

Figure 6-15 Magnetising tubes at θ_2.

6.2.5.1 MAGNETISING TUBES M_{LEFT}

As now stator and rotor teeth do not overlap, a linearised geometry would result excessively unrealistic. The only reasonable simplification is that stator and rotor front surfaces are straight, as shown in Figure 6-16.

Stator paths are elliptical arcs with centre O in the midpoint between the facing stator and rotor corners (see Figure 6-16) and subtend a 90° angle. The stator ellipse length $l_{m\_left\_\theta2}{}^{s}$ is expressed with respect of both x and y_{side} in (6-54), where $\Gamma_x = x$, and $\Gamma_y = h_{st}+l_g/2-y_{side}$. In particular, the formulation with respect of x is used to calculate the permeance. Conversely, formulation with respect of y_{side} is adopted to determine the boundary point between leakage and magnetising paths.

$$\begin{cases} l_{m\_left\_\theta2}{}^{s}(x) = \dfrac{\pi\left(\Gamma_x(x)+\Gamma_y(x)\right)}{4} = \dfrac{\pi}{4}\left(x + \dfrac{x^2}{\frac{l_g}{2}\varepsilon_m + x} + \dfrac{l_g}{2}\right) \\ l_{m\_left\_\theta2}{}^{s}(y_{side}) = \dfrac{\pi\left(\Gamma_x(y_{side})+\Gamma_y(y_{side})\right)}{4} = \\ = \dfrac{\pi}{4}\left(\dfrac{3}{2}(h_{st}-y_{side}) + \dfrac{1}{2}\left(\dfrac{l_g}{2} + \sqrt{(h_{st}-y_{side})^2 + 2\varepsilon_m l_g (h_{st}-y_{side})}\right)\right) \end{cases} . \quad (6\text{-}54)$$

Rotor paths are also elliptical arcs with centre O. As can be observed from Figure 6-16, each line subtends a different angle, which would require an unnecessarily complex analytical expression for the lines' length. However, rotor lines are dramatically shorter than the stator lines. To this cause, the approximation depicted in Figure 6-16 is introduced: rotor lines length is approximated as the difference between the length of an ellipse that subtends a 90° angle and a circular arc with centre in the rotor tooth corner and radius R_c. The latter is equal to the ellipse y-semi-axis minus half the airgap. Then, the rotor tubes length $l_{m\_left\_\theta2}{}^{r}$ is expressed as shown in (6-55).

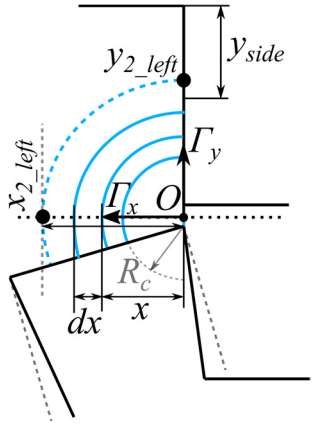

Figure 6-16 Linearized geometry at θ_2, tube paths m_{left}.

$$\begin{cases} l_{m\_left\_\theta 2}{}^{r}(x) = l_{m\_left\_\theta 2}{}^{s}(x) - \left(\frac{\pi}{2} - \theta_2\right)\dfrac{x^2}{\frac{l_g}{2}\varepsilon_m + x} \\ l_{m\_left\_\theta 2}{}^{r}(y_{side}) = l_{m\_left\_\theta 2}{}^{s}(y_{side}) - \left(\frac{\pi}{2} - \theta_2\right)(h_{st} - y_{side}) \end{cases} . \tag{6-55}$$

Finally, the sum of the stator and rotor stretches yields the total paths m_{left} length $l_{m\_left\_\theta 2}$:

$$\begin{cases} l_{m\_left\_\theta 2}(x) = 2l_{m\_left\_\theta 2}{}^{s}(x) - \left(\frac{\pi}{2} - \theta_2\right)\dfrac{x^2}{\frac{l_g}{2}\varepsilon_m + x} \\ l_{m\_left\_\theta 2}(y_{side}) = 2l_{m\_left\_\theta 2}{}^{s}(y_{side}) - \left(\frac{\pi}{2} - \theta_2\right)(h_{st} - y_{side}) \end{cases} . \tag{6-56}$$

At this point, the determination of y_{1_left} and y_{2_left}, needed to evaluate the leakage inductance, can be undertaken. To this end, the length of the paths m_{left}, expressed as a function of y_{side} in (6-56), is equalled with that of the leakage lines l_I and l_{II}, given respectively in (6-6) and (6-13). $y_{II\_m\_left\ \theta 2}$ and $y_{III\_m\_left\_\theta 2}$ are derived in (6-57) and (6-58).

$$\begin{cases} y_{II\_m\_left\_\theta 2} = h_{st} - \dfrac{2ab - \sqrt{\left(2ab - \frac{\varepsilon_m l_g \pi^2}{8}\right)^2 - 4\left(b^2 - \frac{\pi^2}{16}\right)a^2} - \frac{\varepsilon_m l_g \pi^2}{8}}{\frac{\pi^2}{8} - 2b^2} \\ a = \frac{\pi}{4} l_g - h_{st}\left(\frac{\pi}{2} - \delta_{sy}\right)(1 + e_{lI}) \ , \qquad b = \frac{\pi}{4} + \theta_2 + \left(\frac{\pi}{2} - \delta_{sy}\right)(1 + e_{lI}) \end{cases} \tag{6-57}$$

$$\begin{cases} y_{lII\_m\_left\_\theta 2} = h_{st} + \dfrac{\sqrt{\left(\frac{\pi^2}{4} + 4a^2\right)b^2 + \left(2ab + \frac{\varepsilon_m l_g \pi^2}{8}\right)^2} + 2ab + \frac{\varepsilon_m l_g \pi^2}{8}}{\frac{\pi^2}{8} + 2a^2} \\ a = \frac{\pi}{4} + \theta_2 - \zeta_s \ , \qquad b = \left(\frac{\pi}{4} l_g + \frac{D_s}{2}(\zeta_s + \beta_{st})\right) \end{cases} . \tag{6-58}$$

As done for the previous positions, conditions (6-20) and (6-21) are checked and $y_{1\_left\_\theta 2}$ and $y_{2\_left\_\theta 2}$ are finally attained. Leakage contributions $\Psi_{lI\_left\_\theta 2}$ and $\Psi_{lII\_left\_\theta 2}$ are found by (6-59).

$$\begin{aligned}\Psi_{lI\_left\_\theta 2} &= \int_{0}^{y_{1\_left\_\theta 2}} d\Psi_{lI}\left(y_{side}\right) \\ \Psi_{lII\_left\_\theta 2} &= \int_{y_{1\_left\_\theta 2}}^{y_{2\_left\_\theta 2}} d\Psi_{lII}\left(y_{side}\right)\end{aligned} \quad . \tag{6-59}$$

The magnetising contribution $L_{m\_left\_\theta 2}$ of paths m_{left} is now considered. Its derivation is performed through the corresponding permeance $P_{m\_left\_\theta 2}$, as shown in (6-60), bearing in mind that the overall permeance is to be found by summing up the stator and rotor permeances. Moreover, the derivation of stator and rotor permeances $P_{m\_left\_\theta 2}{}^{s}$ and $P_{m\_left\_\theta 2}{}^{r}$ is not straightforward, since flux tubes do not have a constant cross section. Both permeances are derived below, where the symbol // denotes the parallel-connection operator, i.e. $(1/x_1+1/x_2+\ldots+1/x_n)^{-1}$.

$$L_{m\_left\_\theta 2} = N^2 \wp_{m\_left\_\theta 2} = N^2 \left(\wp_{m\_left\_\theta 2}{}^{s} \,//\, \wp_{m\_left\_\theta 2}{}^{r} \right) . \tag{6-60}$$

STATOR

The infinitesimal stator permeance $dP_{m\_left\_\theta 2}{}^{s}$ associated to an infinitesimal mid-airgap section $dx\, L_{stk}$ is initially considered. The length of the lines has been already expressed as a function of x in (6-54). In terms of cross section $dA_{m\_left\_\theta 2}{}^{s}$ (x), [118] shows that it is reasonable to consider the average tube's cross section; the latter is derived in (6-61). Then, stator permeance $P_{m\_left\_\theta 2}{}^{s}$ is found by solving the integral shown in (6-62).

Finally, to complete (6-60), $x_{2\_left\_\theta 2}$ is actually the x-semi-axis of the outermost ellipse of the m_{left} region, whose y-semi-axis depends on $y_{2\_left\_\theta 2}$:

$$\begin{cases} dA_{m\_left\_\theta 2}(x) = \dfrac{1}{2} L_{stk} \left(d\Gamma_x + d\Gamma_y \right) = \dfrac{1}{2} L_{stk} \left(1 + \dfrac{x\left(x+\varepsilon_m l_g\right)}{\left(x+\varepsilon_m \dfrac{l_g}{2}\right)^2} \right) dx \\ d\Gamma_x = dx \\ d\Gamma_y = \dfrac{\partial \Gamma_y}{\partial x} dx = \dfrac{x\left(x+\varepsilon_m l_g\right)}{\left(x+\varepsilon_m \dfrac{l_g}{2}\right)^2} dx \end{cases} . \tag{6-61}$$

$$\begin{cases} d\mathrm{P}_{m\_left\_\theta 2}{}^{s}(x) = \mu_0 \dfrac{dA_{m\_left\_\theta 2}(x)}{l_{m\_left\_\theta 2}{}^{s}(x)} \\ \mathrm{P}_{m\_left\_\theta 2}{}^{s} = \displaystyle\int_0^{x_{2\_left\_\theta 2}} d\mathrm{P}_{m\_left\_\theta 2}{}^{s} = \\ = \dfrac{2}{\pi}\mu_0 L_{stk}\left[\ln\left(x + \varepsilon_m \dfrac{l_g}{2} \right) + \ln\left(x^2 + x\dfrac{l_g}{4}(1+\varepsilon_m) + \dfrac{l_g{}^2}{8} \right) \right]_0^{x_{2\_left\_\theta 2}} \end{cases} . \tag{6-62}$$

$$x_{2\_left\_\theta 2} = \frac{1}{2}\left(h_{st} - y_{2\_left\_\theta 2} + \sqrt{\left(h_{st} - y_{2\_left\_\theta 2} \right)^2 + 2\varepsilon_m l_g \left(h_{st} - y_{2\_left\_\theta 2} \right)} \right). \tag{6-63}$$

ROTOR

As previously observed, rotor lines are considerably shorter than stator lines. Hence, stator permeance provides the greatest contribution to the overall permeance and therefore a small error is incurred if, for the rotor lines, the same cross section used for the stator is considered.

Rotor permeance $P_{m\_left\_\theta 2}{}^{r}$ is found by solving (6-64). The author wishes to highlight that the closed-form solution does exist. However, due to its length, it is not reported in this thesis.

$$\begin{cases} d\mathcal{P}_{m\_left\_\theta 2}{}^{r}(x) = \mu_0 \dfrac{dA_{m\_left\_\theta 2}(x)}{l_{m\_left\_\theta 2}{}^{r}(x)} \\ \mathcal{P}_{m\_left\_\theta 2}{}^{r} = \displaystyle\int_0^{x_{\max}} d\mathcal{P}_{m\_left\_\theta 2}{}^{r} \end{cases} . \tag{6-64}$$

6.2.5.2 MAGNETISING TUBES M_{FRONT_I}, M_{FRONT_II} AND M_{FRONT_III}

As opposed to the positions θ_a and θ_1, front flux tubes might follow different paths. The three possible paths geometries are illustrated in Figure 6-17. Consistently with what has been done for the side region, the shortest line criterion is used to identify the point where one path turns into another. It is observed that tubes m_{front_I} and m_{front_III} are present in any SR machine geometry (at least in those of engineering interest), while m_{front_II} are present only in SR machines with 'short' rotor teeth.

The lengths of the three possible paths are firstly derived. For tubes m_{front_I} and m_{front_II}, the stator stretch length is equal to half the airgap. Then, for tubes m_{front_I}, the same simplification proposed for tubes m_{left} is adopted. Indeed, the portion of ellipse approximated as a circle is very short, so that a great error is not introduced. With regard to the elliptical tubes of tubes m_{front_III}, the airgap considered is the actual distance between the stator corner and the right-hand-side rotor corner. Its x and y components $l_{g\_right\_x\_\theta 2}$ and $l_{g\_right\_y\_\theta 2}$ are shown in Figure 6-17. Finally, for tubes m_{front_II}, it is reasonable to consider their overall length equal to the rotor tooth height h_{rt}.

Lengths expressions are given in (6-65), (6-66) and (6-67) below.

$$l_{mI\_front\_\theta 2}(x) = l_{mI\_front\_\theta 2}{}^{s} + l_{mI\_front\_\theta 2}{}^{r}(x)$$
$$= \frac{l_g}{2} + \frac{\pi}{4}\left(x + \frac{x^2}{\frac{l_g}{2}\varepsilon_m + x} + \frac{l_g}{2} \right) - (\theta_2 - \beta_{re})\left(\frac{x^2}{\frac{l_g}{2}\varepsilon_m + x} \right). \quad (6\text{-}65)$$

$$l_{mII\_front\_\theta 2}(x) \cong h_{rt}\,. \quad (6\text{-}66)$$

$$\begin{cases} l_{mIII\_front\_\theta 2}(t(x)) = l_{mIII\_front\_\theta 2}{}^{s} + l_{mIII\_front\_\theta 2}{}^{r}(t(x)) = \\ = \frac{l_g}{2} + \frac{\pi}{4}\left(t + \frac{t^2}{l_g{}'\varepsilon_m + t} + \right) - \Delta\theta\left(\frac{t^2}{l_g{}'\varepsilon_m + t} \right) \\ t(x) = \left(l_{g\_right\_x\_\theta 2} + \frac{D_s}{2}\beta_{st} - x \right) \\ l_g{}' = \left(l_{g\_right\_y\_\theta 2} - \frac{l_g}{2} \right) \\ \Delta\theta = (\zeta_r - \theta_2 - \beta_{re}) \end{cases}. \quad (6\text{-}67)$$

By equating the paths' length expressions, points $x_{1\_front\_\theta 2}$ and $x_{2\_front\_\theta 2}$, which are required to calculate the front inductance contribution, can be derived. Similarly to the case of the side tubes, the determination of $x_{1\_front\_\theta 2}$ and $x_{2\_front\_\theta 2}$ requires the prior knowledge of the 'height' of the rotor tooth. In this regard, based on h_{rt}, two different configurations can be encountered, i.e. 'short rotor tooth' and 'tall rotor tooth', where tubes m_{front_II} respectively do and do not exist. The procedure requires the knowledge of the three points where the lengths of the three front paths equal each other, namely $x_{I\_II\_front\_\theta 2}$, $x_{I\_III\_front\_\theta 2}$ and $x_{II\_III\_front\_\theta 2}$. Their expressions are provided in (6-68). As these equations are third order polynomials, their closed-form solution is not straightforward. In this thesis, a numeric solution has been adopted.

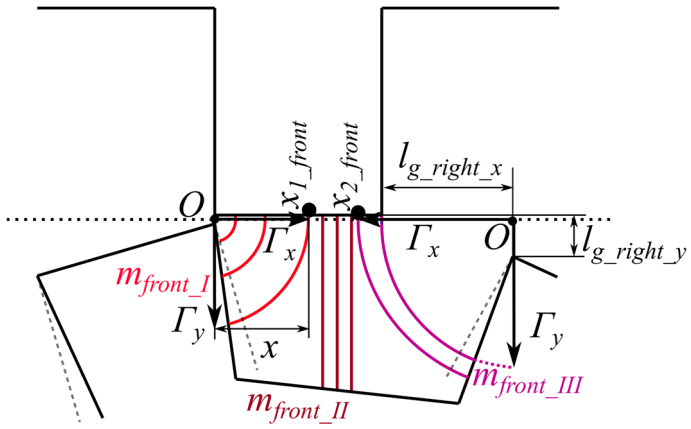

Figure 6-17 Position θ_2, tube paths m_{left}.

$$\begin{aligned} x_{I\_II\_front\_\theta 2} &= \left\{ sol : \left(l_{mI\_front\_\theta 2}(x) = l_{mII\_front\_\theta 2}(x) \right) \right\} \\ x_{I\_III\_front\_\theta 2} &= \left\{ sol : \left(l_{mI\_front\_\theta 2}(x) = l_{mIII\_front\_\theta 2}(x) \right) \right\} \\ x_{II\_III\_front\_\theta 2} &= \left\{ sol : \left(l_{mII\_front\_\theta 2}(x) = l_{mIII\_front\_\theta 2}(x) \right) \right\} \end{aligned} . \quad (6\text{-}68)$$

TALL ROTOR TOOTH

The rotor tooth is referred to as 'tall' when straight tubes m_{front_II} do exist, as illustrated in Figure 6-17. The condition to be verified is that the tubes m_{front_II} are shorter than the other tubes within a portion of the stator front surface. Mathematically, (6-69) describes this case.

$$x_{I\_II\_front\_\theta 2} < x_{I\_III\_front\_\theta 2} < x_{II\_III\_front\_\theta 2} . \quad (6\text{-}69)$$

Then, $x_{1\_\theta 2}$ and $x_{2\_\theta 2}$ are defined as follows:

$$\begin{cases} x_{1\_front\_\theta 2} = x_{I\_II\_front\_\theta 2} \\ x_{2\_front\_\theta 2} = x_{II\_III\_front\_\theta 2} \end{cases} . \quad (6\text{-}70)$$

SHORT ROTOR TOOTH

A 'short' stator tooth is depicted in Figure 6-18. This time, tubes m_{front_II} do not appear. This scenario occurs when (6-71) is verified.

$$x_{I\_II\_front\_\theta 2} > x_{I\_III\_\theta 2} > x_{II\_III\_front\_\theta 2} . \quad (6\text{-}71)$$

Then, to represent the non-existence of paths m_{front_II}, $x_{1\_\theta 2}$ and $x_{2\_\theta 2}$ equal each other:

$$x_{1\_front\_\theta 2} = x_{2\_front\_\theta 2} . \quad (6\text{-}72)$$

Observation: Terms short and tall have been used relatively to the specific position θ_2. However, it is observed that this position represents the case where tubes m_{front_III} length is maximum. Hence, definitions of short-toothed and tall-toothed rotor given above are already in absolute terms. Both SR prototypes considered in this thesis are of the tall-toothed type.

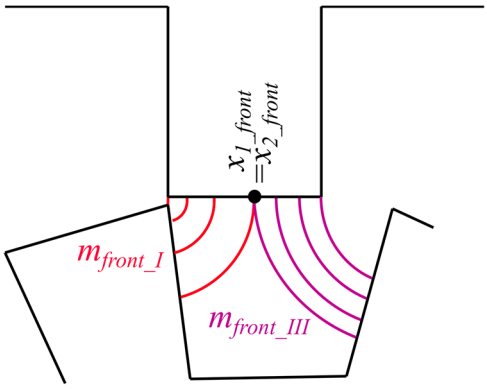

Figure 6-18 Example of short-toothed rotor.

It is now possible to move forward to the derivation of the three permeances related to paths m_{front_I}, m_{front_II} and m_{front_III}. Analytical expressions of the permeances derived below from elliptical flux lines have the same structure as (6-62) and (6-64). Therefore, for the sake of readability, are not given in their explicit forms.

For the rotor paths of m_{front_I}, the average cross section expression is the same as that used for the side flux tubes $dA_{m\_left\_\theta 2}$ given in (6-61). Hence, the inductance contribution, along with the corresponding permeance, are calculated as in (6-73). For convenience, stator and rotor contributions have been separated.

$$\begin{cases} dP_{mI\_front\_\theta 2}{}^{r}(x) = \mu_0 \dfrac{dA_{mI\_front\_\theta 2}{}^{r}(x)}{l_{mI\_front\_\theta 2}{}^{r}(x)} = \mu_0 \dfrac{dA_{m\_left\_\theta 2}(x)}{l_{mI\_front\_\theta 2}{}^{r}(x)} \\ P_{mI\_front\_\theta 2} = P_{mI\_front\_\theta 2}{}^{s} \,//\, P_{mI\_front\_\theta 2}{}^{r} \\ = \left(\mu_0 \dfrac{L_{stk} x_{1\_front\_\theta 2}}{h_{rt}} \right) // \left(\int_0^{x_{1\_front\_\theta 2}} dP_{mI\_front\_\theta 2}{}^{r} \right) \\ L_{mI\_front\_\theta 2} = N^2 P_{mI\_front\_\theta 2} \end{cases} . \tag{6-73}$$

Paths m_{front_II} have constant length. Therefore, the associated inductance contribution and permeance are found straightaway:

$$\begin{cases} P_{mII\_front\_\theta 2} \cong \mu_0 \dfrac{L_{stk}(x_{2\_front\_\theta 2} - x_{1\_front\_\theta 2})}{h_{rt}} \\ L_{mII\_front\_\theta 2} = N^2 P_{mII\_front\_\theta 2} \end{cases} . \tag{6-74}$$

For rotor stretches of m_{front_III}, the cross section must be rearranged to suit the different reference frame:

$$\begin{cases} dA_{mIII\_frontt\_\theta 2}{}^{r}(x) = \dfrac{1}{2} L_{stk} \left(1 + \dfrac{t\left(t + \varepsilon_m \left(l_{g\_right\_y\_\theta 2} - 2 l_g{}' \right)\right)}{\left(t + \varepsilon_m l_g{}' \right)^2} \right) dx \\ t(x) = \left(l_{g\_right\_x\_\theta 2} + \dfrac{D_s}{2} \beta_{st} - x \right) \\ l_g{}' = l_{g\_right\_y\_\theta 2} - \dfrac{l_g}{2} \end{cases} . \tag{6-75}$$

Finally, the inductance contribution and associated permeance are found by (6-76), where stator and rotor contributions have been separated.

6.2.5.3 MAGNETISING TUBES M_{RIGHT_I} AND M_{RIGHT_II}

Figure 6-19 shows the geometry of the right-hand-side magnetising paths. Stator stretches of both paths are elliptical arcs with centre *O* (see Figure 6-16) and subtend an angle of 90°. Rotor stretches are also elliptical arcs, with *O'* their centre. However

stretches of m_{right_I} lead from the stator to the rotor side curling counter clockwise, whilst those of m_{right_II} lead to the rotor front surface along the clockwise direction

$$\begin{cases} dP_{mIII\_front\_\theta 2}{}^{r}(x)=\mu_0\dfrac{dA_{mIII\_front\_\theta 2}{}^{r}(x)}{l_{mIII\_front\_\theta 2}{}^{r}(x)}= \\ P_{mIII\_front\_\theta 2}=P_{mIII\_front\_\theta 2}{}^{s}\,//P_{mIII\_front\_\theta 2}{}^{r}= \\ =\left(\mu_0\dfrac{L_{stk}(\dfrac{D_s}{2}\beta_{st}-x_{2\_front\_\theta 2})}{h_{rt}}\right)//\left(\int_{x_{2\_front\_\theta 2}}^{\frac{D_s}{2}\beta_{st}} dP_{mIII\_front\_\theta 2}{}^{r}\right) \\ L_{mIII\_front\_\theta 2}=N^2P_{mIII\_front\_\theta 2} \end{cases}. \tag{6-76}$$

Firstly, the lengths of the stator and rotor stretches of both m_{right_I} and m_{right_II} are defined. Due to the geometrical symmetry, stator stretches of both m_{right_I} and m_{right_II} have the same expression as the left hand side given in (6-54).

$$\begin{cases} l_{mI\_right\_\theta 2}{}^{s}(x)=l_{mII\_right\_\theta 2}{}^{s}(x)=l_{m\_left\_\theta 2}{}^{s}(x) \\ l_{mI\_right\_\theta 2}{}^{s}(y_{side})=l_{mII\_right\_\theta 2}{}^{s}(y_{side})=l_{m\_left\_\theta 2}{}^{s}(y_{side}) \end{cases}. \tag{6-77}$$

For the m_{right_I} rotor stretches, the expression used for the front paths m_{front_III} (6-67) can be used, bearing in mind that the horizontal coordinate is now $l_{g\_right\_x\_\theta 2}$-x, due to the different reference frame. In the formula below, the variable t is used to give the general expression. Subsequently, t is expressed as a function of the main variables x and y_{side}.

$$\begin{cases} l_{mI\_right\_\theta 2}{}^{r}(t)=\dfrac{\pi}{4}\left(t+\dfrac{t^2}{l_g'\varepsilon_m+t}+l_g'\right)-(\zeta_r-\theta_2-\beta_{re})\left(\dfrac{t^2}{l_g'\varepsilon_m+t}\right) \\ t(x)=\left(l_{g\_right\_x\_\theta 2}-x\right) \\ t(y_{side})=\left(l_{g\_right\_x\_\theta 2}-\dfrac{1}{2}\left(h_{st}-y_{side}+\sqrt{(h_{st}-y_{side})^2+2\varepsilon_m l_g(h_{st}-y_{side})}\right)\right) \\ l_g'=\left(l_{g\_right\_y\_\theta 2}-\dfrac{l_g}{2}\right) \end{cases}. \tag{6-78}$$

For the m_{right_II} rotor stretches, the expressions of the semi-axes are given below as functions of x.

$$\begin{cases} \Gamma_{x\_mII\_right\_\theta_2}{}^{r}(x)=x-l_{g\_right\_x\_\theta 2} \\ \Gamma_{y\_mII\_right\_\theta_2}{}^{r}(x)=\dfrac{(x-l_{g\_right\_x\_\theta 2})^2}{l_g'\varepsilon_m+(x-l_{g\_right\_x\_\theta 2})}+l_g' \\ l_g'=\left(l_{g\_right\_y\_\theta 2}-\dfrac{l_g}{2}\right) \end{cases}. \tag{6-79}$$

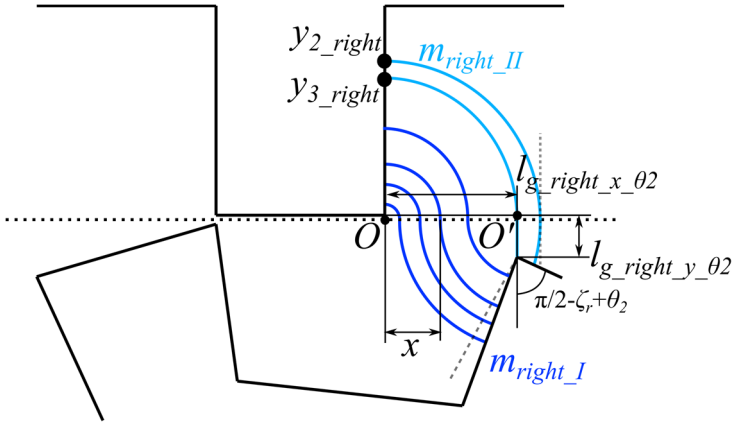

Figure 6-19 Position θ_2, tube paths m_{right_I} and m_{right_II}.

To express the semi-axes as functions of y_{side}, it is sufficient to substitute the x the relationship $x(y_{side})$:

$$x\left(y_{side}\right)=\frac{1}{2}\left(h_{st}-y_{side}+\sqrt{\left(h_{st}-y_{side}\right)^2+2\varepsilon_m l_g\left(h_{st}-y_{side}\right)}\right)-l_{g\_right\_x\_\theta2}. \tag{6-80}$$

Then, semi-axes expressions can be used to derive the lines length:

$$\begin{cases} l_{mII\_right\_\theta2}{}^{r}(x)=\dfrac{\pi}{4}\left(\Gamma_{x\_mI\_right\_\theta_2}{}^{r}(x)+\Gamma_{y\_mI\_right\_\theta_2}{}^{r}(x)\right) \\ l_{mII\_right\_\theta2}{}^{r}\left(y_{side}\right)=\dfrac{\pi}{4}\left(\Gamma_{x\_mI\_right\_\theta_2}{}^{r}\left(y_{side}\right)+\Gamma_{y\_mI\_right\_\theta_2}{}^{r}\left(y_{side}\right)\right) \end{cases}. \tag{6-81}$$

As it has been done for the other side edge, it is now necessary to define the overall distribution between magnetising and leakage paths. In this case, four possible scenarios can incur, which are represented in Figure 6-20:

1. 'short and wide-gapped' stator, when only leakage paths l_I and magnetising path m_{right_I} occur;
2. 'tall and wide-gapped' stator, when both leakage paths l_I and l_{II} appear, along with magnetising path m_I;
3. 'short and narrow-gapped' stator, when only leakage paths l_I appear but with both magnetising paths m_{right_I} and m_{right_II};
4. 'tall and narrow-gapped' stator, when all paths l_I, l_{II}, m_I and m_{II} appear.

As observed, terms tall and short have been used consistently to the other cases discussed before. This time, terms wide-gapped and narrow-gapped have been

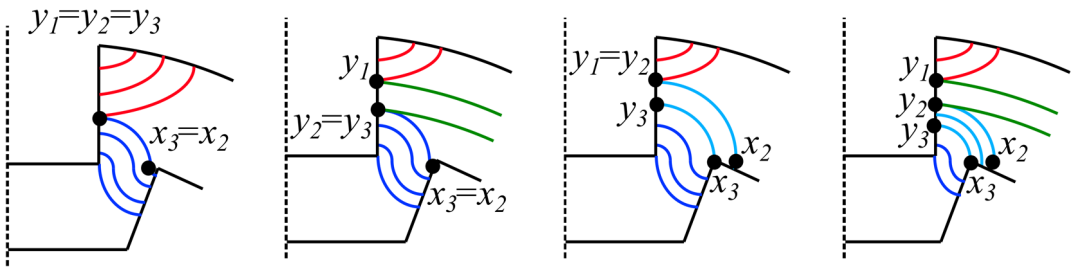

Figure 6-20 Possible stator outlooks with respect of its right-hand-side tubes at θ_2 a) short and wide-gapped, b) tall and wide-gapped c) short and narrow-gapped and d) tall and narrow-gapped

introduced to describe the absence/presence of paths m_{right_II}.

To understand to which case the SR machine at hand belongs to, side tubes lines length shall be compared. To simplify this procedure, the magnetising lines are considered as a single, piecewise expression $l_{m\_right\_\theta 2}$, as shown in (6-82) below, where y_{mI_mII} is the point where lines m_{right_I} turns to m_{right_II}. In other terms, the x-semi-axis of the ellipses is $l_{g\_right\_x\_\theta 2}$.

$$\begin{cases} l_{m\_right\_\theta 2}\left(y_{side}\right) = \begin{cases} l_{mI\_right\_\theta 2}^{\ s}\left(y_{side}\right) + l_{mI\_right\_\theta 2}^{\ r}\left(y_{side}\right) & y_{side} \le y_{mI\_mI\_\theta 2} \\ l_{mII\_right\_\theta 2}^{\ s}\left(y_{side}\right) + l_{mII\_right\_\theta 2}^{\ r}\left(y_{side}\right) & y_{side} > y_{mI\_mII\_\theta 2} \end{cases} \\ y_{mI\_mII\_\theta 2} = \dfrac{\left(l_{g\_right\_x\_\theta 2}\right)^2}{\left(l_{g\_right\_y\_\theta 2} - \dfrac{l_g}{2}\right)\varepsilon_m + \left(l_{g\_right\_x\_\theta 2}\right)} + \left(l_{g\_right\_y\_\theta 2} - \dfrac{l_g}{2}\right) \end{cases} . \tag{6-82}$$

Then, the following three points along the stator tooth side are to be defined:

- y_{lI_lII}, when the length of leakage paths l_I and l_{II} is equal, whose expression is position-independent and is already provided in (6-19);
- $y_{lI\_m\_right\_\theta 2}$, when the length of l_I and m_{right} equal each other;

$$y_{lI\_m\_right\_\theta 2} = \left\{ sol : \left(l_{m\_right\_\theta 2}(y_{side}) = l_{lI}(y_{side}) \right) \right\}. \tag{6-83}$$

- $y_{lII\_m\_right\_\theta 2}$, when the length of l_{II} and m_{right} equal each other;

$$y_{lII\_m\_right\_\theta 2} \left\{ sol : \left(l_{m\_right\_\theta 2}(y_{side}) = l_{lII}(y_{side}) \right) \right\}. \tag{6-84}$$

Since the $l_{m\_right\_\theta 2}$ is a piecewise expression, the closed-form analytical solutions of (6-83) and (6-84) are not straightforward and hence are not reported in this thesis.

The four cases are discussed below.

SHORT AND WIDE-GAPPED STATOR

This scenario is described mathematically by the following condition.

$$y_{mI\_mII\_\theta 2} < y_{lI\_m\_right\_\theta 2}. \tag{6-85}$$

Then, $y_{1\_right\_\theta 2}$, $y_{2\_right\_\theta 2}$ and $y_{3\_right\_\theta 2}$ that are required to derive the inductance contributions along the right hand side are as follows:

$$y_{1\_right\_\theta 2} = y_{2\_right\_\theta 2} = y_{3\_right\_\theta 2} = y_{lI\_m\_right\_\theta 2}. \tag{6-86}$$

TALL AND WIDE-GAPPED STATOR

Expression (6-87) describes the scenario being considered:

$$y_{mI\_mII\_\theta 2} < y_{lI\_m\_right\_\theta 2}. \tag{6-87}$$

In this case, $y_{1\_right\_\theta 2}$, $y_{2\_right\_\theta 2}$ and $y_{3\_right\_\theta 2}$ are expressed as follows:

$$\begin{cases} y_{1\_right\_\theta 2} = y_{lI\_lII} \\ y_{2\_right\_\theta 2} = y_{3\_right\_\theta 2} = y_{lII\_m\_right\_\theta 2} \end{cases}. \tag{6-88}$$

SHORT AND NARROW-GAPPED STATOR

The mathematical condition that describes this geometric configuration is expressed by (6-89).

$$y_{mI\_mII\_\theta 2} > y_{lI\_m\_right\_\theta 2}. \tag{6-89}$$

The corresponding values of $y_{1\_right\_\theta 2}$, $y_{2\_right\_\theta 2}$ and $y_{3\_right\_\theta 2}$ can be found through (6-90).

$$\begin{cases} y_{1\_right\_\theta 2} = y_{2\_right\_\theta 2} = y_{lI\_m\_right\_\theta 2} \\ y_{3\_right\_\theta 2} = y_{mI\_mII\_right\_\theta 2} \end{cases}. \tag{6-90}$$

TALL AND NARROW-GAPPED STATOR

This scenario is mathematically described by (6-91).

$$y_{mI\_mII\_\theta 2} > y_{lII\_m\_right\_\theta 2} > y_{lI\_m\_right\_\theta 2}. \tag{6-91}$$

Values of $y_{1\_right\_\theta 2}$, $y_{2\_right\_\theta 2}$ and $y_{3\_right\_\theta 2}$ are as given below:

$$\begin{cases} y_{1\_right\_\theta 2} = y_{lI\_lII} \\ y_{2\_right\_\theta 2} = y_{lII\_m\_right\_\theta 2} \\ y_{3\_right\_\theta 2} = y_{mI\_mII\_right\_\theta 2} \end{cases}. \tag{6-92}$$

Since $y_{1\_right\_\theta 2}$, $y_{2\_right\_\theta 2}$ and $y_{3\_right\_\theta 2}$ are now available, it is possible to finalise the inductance contributions provided by the stator-right-edge paths.

Firstly, leakage contributions $\Psi_{lI\_right\_\theta 2}$ and $\Psi_{lII\_right\_\theta 2}$ are found by (6-93).

$$\begin{aligned} \Psi_{lI\_right\_\theta 2} &= \int_{0}^{y_{1\_right\_\theta 2}} d\Psi_{lI}\left(y_{side}\right) \\ \Psi_{lII\_right\_\theta 2} &= \int_{y_{1\_right\_\theta 2}}^{y_{2\_right\_\theta 2}} d\Psi_{lII}\left(y_{side}\right) \end{aligned}. \tag{6-93}$$

Secondly, the two magnetising inductance contributions from m_{right_I} and m_{right_II} are determined.

By observing the geometrical configuration, one notes that for both stator permeances at hand $P_{mI\_right\_\theta 2}^{s}$ and $P_{mII\_right\_\theta 2}^{s}$ the mathematical expression given in (6-62) can be used. However, integration bounds must be adjusted. To this end, as the permeances are formulated with respect of the horizontal coordinate x, points $x_{2\_right\_\theta 2}$

and $x_{3\_right\_\theta 2}$, which correspond to $y_{2\_right\_\theta 2}$ and $y_{3\_right\_\theta 2}$ along the mid-airgap surface are found:

$$x_{2\_right\_\theta 2}=\frac{1}{2}\left(h_{st}-y_{2\_right\_\theta 2}+\sqrt{\left(h_{st}-y_{2\_right\_\theta 2}\right)^2+2\varepsilon_m l_g\left(h_{st}-y_{2\_right\_\theta 2}\right)}\right). \tag{6-94}$$

$$x_{3\_right\_\theta 2}=\frac{1}{2}\left(h_{st}-y_{3\_right\_\theta 2}+\sqrt{\left(h_{st}-y_{3\_right\_\theta 2}\right)^2+2\varepsilon_m l_g\left(h_{st}-y_{3\_right\_\theta 2}\right)}\right). \tag{6-95}$$

Finally, $P_{mI\_right\_\theta 2}{}^s$ and $P_{mII\_right\_\theta 2}{}^s$ are expressed by (6-96) and (6-97) respectively. In order to keep a consistent notation, $x_{2\_right\_\theta 2}$ is the outermost integration bound.

$$\mathfrak{P}_{mI\_right\_\theta 2}{}^s=\frac{2}{\pi}\mu_0 L_{stk}\left[\ln\left(x+\varepsilon_m\frac{l_g'}{2}\right)+\ln\left(x^2+x\frac{l_g'}{4}\left(1+\varepsilon_m\right)+\frac{l_g'^2}{8}\right)\right]\Bigg|_0^{x_{3\_right\_\theta 2}}. \tag{6-96}$$

$$l_g'=l_{g\_right\_y}$$

$$\mathfrak{P}_{mII\_right\_\theta 2}{}^s=\frac{2}{\pi}\mu_0 L_{stk}\left[\ln\left(x+\varepsilon_m\frac{l_g'}{2}\right)+\ln\left(x^2+x\frac{l_g'}{4}\left(1+\varepsilon_m\right)+\frac{l_g'^2}{8}\right)\right]\Bigg|_{x_{3\_right\_\theta 2}}^{x_{2\_right\_\theta 2}}. \tag{6-97}$$

$$l_g'=l_{g\_right\_y}$$

Rotor tubes m_{right_I} are nothing else than the continuation of lines m_{front_III}. Hence, $P_{mI\_right\_\theta 2}{}^r$ is given by (6-76) with different integral bounds. To keep the expression complexity at its lowest, the reference frame considered for m_{front_III} is maintained.

$$\mathfrak{P}_{mI\_right\_\theta 2}{}^r=\int_{\frac{D_s}{2}\beta_{st}}^{\frac{D_s}{2}\beta_{st}+x_{3\_right\_\theta 2}} d\mathfrak{P}_{mIII\_front\_\theta 2}{}^r. \tag{6-98}$$

Rotor tubes m_{right_II} have the same configuration as rotor tubes m_{left}. However, some adjustments are required. Bearing in mind the approximation that tubes length is given by the difference between a 90° ellipse and a circle, this time the angle that the circle spans is now $\pi/2-\zeta_r+\theta_2$., as illustrated in Figure 6-19. Moreover, the airgap to consider is now:

$$l_g'=l_{g\_right\_y\_\theta 2}-\frac{l_g}{2}.$$

The integral bounds must be changed. The resulting expression is provided in (6-99).

$$\mathfrak{P}_{mII\_right\_\theta 2}{}^r=\int_0^{x_{2\_right\_\theta 2}-l_{g\_right\_x\_\theta 2}} d\mathfrak{P}_{m\_left\_\theta 2}{}^r\Bigg|_{\substack{\Delta\theta=\frac{\pi}{2}-\zeta_r+\theta_2\\ l_g'=l_{g\_right\_y\_\theta 2}-\frac{l_g}{2}}}. \tag{6-99}$$

Finally, the inductance contributions provided by the right-side magnetising paths are given by (6-100) and (6-101) below:

$$L_{mI\_right\_\theta 2} = N^2 \mathfrak{P}_{mI\_right\_\theta 2} = N^2 \left(\mathfrak{P}_{mI\_right\_\theta 2}{}^{s} \,//\, \mathfrak{P}_{mI\_right\_\theta 2}{}^{r} \right). \tag{6-100}$$

$$L_{mII\_right\_\theta 2} = N^2 \mathfrak{P}_{mII\_right\_\theta 2} = N^2 \left(\mathfrak{P}_{mII\_right\_\theta 2}{}^{s} \,//\, \mathfrak{P}_{mII\_right\_\theta 2}{}^{r} \right). \tag{6-101}$$

6.2.5.4 INDUCTANCE L_2

As all the inductance contributions have been determined, (6-1) is now applied to sum all of them up and attain the inductance L_2. Leakage contributions are given by (6-59) and (6-93), for the left and right side edges respectively. The phase current i_{ph} is set to 1A, assuming that with this value core saturation does not occur.

$$L_{l\_right\_\theta 1} = \left(\frac{\Psi_{lI\_right\_\theta 1}}{i_{ph}} + \frac{\Psi_{lII\_right\_\theta 1}}{i_{ph}} \right)\Bigg|_{i_{ph}=1}$$

$$L_{l\_left\_\theta 1} = \left(\frac{\Psi_{lI\_left\_\theta 1}}{i_{ph}} + \frac{\Psi_{lII\_left\_\theta 1}}{i_{ph}} \right)\Bigg|_{i_{ph}=1}.$$

Side magnetising contributions are expressed by: (6-60) for the left-hand side and (6-100)-(6-101) for the right-hand side:

$$L_{m\_left\_\theta 2} = L_{mI\_right\_\theta 2} + L_{mII\_right\_\theta 2}.$$

Front magnetising contribution is given by the sum of (6-73), (6-74) and (6-75), as shown below:

$$L_{front\_\theta 2} = L_{mI\_front\_\theta 2} + L_{mII\_front\_\theta 2} + L_{mIII\_front\_\theta 2}.$$

Finally, L_2 can be found by (6-102).

$$L(\theta_2) = L_2 = L_{l\_left\_\theta 2} + L_{m\_left\_\theta 2} + L_{front\_\theta 2} + L_{m\_right\_\theta 2} + L_{l\_right\_\theta 2}. \tag{6-102}$$

6.2.6 θ_U

At the maximum misalignment position θ_u, the magnetising tubes outlook is illustrated in Figure 6-21. Due to the geometrical symmetry, subscript 'side' stands for both right and left. Tubes geometry is discussed below:

- m_{front_I}: made by a stator straight line, leading from the stator front surface to the rotor yoke.
- m_{front_II}: made by a straight line connecting the stator front surface to the rotor yoke.
- m_{front_III}: made by a straight segment up to the mid-airgap surface and an elliptical line closing up to the rotor's right tooth side.
- m_{side_I}: made by a stator elliptic line leading from the stator side surface to the mid-airgap, and the rotor elliptic line closing up to the rotor's right tooth side.

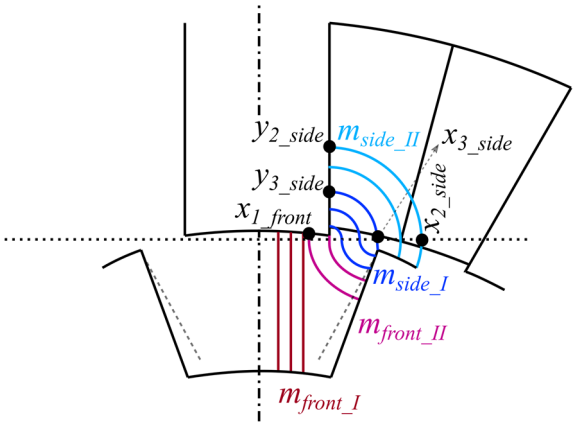

Figure 6-21 Magnetising tubes at θ_u.

- m_{side_II}: made by a stator elliptic line leading from the stator side surface to the mid-airgap, and the rotor elliptic line closing up to the rotor's front surface.

It can be noted that tubes geometry is identical to the right-side edge at position θ_2. Indeed, results attained in this subsection are a just simplification of the expressions developed for the previous rotor position.

6.2.6.1 MAGNETISING TUBES M_{SIDE_I} AND M_{SIDE_II}

To begin with, the outermost magnetising path m_{side_II} is taken into account. As opposed to the position θ_2, this time it is reasonable to assume that these magnetising paths do exist regardless of the machine geometry. In fact, in all SR machines of engineering interest, the corner-to-corner distance at maximum misalignment, i.e. $l_{g\_u\_x\_\theta u}$, is small enough to justify this assumption.

The lines' geometry is represented in Figure 6-22. Stator ellipses have their centre in O^s, whilst rotor ellipses in O^r. Line length $l_{mII\_side\_\theta u}$ is given by the sum of the stator and rotor contributions, $l_{mII\_side\_\theta u}{}^s$ and $l_{mII\_side\_\theta u}{}^r$ respectively:

$$l_{mII\_side\_\theta u}(y_{side}) = l_{mII\_side\_\theta u}{}^{s}(y_{side}) + l_{mII\_side\_\theta u}{}^{r}(y_{side}) . \tag{6-103}$$

Expressions with respect to y_{side} are provided in (6-104) and (6-105). As the path length is now available, it can be compared with that of the leakage lines to derive $y_{1\_\theta u}$

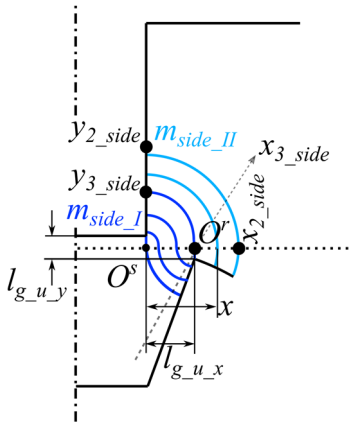

Figure 6-22 Geometry at θ_u, tube paths m_{side_II} and m_{side_II}.

and $y_{2\_\theta u}$, in order to define the leakage contributions. To this end, points $y_{lI\_m\_side\_\theta u}$ and $y_{lII\_m\_side\_\theta u}$ where m_{side_II} length equals that of the leakage paths l_I and l_{II} are required. Due to their complexity, their closed-form expressions are not reported in this thesis.

$$\begin{cases} l_{mII\_side\_\theta u}{}^{s}(y_{side}) = \dfrac{\pi}{4}\left(\Gamma_{x\_mII\_side\_\theta u}{}^{s}(x) + \Gamma_{y\_mII\_side\_\theta u}{}^{s}(x)\right) \\ \Gamma_{x\_mII\_side\_\theta u}{}^{s}(y_{side}) = \dfrac{1}{2}\left(h_{st} - y_{side} + \sqrt{(h_{st} - y_{side})^2 + 2\varepsilon_m l_{g\_u\_y}(h_{st} - y_{side})}\right) \\ \Gamma_{y\_mII\_side\_\theta u}{}^{s}(y_{side}) = (h_{st} - y_{side}) \end{cases} . \quad (6\text{-}104)$$

$$\begin{cases} l_{mII\_side\_\theta u}{}^{r}(y_{side}) = \dfrac{\pi}{4}\left(\Gamma_{x\_mII\_side\_\theta u}{}^{r}(y_{side}) + \Gamma_{y\_mII\_side\_\theta u}{}^{r}(y_{side})\right) - \\ \qquad -\left(\dfrac{\pi}{2} - \theta_u\right)\left(\Gamma_{y\_mII\_side\_\theta u}{}^{r}(y_{side}) - \dfrac{l_{g\_u\_y}}{2}\right) \\ \Gamma_{x\_mI\_side\_\theta u}{}^{r}(y_{side}) = \Gamma_{x\_mII\_side\_\theta u}{}^{s}(y_{side}) - l_{g\_u\_x} \\ \Gamma_{y\_mII\_side\_\theta u}{}^{r}(y_{side}) = \dfrac{\left(\Gamma_{x\_mI\_side\_\theta u}{}^{r}(y_{side})\right)^2}{\varepsilon_m \dfrac{l_{g\_u\_y}}{2} + \Gamma_{x\_mI\_side\_\theta u}{}^{r}(y_{side})} + \dfrac{l_{g\_u\_y}}{2} \end{cases} . \quad (6\text{-}105)$$

$$y_{lI\_m\_side\_\theta u} = \left\{ sol : \left(l_{mII\_side\_\theta u}(y_{side}) = l_{lI}(y_{side})\right)\right\} . \quad (6\text{-}106)$$

$$y_{lII\_m\_side\_\theta u} = \left\{ sol : \left(l_{mII\_side\_\theta u}(y_{side}) = l_{lII}(y_{side})\right)\right\} . \quad (6\text{-}107)$$

Likewise the previous positions, conditions (6-20) and (6-21) are checked and $y_{1\_\theta u}$ and $y_{2\_\theta u}$ are finally attained. Leakage contributions $\Psi_{lI\_side\_\theta u}$ and $\Psi_{lII\_side\_\theta u}$ are found by (6-108).

$$\begin{aligned} \Psi_{lI\_side\_\theta u} &= \int_{0}^{y_{1\_\theta u}} d\Psi_{lI}(y_{side}) \\ \Psi_{lII\_side\_\theta u} &= \int_{y_{1\_\theta u}}^{y_{2\_\theta u}} d\Psi_{lII}(y_{side}) \end{aligned} . \quad (6\text{-}108)$$

To undertake the permeance determination, the similarity with the position θ_2 can be exploited.

Stator permeances, $P_{mI\_side\_\theta u}{}^{s}$ and $P_{mII\_side\_\theta u}{}^{s}$ are derived straightforwardly from respectively (6-96) and (6-97) developed in Subsection 6.2.5.3, by simply updating l_g':

$$\begin{cases} \mathfrak{P}_{mI\_side\_\theta u}{}^{s} = \dfrac{2}{\pi}\mu_0 L_{stk}\left[\ln\left(x + \varepsilon_m \dfrac{l_g'}{2}\right) + \ln\left(x^2 + x\dfrac{l_g'}{4}(1+\varepsilon_m) + \dfrac{l_g'^2}{8}\right)\right]_0^{l_{g\_u\_x\_\theta u}} \\ l_g' = l_{g\_u\_y} \end{cases} . \quad (6\text{-}109)$$

$$\mathfrak{P}_{mII\_side\_\theta u}{}^{s}=\frac{2}{\pi}\mu_0 L_{stk}\left[\ln\left(x+\varepsilon_m\frac{l_g{}'}{2}\right)+\ln\left(x^2+x\frac{l_g{}'}{4}\left(1+\varepsilon_m\right)+\frac{l_g{}'^2}{8}\right)\right]\Bigg|_{l_{g\_u\_x\_\theta u}}^{x_{2\_side\_\theta u}}. \tag{6-110}$$

$$l_g{}'=l_{g\_u\_y}$$

The missing integration bound $x_{2\_side\_\theta u}$ is found from $y_{2\_\theta u}$:

$$x_{2\_side\_\theta u}=\frac{1}{2}\left(h_{st}-y_{2\_\theta u}+\sqrt{\left(h_{st}-y_{2\_\theta u}\right)^2+2\varepsilon_m l_g\left(h_{st}-y_{2\_\theta u}\right)}\right). \tag{6-111}$$

The rotor contributions $P_{mI\_side\_\theta u}{}^{r}$ and $P_{mII\_side\_\theta u}{}^{r}$ are now considered. Due to the geometrical similarity, the infinitesimal permeance expressions given in (6-98) and (6-99) can be used. However, some adjustments are required to suit the maximum misalignment condition, which are shown below:

$$\mathfrak{P}_{mI\_side\_\theta u}{}^{r}=\int_{\frac{D_s}{2}\beta_{st}}^{\frac{D_s}{2}\beta_{st}+l_{g\_u\_x\_\theta u}} d\mathfrak{P}_{mIII\_front\_\theta 2}{}^{r}\Bigg|_{\substack{\Delta\theta=\zeta_r-\theta_u-\beta_{re}\\ l_g{}'=\frac{l_{g\_u\_y\_\theta u}}{2}}}. \tag{6-112}$$

$$\mathfrak{P}_{mII\_side\_\theta u}{}^{r}=\int_{0}^{x_{2\_side\_\theta 2}-l_{g\_u\_x\_\theta 2}} d\mathfrak{P}_{m\_left\_\theta 2}{}^{r}\Bigg|_{\substack{\Delta\theta=\frac{\pi}{2}-\zeta_r+\theta_u\\ l_g{}'=\frac{l_{g\_right\_y\_\theta u}}{2}}}. \tag{6-113}$$

Finally, the corresponding side-edge inductance contributions can be found via (6-114) and (6-115).

$$L_{mI\_side\_\theta u}=N^2\mathfrak{P}_{mI\_side\_\theta u}=N^2\left(\mathfrak{P}_{mI\_side\_\theta u}{}^{s}//\mathfrak{P}_{mI\_side\_\theta u}{}^{r}\right). \tag{6-114}$$

$$L_{mII\_side\_\theta u}=N^2\mathfrak{P}_{mII\_side\_\theta u}=N^2\left(\mathfrak{P}_{mII\_side\_\theta u}{}^{s}//\mathfrak{P}_{mII\_side\_\theta u}{}^{r}\right). \tag{6-115}$$

6.2.6.2 MAGNETISING TUBES M_{FRONT_I} AND M_{FRONT_II}

Due to the geometrical symmetry, only two front paths might exist at maximum misalignment. Both are illustrated in Figure 6-23. To begin with, their length is defined.

For paths m_{front_I}, as it has been discussed for position θ_2, the length can be assumed to be equal to the rotor tooth height h_{rt}:

For paths m_{front_II}, the stator stretch length IS equal to half the y component of the unaligned airgap. On the other hand, rotor stretches are observed to have the same geometry as the front paths m_{front_III} at θ_2. Therefore, their length expression is found by rearranging (6-67):

$$l_{mI\_front\_\theta u}(x)\cong h_{rt}. \tag{6-116}$$

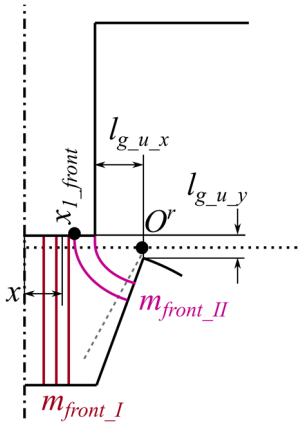

Figure 6-23 Geometry at θ_u, tube paths m_{front_I} and m_{front_II}.

$$\begin{cases} l_{mII\_front\_\theta u}(t(x)) = l_{mII\_front\_\theta u}{}^{s} + l_{mII\_front\_\theta u}{}^{r}(t(x)) = \\ = l_g' + \frac{\pi}{4}\left(t + \frac{t^2}{l_g'\varepsilon_m + t} + l_g'\right) - (\zeta_r - \theta_u - \beta_{re})\left(\frac{t^2}{l_g'\varepsilon_m + t}\right) \\ t(x) = \left(l_{g\_u\_x\_\theta u} + \frac{D_s}{2}\beta_{st} - x\right) \\ l_g' = \frac{l_{g\_u\_y\_\theta u}}{2} \end{cases} \quad (6\text{-}117)$$

The comparison of the lengths expressed in (6-116) and (6-117) is needed to verify the existence/absence of paths m_{front_I}. In fact, two cases are possible, namely a 'tall-toothed' rotor, where paths m_{front_I} do not exist, or a 'short-toothed' rotor, if paths m_{front_I} do exist. A short-toothed rotor is shown in Figure 6-23. An example of a tall-toothed rotor is depicted in Figure 6-24.

Observation: In this case, terms short and tall have been used relatively to the specific position θ_u. Absolute terms are related to the worst case scenario represented by position θ_2.

To understand which case the SR machine at hand belongs to it is sufficient to calculate the intersection $x_{mI\_II\_front\_\theta u}$ between the expressions (6-116) and (6-117):

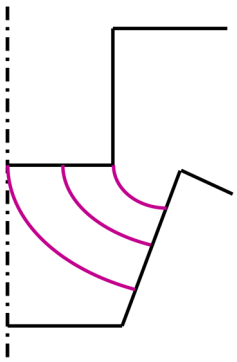

Figure 6-24 Example of tall-toothed rotor at θ_u.

$$\begin{cases} x_{mI\_II\_front\_\theta u} = l_{g\_u\_x\_\theta u} + \dfrac{D_s}{2}\beta_{st} + \dfrac{B+\sqrt{B^2-4AC}}{2A} \\ A = \dfrac{\pi}{2} - \left(\zeta_r - \theta_u - \beta_{re}\right) \\ B = \dfrac{\pi}{8} l_{g\_u\_y\_\theta u}\left(1+\varepsilon_m\right) - \left(h_{st} - \dfrac{l_{g\_u\_y\_\theta u}}{2}\right) \\ C = \varepsilon_m \dfrac{l_{g\_u\_y\_\theta u}}{2}\left(\dfrac{\pi}{8} l_{g\_u\_y\_\theta u} - \left(h_{st} - \dfrac{l_{g\_u\_y\_\theta u}}{2}\right)\right) \end{cases} . \tag{6-118}$$

This intersection is needed to attain the position $x_{1\_front\_\theta u}$ where paths turns from m_{front_I} to m_{front_II}.

TALL-TOOTHED ROTOR

This case occurs when $x_{mI\_II\_front\_\theta u}$ does not belong to the stator front surface. Mathematically, the condition is described as follows:

$$x_{mI\_II\_front\_\theta u} \notin \left(0, \frac{D_s}{4}\beta_{st}\right). \tag{6-119}$$

Then, $x_{1\_front\_\theta u}$ is simply set to zero to indicate the non-existence of paths m_{front_I}.

SHORT-TOOTHED ROTOR

This case verifies for $x_{mI\_II\_front\_\theta u}$ falling onto the stator front surface. The mathematically condition to be verified is (6-120).

$$x_{mI\_II\_front\_\theta u} \in \left(0, \frac{D_s}{4}\beta_{st}\right). \tag{6-120}$$

Then, $x_{1\_front\_\theta u}$ is equal to $x_{mI\_II\_front\_\theta u}$.

Magnetising contributions given by the front flux paths are now considered. Once again, formulas developed for position θ_2 in Subsection 6.2.5.2 can be reused, by adjusting some parameters:

$$\begin{cases} \mathrm{P}_{mI\_front\_\theta u} \cong \mu_0 \dfrac{L_{stk} x_{1\_front\_\theta u}}{h_{rt}} \\ L_{mI\_front\_\theta u} = N^2 \mathrm{P}_{mI\_front\_\theta u} \end{cases} . \tag{6-121}$$

6.2.6.3 UNALIGNED INDUCTANCE L_U

From the equations derived in Subsections 6.2.6.1 and 6.2.6.2, the unaligned inductance L_u is derived by means of (6-1).

Leakage contributions are expressed in (6-108), where a 1A current is considered. This value is assumed to be low enough not to induce saturation in the magnetic core.

$$L_{l\_left\_\theta u} = L_{l\_right\_\theta u} = \left(\frac{\Psi_{lI\_side\_\theta u}}{i_{ph}} + \frac{\Psi_{lII\_side\_\theta u}}{i_{ph}}\right)\Bigg|_{i_{ph}=1} .$$

Side magnetising contributions are expressed by (6-114) and (6-115):

$$L_{m\_left\_\theta u} = L_{m\_right\_\theta u} = L_{mI\_side\_\theta u} + L_{mII\_side\_\theta u}.$$

$$\begin{cases} dP_{mII\_front\_\theta u}{}^{r}(x) = dP_{mIII\_front\_\theta 2}{}^{r}(t(x)) \Big| \begin{matrix} t(x)=l_{g\_u\_x\_\theta u}+\frac{D_s}{2}\beta_{st}-x \\ l_g{}'=\frac{l_{g\_u\_x\_\theta u}}{2} \\ \Delta\theta=\zeta r-\theta_u-\beta_{re} \end{matrix} \\ P_{mII\_front\_\theta u} = P_{mII\_front\_\theta u}{}^{s} \,//\, P_{mII\_front\_\theta u}{}^{r} = \\ = \left(\mu_0 \dfrac{L_{stk}(\frac{D_s}{2}\beta_{st} - x_{2\_front\_\theta u})}{h_{rt}} \right) // \left(\int_{x_{2\_front\_\theta u}}^{\frac{D_s}{2}\beta_{st}} dP_{mII\_front\_\theta u}{}^{r} \right) \\ L_{mII\_front\_\theta u} = N^2 P_{mII\_front\_\theta u} \end{cases} . \quad (6\text{-}122)$$

Due to the geometrical symmetry, front magnetising contributions are provided by two times the sum of (6-121) and (6-122). Eq. (6-123) expresses the final formula.

$$L_{front\_\theta u} = 2\left(L_{mI\_front\_\theta u} + L_{mII\_front\_\theta u}\right).$$

$$L(\theta_u) = L_u = L_{l\_left\_\theta u} + L_{m\_left\_\theta u} + L_{front\_\theta u} + L_{m\_right\_\theta u} + L_{l\_right\_\theta u}. \quad (6\text{-}123)$$

6.3 VALIDATION

This Subsection is devoted to the validation of the analytical model presented above. Bearing in mind that the method's objective is to estimate L_a, L_1, L_2 and L_u, for ideally any possible SR machine geometry, the validation is conducted against the experimentally-validated FEA models of the SR prototypes described in Chapter 4.

The proposed elliptical-shaped flux tubes are compared against the real flux paths attained via FEA from Figure 6-25 to Figure 6-27. Each figure illustrates the flux tubes' paths for both prototypes at a given rotor position.

At all of the four positions, the predicted SRMyld's flux-tubes shapes are quite similar to the real ones, including the points along the stator tooth side and front edges where flux tubes turn from one group to another. On the other hand, SRFly's real leakage tubes show a highly irregular and hence unpredictable behaviour. This is due to the fact that the stator tooth height is dramatically smaller that the slot width, along with the tapered rotor teeth. The most significant flux tubes, i.e. the shortest ones, remain well-predicted, so that inductance estimation accuracy remains ensured.

Overall, given the limitations in considering predefined flux tubes, similarity achieved between analytical and FEA tubes shapes is more than acceptable, which demonstrates the flexibility of the proposed model to remap the tubes shape in accordance with the SR machine geometry.

Finally, Table 6-II compares the analytical estimations of the four inductances against FEA results. As expected, passing the greatest amount of flux through the front of the facing teeth pair, prediction of the main flux path is straightforward and hence errors for L_a, L_1 are negligible. When it comes to L_u, an extremely low error is attained for SRMyld, which demonstrates that the implementation of elliptical-shaped flux tubes yields a huge improvement compared to the traditional methods (see Table 6-I). On the other hand, a 10% error is incurred for SRFly. This fact highlights that the proposed elliptical-shaped flux tubes work well for geometries having a wide gap between stator and rotor at the unaligned position, whereas accuracy decreases as this gap reduces. This is due to the simplification proposed in [118] of considering a flux tube's cross section equal to the average value between the cross sections taken along the x-semi-axis and y-semi-axis, as expressed in (6-61). Indeed, it can be demonstrated that this simplification grows in accuracy along with the flux tubes' length.

Table 6-II Analytical and FEA values of L_a, L_1, L_2 and L_u or the two SR prototypes.

	SRMyld			**SRFly**		
	Analytical	**FEA**	**Error (%)**	**Analytical**	**FEA**	**Error (%)**
L_a (mH)	1.507	1.527	-1.31	4.051	3.970	2.04
L_1 (mH)	1.490	1.517	-1.78	4.012	3.953	1.49
L_2 (mH)	0.367	0.393	-6.61	0.742	0.830	-10.60
L_u (mH)	0.253	0.269	-5.95	0.676	0.757	-10.70

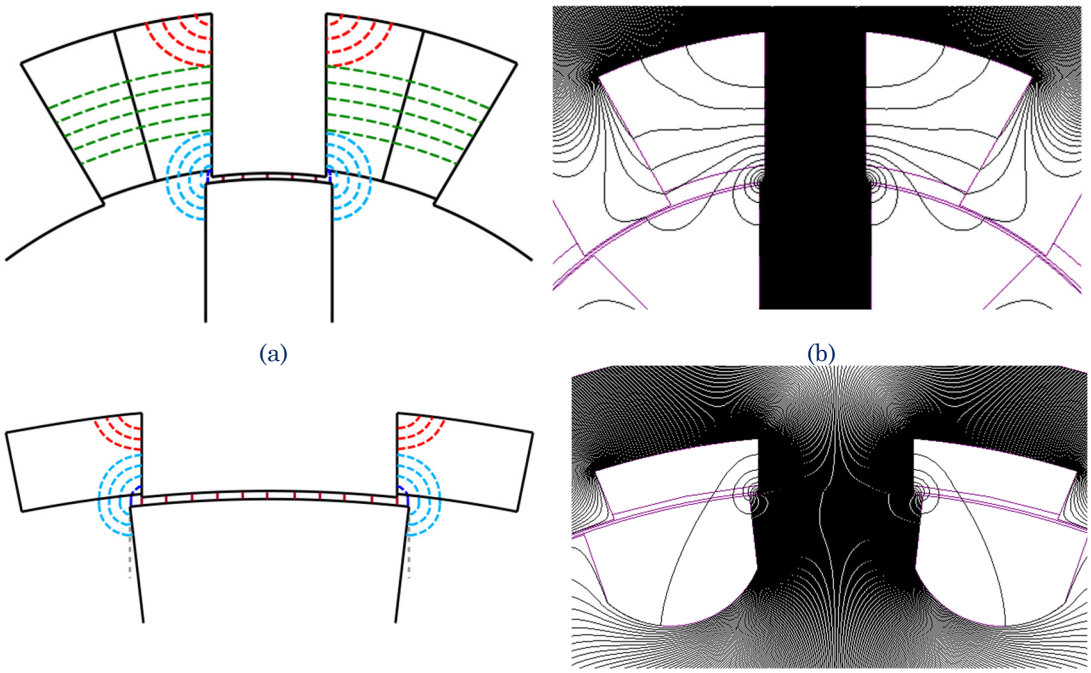

(a) (b)

(c) (d)

Figure 6-25 Flux tubes paths at θ_a: a) SRMyld analytical, b) SRMyld FEA, c) SRFly analytical and d) SRFly FEA.

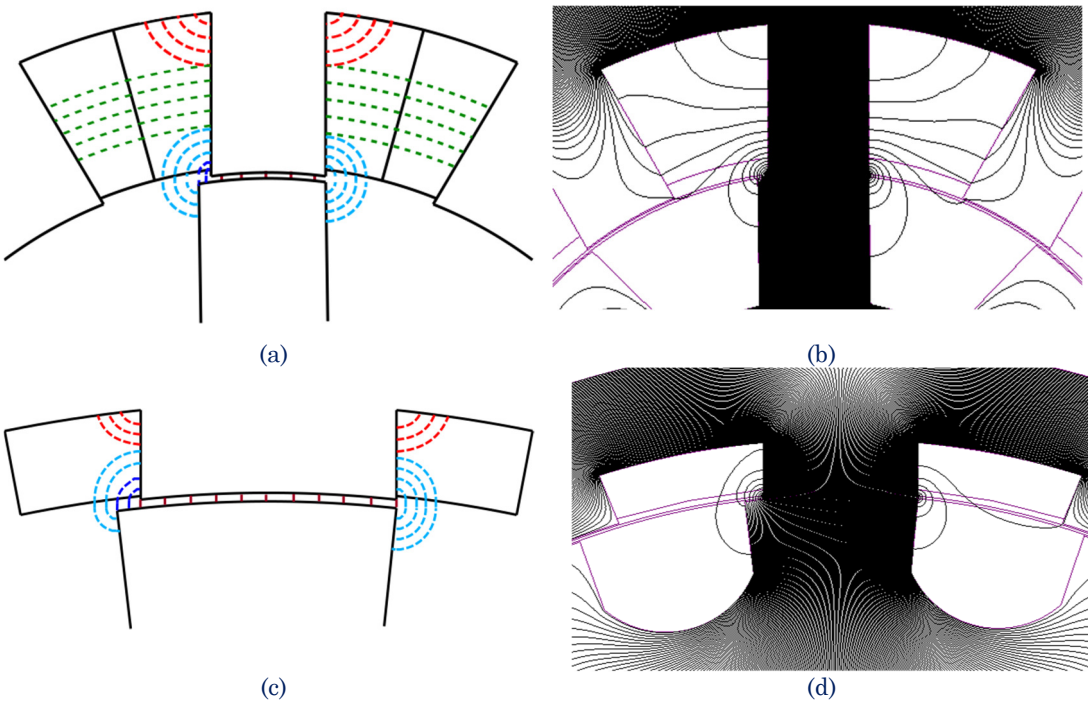

(a) (b)

(c) (d)

Figure 6-26 Flux tubes paths at θ_1: a) SRMyld analytical, b) SRMyld FEA, c) SRFly analytical and d) SRFly FEA.

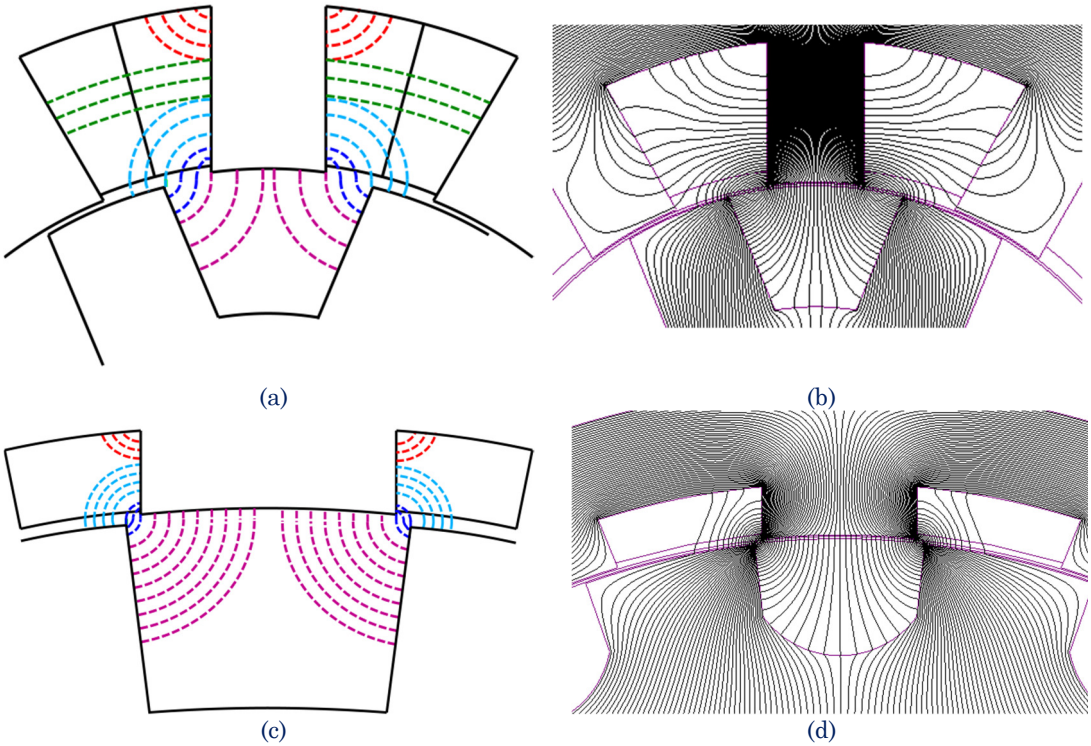

(a) (b)

(c) (d)

Figure 6-27 Flux tubes paths at θ_u: a) SRMyld analytical, b) SRMyld FEA, c) SRFly analytical and d) SRFly FEA.

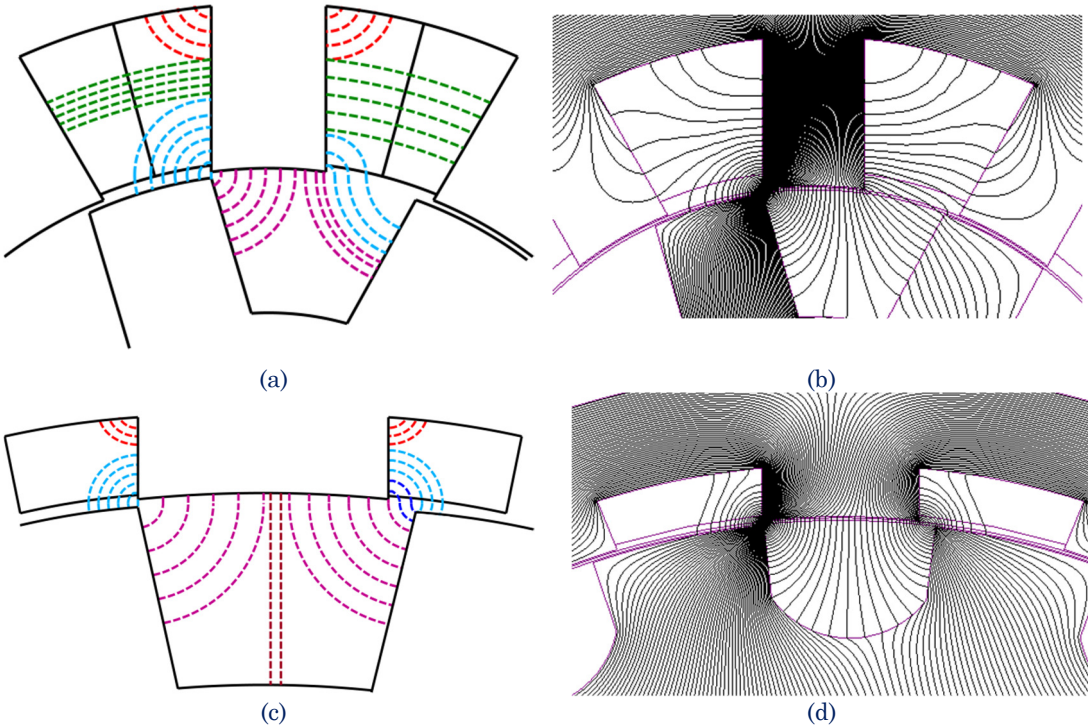

(a) (b)

(c) (d)

Figure 6-28 Flux tubes paths at θ_2: a) SRMyld analytical, b) SRMyld FEA, c) SRFly analytical and d) SRFly FEA.

6.4 CONCLUSION

This Chapter proposed an analytical model to derive L_a, L_1, L_2 and L_u, which are needed to reconstruct the unsaturated inductance profile described in Subsection 5.3.1.3. Accuracies attained are almost perfect for L_a and L_1, whereas, as expected, it varies from approximately 5% to 10% when the maximum misalignment is considered. As an average error lower than traditional methods is incurred, the proposed method is preferable for the ADS generation process. In fact, a more uniformly distributed error across the entire ADS is achieved, which yields a more uniform ADS clearance δ_{ADS}.

In future work, the two model's limitations highlighted in the validation will be addressed. In particular, the simplification concerned with the tubes' cross section expressed in (6-61) will be removed, even at the price of a much more complex mathematical formulation. Once these tasks are accomplished, the content of this Chapter will be the subject of future publications.

Finally, it is Author's opinion that the historical use of straight lines and circular arcs to model the machine's flux tubes has been so widely investigated that no room for improvement is left. On the other hand, despite the limitations highlighted above, the proposed approach based on elliptical flux lines possesses the potential to provide more accurate results compared to the historical methods by maintaining a relatively small implementation effort. Therefore, it is worthwhile to carry on with its investigation.

7 ANALYTICAL THERMAL MODELLING OF THE SR MACHINE FOR ADS DETERMINATION

Thermal modelling developed to build up the SR machine ADS is discussed in this Chapter. The main challenge lies in the definition of the convection factors that determine the heat that active and inactive components exchange with internal and external air. Several models available in the literature have been gathered and implemented in this Chapter, even though some adjustments have been necessary, since most of the models have been originally developed for other electrical machine classes.

7.1 SR MACHINE EQUIVALENT THERMAL NETWORK

As discussed in Chapter 3, the SR machine can be subdivided into ten thermal subdomains, that are:

1. Housing or Frame,
2. Stator Yoke,
3. Stator Teeth,
4. Stator Slots,
5. End-windings,
6. Airgap,
7. End-Caps air,
8. Rotor Teeth,
9. Rotor Yoke,
10. Shaft.

As already pointed out in Chapter 3, tests conducted on the SRMyld prototype showed that the temperature distribution is considerably influenced by the mounting flange, which is necessary for obvious practical reasons. However, including the flange in the analytical model would require a dramatic change in the LPTN topology, since temperature distribution would no longer be axisymmetric. From the design

perspective, the machine's mounting architecture, and hence the amount of heat that can be rejected through it, depends on the specific installation site. Therefore, it is perfectly reasonable to account for a mounting system within the model, by introducing a thermal boundary condition, i.e. setting the end-plate temperature.

To this cause, the LPTN shown in Figure 3-12 of Chapter 3 is slightly modified. The topology of the new equivalent thermal network is illustrated in Figure 7-1. As it can be noted, the network is constructed so that the two main heat exchange directions are easily identified: moving from top to bottom is equivalent to moving from the machine housing towards the machine centre along the radial direction, whereas moving from left to right indicates that one is moving from the housing towards the centre along the axial direction. Figure 7-1 also highlights the end-plate subnetwork, which is composed of the following components: 1) an ideal voltage source indicating the end-plate temperature rise $\Delta\Theta_{ep}$, 2) contact resistance between end-plate and housing R_{ep_fr}, which is modelled as a $0.005mm$ air-layer, 3) end-plate-to-ambient convective resistance R_{ep_amb} and 4) convective resistance between end-cap air and end-plate $R_{ec,r,a}$.

7.1.1 NETWORK SOLUTION

Thirty-eight resistances, six power injections and fifteen nodes define the equivalent thermal network. As power is injected by ideal current source components, the most convenient solution strategy is through the node potential method. Recalling what said in Chapter 3, the node potential method results in the matrix relationship (3-23), which is also reported below:

$$[\Delta\Theta] = [C]^{-1}[P]. \tag{7-1}$$

$[\Delta\Theta]$ is the 15-element column vector containing the node temperatures. $[C]$ is the 15x15 matrix containing the nodal conductances. Diagonal elements C_{xx} represent the sum of all of the thermal conductances connected to node x. Non-diagonal elements C_{xy} are negative and indicate the overall conductance between nodes x and y. Finally, $[P]$ is the 15-element column vector containing the six power injections, i.e.:

- P_{sy} for stator yoke iron loss,
- P_{st} for stator teeth iron loss,
- P_{ss} for stator slot copper loss,
- P_{ew} for end-winding copper loss,
- P_{rt} for rotor teeth iron loss,
- P_{ry} for rotor yoke iron loss.

7.2 CONVECTIVE HEAT TRANSFER THERMAL RESISTANCES

Convection heat transfer is the process concerned with in fluids in motion. Natural and forced convection heat exchanges are possible. In natural convection, fluid motion is caused entirely by buoyance forces generated from density gradients inside the fluid.

On the other hand, in forced convection, fluid motion is imposed by an external force, such as pump or a blower.

Convection heat transfer has been historically described through empirical, or semi-empirical relationships based on a set of dimensionless parameters. Dimensionless parameters involved in the convection heat transfer in electrical machines are listed below:

$$\mathrm{Nu} = \frac{\chi L}{\lambda}, \tag{7-2}$$

$$\mathrm{Re} = \frac{\rho v L}{\xi}, \tag{7-3}$$

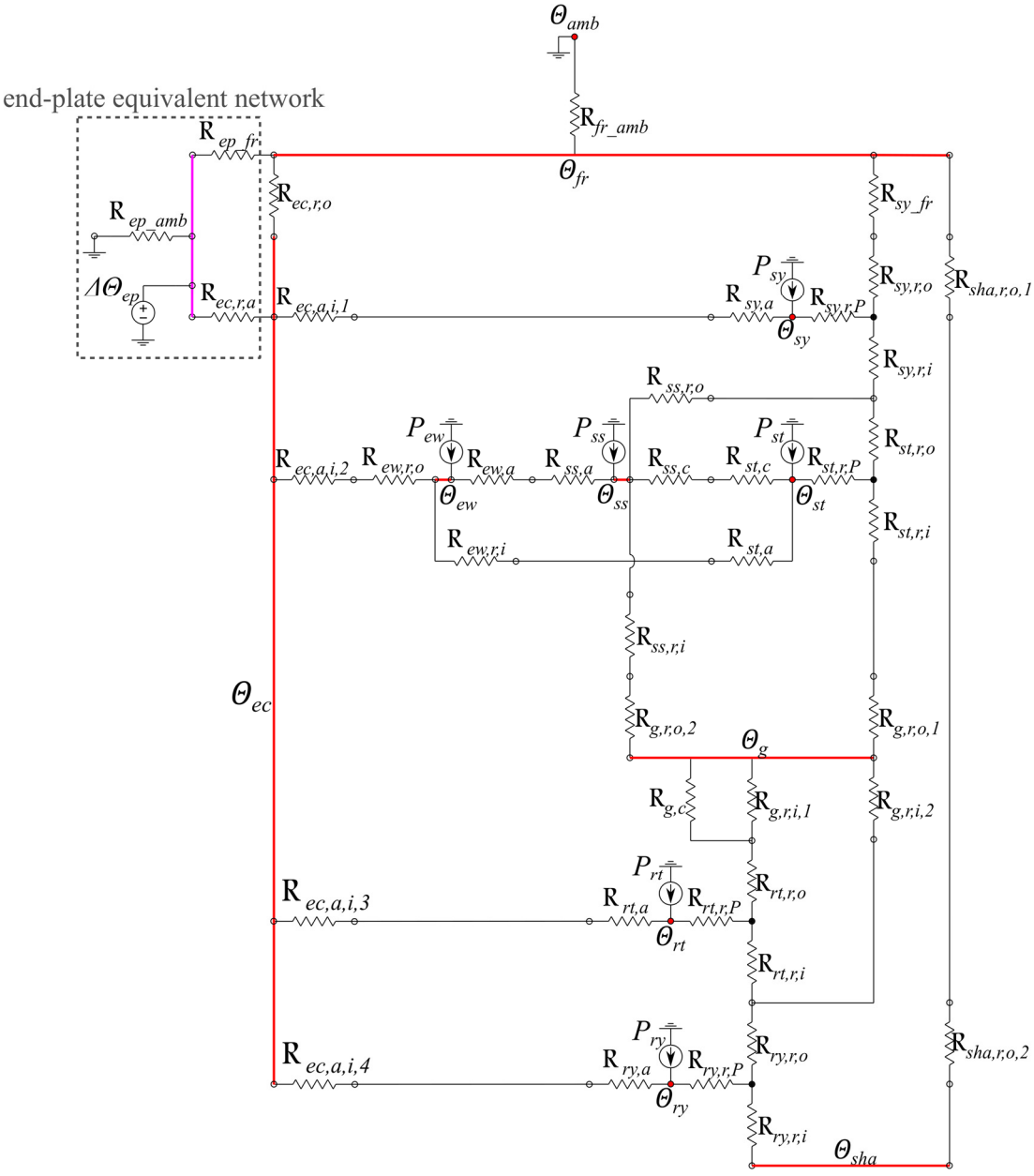

Figure 7-1 Equivalent 15-node LPTN of an SR machine with superimposed end-plate temperature.

$$\mathrm{Pr} = \frac{c_p \xi}{\lambda}, \tag{7-4}$$

$$\mathrm{Gr} = \frac{\beta g \Delta\Theta \rho^2 L^3}{\xi}, \tag{7-5}$$

Nu is the Nusselt number, which expresses the ratio between heat exchanged by convection and heat that would be theoretically transferred via conduction if buoyance forces could not set the fluid in motion. Re is the Reynolds number expressing the ratio between the kinetic energy and the energy dissipated due to the drag forces. Pr is the Prandtl number that defines the ratio between momentum diffusivity and thermal diffusivity. Gr is the Grashof number, which denotes the ratio of buoyance to viscus forces. Other parameters are as follows:

χ is the convection heat transfer factor;

L is a characteristic length of the surface;

λ is the fluid thermal conductivity;

ρ is the fluid density;

v is the fluid velocity;

ξ is the fluid dynamic viscosity;

c_p is the fluid isobaric specific heat;

β is the fluid coefficient of cubical expansion;

g is the gravity acceleration;

$\Delta\Theta$ is the temperature gradient between fluid and surface.

In the following subsections, dimensionless analysis is used to define the convection thermal resistances of the SR machine LPTN.

7.2.1 Frame-to-Ambient Convection Factor

As already discussed in Chapter 3, the frame-to ambient heat exchange represents one of the two degrees of freedom provided by the thermal design of an SR machine. With regard to this, two possible options are available, namely a natural cooling system or a forced cooling system.

7.2.1.1 Natural Convection

For natural convection heat exchange, correlation between dimensionless parameters that define the heat transfer is expressed in terms of the Gr Pr product. For smooth surfaces, the correlation is in the form of (7-6). Parameters a_N and b_N depend on surface shape and orientation; typical values are reported in Table 7-I, [90].

Table 7-I Analytical and FEA values of L_a, L_1, L_2 and L_u or the two SR prototypes.

Shape/Orientation	Gr Pr lam to turn	a_N laminar	b_N laminar	a_N turbulent	b_N turbulent
Horizontal Cylinder	10^9	0.525	0.25	0.129	0.33
Vertical Cylinder	10^9	0.59	0.25	0.129	0.33
Vertical plate	10^9	0.59	0.25	0.129	0.33
Horizontal Cylinder (upper)	10^8	0.54	0.25	0.14	0.33
Horizontal Cylinder (lower)	10^5	0.25	0.25	n.a.	n.a.

$$\mathrm{Nu} = a_N \left(\mathrm{Gr}\,\mathrm{Pr}\right)^{b_N}. \tag{7-6}$$

On the other hand, most of the naturally-cooled SR machines are designed with an outer finned surface, in order to enhance the heat exchange. A sketch of a finned housing is represented in Figure 7-2. The most common approach to determine the convection factor is to consider the fluid comprised between two adjacent fins as a U-shaped channel, where the fins pitch b_{fin} is the characteristic length to be used in Gr_{fin} and Nu_{fin}:

$$b_{fin} = \frac{\left(OD + 2h_{fin}\right)\pi}{n_{fin}}, \tag{7-7}$$

where n_{fin} is the number of fins in the array and h_{fin} is the fins' height.

In [119], C.D. Jones and L.F. Smith gather some experimental data to correlate Nu_{fin} and Gr_{fin} Pr for several finned arrays. Five points taken from the Nu_{fin} vs. Gr_{fin} Pr characteristics plotted in [119] are represented in Figure 7-3. However, it is found that the mathematical expression proposed by the Authors does not correspond with the plotted characteristics (it turns out to give complex numbers). To overcome this issue, in this thesis, the five points taken from the plotted correlation in [119] have been fitted into an 'exponential' spline. In simple words, spline coefficients have been determined considering the logarithms of the x and y coordinates of the five interpolated points.

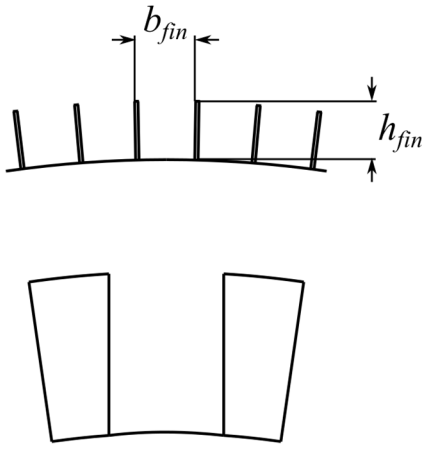

Figure 7-2 Finned housing.

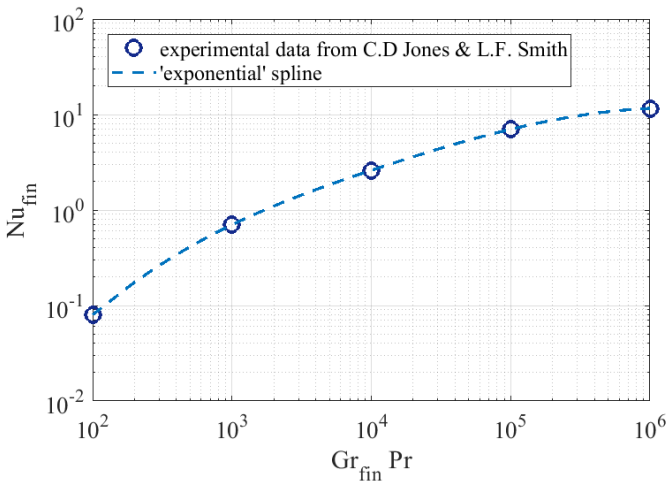

Figure 7-3 Five points of the Nu_{fin} vs. Gr_{fin} Pr correlation proposed in [119] fitted by the proposed exponential' spline.

Therefore, a linear-to-logarithmic and logarithmic-to-linear transformation is required in order to respectively feed and receive values to/from the spline.

Once Nu_{fin} has been found, the convection factor associated to each U-shaped channel is calculated by (7-8). Finally, the overall finned-surface thermal resistance R_{fin} is found by the parallel connection of the n_{fin} U-shaped channels, as shown in (7-9):

$$\chi_{fin} = \frac{\mathrm{Nu}_{fin}\lambda}{b_{fin}}, \tag{7-8}$$

$$\mathrm{R}_{fin} = \frac{1}{n_{fin}}\left[\frac{1}{\chi_{fin}\left(b_{fin}+2h_{fin}\right)L_{sha}}\right]. \tag{7-9}$$

VALIDATION

The analytical model presented above is now applied to calculate the frame-to-ambient thermal resistance of the SRMyld prototype R_{fin}.

Given that the SRMyld frame has twenty-eight fins, which are $4.5mm$ tall, R_{fin} is calculated via (7-9). Analytical values of R_{fin} are compared against MotorCad results in Table 7-II. As observed, a very small error, i.e. 1.8%, is incurred. The main source of error lies in the fact that the Nu_{fin} vs. Gr_{fin} Pr correlation has been developed for flat fin arrays, so that curvature effects are neglected.

7.2.1.2 FORCED CONVECTION

Forced convection cooling of the outer machine surface is adopted when higher heat

Table 7-II Analytical and MotorCad values of the frame-to-ambient resistance.

	R_{fin}
Analytical	1.457
MotorCad	1.484
Error (%)	-1.82

exchange rates are necessary. Forced convection systems are classified into forced-air or liquid-cooled. In forced air systems, airflow is forced around the machine's surface by means of a fan or blower. In liquid-cooled machines, heat is extracted by a coolant flow, which is forced through a pipes arrangement that wraps the machine's surface.

For forced-convection cooling systems, simple analytical correlations are harder to achieve, since fluid dynamics modelling should also be accounted for. However, as a first-attempt approximation, it is possible to estimate a 'reasonable' heat exchange factor between the machine's outer surface and the air or liquid χ_{fluid}, from which R_{fr_amb} can be calculated and the LPTN solved.

7.2.2 AIRGAP HEAT EXCHANGE

Airgap heat exchange correlations derive from the studies conducted on smooth concentric rotating cylinders, as shown in Figure 7-4. This approach usually provides excellent results in electrical machines showing no saliencies along the rotor periphery. On the other hand, this approach can be also applied for salient-rotor machines, such as the SR machine, when the peripheral speed is low enough not to induce an excessive additional turbulence to the airflow.

In order to judge the kind of motion within the airgap, i.e. laminar, vortex or turbulent, the dimensionless Taylor number Ta is introduced [120]. By indicating with r_o and r_i, the outer and inner radii of the annulus, Ta is defined as follows:

$$\begin{cases} \mathrm{Ta} = \dfrac{\omega r_m^{\,0.5}\left(r_o - r_i\right)^{1.5}}{\xi} \\ r_m = \dfrac{1}{2}\left(r_o + r_i\right) \end{cases}. \tag{7-10}$$

As proposed by Howey *et al.*, [120], a geometrical form factor f_g is needed to understand the typology of fluid motion:

$$\begin{cases} f_g = \dfrac{\pi^2}{41.49\sqrt{S_g}}\left(1 - \dfrac{r_o - r_i}{2r_m}\right)^{-1} \\ S_g = 0.0571\left(1 - \dfrac{0.652\left(\dfrac{r_o - r_i}{2r_m}\right)}{\left(1 - \dfrac{r_o - r_i}{2r_m}\right)}\right) + 0.00056\left(1 - \dfrac{0.652\left(\dfrac{r_o - r_i}{2r_m}\right)}{\left(1 - \dfrac{r_o - r_i}{2r_m}\right)}\right)^{-1} \end{cases}. \tag{7-11}$$

Then, Nu derives from the ratio between Ta and f_g squared, as reported in (7-12). In particular, for Ta^2/f_g^2 smaller than 1700, fluid motion is laminar and hence heat transfer undergoes mainly for conduction. As observed, heat exchange is not a function of the fluid velocity. When Ta^2/f_g^2 is comprised between 1700 and 10000, fluid motion enters a transition zone when Taylor's vortices begin to form. As a consequence, fluid velocity influences the heat transfer. Finally, for Ta^2/f_g^2 greater than 10000 motion is purely turbulent.

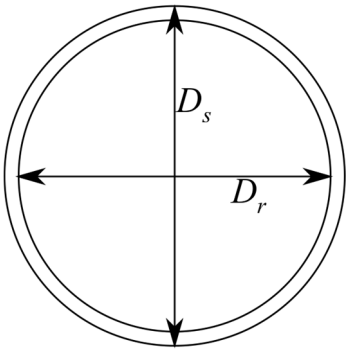

Figure 7-4 Annulus considered for airgap heat exchange.

For the particular case of the airgap-to-rotor-yoke convection factor, since most of the rotor heat transfer is inside the metal parts, it is reasonable to consider the rotor yoke radius as the inner annulus for the convection heat exchange.

$$\begin{cases} \mathrm{Nu}=\dfrac{2\left(\dfrac{r_o-r_i}{r_i}\right)}{\ln\left(1-\dfrac{r_o-r_i}{r_i}\right)} & \dfrac{\mathrm{Ta}^2}{f_g{}^2}\le 1700 \\ \mathrm{Nu}=0.128\left(\dfrac{\mathrm{Ta}^2}{f_g{}^2}\right)^{0.367} & 1700<\dfrac{\mathrm{Ta}^2}{f_g{}^2}\le 10000 \\ \mathrm{Nu}=0.409\left(\dfrac{\mathrm{Ta}^2}{f_g{}^2}\right)^{0.241} & \dfrac{\mathrm{Ta}^2}{f_g{}^2}>10000 \end{cases} . \tag{7-12}$$

7.2.3 End-Cap Air Heat Exchange

Convection heat exchange undergoing inside the end-caps air is a critical aspect, since the end-windings are normally the hottest part of the machine. The greatest challenge in studying the convection cooling of the internal surfaces is that the fluid flow depends on many factors, such as the end-winding shape and length, added fanning effects introduced by proper fans or fanning features (e.g. wafers used on the squirrel cage rotors), surface finish of the rotor-end sections and finally, turbulence, [90].

Many authors dealt with this phenomenon achieving relatively similar results. In [121], A. Boglietti *et al.* gathered all of the aforementioned results in the general formulation reported in (7-13). As observed, the end-winding heat-transfer coefficient is composed of a constant part, which represents the heat exchange with the fluid at rest, and of a second part proportional to the first power of the fluid's velocity v.

$$\chi_{ec,N/F}(v)=41.4+6.22v\,. \tag{7-13}$$

7.3 VALIDATION

In this Subsection, temperature distribution estimated by the LPTN described above is compared against results attained from MotorCad. For the validation, the SRMyld prototype is considered in the same operating conditions used in Chapter 4, where MotorCad results have been experimentally validated:

a. $36V$, $6000rpm$ and $0.9kW$ mechanical output power,

b. $36V$, $1500rpm$ and $0.9kW$ mechanical output power.

For the operating conditions a, analytical and MotorCad results are compared in Table 7-III. MotorCad results are also shown in Figure 7-5 (a). Analytical results show an excellent agreement with MotorCad in all components, save the end-windings, with errors below 3%. For the end-windings, a 7.45% error is incurred. The reason for this discrepancy are analysed in detail at the end of this Section.

For operating conditions b, analytical and MotorCad results are reported in Table 7-IV. Since no analytical modelling for the low-speed chopping-mode operation has been developed in this thesis, FEA losses have been considered for both LPTN and MotorCad. Similarly to operating condition a, errors for all components are well below 5% except for the end-winding, where a 7.11% error is incurred.

A final observation is that MotorCad temperature distributions achieved by imposing the end-plate temperature are practically identical to the cases with the mounting flange shown in Figure 7-5 and Figure 4-11.

DISCUSSION

By observing the results attained for operating conditions a and b, it is noted that the LPTN provides excellent results for all components save the end-windings, where the error is around 7%. This result remains more than acceptable for the purpose of generating the ADS; the rest of this subsection provides a deeper insight about the origin of this discrepancy.

Table 7-III SRMyld temperatures $6000rpm$, Analytical vs. MotorCad results.

Component	Analytical [°C]	MotorCad [°C]	Error [%]
Frame	70.04	71.3	-1.76
Stator Yoke	74.16	75.1	-1.25
Stator Tooth	77.31	77.4	-0.11
End-winding	90.69	84.4	7.45
Airgap	79.54	77.4	2.76
Rotor Tooth	77.65	75.6	2.71
Rotor Yoke	77.19	75.3	2.51
End-Plates	64	64	-
Ambient	22	22	-

Table 7-IV SRMyld temperatures 1500*rpm*, Analytical vs. MotorCad results.

Component	Analytical [°C]	MotorCad [°C]	Error [%]
Frame	114.47	119.9	-4.53
Stator Yoke	124.20	129.7	-4.24
Stator Tooth	131.90	135.9	-2.94
End-winding	165.82	154.8	7.11
Airgap	136.95	135.8	0.84
Rotor Tooth	131.36	132.9	-1.15
Rotor Yoke	130.36	132.7	-1.76
End-Plates	101	101	-
Ambient	18	18	-

Heat exchange inside the stator slot is probably the most difficult thermal aspect to model in an electric machine. Indeed, the slot is filled by a bundle of copper conductors coated with an insulating layer, varnish, tiny air bubbles whose size depends on the impregnation goodness, slot liners, etc. From this description, it emerges that moving from the slot centre towards the periphery heat crosses several different materials, whose amount changes drastically in each application. For this reason, finding a general formulation for the heat transfer across the slot is a very hard task. In this work, the approach based on the equivalent insulating layer proposed in [122] has been implemented. The main model limitation is that the conductor's dimension is not taken into account. In fact, it is easy to observe that heat transfer in a slot with few conductors has a dramatically lower thermal resistance than a slot with hundreds of conductors, since heat would be transferred almost only through a copper path. This trend is confirmed by Figure 7-6, where the end-winding temperature of the SRMyld prototype is plotted for different conductors sizes, i.e. AWG gauges. As expected, temperature rise is inversely proportional to the wire's size.

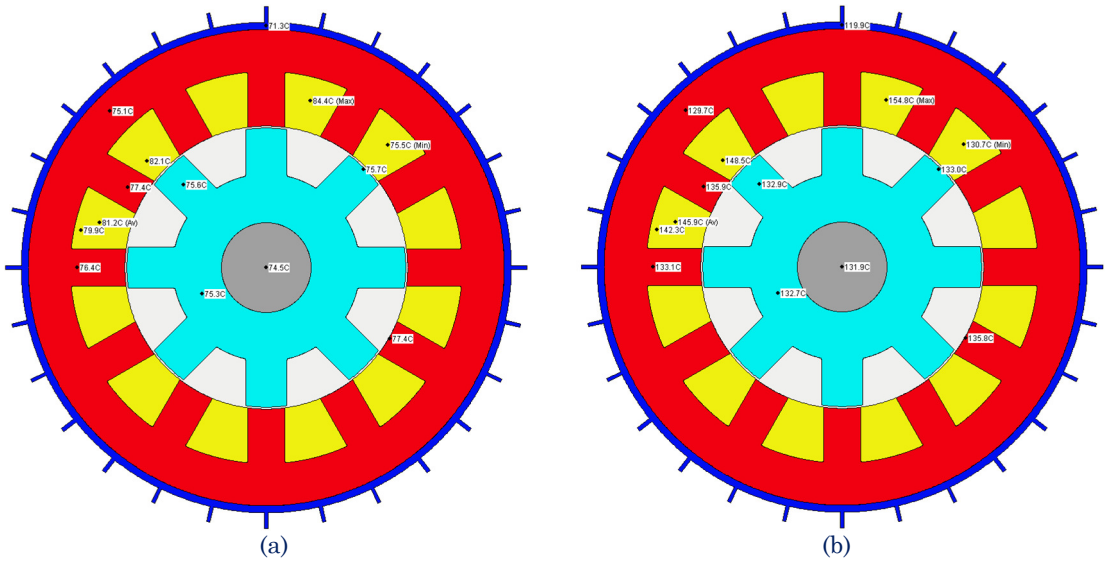

(a) (b)

Figure 7-5 SRMyld MotorCad results at a) 6000*rpm* and b) 1500*rpm*: components' temperature with imposed end-plate temperature.

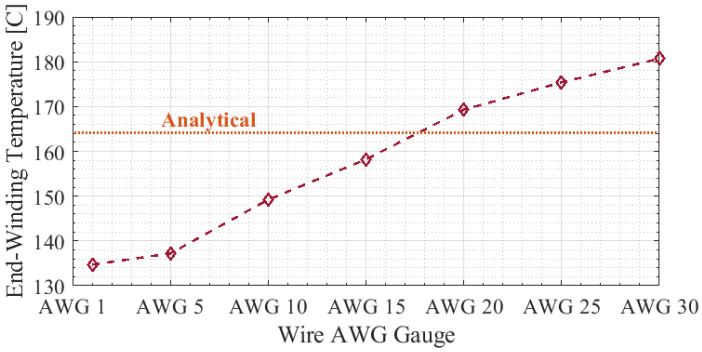

Figure 7-6 Maximum end-winding temperature for different wire AWG gauges.

All the above indicates that there is still room for improving the model in [122] and thus reduce the error in the end-winding temperatures.

7.4 Conclusion

This Chapter has discussed the analytical thermal modelling of the SR machine by means of a LPTN. Most of the effort is required to model the thermo-fluid-dynamics aspects, which define the convection factors: 1) between SR machine's frame and outer coolant, and 2) within the airgap and the end-caps' air regions.

The thermal model described in this Chapter completes the set of models required in order to account for the electromagnetic+thermal design aspects. Therefore, it is now possible to undertake the fully analytical multiphysics definition of the ADS, which is the main goal of this thesis. An example of a practical application is the subject of the next Chapter.

8 ACTUAL DESIGN SPACE FOR A MILD-HYBRID ELECTRIC MOTOR: A DESIGN CASE STUDY

This Chapter presents a design case study where the proposed ADS methodology is adopted for the design of a mild-hybrid vehicle's electric motor. As already pointed out in the initial Chapters, the ADS methodology consists of a preliminary analytical stage to be conducted prior to the Finite-Element-based finalisation. To this end, the intention in this Chapter is to provide a simple yet insightful example about the effectiveness of the ADS to prepare the ground for the finalisation. In particular, objectives of the design case study are as follows:

- Illustrate how the ADS methodology can provide designers with a deep and clear insight of the design problem,
- Indicate the correct direction to take when embarking on the FEA finalization. In this regard, the case study discusses the preparation for both an heuristic and an optimizer-based finalization.

8.1 MILD-HYBRID POWER TRAIN: APPLICATION OVERVIEW

Conventional hybrid-electric vehicles have their electric motor drives sized for at least 50% of the vehicle's rated power, which requires a non-negligible impact on the vehicle's architecture. Thus, to turn from conventional drive trains to hybrid-electric drive trains, a huge investment of time and money is needed. Mild hybrid drive trains provide an interesting compromise to smooth the transition to the next-generation vehicles and yet are more efficient than conventional drive trains. As a matter of fact, most of the hybrid-electric vehicles nowadays on the market are actually mild hybrids.

In mild hybrid or soft hybrid electric drive trains, a small electric motor is installed directly behind the Internal Combustion Engine (ICE), as illustrated in Figure 8-1, [123]. The small electric motor fulfils several functions: such as engine starter, electrical generator, adds additional power to the drive train when high power is demanded and

finally recovers part of the braking energy to the storage unit. In terms of ratings, electric motors for mild hybrid applications are rated usually around the 10% of the ICE power rating. In this way, the 36V or 48V electrical system available aboard may be sufficient to meet the requirements. Due to the direct mechanical coupling, a further requirement is to operate in the same Constant Power Speed Range (CPSR) as the ICE.

Research around mild-hybrid drive trains revolves mainly on energy management optimisation, rather than on the design of individual components. However, even from the few contributions on motor design for mild-hybrid vehicles, [124-126], it is possible to identify the most important design features, which translate into the following typical design specifications:

1. The electric motor is normally connected directly to the ICE and in many cases entirely replaces the clutch. For this reason, the motor is designed with a stack length L_{stk} of $60mm$.
2. Due to the direct coupling to the ICE, maximum speed is in the order of $6000rpm$, [124], to $8000rpm$, [126].
3. Ratio between base and maximum speed is 4 or greater.
4. As the electric motor serves both as starter and for energy recovery purposes, a high overload capability is demanded.
5. The same water used to cool down the ICE can be used, so that water jacket solutions are highly suitable, [125].

8.2 Design Specifications

Basing on the aforementioned contributions, for the case study proposed in this Chapter, the main design specifications are given in Table 8-I.

For the cooling system, the water jacket designed by A. Fatemi *et al.* in [125] is taken, since the same outer diameter and overall length have been considered. Among the options investigated in [125], the water jacket arrangement with the lowest frame-to-water heat transfer coefficient is considered, i.e. $687W/(m^2K)$.

8.3 Actual Design Space Definition

The flowchart illustrated in Figure 8-2 summarises the thinking pattern to follow for the initial steps of the ADS generation. In the following, the most important steps are

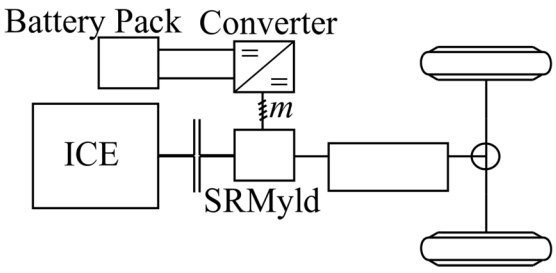

Figure 8-1 Schematic mild hybrid drive train.

Table 8-I Design Case study Constraints and Requirements

Parameter	Measure Unit	Value
DC-bus Voltage	V	48
Peak Phase Current	A_{pk}	375
Rated Power	kW	7
Base Speed	rpm	2000
Maximum Speed	rpm	8000
Overall Length	mm	110
Overall Diameter	mm	160
Minimum Efficiency	%	85

taken to define the ADS of the design problem at hand.

8.3.1 APPLICATION ANALYSIS

Once the Constraints and Requirements have been formulated, such as in Subsection 8.2 (this step is normally taken by the 'customer'), the first step that the designer shall take is to analyse the application and introduce further design Constraints, if necessary.

For the case of the mild-hybrid electric motor, the initial design consideration is aimed at the translation of the overall space limitations into the maximum iron core

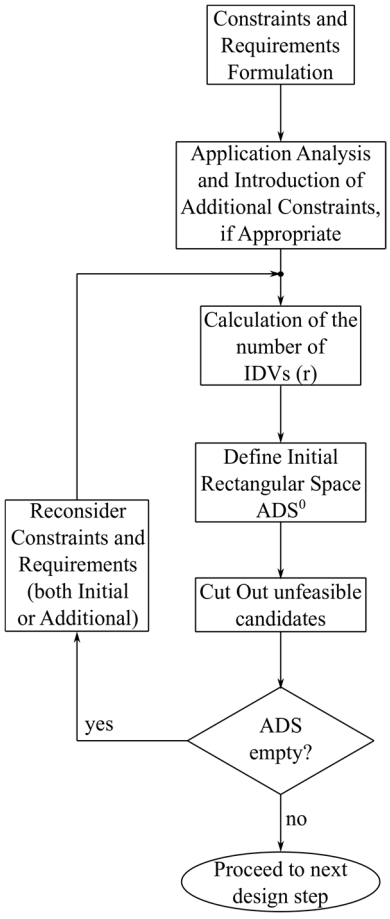

Figure 8-2 ADS generation flow-chart, initial steps.

dimensions. To this end, an $8mm$ water jacket diameter is considered to acknowledge that the maximum outer diameter is:

$$OD_{\max} = 144mm\,.$$

For the maximum axial lamination stack length, it is reasonable to consider the relation below:

$$L_{stk\_\max} = L_{sha} - \underbrace{(3d_{ew} + 2b_{fr})}_{\Delta L_{ax}},$$

where d_{ew} denotes the end-winding overhang length and b_{fr} is the frame/end-plates thickness.

Following from the lamination dimensions it is then possible to imagine that a relatively small airgap is required. For this reason, a $0.3mm$ value is considered, [92].

Finally, the most important step to take at this stage is probably the materials selection. Due to the high demanded power density, low-loss NO20 electrical steel sheets from the Cogent Power catalogue are considered, [127].

8.3.2 Calculation of the IDVs Number

In this example, in order to maintain the analysis of the proposed methodology at its simplest and also to be able to produce a graphical representation of the ADS, a 3-IDV ADS is considered. Indeed, considering a multidimensional ADS would give no additional insight to the proposed methodology and thus would add no benefit to the discussion proposed below.

For this purpose, a number of External Relationships (ERs) are expressed as equations, rather than inequalities. In this case, ERs act exactly as if they were IRs. Thus, basing on (3-1), each of them reduces the number of IDVs by one.

Starting from the design specifications gathered in Table 8-I along with the considerations made in Subsection 8.2, it is possible to introduce the following seven equation-expressed ERs:

1. $OD = OD_{\max}$;
1. $L_{stk\_\max} = L_{sha} - (3d_{ew}+2b_{fr})$;
2. $l_g = 0.3mm$;
3. $V_{DC} = 48V$;
4. $i_{pk} = 375A$;
5. Water jacket cooling;
6. No inner fans.

Points 6 and 7 are used to take into account the two IDVs that are provided by the thermal design aspect (see Table 3-X). Subsequently, five additional equation-expressed ERs are added basing on the Author's expertise, as well as on widely accepted design assumptions.

For the stator and rotor teeth angles, various are taken from an optimisation process conducted by the Author in a previous work, [128], which are similar to the guidelines provided by, [85]:

7. $\beta_{st} = \left(\frac{3\zeta r}{8} + \frac{3\pi}{N_s N_r} \right) * 0.975$,
8. $\beta_{rt} = 1.1 * \beta_{st}$.

For the magnetic core design, as a high number of phases is expected to satisfy the wide constant power speed range requirement, it is reasonable to allow for the same stator and rotor yokes to have the same stator tooth's flux density. This results in imposing iron utilisation factors u_{FE_sy} and u_{FE_ry} equal to 1 (see Subsection 3.5.5). Geometrically, this ER translates to:

9. $b_{sy} = \frac{D_s}{2} \beta_{st}$,
10. $b_{ry} = \frac{D_s}{2} \beta_{st}$.

A straight-toothed rotor geometry is chosen, so that the following ER is introduced:

11. $\beta_{re} = 0$.

Finally, an important consideration about the number of repetitions P can be made. As P increases, the stator yoke thickness reduces, since the flux per phase is shared between the higher number of stator teeth. Moreover, a high number of repetitions is desirable in an automotive application, since vibration issues are considerably mitigated, [60]. On the other hand, an extremely high number of repetitions would lead to high fundamental stator frequencies, along with very narrow stator teeth with inherent mechanical issues. Therefore, it is reasonable to set the number of repetitions to two:

12. $P = 2$.

At this point, given that the number of IDVs that characterise the electromagnetic+thermal design of an SR machine is seventeen (see Table 3-XI), and that twelve equation-expressed ERs have been added, the number of IDVs becomes:

$$17 - 13 = 4.$$

The design variables selected as 'independent' are listed below:

1) m, number of phases;
2) D_s, stator bore diameter;
3) B_{st}, stator tooth average flux density at maximum alignment and maximum phase current;
4) N_{st}, number of series-connected turns per stator tooth.

The analysis is now conducted by defining a 3D-ADS for three different numbers of phases, namely 4, 5 and 6. Hence, three different pole configurations will be investigated: 16/12, 20/16 and 24/20.

To conclude this analysis, the initial rectangular space DS^0 shall be defined. Maximum and minimum values considered for D_s, B_{st} and N_{st}, along with the discretization steps, have been chosen basing on good engineering judgement and are shown in Table 8-II.

8.3.3 ADS FOR INITIAL SPECIFICATIONS AND CRITICAL DISCUSSION

In this Subsection, the design for the required $7kW$ is attempted with the three aforementioned poles configuration. The process is divided in a sequence of three cut-outs. In each of them, the Cnts and/or Rqms listed below are applied, so that the unfeasible candidates are progressively discarded:

- Cut-Out 1: Geometrical and Electromagnetic Constraints;
- Cut-Out 2: Power and Efficiency Requirements at the base-speed node;
- Cut-Out 3 Power and Efficiency Requirements at the maximum-speed node.

Initially, an overestimated maximum J_{ss} of $25A/mm^2$ is used, i.e. all candidates with a slot current density higher than $25A/mm^2$ are discarded. This is done with the only intention to exclude all of the design candidates that are 'obviously' unfeasible in the first Cut-Out and hence reduce the overall computation time. Then, compliance with the thermal limitations is directly verified by means of the LPTN.

Table 8-III reports the ADS population for the three topologies under investigation, whilst Figure 8-3 to Figure 8-5 provide a graphical representation of the ADSs.

For all of the three pole configurations analysed, an empty ADS is found, meaning that the design specifications are over-restrictive and therefore cannot be met. This conclusion might not be so surprising. In fact, the specifications have been taken from a Permanent-Magnet machine, [125], which is well-known for providing around double the power density of an SR machine, [129].

Further, less intuitive considerations can be made in relation to the magnetic circuit design. It is found that none of the three topologies allow for candidates with one turn per tooth. This result derives from an insufficient magnetomotive force to reach the minimum stator tooth flux density. This, in turn, is insufficient to meet the torque

Table 8-II Initial rectangular space DS^0.

IDV	Minimum Value	Maximum Value	Discretisation Step
D_s	$80[mm]$	$120[mm]$	$1[mm]$
B_{st}	$1.8[T]$	$2.3[T]$	$0.01[T]$
N_{st}	1	5	1

requirement.

A final observation is that the maximum stator tooth flux density found is 2.02T, even with a hugely overestimated maximum current density. A possible solution could be to adopt an electrical steel with a higher permeability, such as a cobalt iron. However, due to the extremely high price of these materials, this solution is discarded.

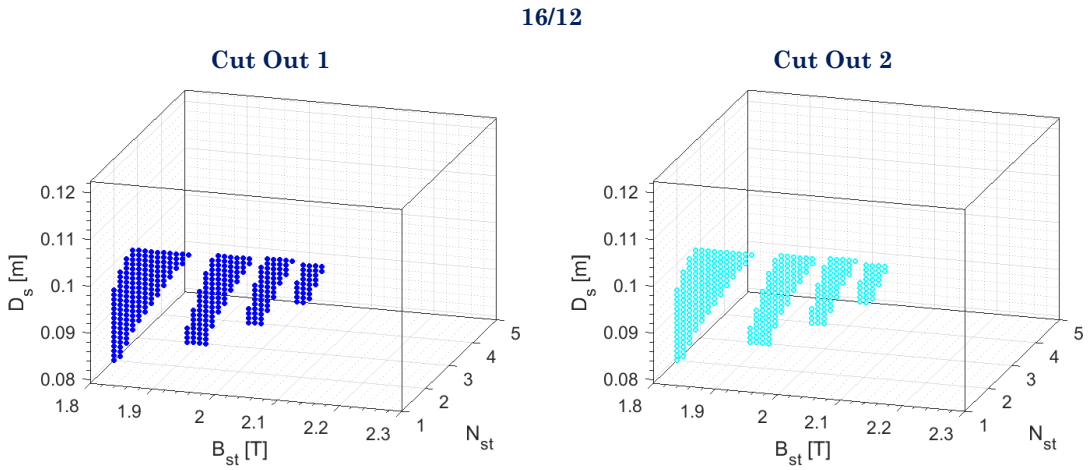

Figure 8-3 ADS at 7kW for 16/12 topology: Cut-Out 1 and Cut-Out 2.

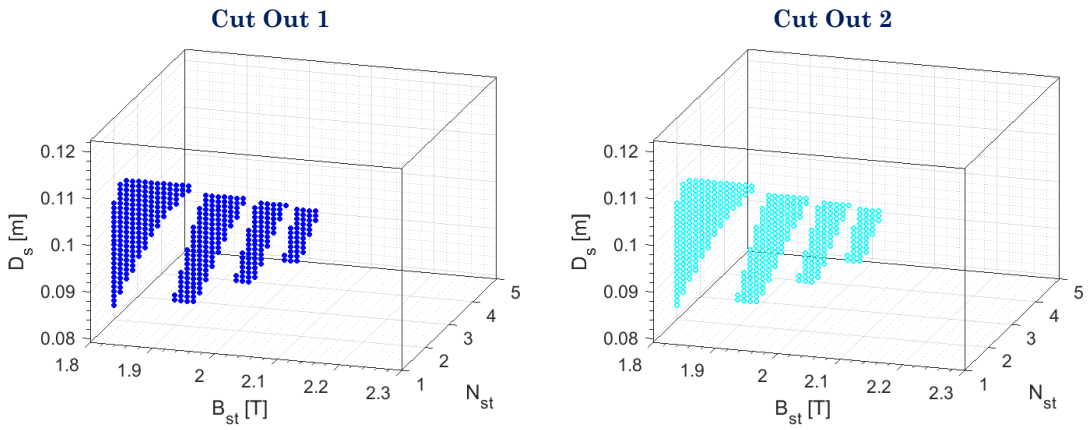

Figure 8-4 ADS at 7kW for 20/16 topology: Cut-Out 1 and Cut-Out 2.

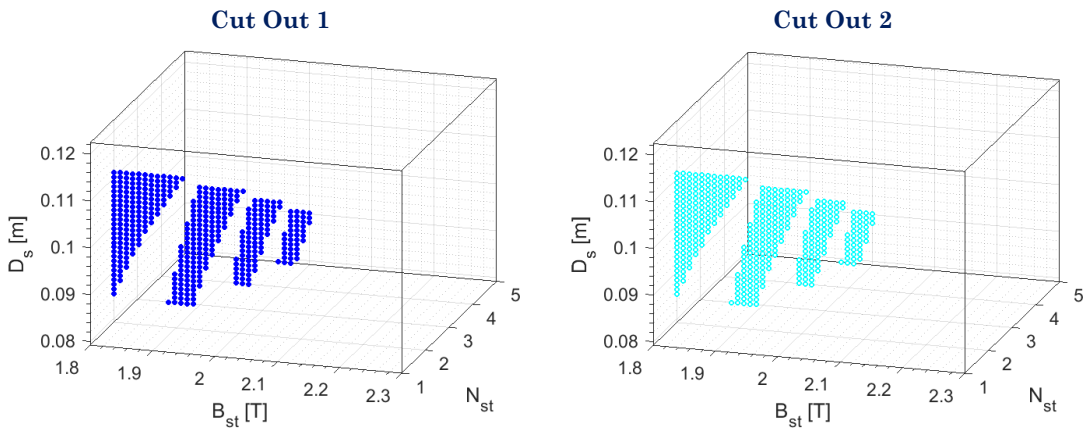

Figure 8-5 ADS at 7kW for 24/20 topology: Cut-Out 1 and Cut-Out 2.

Table 8-III ADS population for $7kW$ rated power.

	16/12	20/16	24/20
Cut Out 1	322	410	422
Cut Out 2	0	0	0
Cut Out 3	**0**	**0**	**0**

8.3.4 ADS FOR RECONSIDERED SPECIFICATIONS

Based on the flowchart in Figure 8-2, once the unfeasibility of the design has been proven, Constraints and/or Requirements are to be reconsidered.

For the example at hand, based on typical power densities of SR machines, it is decided to reduce the rated power to $5.5kW$.

Similarly to the previous case, the same overestimated maximum J_{ss} of $25A/mm^2$ is used, starting from the same rectangular space ADS^0 defined in Table 8-II.

The population of the ADSs determined for the three poles configurations is listed in Table 8-IV. This time, the three topologies 'survived' the Cut-Out 1, but only the 24/20 topology provided a non-empty ADS. The latter is shown in Figure 8-6. As expected, a higher number of phases is a desirable feature for applications requiring a wide constant power speed range, especially with an ultra-low DC-bus voltage.

Results in Table 8-IV provide one step forward in the design process, since they allow the exclusion of two poles topologies. On the other hand, the results are not sufficient to prove the existence of at least one feasible design. Indeed, thermal verification has not been yet accounted for.

8.3.4.1 MULTIPHYSICS ADS

In this Subsection, the thermal design boundary provided by the cooling system is introduced. Thermal limitations imposed over the winding insulation and lamination coating are as follows:

- Maximum copper temperature 180°C,
- Maximum electrical steel temperature 220°C.

This time, during Cut Out 2, after verifying the compliance with the power requirement, the LPTN has been solved and thus all of the candidates that exceed the temperature limitations have been discarded.

Table 8-IV ADS population for $5.5kW$ rated power.

	16/12	20/16	24/20
Cut Out 1	322	410	422
Cut Out 2	20	56	61
Cut Out 3	0	0	61

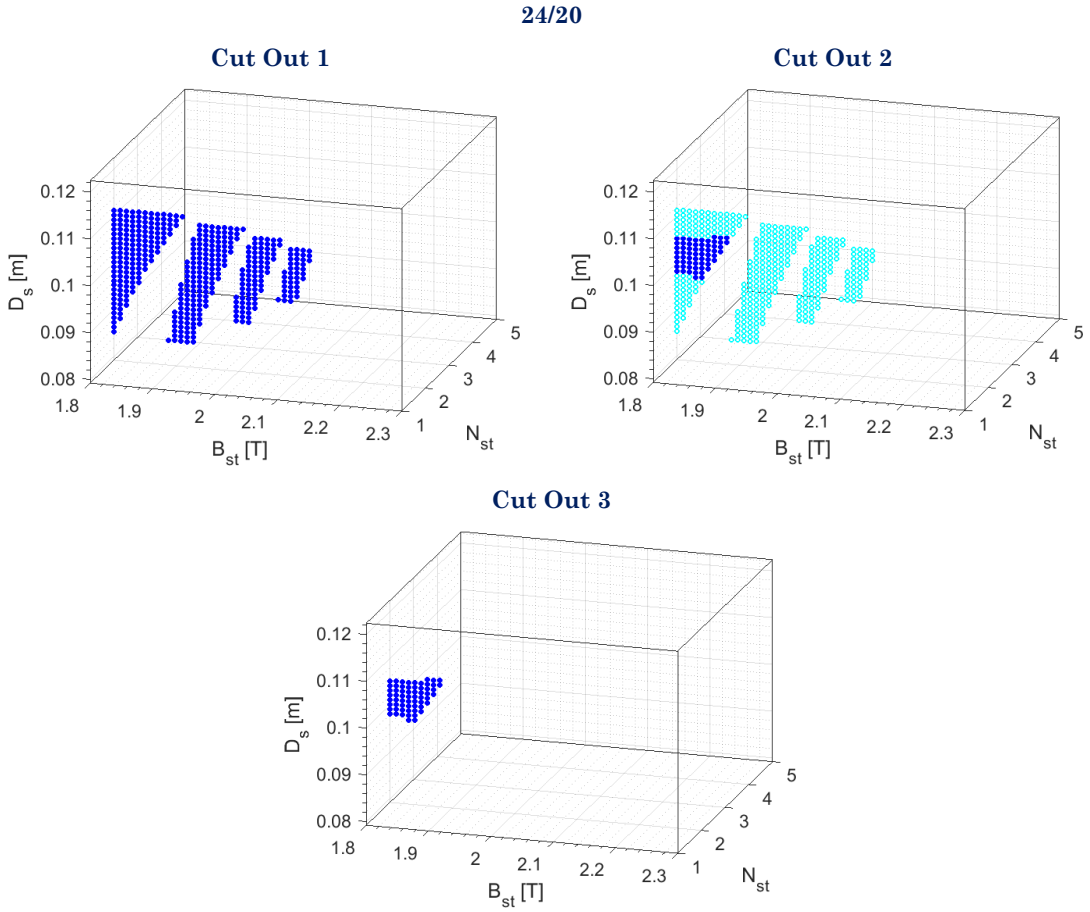

Figure 8-6 ADS at 5.5kW for 24/20 topology: Cut-Out 1, Cut-Out 2 and Cut-Out 3.

It is observed that, since a specific analytical model that predicts the current waveform at base speed has not been developed in this thesis, iron losses at base speed have been estimated basing on idealised flux linkages waveforms, [85]. Since copper losses are dominant in this application, a great error is not incurred. After the introduction of the thermal limitations, the ADS population is shown in Table 8-V.

As it can be observed, another empty ADS is found, meaning that none of the 61 candidates found with the purely electromagnetic process resulted feasible.

To arrive at a feasible design, thermal constraints are reconsidered. In this case, a 190°C maximum temperature is now allowed for the windings and an improved water jacket from [125], with a 755W/m^2K heat exchange factor, is taken. Results for the upgraded thermal design are presented in Table 8-VI, where 19 feasible candidates are found. It is found that all feasible candidates have a slot current density in the range of 17.5A/mm^2, in accordance with the guidelines discussed in Table 3-XII. In Figure 8-7, the ADS attained for the improved water jacket overlaps the purely electromagnetic ADS shown in Figure 8-6. This highlights the 'thermal boundary', i.e. the boundary between the candidate that are thermally feasible and unfeasible.

Table 8-V ADS population for 5.5kW rated power.

	24/20
Cut Out 1	422
Cut Out 2	0
Cut Out 3	0

Table 8-VI ADS population for 5.5kW rated power with upgraded water jacket.

	24/20
Cut Out 1	422
Cut Out 2	19
Cut Out 3	19

After two reconsiderations of Cnts and Rqms, a non-empty ADS has been finally attained. The next two Subsections illustrate a possible way to use the results from the ADS to finalise the design.

8.3.4.2 CONSIDERATIONS FOR HEURISTIC FEA FINALISATION

The case where the design is finalised via FEA following an heuristic approach, is now analysed. In this case, after verifying the design feasibility, the ADS methodology is used to select a convenient first design candidate to start the finalisation.

To do so, the evaluation of a performance index is added to the Cut Out process. The flow chart in Figure 8-8 illustrates the concept. In particular, beside the feasibility verification of the candidates, performance are used to determine a performance index. Then, indices from all feasible candidates are compared, so that the candidate having the highest index is taken to start the design finalisation. For the case study at hand, a performance index ip is constructed in a similar way as a single-objective function, where powers at the two nodes P_b and P_m are weighted 0.3, whilst efficiencies η_b, η_m weight 0.2:

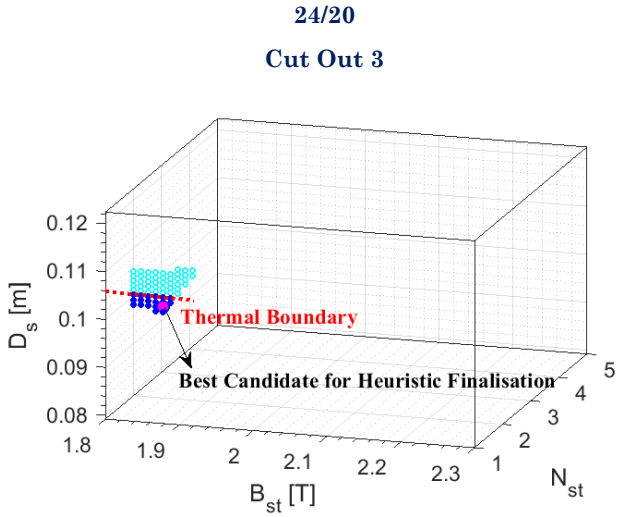

Figure 8-7 ADS at 5.5kW for 24/20 topology with improved water jacket: Cut-Out 1, Cut-Out 2 and Cut-Out 3.

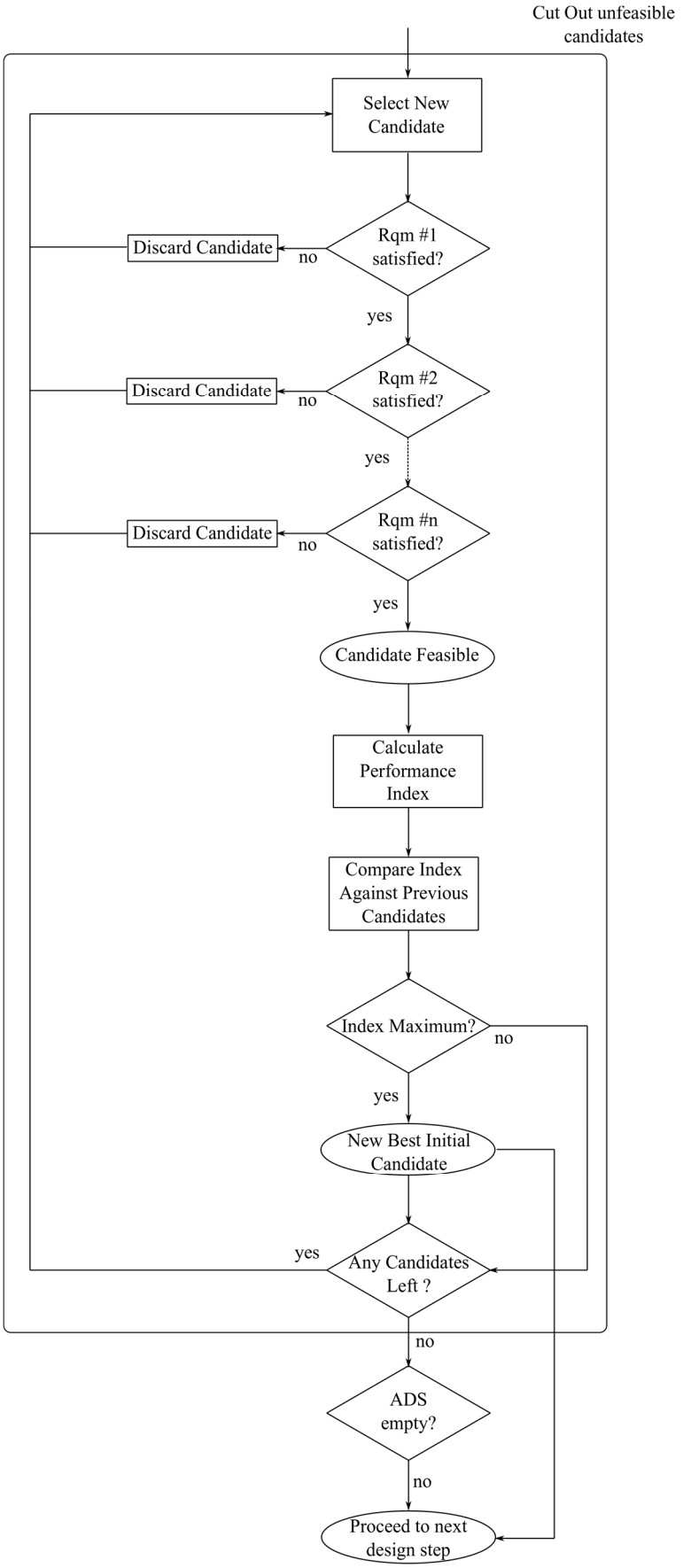

Figure 8-8 Preparation for heuristic finalization flow chart.

$$ip = 0.3*\left(\frac{P_b}{P_{rated}}\right)+0.3*\left(\frac{P_m}{P_{rated}}\right)+0.2*(\eta_b)+0.2*(\eta_m)\,.$$

The best candidate within the ADS attained for the mild hybrid electric motor is reported in the ADS OF Figure 8-7. The motor's outlook is shown in Figure 8-9.

8.3.4.3 CONSIDERATIONS FOR OPTIMISATION-BASED FEA FINALISATION

In this Subsection, the finalisation via an optimiser is considered. Ideally, the optimisation algorithm could be re-programmed in order to take into account only candidates that belong to the ADS. In this case, the only concerns in terms of convergence would lie on the ADS clearance δ_{ADS}.

Another, more straightforward option is to maintain the optimisation algorithm as it is, and use the ADS to define an improved rectangular space wherein the optimiser will move.

In the design case under consideration, the relatively simple ADS in Figure 8-7 already provides extremely useful information for this purpose. Indeed, it shows that it is perfectly reasonable to consider only machines with two turns, so that an additional equation-expressed ER can be introduced:

$$N_{st} = 2\,.$$

On the other hand, since the process is now more optimisation-oriented, it is convenient to increase the number of IDVs. To this end, ERs fixing the stator and rotor teeth angles β_{st} and β_{rt} are removed, resulting in a 4-D rectangular design space DS^0, which is defined in Table 8-VII. For β_{st} and β_{rt}, maximum and minimum values are expressed in terms of the Stephenson's triangle defined in Subsection 3.5.4.

In this case, as the existence of at least 19 feasible candidates is guaranteed, the objective during the ADS determination is to determine the rectangular space wherein to let the optimiser will move.

The idea is to define a new rectangular space that 'enshrines', i.e. to be the 'frame' of the ADS. To do so, at the end of each Cut-Out, the maximum and minimum value of each IDV, for which at least one feasible candidate exists are recorded. In this way, the maximum values of the IDVs progressively reduce, whereas their minimum values

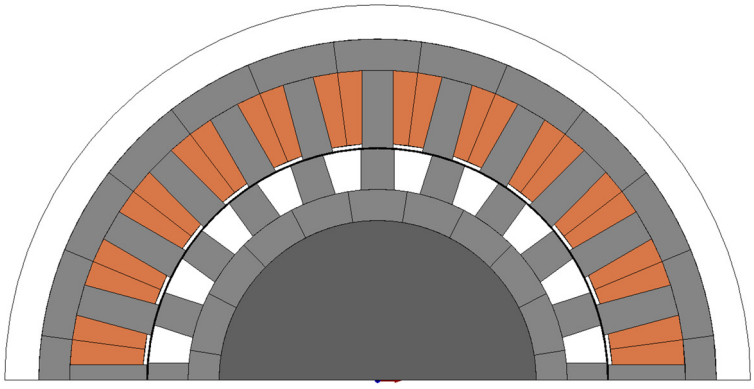

Figure 8-9 Best initial candidate for heuristic FEA design finalization: SR machine's outlook.

progressively increase. At the end of the Cut-Outs, the rectangular space wherein the ADS 'fits perfectly' is defined. The improved 4-D rectangular space for the design case at hand is defined in Table 8-VIII. It is observed that the ADS-based reconsideration of the rectangular space allowed the reduction of the initial, engineering-judgement-based population of 1.7 million members to just 400 individuals.

8.4 CONCLUSION

This Chapter discussed a practical design case study where the ADS methodology has been used to pave the way to the FEA design finalisation. Objectives of this case study were to demonstrate that the proposed ADS method allowed to:

1. Promptly identify an impossible design problem, allowing the designer to reconsider immediately Constraints and Requirements. It is of particular importance the case of the 'Thermal Boundary', which proved the importance of using a multiphysics approach from the very beginning of the design process;
2. For an heuristic FEA finalization strategy, identify a convenient start-up candidate;
3. For an optimization-based FEA finalization strategy, reduce the space wherein to run the optimization, following a physics-based criteria rather than good engineering judgement.

This Chapter confirmed that the ADS methodology provides a simple yet effective tool to set up the ground for the FEA design finalisation, shall an heuristic or optimisation-based approach chosen.

Table 8-VII Initial 4D rectangular space DS^0.

IDV	Minimum Value	Maximum Value	Discretisation Step
D_s	80[mm]	120[mm]	1[mm]
B_{st}	1.8[T]	2.3[T]	0.01[T]
β_{st}	$4\pi / (N_s N_r)$	$\pi / (N_r)$	0.005[rad]
β_{rt}	$4\pi / (N_s N_r)$	$2\pi / (N_r) - 4\pi / (N_s N_r)$	0.005[rad]

Table 8-VIII Upgraded 4D rectangular space wherein to let optimiser move.

IDV	Minimum Value	Maximum Value	Discretisation Step
D_s	96[mm]	107[mm]	1[mm]
B_{st}	1.8[T]	1.9[T]	0.01[T]
β_{st}	0.108	0.135	0.005[rad]
β_{rt}	0.113	0.160	0.005[rad]

DISCUSSION, CONCLUSION AND FUTURE WORK

A FINAL THESIS OVERVIEW

This thesis has proposed and discussed a new approach to the design of the next-generation, high-performance SR machines. The approach has demonstrated that, by means of a set of simple and computationally cheap analytical models, the Actual Design Space can be individuated straightforwardly. Further to the ADS definition, the designer is in the position to:

1) ensure that the design problem is feasible, by simply acknowledging that the ADS is not empty;

2) if the design feasibility has been proven, the ADS itself can lead the designer in the selection of the most appropriate strategy to finalise the design via Finite Elements.

Consequently, by introducing the ADS generation prior to any FEA finalization stage, a more simple and straightforward design process is achieved, with the chances of a successful outcome being significantly enhanced.

A further point of merit of the ADS method, shown in Chapter 8, is its inherent multiphysics nature. In fact, electromagnetic and thermal aspects have been handled together from the very beginning of the design process, arriving to a start-up candidate which complies with both aspects.

OBJECTIVES FULFILMENT ANALYSIS AND PROPOSED FUTURE WORK

In the following, the four main objectives of this thesis listed in subsection 1.4 are analysed. Based on their successful or partial achievement, recommendations for future works are given.

OBJ. 1 and OBJ. 2 are concerned with the ADS method's formulation and the subsequent count of the number of Independent Design Variables (IDVs). The two objectives have been successfully achieved in chapter 3, where the count of 15 IDVs has been proven. However, the multiphysics analysis has been limited to the electromagnetic and thermal aspects. Hence, future work needed is:

FW 1) Include the mechanical design aspects into the methodology and update the count of the number of the IDVs;

FW 2) Extend the ADS methodology to the other electrical machine classes and carry out a general comparison of the number of IDVs that each class offers;

OBJ. 3 and OBJ. 4 are concerned with the analytical modelling for the performance prediction. This objective has been pursued in chapter 5. The analytical model developed for the high-speed condition proved sufficient accuracy and robustness. Hence, no further work is required. The proposed model for the low-speed condition is limited to the average output torque. Therefore, future work will need:

FW 3) More advanced nonlinear model that predict instantaneous values of torque, phase current and phase flux linkage in conditions of low speeds, i.e. heavy saturation levels.

The analytical model developed for the iron loss estimation showed some limitations in its accuracy due to the fact that 'local' effects are not considered (see Figure 5-30). Therefore, future work will require:

FW 4) More advanced iron loss model where effects of local saturation are taken into account.

This thesis has highlighted that the 'best' analytical model is the one that provides the best compromise between computation time, implementation efforts and clearance δ_{ADS}. Hence, a further piece of future work could be:

FW 5) rigorous formulation of the criteria/guidelines to choose the 'best' analytical model to predict each desired performance.

Another critical aspect highlighted in this thesis is the integration between ADS generation and the finalisation. Possible future work may be focusing on:

FW 6) Investigation of the potential strategies to integrate the ADS with the finalization stage, with particular attention to be paid on optimization algorithms.

Finally, it is observed that the models developed in this thesis have a great potential for being implemented in control strategies. Another possible follow-up work for this thesis could be:

FW 7) Implementation of the proposed high-speed analytical model for novel control strategy, as well as for sensorless controls. In particular, the main advantage would be the very low number of operations to be performed per unit of time, which makes this option extremely interesting for high-speed SR drives.

APPENDIX 1: MANUFACTURING AND TESTING FACILITY SETUP FOR THE SRFLY PROTOTYPE

This Appendix describes the manufacturing work of the SRFly former prototype described in Chapter 4, together with the construction of its testing facility.

The greatest challenge encountered in the prototype manufacturing has been undoubtedly its high mass, literally unusual for a high-speed machine, i.e. $190 m/s$ rotor peripheral speed. To give an idea of the massive dimensions handled, the stator, rotor and overall weight are as follows:

- Stator laminations weight: $450 kg$;
- Rotor assembly weight (laminations + endplates + shaft): $600 kg$;
- Overall weight, including inactive parts: $1700 kg$.

In this regard, it is highlighted that the manufacturing of the SRFly rotor assembly has been a literally pioneering experience. Indeed, to the best of the Author's knowledge, there are no other recorded attempts of interference fit assemblies of high-speed rotors having so massive dimensions and weight.

A1_1 LAMINATION STACKS PROCUREMENT

The stator and rotor lamination stacks resulted of 472 laminations each. Laminations have been produced by Union Steel Products LTD (Gloucestershire, UK). Each lamination has been laser-cut from a M270-35A roll, ensuring the desired tolerance of $0.1 mm$. The stator and rotor lamination packs are shown in Figure A1_1.

A1_2 ROTOR MANUFACTURING

As it has been mentioned above, a thermal-shrink interference fit has been chosen for the rotor-laminations+shaft+support-plate assembly, since this last is the technology that ensures the highest SR rotor speeds. Components are shown in Figure A1_2.

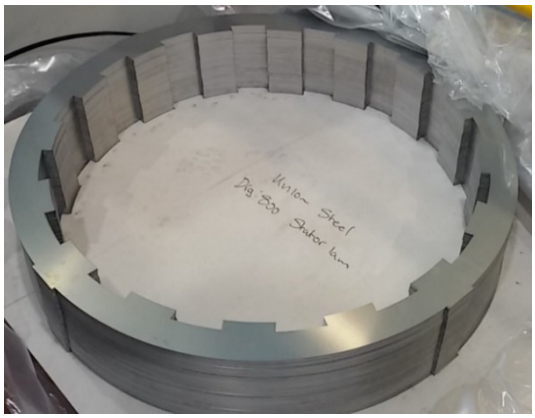

(a)

(b)

Figure A1_1 SRFLY laminations stacks after delivery: a) stator and b)rotor.

For a successful interference fit, a dramatically smaller tolerance than $0.1mm$ for the two contact surfaces is necessary, i.e. shaft outer surface and laminations inner hole. To this end, these components have been re-machined as follows:

- The 17-4PH-made shaft has been milled in the L2 workshop of the University of Nottingham, achieving a sufficiently smooth surface finishing;
- The inner hole of the rotor laminations has been machined by means of an EDM in the University of Nottingham Tower Building's workshop, achieving a $5\mu m$ tolerance.

Subsequently, the interference fit process has been performed by Sulzer Electromechanical Services (Sutton in Ashfield, Nottinghamshire, UK). For the transportation, the rotor lamination stack has been held together with a custom-made cage, which is shown in Figure A1_4. Moreover, in order to impede any loss of alignment, the laminations central hole has been filled with the special filler shown in Figure A1_2.

Before the fitting process, the rotor stack has been slowly heated up in an industrial oven up to $180C$, whereas the shaft has been cooled down in liquid nitrogen at around $-200C$. The liquid nitrogen canister is shown in Figure A1_3. The final assembly can be seen in Figure A1_4.

A1_3 Windings and Stator Lamination Stack Manufacturing

The final stator assembly has been realized entirely in the workshop of the University of Nottingham Tower Building. Stator laminations have been manually stacked into their holding system into the machine's chassis, as shown in Figure A1_5. The 16 coils have been winded with an automatic machine. Then, they have been popped in around the stator teeth and the pair of coils belonging to the same phase has been connected in series. Finally, all of the active parts have been varnished to ensure adequate insulation level.

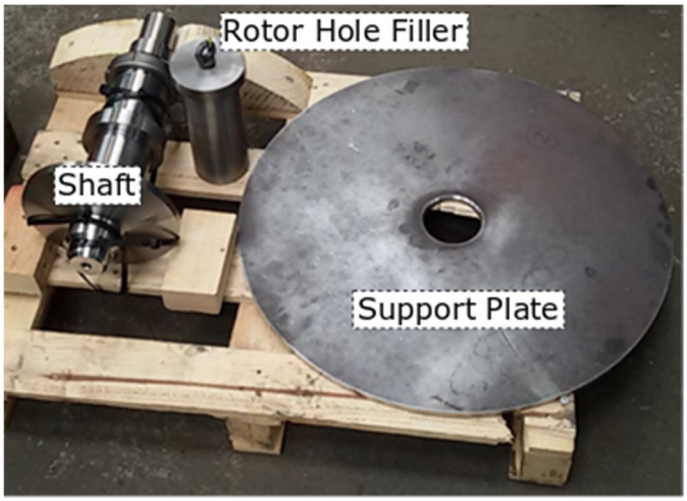

Figure A1_2 SRFLY rotor assembly components: shaft, rotor hole filler and support plate.

Figure A1_3 Liquid nitrogen being poured to cool down the shaft.

A1_4 FINAL ASSEMBLY AND VACUUM SEALING

The mechanical arrangement designed by OXTO, locates the thrust bearings in the top plate, realizing a pendulum-like structure. To realise the final machine assembly, the bottom-bearing housing has been firstly fastened to the chassis. Then, the bottom-bearing has been fitted into its sit, prior to the final shaft drop. In the meanwhile, the top-bearing housing has been fastened to the top lead, with the top-bearings already at place inside it.

As the rotor has been gently dropped into the chassis, the press-fit required to fasten the bottom-bearing to the shaft has been achieved by exploiting the rotor's own weight. Conversely, the exertion of an external vertical force has been necessary to let the top lid slide into the chassis and, at the same time, lock the top bearings onto the shaft.

One of the most important aspects of the SRFly prototype is its sealing, required for the vacuum operation, as for any flywheel body. To this cause, a number of design arrangements has been taken in order to seal up the chassis and turn it into a vacuum chamber:

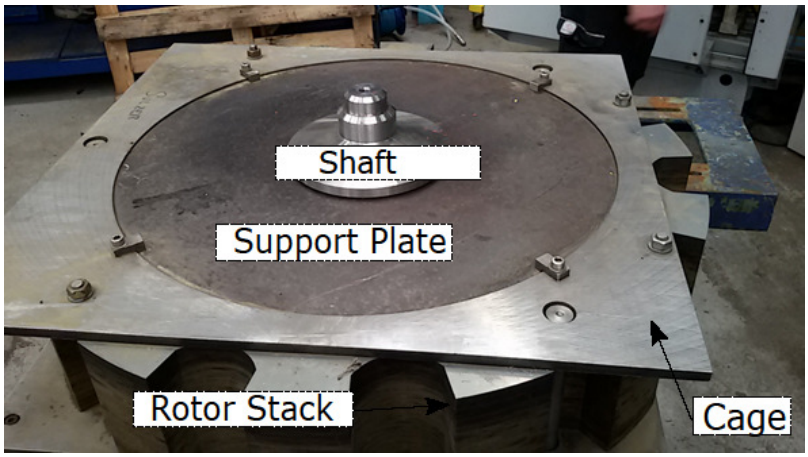

Figure A1_4 Finalised rotor assembly after successful interference fit.

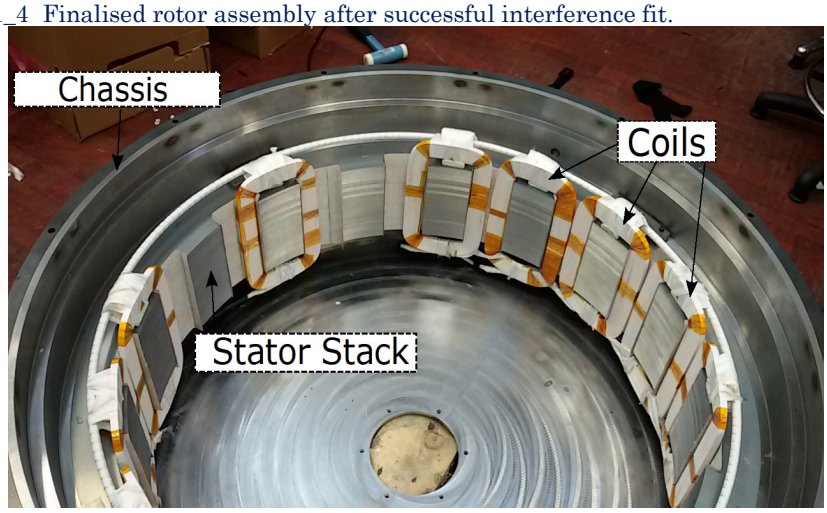

Figure A1_5 Chassis, Stator stack and some coils during the coils installation.

1. Each sensor has been connected to the outside instrumentation via a sealed vacuum plug threaded onto the chassis surface;
2. Windings have been connected with the outside cables through 16 vacuum connectors, which are shown in Figure A1_6;
3. Every gap where air might have been able to flow trough has been sealed with silicon paste or a special tape.

Figure A1_7 shows the final assembly before the top lid fitting.

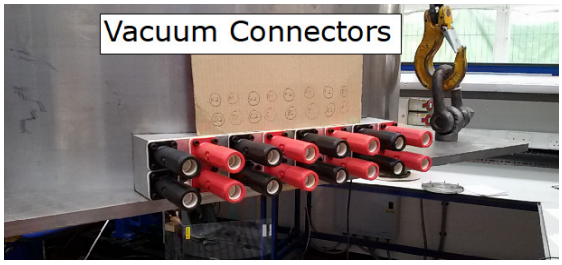

Figure A1_6 Vacuum connectors of the 16 terminations.

Figure A1_7 Final assembly before the top lid insertion.

A1_5 Testing Facility Set-Up

The main rig components are the following:

- Integrated-Flywheel Energy Storage System Switched Reluctance Machine;
- 8-phase SRM converter;
- Control platform.

Due to the high risks related to a flywheel testing, a special high-safety testing area has been arranged. SR machine, converter and controller, along with the measurement equipment and the rig's PC, have been installed in the LEANTO of the University of Nottingham Tower building, a non-access room with $25mm$-thick concrete walls, to contain eventual ejected objects. The LEANTO testing area is shown in Figure A1_8. In the picture, converter and control board are already at place on their trolley. The SRFly prototype has been subsequently bolted on the ground. A control station has been set up just behind the LEATO wall.

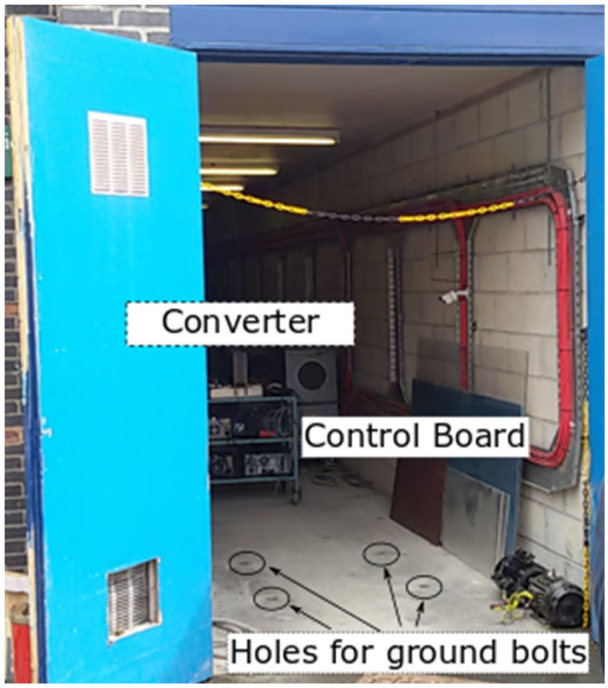

Figure A1_8 The LEANTO SRFly testing area.

APPENDIX 2: SR MACHINE COMPONENTS THERMAL SUBNETWORKS

This Appendix is aimed at completing the information concerned with the LPTN given in Subsection 3.4.5.2. In the following, the thermal subnetworks related to the ten subdomains are derived and discussed individually.

1) FRAME

A schematic illustration of the machine's frame, which is represented as a simple hollow cylinder, is given in Figure A2_1, along with the corresponding thermal subnetwork. In this case, two equivalent thermal resistances are considered, namely R_{amb} and R_{sy_fr}. R_{amb} represents the convective thermal resistance between the housing and the outer environment and is expressed by (A2-1). A deeper discussion about R_{amb} has been already given in Subsection 3.4.5.4. R_{sy_fr} is the contact resistance between laminations and housing and is given in (A2-2).

χ_{amb} denotes the convective heat exchange factor between the machine's housing and the ambient fluid. As it has been already discussed in Chapter 3, χ_{amb} depends on the cooling system and therefore can be considered as a designer's deliberate choice.

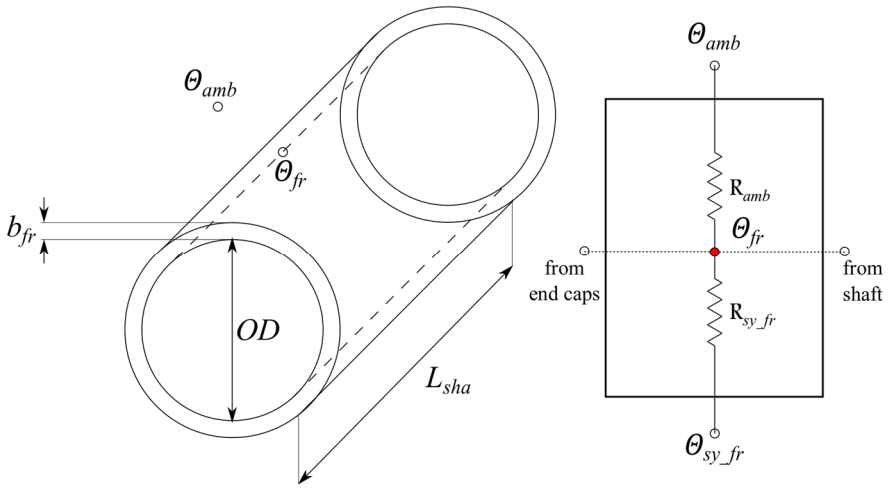

Figure A2_1 Illustration of the frame geometry and thermal subnetwork.

Conversely, χ_{c_fr} expresses the stator laminations-to-frame contact factor, which can be reasonably assumed as a material-dependent quantity.

$$R_{amb} = \frac{1}{\chi_{amb} L_{sha} \pi OD}, \tag{A2-1}$$

$$R_{sy\_fr} = \frac{1}{\pi L_{stk} OD \ \chi_{c\_fr}}, \tag{A2-2}$$

2) STATOR YOKE

The stator yoke is also modelled as a hollow cylinder, which is schematically illustrated in Figure A2_2. In this case, an equivalent T-shaped thermal subnetwork is used to include the inner heat generation P_{sy}. The four thermal resistances are expressed in (A2-3) to (A2-5), where $\lambda_{FE,a}$ and $\lambda_{FE,r}$ indicate the iron thermal conductivity along the axial and radial directions.

$$R_{sy,a} = \frac{L_{stk}}{6\pi\lambda_{FE,a}\left(ODb_{sy} - b_{sy}^{\ 2}\right)}, \tag{A2-3}$$

$$R_{sy,r,i} = \frac{1}{2\pi\lambda_{FE,r} L_{stk}} \left(\frac{OD^2 \ln\left(\frac{OD}{OD - 2b_{sy}}\right)}{2\left(ODb_{sy} - b_{sy}^{\ 2}\right)} - 1 \right), \tag{A2-4}$$

$$R_{sy,r,P} = -\frac{1}{4\pi\lambda_{FE,r} L_{stk}\left(ODb_{sy} - b_{sy}^{\ 2}\right)} \left(\frac{OD^2 + 2b_{sy}^{\ 2} - 2ODb_{sy}}{2} - \frac{OD^2\left(\frac{OD}{2} - b_{sy}\right)^2 \ln\left(\frac{OD}{OD - 2b_{sy}}\right)}{ODb_{sy} - b_{sy}^{\ 2}} \right), \tag{A2-5}$$

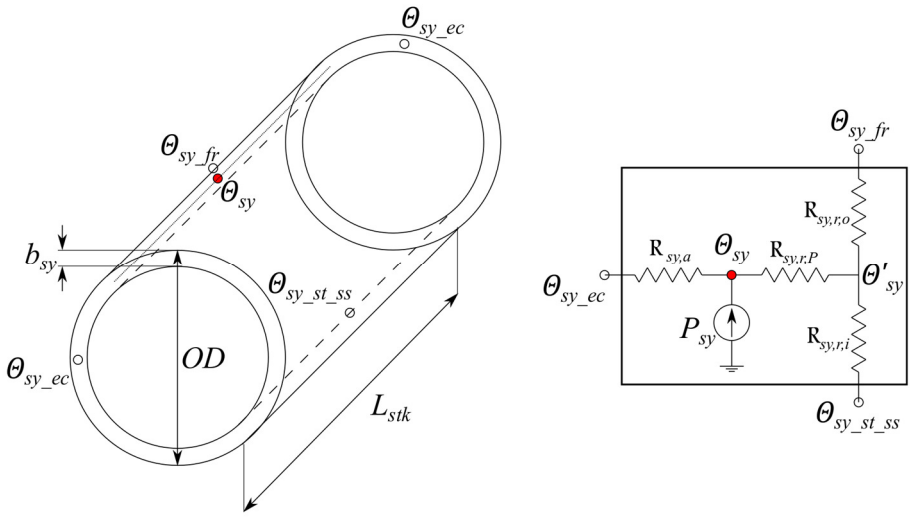

Figure A2_2 Illustration of the stator yoke geometry and thermal subnetwork.

$$R_{sy,r,o}=\frac{1}{2\pi\lambda_{FE,r}L_{stk}}\left(1-\frac{2\left(\frac{OD}{2}-b_{sy}\right)^2\ln\left(\frac{OD}{OD-2b_{sy}}\right)}{ODb_{sy}-{b_{sy}}^2}\right) \tag{A2-6}$$

3) STATOR TEETH

The geometrical scheme of a pair of stator teeth, as well as the T-shape thermal subnetwork equivalent to the entire set of N_s stator teeth is represented in Figure A2_3. Thermal resistances are expressed by (A2-7) to (A2-11).

$$R_{st,a}=\frac{\zeta_s L_{stk}}{6\pi\lambda_{FE,a}\beta_{st}\left(D_s h_{st}+{h_{st}}^2\right)}, \tag{A2-7}$$

$$R_{st,c}=\frac{\pi\beta_{st}\left(D_s h_{st}+{h_{st}}^2\right)}{\lambda_{FE,r}L_{stk}\zeta_s{h_{st}}^2{N_s}^2}, \tag{A2-8}$$

$$R_{st,r,i}=\frac{\zeta_s}{2\pi\lambda_{FE,r}L_{stk}\beta_{st}}\left(\frac{2\left(\frac{D_s}{2}+h_{st}\right)^2\ln\left(1+\frac{2h_{st}}{D_s}\right)}{\left(D_s h_{st}+{h_{st}}^2\right)}-1\right), \tag{A2-9}$$

$$R_{st,r,o}=\frac{\zeta_s}{2\pi\lambda_{FE,r}L_{stk}\beta_{st}}\left(1-\frac{\frac{{D_s}^2}{2}\ln\left(1+\frac{2h_{st}}{D_s}\right)}{\left(D_s h_{st}+{h_{st}}^2\right)}\right), \tag{A2-10}$$

$$R_{st,r,P}=-\frac{\zeta_s}{4\pi\lambda_{FE,r}L_{stk}\beta_{st}\left(D_s h_{st}+{h_{st}}^2\right)}\left(\begin{array}{l}\frac{{D_s}^2+2{h_{st}}^2+2D_s h_{st}}{2}-\\ \frac{{D_s}^2\left(\frac{D_s}{2}+h_{st}\right)^2\ln\left(1+\frac{2h_{st}}{D_s}\right)}{\left(D_s h_{st}+{h_{st}}^2\right)}\end{array}\right) \tag{A2-11}$$

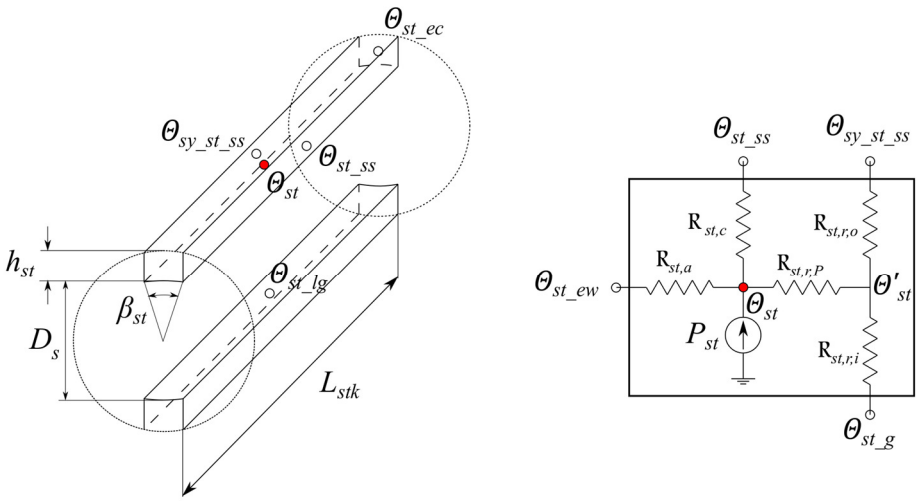

Figure A2_3 Illustration of the stator teeth geometry and thermal subnetwork.

4) STATOR SLOTS

A schematic representation of the stator slots, along with the equivalent thermal network of the full set of N_s stator slots is shown in Figure A2_4. Stator slot are filled with an array of conductors and insulation. Thus, for the axial heat flow, it is reasonable to assume that only the copper conductors transfer heat towards the end-winding, so that the traditional conduction formulas can be used: Thus, axial thermal resistance $R_{ss,a}$ results in (A2-12).

$$R_{ss,a} = \frac{L_{stk}}{6\lambda_{CU} A_{ss} f_{CU} N_s}, \tag{A2-12}$$

On the other hand, for the heat flow toward the radial and circumferential direction, presence of insulation and residual air shall be taken into account. In [122], a simple, geometry-based model is presented, where copper is concentrated at the centre of the slot and is surrounded by an equivalent impregnation-insulation layer, having thickness $b_{IS\_ss\_eq}$, (see Figure A2_5). Hence, $b_{IS\_ss\_eq}$ is directly expressed by (A2-13), where $l_{\_ss}$ is given in (A2-14) and represents the slot perimeter.

$$b_{IS\_ss\_eq} = \frac{A_{ss}\left(1 - f_{CU}\right)}{l_{ss}}, \tag{A2-13}$$

$$l_{ss} = 2h_{st} + \beta_{ss}\left(D_s + h_{st}\right). \tag{A2-14}$$

Finally, the equivalent circumferential and radial thermal resistances are given in (A2-15) to (A2-17), where λ_{CU} expresses the copper thermal conductivity.

$$R_{ss,c} = \frac{b_{IS\_ss\_eq}}{2\lambda_{IS} h_{st} L_{stk} N_s}, \tag{A2-15}$$

$$R_{ss,r,i} = \frac{2b_{IS\_ss\_eq}}{\lambda_{IS} D_s \beta_{ss} L_{stk} N_s}, \tag{A2-16}$$

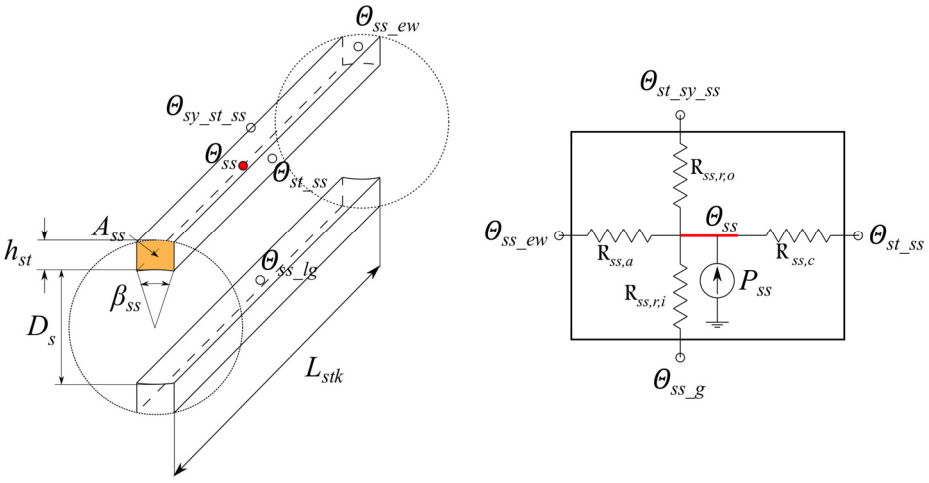

Figure A2_4 Illustration of the stator slots geometry and thermal subnetwork.

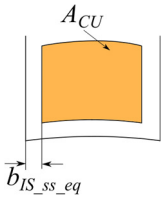

Figure A2_5 Equivalent impregnation-insulation layer.

$$R_{ss,r,o} = \frac{b_{IS\_ss\_eq}}{\lambda_{IS}\left(\frac{D_s}{2}+h_{st}\right)\beta_{ss}L_{stk}N_s}, \tag{A2-17}$$

5) END-WINDING

The end-windings configuration is schematically shown in Figure A2_6. As it can be observed in in Figure A2_6 (a), the typical geometry of concentrated-tooth winding has been considered. Hence, heat rejected axially by the stator tooth is exchanged only with the end-windings. For this geometry, an equivalent circular cross-section with diameter d_{ew} is considered, as shown in Figure A2_6(b). d_{ew} is expressed in (A2-18), where the cross section is considered to be equal to that of half a slot, whereas the end-winding length l_{ew} is considered as the composition of two side stretches, which span and angle of 90° and have an equivalent radius of $d_{ew}/2$, and one stretch parallel to the stator tooth side and having its same length. Similarly to the previous case, an equivalent layer of insulation-impregnation is considered to define the radial thermal resistances (A2-21) and (A2-22). Here, an equal distribution between inner and outer direction is assumed. Finally, (A2-23) gives the copper thermal resistance towards the stator slot.

$$\mathrm{d}_{ew} = \sqrt{\frac{2A_{ss}}{\pi}}, \tag{A2-18}$$

$$l_{ew} = \frac{D_s}{2}\beta_{st} + \pi\frac{d_{ew}}{2}, \tag{A2-19}$$

$$\mathrm{d}_{cond} = \sqrt{\frac{2A_{ss}f_{CU}}{\pi N_{tooth}}}, \tag{A2-20}$$

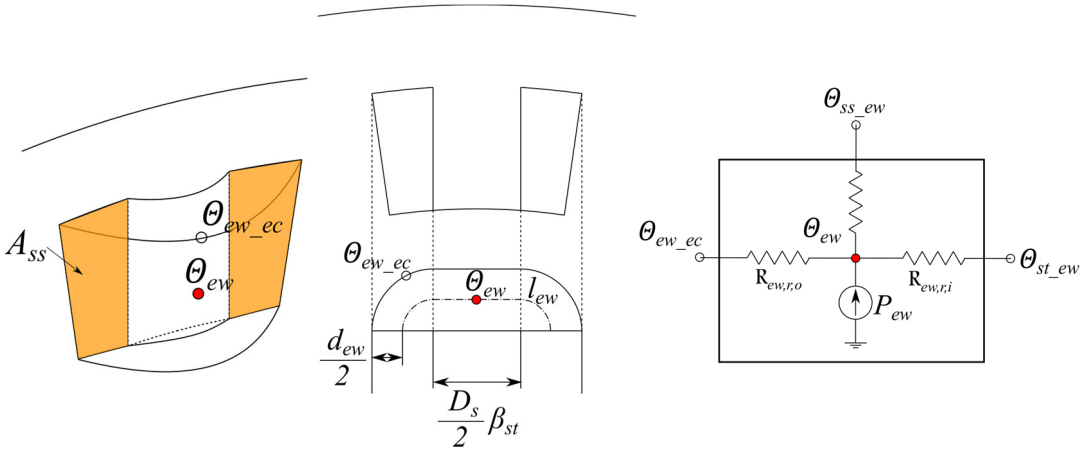

(a) (b) (c)

Figure A2_6 Illustration of the end-windings geometry and thermal subnetwork.

$$R_{ew,r,i} = \frac{b_{IS\_ss\_eq}}{\lambda_{IS}\pi d_{ew} N_s}, \tag{A2-21}$$

$$R_{ew,r,o} = \frac{b_{IS\_ss\_eq}}{\lambda_{IS}\pi d_{ew} N_s}, \tag{A2-22}$$

$$R_{ew,a} = \frac{d_{ew}}{\lambda_{CU} A_{ss} f_{CU} N_s}. \tag{A2-23}$$

6) AIR GAP

Figure A2_7 illustrates the airgap geometry and the equivalent thermal subnetwork. Convective heath exchange that undergoes between stator/rotor and the airgap is expressed by the convective factor $\chi_g(\omega)$, which depends on the rotating speed ω. The greatest challenge in modelling the heat exchange in a salient-rotor machine is the turbulence arising inside the rotor slots, as it causes a convective heath exchange along the teeth edges. In this regard, some works assume the rotor teeth edges to be adiabatic surfaces, i.e. convective heat exchange is entirely neglected. However, this assumption might result excessively restrictive. To this cause, this thesis follows the idea proposed by [89]: an additional thermal resistance $R_{g,c}$ is introduced in parallel to the main resistance $R_{g,r,i,2}$, connecting the airgap temperature Θ_g to the airgap/rotor-yoke interface temperature Θ_{g_ry}. Given that most of the rotor losses are dissipated through the shaft, it is reasonable to introduce some gross simplifications to estimate $R_{g,c}$. In particular, the air velocity along the tooth surface can be assumed to be equal to the rotor speed. Hence, rather than considering a convective heat transfer, it is possible to assume a conductive heat transfer across a thin air layer having the same airgap thickness l_g. as shown in (A2-24).

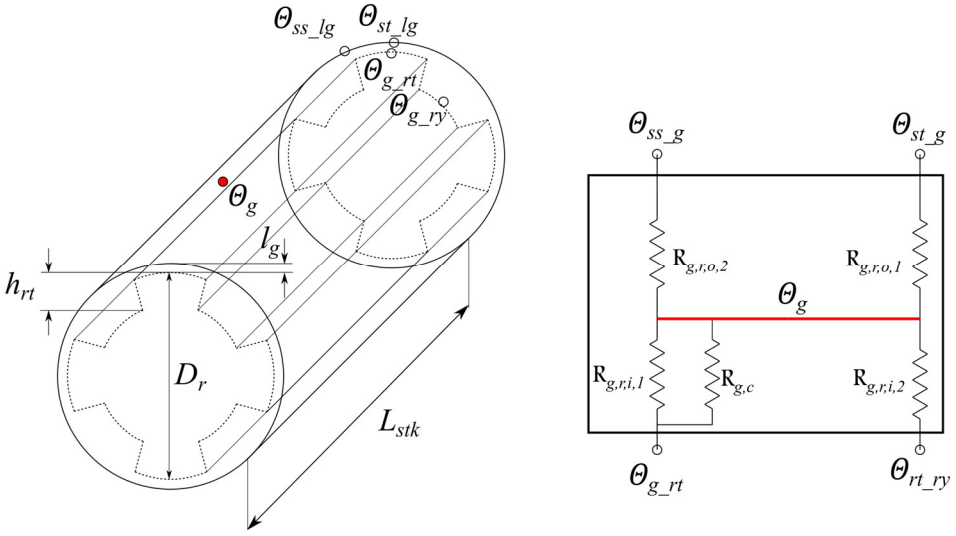

Figure A2_7 Illustration of the airgap geometry and thermal subnetwork.

The final parameter to define for the airgap-to-rotor heat exchange is the convective factor between airgap and rotor yoke along the radial direction. Figure A2_8 shows the

typical air speed distribution inside the rotor slot. As observed, the speed gradient above the rotor tooth front surface $dv(y)_{rt}$ is much smaller than the gradient above the rotor yoke $dv(y)_{ry}$. Reminding that the heat exchange increases with the fluid speed, it is reasonable to assume that the convection factor between rotor yoke and the air gap is the same as the factor between the rotor tooth and the airgap $\chi_g(\omega)$.

$$R_{g,c} = \frac{l_g}{2\lambda_{air} h_{rt} L_{stk} N_r}, \tag{A2-24}$$

$$R_{g,r,o,1} = \frac{1}{\frac{\beta_{st}}{\zeta_s}\pi\frac{D_s}{2}L_{stk}\,\chi_g(\omega)}, \tag{A2-25}$$

$$R_{g,r,o,2} = \frac{1}{\frac{\beta_{ss}}{\zeta_s}\pi\frac{D_s}{2}L_{stk}\,\chi_g(\omega)}, \tag{A2-26}$$

$$R_{g,r,i,1} = \frac{1}{\frac{\beta_{rt}}{\zeta_r}\pi\frac{D_r}{2}L_{stk}\,\chi_g(\omega)}, \tag{A2-27}$$

$$R_{g,r,i,2} = \frac{1}{\left(1-\frac{\beta_{rt}}{\zeta_r}\right)\pi\left(\frac{D_r}{2}-h_{rt}\right)L_{stk}\,\chi_g(\omega)}. \tag{A2-28}$$

7) END-CAPS

The end-caps region is schematically represented in Figure A2_9. As observed, four active parts exchange heat with the end-caps air, resulting in four parallel-connected resistances, whose expressions are provided in (A2-29) to (A2-32). To define the convection factor of each component, the common approach is to try to estimate the average air velocity for each component's surface v, [90]. As already discussed in Chapter 3, the presence or absence of inner fans defines the convection factor $\chi_{ec,N/F}$ between end-caps-to-stator and end-caps-to-end-winding:

- If no fans are installed, air surrounding stator and end-windings is not in motion, and therefore a natural convection factor $\chi_{ec,N}(\omega)$ is used.
- If a fan or any other fanning rotor feature is installed, forced convection shall be considered for $\chi_{ec,F}(\omega)$.

Conversely, with regard to the moving components, forced convection may be always considered $\chi_{ec,F}(\omega)$.

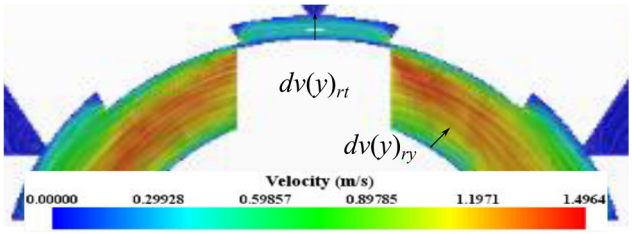

Figure A2_8 Air speed distribution inside the rotor slots, [130].

$$R_{ec,a,i,1} = \frac{1}{2\pi\left(ODh_{st} + h_{st}^{\,2}\right)\ \chi_{ec,N/F}(\upsilon_1)}, \tag{A2-29}$$

$$R_{ec,a,i,2} = \frac{1}{2\pi l_{ew} d_{ew} N_s\ \chi_{ec,N/F}(\upsilon_2)}, \tag{A2-30}$$

$$R_{ec,a,i,3} = \frac{1}{2\pi \frac{\beta_{rt}}{\zeta_r}\left(D_r h_{rt} - h_{rt}^{\,2}\right)\ \chi_{ec,F}(\upsilon_3)}, \tag{A2-31}$$

$$R_{ec,a,i,4} = \frac{1}{2\pi\left(\left(\frac{D_r}{2} - h_{rt}\right)^2 - \left(\frac{D_{sha}}{2}\right)^2\right)\ \chi_{ec,F}(\upsilon_4)}, \tag{A2-32}$$

$$R_{ec,a,o} = \frac{2}{\pi\left(OD^2 - Dsha^2\right)\chi_{ec,N/F}(\upsilon_1)} \tag{A2-33}$$

8) ROTOR TEETH

For the rotor teeth, apart from the different number, the T-shaped thermal subnetwork is equal to the stator teeth. Hence, Figure A2_10 shows the equivalent geometry along with the corresponding thermal subnetwork, whereas thermal resistances are expressed by (A2-34)-(A2-37).

$$R_{rt,a} = \frac{\zeta_r L_{stk}}{6\pi\lambda_{FE,a}\beta_{rt}\left(D_r h_{rt} - h_{rt}^{\,2}\right)}, \tag{A2-34}$$

$$R_{rt,r,o} = \frac{\zeta_r}{2\pi\lambda_{FE,r} L_{stk}\beta_{rt}}\left(1 - \frac{2\left(\frac{D_r}{2} - h_{rt}\right)^2 \ln\left(\frac{D_r}{D_r - 2h_{rt}}\right)}{D_r h_{rt} - h_{rt}^{\,2}}\right), \tag{A2-35}$$

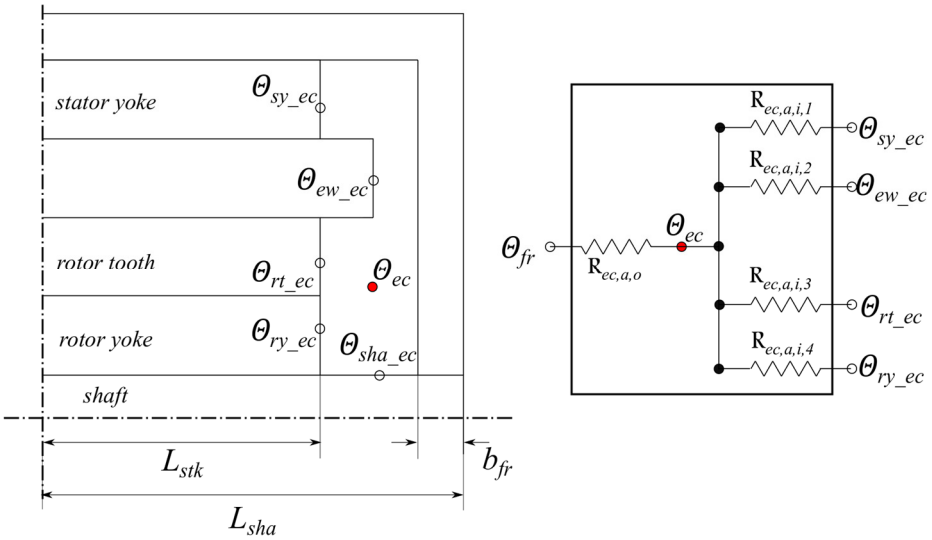

Figure A2_9 Illustration of the end-caps geometry and thermal subnetwork.

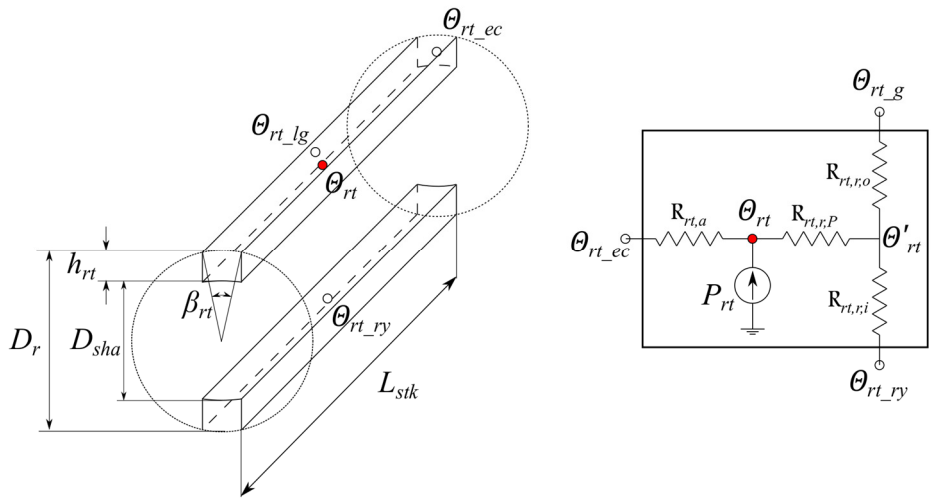

Figure A2_10. Illustration of the rotor teeth geometry and thermal subnetwork.

$$R_{st,r,i} = \frac{\zeta_r}{2\pi\lambda_{FE,r}L_{stk}\beta_{rt}}\left(\frac{D_r^{\,2}\ln\left(\frac{D_r}{D_r-2h_{rt}}\right)}{2\left(D_r h_{rt}-h_{rt}^{\,2}\right)}-1\right), \tag{A2-36}$$

$$R_{rt,r,P} = -\frac{\zeta_r}{4\pi\lambda_{FE,r}L_{stk}\beta_{rt}\left(D_r h_{rt}-h_{rt}^{\,2}\right)}\left(\frac{\frac{D_r^{\,2}+2h_{rt}^{\,2}-2D_r h_{rt}}{2}-}{\frac{D_r^{\,2}\left(\frac{D_r}{2}-h_{rt}\right)^2\ln\left(\frac{D_r}{D_r-2h_{rt}}\right)}{D_r h_{rt}-h_{rt}^{\,2}}}\right). \tag{A2-37}$$

9) ROTOR YOKE

The rotor yoke is modelled as a hollow cylinder, as it is shown in Figure A2_11. As it can be noted, the T-shaped thermal subnetwork is perfectly equal to that of the stator yoke. Thermal resistances are given by (A2-38) - (A2-41).

$$R_{ry,a} = \frac{L_{stk}}{6\pi\lambda_{FE,a}\left(D_{sha}b_{ry}+b_{ry}^{\,2}\right)}, \tag{A2-38}$$

$$R_{ry,r,o} = \frac{1}{2\pi\lambda_{FE,r}L_{stk}}\left(1-\frac{\frac{D_{sha}^{\,2}}{2}\ln\left(1+\frac{2b_{ry}}{D_{sha}}\right)}{\left(D_{sha}b_{ry}+b_{ry}^{\,2}\right)}\right), \tag{A2-39}$$

$$R_{ry,r,i} = \frac{1}{2\pi\lambda_{FE,r}L_{stk}}\left(\frac{2\left(\frac{D_{sha}}{2}+b_{ry}\right)^2\ln\left(1+\frac{2b_{ry}}{D_{sha}}\right)}{\left(D_{sha}b_{ry}+b_{ry}^{\,2}\right)}-1\right), \tag{A2-40}$$

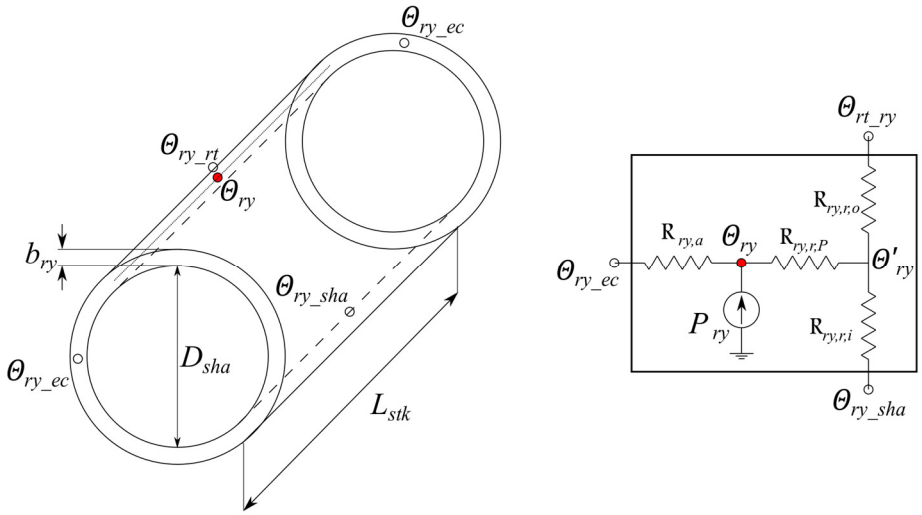

Figure A2_11 Illustration of the rotor yoke geometry and thermal subnetwork.

$$R_{ry,r,P} = -\frac{1}{4\pi\lambda_{FE,r}L_{stk}\left(D_{sha}b_{ry}+b_{ry}{}^2\right)}\left(\frac{D_{sha}{}^2+2b_{ry}{}^2+2D_{sha}b_{ry}}{2} - \frac{D_{sha}{}^2\left(\frac{D_{sha}}{2}+b_{ry}\right)^2\ln\left(1+\frac{2b_{ry}}{D_{sha}}\right)}{\left(D_{sha}b_{ry}+b_{ry}{}^2\right)}\right). \quad \text{(A2-41)}$$

10) SHAFT

The shaft geometry and equivalent thermal subnetwork are represented in Figure A2_12. As it can be seen, heat is exchanged with the rotor yoke through $R_{sha,r,o,1}$ and with the frame through $R_{sha,r,o,2}$. These two thermal resistances are expressed respectively by (A2-42) and (A2-43).

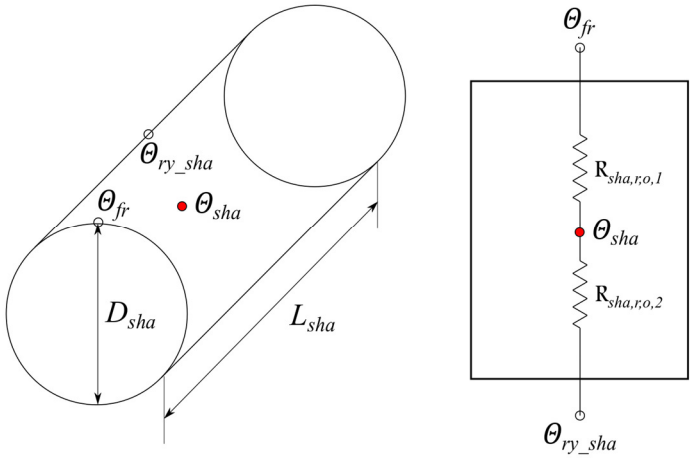

Figure A2_12 Illustration of the shaft geometry and thermal subnetwork.

$$R_{sha,r,o,1} = \frac{1}{2\pi L_{stk}\ \lambda_{IR}}, \tag{A2-42}$$

$$R_{sha,r,o,2} = \frac{1}{4\pi b_{fr}\ \lambda_{IR}}. \tag{A2-43}$$

APPENDIX 3: FEA-BASED PROCEDURE FOR THE DETERMINATION OF THE FLUX LEAKAGE TUBES COEFFICIENTS

This Appendix describes the FEA-based procedure that has been used to determine the flux leakage tubes coefficients a_{II}, b_{II}, c_{II} and d_{II} introduced in subsection 6.2.1.1.

Elliptical leakage tubes of type I are expressed mathematically in terms of their x- and y- semi-axes Γ_x and Γ_y (see Figure A3_1), which are related to each other by (A3-1).

$$\Gamma_x = e_{II}\Gamma_y . \tag{A3-1}$$

As already observed in in subsection 6.2.1.1, e_{II} has been preferred to the traditional definition of eccentricity in a bid to keep the mathematical formulation at its simplest. For the determination of e_{II} as a function of the machine geometry, the following approximations are introduced. These last can be justified by the fact that leakage lines have a much smaller contribution to the overall inductance than the magnetising lines:

- The shape of the leakage tubes is not affected by the airgap length and does not change with the rotor position;
- For a given slot geometry, all the leakage tubes have the same e_{II}.

As a result, e_{II} can be related to the slot geometry by means of two parameters, i.e. the ratio between the tooth height and the bore diameter h_{st}/D_s and the slot angle β_{ss}:

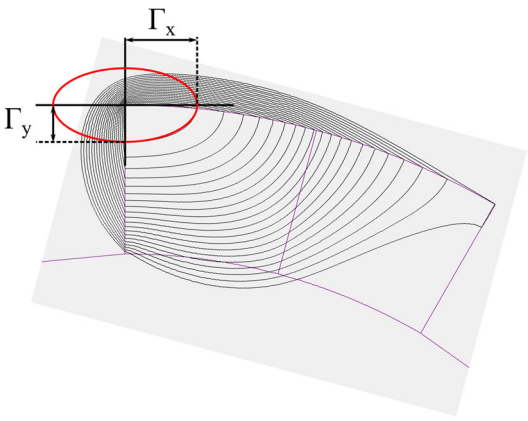

Figure A3_1 Example of leakage tube pseudo-eccentricity measurement.

$$e_{II} = f\left(\frac{h_{st}}{D_s}, \beta_{ss}\right).$$

To determine the function f above, a FEA simulation campaign has been conducted. A static simulation has been performed for all of the slots geometries identified by the values of h_{st}/D_s and β_{ss} reported in Table A3-I

. An example of slot geometry simulated is given in Figure A3_1. For each geometry, the 20 innermost leakage flux lines have been plotted and the length of its x- and y- semi-axes of the innermost one has been 'measured' by means of the INKSCAPE graphics software. The values of e_{II} found for each slot geometry are reported in Table A3-Iand are plotted as yellow dots in Figure A3_2.

Based on the Author's experience, the slot height tends to decrease along with the slot angle, so that not all of the geometries considered in the analysis are of 'engineering' interest, i.e. correspond to SR machines of practical interest. In Figure A3_2, slot geometries that correspond to SR machines of 'engineering' interest are those that fall into the are marked as '*zone of engineering interest*'. At this point, it can be noted that all of the yellow dots from inside the '*zone of engineering interest*' lie on the same plane. This last can be described by the following 3-variable equation:

$$a_{II}\beta_{ss} + b_{II}\frac{h_{st}}{D_s} + c_{II}e_{II} + d_{II}. \tag{A3-2}$$

Based on the values reported Table A3-I, coefficients a_{II}, b_{II}, c_{II} and d_{II} have been determined via 3D least-square method. Their values are as follows:

$$\begin{cases} a_{II} = 4.83 \\ b_{II} = 0.607 \\ c_{II} = 6.75 \\ d_{II} = 6.93 \end{cases}.$$

Table A3-I Values of e_{II} as a function of h_{st}/D_s and β_{ss}.

e_{II}		β_{ss}					
		7.5	**12**	**16.5**	**21**	**25.5**	**30**
h_{st}/D_s	**0.2**	1.103	1.182	1.316	1.475	1.694	1.950
	0.3	1.099	1.144	1.217	1.294	1.383	1.496
	0.4	1.082	1.134	1.192	1.282	1.322	1.372
	0.5	1.076	1.128	1.185	1.252	1.309	1.357

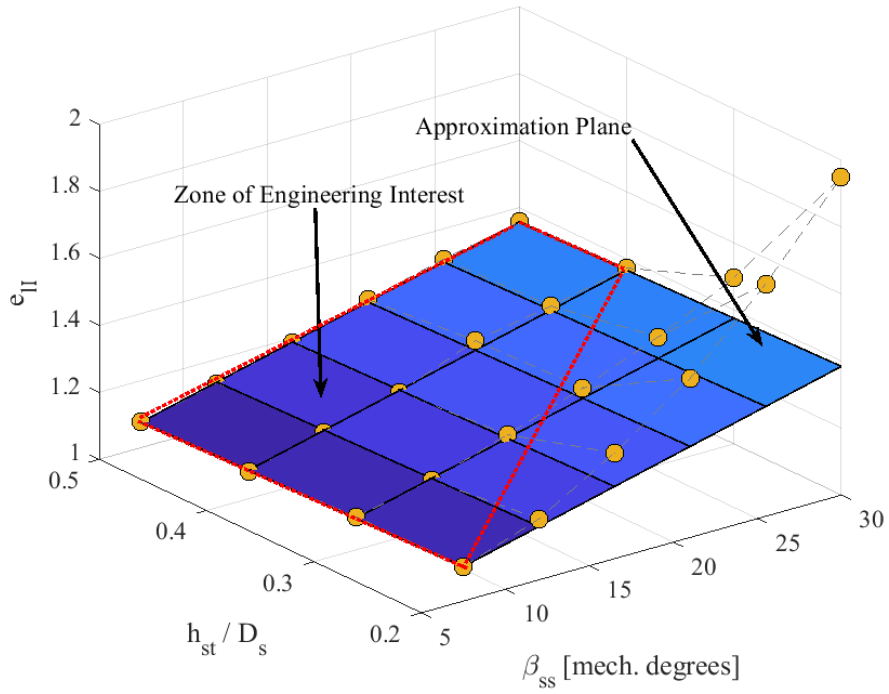

Figure A3_2 FEA-measured values of e_{II}.

REFERENCES

[1] J. B. Bartolo, M. Degano, J. Espina, and C. Gerada, "Design and Initial Testing of a High-Speed 45-kW Switched Reluctance Drive for Aerospace Application," *IEEE Transactions on Industrial Electronics,* vol. 64, no. 2, pp. 988-997, 2017.

[2] D. H. Lee, T. H. Pham, and J. W. Ahn, "Design and Operation Characteristics of Four-Two Pole High-Speed SRM for Torque Ripple Reduction," *IEEE Transactions on Industrial Electronics,* vol. 60, no. 9, pp. 3637-3643, 2013.

[3] C. A. Ferreira, S. R. Jones, W. S. Heglund, and W. D. Jones, "Detailed design of a 30-kW switched reluctance starter/generator system for a gas turbine engine application," *IEEE Transactions on Industry Applications,* vol. 31, no. 3, pp. 553-561, 1995.

[4] A. V. Radun, "High-power density switched reluctance motor drive for aerospace applications," *IEEE Transactions on Industry Applications,* vol. 28, no. 1, pp. 113-119, 1992.

[5] H. Zhang, W. Xu, S. Wang, Y. Huangfu, G. Wang, and J. Zhu, "Optimum Design of Rotor for High-Speed Switched Reluctance Motor Using Level Set Method," *IEEE Transactions on Magnetics,* vol. 50, no. 2, pp. 765-768, 2014.

[6] K. M. Rahman and M. Ehsani, "Performance analysis of electric motor drives for electric and hybrid electric vehicle applications," in *Power Electronics in Transportation*, Dearborn, MI, USA, 1996, pp. 49-56.

[7] V. Madonna, P. Giangrande, and M. Galea, "Electrical Power Generation in Aircraft: review, challenges and opportunities," *IEEE Transactions on Transportation Electrification,* pp. 1-1, 2018.

[8] G. Bramerdorfer, J. A. Tapia, J. J. Pyrhönen, and A. Cavagnino, "Modern Electrical Machine Design Optimization: Techniques, Trends, and Best Practices," *IEEE Transactions on Industrial Electronics,* vol. 65, no. 10, pp. 7672-7684, 2018.

[9] S. A. Nasar, "D.C.-switched reluctance motor," *Proceedings of the Institution of Electrical Engineers,* vol. 116, no. 6, pp. 1048-1049, 1969.

[10] B. Multon, *Historique des machines électriques et plus particulièrement des machines à réluctance variable*. 1995.

[11] J. T. Charton, J. Corda, J. M. Stephenson, and S. P. Randall, "Dynamic modelling of switched reluctance machines with iron losses and phase interactions," *IEE Proceedings - Electric Power Applications,* vol. 153, no. 3, pp. 327-336, 2006.

[12] W. F. Ray and R. M. Davis, "Inverter Drive for Doubly Salient Reluctance Motor: Its Fundamental Behaviour, Linear Analysis and Cost Implications," *Electric Power Applications, IEE Journal on,* vol. 2, no. 6, pp. 185-193, 1979.

[13] W. F. Ray, P. J. Lawrenson, R. M. Davis, J. M. Stephenson, N. N. Fulton, and R. J. Blake, "High-Performance Switched Reluctance Brushless Drives," *IEEE Transactions on Industry Applications,* vol. IA-22, no. 4, pp. 722-730, 1986.

[14] P. J. Lawrenson, J. M. Stephenson, P. T. Blenkinsop, J. Corda, and N. N. Fulton, "Variable-speed switched reluctance motors," *IEE Proceedings B - Electric Power Applications,* vol. 127, no. 4, pp. 253-265, 1980.

[15] J. D. Widmer, R. Martin, and M. Kimiabeigi, "Electric vehicle traction motors without rare earth magnets," *Sustainable Materials and Technologies,* vol. 3, pp. 7-13, 2015.

[16] K. Hamada, M. Nagao, M. Ajioka, and F. Kawai, "SiC—Emerging Power Device Technology for Next-Generation Electrically Powered Environmentally Friendly Vehicles," *IEEE Transactions on Electron Devices,* vol. 62, no. 2, pp. 278-285, 2015.

[17] C. Chen, M. Su, Z. Xu, and X. Lu, "SiC-based automotive traction drives, opportunities and challenges," in *2017 IEEE 5th Workshop on Wide Bandgap Power Devices and Applications (WiPDA)*, 2017, pp. 25-30.

[18] C. Liu, "Emerging Electric Machines and Drives — An Overview," *IEEE Transactions on Energy Conversion,* vol. 33, no. 4, pp. 2270-2280, 2018.

[19] T. A. Lipo, *Introduction to AC Machine Design*, 3rd ed. Wisconsin-Madison: WisPERC, 2007.

[20] D. Gerada, A. Mebarki, N. L. Brown, C. Gerada, A. Cavagnino, and A. Boglietti, "High-Speed Electrical Machines: Technologies, Trends, and Developments," *IEEE Transactions on Industrial Electronics,* vol. 61, no. 6, pp. 2946-2959, 2014.

[21] E. Richter and C. Ferreira, "Performance evaluation of a 250 kW switched reluctance starter generator," in *Industry Applications Conference, 1995. Thirtieth IAS Annual Meeting, IAS '95., Conference Record of the 1995 IEEE*, 1995, vol. 1, pp. 434-440 vol.1.

[22] J. Kim and R. Krishnan, "High Efficiency Single-Pulse Controlled Switched Reluctance Motor Drive for High Speed (48k RPM) Application: Analysis, Design, and Experimental Verification," in *2008 IEEE Industry Applications Society Annual Meeting*, 2008, pp. 1-8.

[23] M. Besharati, K. R. Pullen, J. D. Widmer, G. Atkinson, and V. Pickert, "Investigation of the mechanical constraints on the design of a super-high-speed Switched Reluctance Motor for automotive traction," in *7th IET International Conference on Power Electronics, Machines and Drives (PEMD 2014)*, 2014, pp. 1-6.

[24] J. B. Bartolo, "A High Performance Switched Reluctance Drive For Aerospace Applications," Ph.D., Electrical and Electronic Engineering, The University of Nottingham, Nottingham, 2015.

[25] C. Gong, S. Li, and T. G. Habetler, "Analysis of Rotor Robustness of Ultra-high Speed Switched Reluctance Machines over 1 Million rpm Using Cohesive Zone

Model," in *2018 IEEE Energy Conversion Congress and Exposition (ECCE)*, 2018, pp. 2401-2406.

[26] C. Gong and T. Habetler, "A novel rotor design for ultra-high speed switched reluctance machines over 1 million rpm," in *2017 IEEE International Electric Machines and Drives Conference (IEMDC)*, 2017, pp. 1-6.

[27] L. Bernard, X. Mininger, L. Daniel, G. Krebs, F. Bouillault, and M. Gabsi, "Effect of Stress on Switched Reluctance Motors: A Magneto-Elastic Finite-Element Approach Based on Multiscale Constitutive Laws," *IEEE Transactions on Magnetics,* vol. 47, no. 9, pp. 2171-2178, 2011.

[28] S. Papadopoulos, R. Rocca, M. Galea, and M. Rashed, "SRFly, Final Project Report," University of Nottingham, Nottingham2019.

[29] R. Rocca, M. Galea, and M. Rashed, "SRFly, Machine Trade-off Studies Report," University of Nottingham, Nottingham2016.

[30] R. Rocca, S. Papadopoulos, M. Rashed, G. Prassinos, and M. Galea, "Design Considerations on a Switched Reluctance Machine for a High Inertia, High Speed Ratio Application," Conference Proceeding Paper, 2017.

[31] J. S. Lawler, J. M. Bailey, J. W. McKeever, and P. J. Otaduy, "Impact of Continuous Conduction on the Constant Power Speed Range of the Switched Reluctance Motor," in *IEEE International Conference on Electric Machines and Drives*, San Antonio, TX, USA, 2005.

[32] T. Yuichi *et al.*, "Operating area of a Switched Reluctance Motor with continuous current operation," in *IEEE PES General Meeting*, 2010, pp. 1-4.

[33] H. Hannoun, M. Hilairet, and C. Marchand, "Design of an SRM Speed Control Strategy for a Wide Range of Operating Speeds," *IEEE Transactions on Industrial Electronics,* vol. 57, no. 9, pp. 2911-2921, 2010.

[34] H. Hannoun, M. Hilairet, and C. Marchand, "Experimental Validation of a Switched Reluctance Machine Operating in Continuous-Conduction Mode," *IEEE Transactions on Vehicular Technology,* vol. 60, no. 4, pp. 1453-1460, 2011.

[35] A. Chiba, M. Takeno, N. Hoshi, M. Takemoto, S. Ogasawara, and M. A. Rahman, "Consideration of Number of Series Turns in Switched-Reluctance Traction Motor Competitive to HEV IPMSM," *IEEE Transactions on Energy Conversion,* vol. 48, no. 6, pp. 2333-2340, 2012.

[36] N. Schofield, S. A. Long, D. Howe, and M. McClelland, "Design of a Switched Reluctance Machine for Extended Speed Operation," *IEEE Transactions On Industry Applications,* vol. 45, no. 1, pp. 116-122, 2009.

[37] K. Kiyota and A. Chiba, "Design of Switched Reluctance Motor Competitive to 60-kW IPMSM in Third-Generation Hybrid Electric Vehicle," *IEEE Transactions on Industry Applications,* vol. 48, no. 6, pp. 2303-2309, 2012.

[38] M. Rekik, M. Besbes, C. Marchand, B. Multon, S. Loudot, and D. Lhotellier, "Improvement in the field-weakening performance of switched reluctance machine with continuous mode," *IET Electr. Power Appl,* vol. 1, no. 5, pp. 785–792, 2007.

[39] A. Parsapour, B. M. Dehkordi, and M. Moallem, "Predicting core losses and efficiency of SRM in continuous current mode of operation using improved

analytical technique," *Journal of Magnetism and Magnetic Materials,* vol. 378, pp. 118-127, 2015/03/15/ 2015.

[40] A. V. Radun, "Design considerations for the switched reluctance motor," *IEEE Transactions on Industry Applications,* vol. 31, no. 5, pp. 1079-1087, 1995.

[41] G. Bertotti, "General properties of power losses in soft ferromagnetic materials," *IEEE Transactions on Magnetics,* vol. 24, no. 1, pp. 621-630, 1988.

[42] R. Wrobel, P. H. Mellor, M. Popescu, and D. A. Staton, "Power Loss Analysis in Thermal Design of Permanent-Magnet Machines—A Review," *IEEE Transactions on Industry Applications,* vol. 52, no. 2, pp. 1359-1368, 2016.

[43] M. Popescu, D. A. Staton, A. Boglietti, A. Cavagnino, D. Hawkins, and J. Goss, "Modern Heat Extraction Systems for Power Traction Machines—A Review," *IEEE Transactions on Industry Applications,* vol. 52, no. 3, pp. 2167-2175, 2016.

[44] V. Madonna, P. Giangrande, and M. Galea, "Electrical Power Generation in Aircraft: Review, Challenges, and Opportunities," *IEEE Transactions on Transportation Electrification,* vol. 4, no. 3, pp. 646-659, 2018.

[45] H. Hayashi, A. Chiba, and T. Fukao, "Efficiency Comparison of Switched Reluctance Motors with Low Loss Materials," in *2007 IEEE Power Engineering Society General Meeting*, 2007, pp. 1-6.

[46] P. Chang, E. Chang, P. Liang, and J. Lin, "The Development of High Speed and Low Loss Materials," in *2008 3rd International Microsystems, Packaging, Assembly & Circuits Technology Conference*, 2008, pp. 174-176.

[47] X. Liang, G. Li, J. Ojeda, M. Gabsi, and Z. Ren, "Comparative Study of Classical and Mutually Coupled Switched Reluctance Motors Using Multiphysics Finite-Element Modeling," *IEEE Transactions on Industrial Electronics,* vol. 61, no. 9, pp. 5066-5074, 2014.

[48] J. M. Kokernak and D. A. Torrey, "Magnetic circuit model for the mutually coupled switched-reluctance machine," *IEEE Transactions on Magnetics,* vol. 36, no. 2, pp. 500-507, 2000.

[49] B. C. Mecrow, E. A. El-Kharashi, J. W. Finch, and A. G. Jack, "Performance evaluation of switched reluctance motors with segmental rotors," in *IEEE International Electric Machines and Drives Conference, 2003. IEMDC'03.*, 2003, vol. 1, pp. 568-574 vol.1.

[50] B. C. Mecrow, E. A. El-Kharashi, J. W. Finch, and A. G. Jack, "Preliminary performance evaluation of switched reluctance motors with segmental rotors," *IEEE Transactions on Energy Conversion,* vol. 19, no. 4, pp. 679-686, 2004.

[51] B. C. Mecrow, E. A. El-Kharashi, J. W. Finch, and A. G. Jack, "Segmental rotor switched reluctance motors with single-tooth windings," *IEE Proceedings - Electric Power Applications,* vol. 150, no. 5, pp. 591-599, 2003.

[52] B. C. Mecrow, "Fully pitched-winding switched-reluctance and stepping-motor arrangements," *IEE Proceedings B - Electric Power Applications,* vol. 140, no. 1, pp. 61-70, 1993.

[53] B. C. Mecrow, "New winding configurations for doubly salient reluctance machines," *IEEE Transactions on Industry Applications,* vol. 32, no. 6, pp. 1348-1356, 1996.

[54] J. D. Widmer, R. Martin, and B. C. Mecrow, "Optimisation of an 80kW Segmental Rotor Switched Reluctance Machine for automotive traction," in *2013 International Electric Machines & Drives Conference*, 2013, pp. 427-433.

[55] Z. Zhou *et al.*, "A segmented rotor type switched reluctance machine for BSGs of hybrid electric vehicles: Concept, design and analysis," in *2017 20th International Conference on Electrical Machines and Systems (ICEMS)*, 2017, pp. 1-4.

[56] P. Andrada, E. Martínez, M. Torrent, B. Blanqué, and J. I. Perat, "Novel in-wheel axial-flux segmented switched reluctance motor," in *2017 19th European Conference on Power Electronics and Applications (EPE'17 ECCE Europe)*, 2017, pp. P.1-P.8.

[57] R. Madhavan and B. G. Fernandes, "Axial Flux Segmented SRM With a Higher Number of Rotor Segments for Electric Vehicles," *IEEE Transactions on Energy Conversion,* vol. 28, no. 1, pp. 203-213, 2013.

[58] R. Hall, A. G. Jack, B. C. Mecrow, and A. J. Mitcham, "Design and initial testing of an outer rotating segmented rotor switched reluctance machine for an aero-engine shaft-line-embedded starter/generator," in *IEEE International Conference on Electric Machines and Drives, 2005.*, 2005, pp. 1870-1877.

[59] J. D. Widmer and B. C. Mecrow, "Optimized Segmental Rotor Switched Reluctance Machines With a Greater Number of Rotor Segments Than Stator Slots," *IEEE Transactions on Industry Applications,* vol. 49, no. 4, pp. 1491-1498, 2013.

[60] D. E. Cameron, J. H. Lang, and S. D. Umans, "The origin and reduction of acoustic noise in doubly salient variable-reluctance motors," *IEEE Transactions on Industry Applications,* vol. 28, no. 6, pp. 1250-1255, 1992.

[61] R. S. Colby, F. M. Mottier, and T. J. E. Miller, "Vibration modes and acoustic noise in a four-phase switched reluctance motor," *IEEE Transactions on Industry Applications,* vol. 32, no. 6, pp. 1357-1364, 1996.

[62] C. Lin and B. Fahimi, "Prediction of Acoustic Noise in Switched Reluctance Motor Drives," *IEEE Transactions on Energy Conversion,* vol. 29, no. 1, pp. 250-258, 2014.

[63] N. H. Fuengwarodsakul, J. O. Fiedler, S. E. Bauer, and R. W. D. Doncker, "New methodology in sizing and predesign of switched reluctance machines using normalized flux-linkage diagram," in *Fourtieth IAS Annual Meeting. Conference Record of the 2005 Industry Applications Conference, 2005.*, 2005, vol. 4, pp. 2704-2711 Vol. 4.

[64] E. M. Hall, S. S. Ramamurthy, and J. C. Balda, "Analysis, dimensional sizing and configuration comparison of switched-reluctance motors operating under multiphase excitation," *IEEE Transactions on Energy Conversion,* vol. 17, no. 3, pp. 325-331, 2002.

[65] S. S. Ramamurthy, J. C. Balda, and T. Ericsen, "Sizing a switched reluctance motor for electric vehicles," in *Conference Record of the 2000 IEEE Industry Applications Conference. Thirty-Fifth IAS Annual Meeting and World Conference*

on Industrial Applications of Electrical Energy (Cat. No.00CH37129), 2000, vol. 1, pp. 71-78 vol.1.

[66] R. Krishnan, R. Arumugan, and J. F. Lindsay, "Design procedure for switched-reluctance motors," *IEEE Transactions on Industry Applications,* vol. 24, no. 3, pp. 456-461, 1988.

[67] G. Lei, J. Zhu, Y. Guo, C. Liu, and B. Ma, "A Review of Design Optimization Methods for Electrical Machines," *Energies,* vol. 10, no. 12, 2017, Art. no. 1962.

[68] S. Li, S. Zhang, T. G. Habetler, and R. G. Harley, "Modeling, Design Optimization, and Applications of Switched Reluctance Machines—A Review," *IEEE Transactions on Industry Applications,* vol. 55, no. 3, pp. 2660-2681, 2019.

[69] X. D. Xue, K. W. E. Cheng, T. W. Ng, and N. C. Cheung, "Multi-Objective Optimization Design of In-Wheel Switched Reluctance Motors in Electric Vehicles," *IEEE Transactions on Industrial Electronics,* vol. 57, no. 9, pp. 2980-2987, 2010.

[70] A. M. Omekanda, "A new technique for multi-dimensional performance optimization of switched reluctance motors for vehicle propulsion," in *Conference Record of the 2002 IEEE Industry Applications Conference. 37th IAS Annual Meeting (Cat. No.02CH37344)*, 2002, vol. 1, pp. 22-26 vol.1.

[71] H. Cheng, H. Chen, and Z. Yang, "Design indicators and structure optimisation of switched reluctance machine for electric vehicles," *IET Electric Power Applications,* vol. 9, no. 4, pp. 319-331, 2015.

[72] J. W. Jiang, B. Bilgin, B. Howey, and A. Emadi, "Design optimization of switched reluctance machine using genetic algorithm," in *2015 IEEE International Electric Machines & Drives Conference (IEMDC)*, 2015, pp. 1671-1677.

[73] S. Smaka, S. Konjicija, S. Masic, and M. Cosovic, "Multi-objective design optimization of 8/14 switched reluctance motor," in *2013 International Electric Machines & Drives Conference*, 2013, pp. 468-475.

[74] E. Öksüztepe, "In-Wheel Switched Reluctance Motor Design for Electric Vehicles by Using a Pareto-Based Multiobjective Differential Evolution Algorithm," *IEEE Transactions on Vehicular Technology,* vol. 66, no. 6, pp. 4706-4715, 2017.

[75] C. Ma and L. Qu, "Multiobjective Optimization of Switched Reluctance Motors Based on Design of Experiments and Particle Swarm Optimization," *IEEE Transactions on Energy Conversion,* vol. 30, no. 3, pp. 1144-1153, 2015.

[76] R. Ziyan, D. Zhang, and C. S. Koh, "Multi-objective worst-case scenario robust optimal design of switched reluctance motor incorporated with FEM and Kriging," in *2013 International Conference on Electrical Machines and Systems (ICEMS)*, 2013, pp. 716-719.

[77] J. H. Fisch, Y. Li, P. C. Kjaer, J. J. Gribble, and T. J. E. Miller, "Pareto-Optimal Firing Angles for Switched Reluctance Motor Control," in *Second International Conference On Genetic Algorithms In Engineering Systems: Innovations And Applications*, Glasgow, 1997, pp. 90-96.

[78] C. Ma, L. Qu, R. Mitra, P. Pramod, and R. Islam, "Vibration and torque ripple reduction of switched reluctance motors through current profile optimization," in

2016 IEEE Applied Power Electronics Conference and Exposition (APEC), 2016, pp. 3279-3285.

[79] D. Ilea, M. M. Radulescu, F. Gillon, and P. Brochet, "Multi-objective optimization of a switched reluctance motor for light electric traction applications," in *2010 IEEE Vehicle Power and Propulsion Conference*, 2010, pp. 1-6.

[80] S. Zhang, S. Li, J. Dang, R. G. Harley, and T. G. Habetler, "Multi-objective design and optimization of generalized switched reluctance machines with particle swarm intelligence," in *2016 IEEE Energy Conversion Congress and Exposition (ECCE)*, 2016, pp. 1-7.

[81] M. Mitolo and M. Tartaglia, "Galileo Farraris - A Life Dedicated to the Electric Sciences [History]," *IEEE Industry Applications Magazine,* vol. 22, no. 5, pp. 8-11, 2016.

[82] T. J. E. Miller, *Switched Reluctance Motors and their Control* (Monographs in Electrical and Electronic Engineering). Oxford, 1993.

[83] A. E. Fitzgerald, C. K. Jr., and S. D. Umans, M.-H. H. Education, Ed. *ELECTRIC MACHINERY*, VI ed. New York, NY, 2003, p. 688.

[84] R. Rocca, F. G. Capponi, G. D. Donato, M. Rashed, S. Papadopoulos, and M. Galea, "Analytical Approach for the Identification of an Optimal Design Space for Switched Reluctance Machines," in *2018 XIII International Conference on Electrical Machines (ICEM)*, 2018, pp. 569-575.

[85] R. Krishnan, *Switched reluctance motor drives: modeling, simulation, analysis, design, and applications* (Industrial Electronics Series). Florida: CRC Press LLC, 2001.

[86] *IEC Publication 60085:2007*, 2007.

[87] *ASTM A976 - 97*, 1997.

[88] J. Nerg, M. Rilla, and J. Pyrhonen, "Thermal Analysis of Radial-Flux Electrical Machines With a High Power Density," *IEEE Transactions on Industrial Electronics,* vol. 55, no. 10, pp. 3543-3554, 2008.

[89] H. Rouhani, J. Faiz, and C. Lucas, "Lumped thermal model for switched reluctance motor applied to mechanical design optimization," *Mathematical and Computer Modelling,* vol. 45, no. 5, pp. 625-638, 2007/03/01/ 2007.

[90] D. A. Staton and A. Cavagnino, "Convection Heat Transfer and Flow Calculations Suitable for Electric Machines Thermal Models," *IEEE Transactions on Industrial Electronics,* vol. 55, no. 10, pp. 3509-3516, 2008.

[91] W. Tong, *Mechanical Design of Electric Motors*. Boca Raton, FL: CRC Press, 2014.

[92] T. J. E. Miller, *Switched Reluctance Motors and their Control* (Monographs in Electrical and Electronic Engineering). Oxford: Oxford University Press, 1993.

[93] W. Uddin and Y. Sozer, "Analytical Modeling of Mutually Coupled Switched Reluctance Machines Under Saturation Based on Design Geometry," *IEEE Transactions on Industry Applications,* vol. 53, no. 5, pp. 4431-4440, 2017.

[94] J. M. Stephenson and J. Corda, "Computation of torque and current in doubly salient reluctance motors from nonlinear magnetisation data," *Proceeding of the Institution of Electrical Engineers,* vol. 126, no. 5, pp. 393-396, 1979.

[95] Available and Online. https://oxtoenergy.com.

[96] S. Vukosavic and V. R. Stefanovic, "SRM inverter topologies: a comparative evaluation," *IEEE Transactions on Industry Applications,* vol. 27, no. 6, pp. 1034-1047, 1991.

[97] K. Vijayakumar, R. Karthikeyan, S. Paramasivam, R. Arumugam, and K. N. Srinivas, "Switched Reluctance Motor Modeling, Design, Simulation, and Analysis: A Comprehensive Review," *IEEE Transactions on Magnetics,* vol. 44, no. 12, pp. 4605-4617, 2008.

[98] A. Radun, "Analytical calculation of the switched reluctance motor's unaligned inductance," *IEEE Transactions on Magnetics,* vol. 35, no. 6, pp. 4473-4481, 1999.

[99] S. Li, S. Zhang, C. Gong, T. Habetler, and R. Harley, "An Enhanced Analytical Calculation of the Phase Inductance of Switched Reluctance Machines," *IEEE Transactions on Industry Applications,* pp. 1-1, 2018.

[100] C. Wesley Pacheco *et al.*, "Electromagnetic Problems Solving by Conformal Mapping: A Mathematical Operator for Optimization," *Mathematical Problems in Engineering,* vol. 2010, 2010.

[101] P. Materu and R. Krishnan, "Analytical prediction of SRM inductance profile and steady-state average torque," in *Conference Record of the 1990 IEEE Industry Applications Society Annual Meeting*, 1990, pp. 214-223 vol.1.

[102] A. Deihimi, S. Farhangi, and G. Henneberger, "A general nonlinear model of switched reluctance motor with mutual coupling and multiphase excitation," *Electrical Engineering,* vol. 84, no. 3, pp. 143-158, 2002/07/01 2002.

[103] T. J. E. Miller and M. McGilp, "Nonlinear theory of the switched reluctance motor for rapid computer-aided design," *IEE Proceedings B - Electric Power Applications,* vol. 137, no. 6, pp. 337-347, 1990.

[104] M. Rekik, M. Besbes, C. Marchand, B. Multon, S. Loudot, and D. Lhotellier, "High-speed-range enhancement of switched reluctance motor with continuous mode for automotive applications," *European Transactions on Electrical Power,* vol. 18, pp. 674-693, 2008.

[105] M. Lipták, "Principle of Design of Four Phase Low Power Switched Reluctance Machine Aimed to the Maximum Torque Production," *Journal of ELECTRICAL ENGINEERING,* vol. 55, no. 5-6, pp. 138-143, 2004.

[106] M. Moallem and C. M. Ong, "Predicting the steady-state performance of a switched reluctance machine," *IEEE Transactions on Industry Applications,* vol. 27, no. 6, pp. 1087-1097, 1991.

[107] S. Roggia, Y. C. Chong, Y. Gai, M. Popescu, D. Staton, and J. Goss, "Switched Reluctance Machine Peak and Continuous Performance using a Routine Optimised Tool," in *2019 IEEE International Electric Machines & Drives Conference (IEMDC)*, San Diego, CA, 2019, pp. 584-590.

[108] G. Volpe, M. Popescu, F. Marignetti, and J. Goss, "AC Winding Losses in Automotive Traction E-Machines: A New Hybrid Calculation Method," in *2019 IEEE International Electric Machines & Drives Conference (IEMDC)*, 2019, pp. 2115-2119.

[109] G. Volpe, M. Popescu, F. Marignetti, and J. Goss, "Modelling AC Winding Losses in a PMSM with High Frequency and Torque Density," in *2018 IEEE Energy Conversion Congress and Exposition (ECCE)*, 2018, pp. 2300-2305.

[110] Q. Yu, B. Bilgin, and A. Emadi, "Loss and Efficiency Analysis of Switched Reluctance Machines Using a New Calculation Method," *IEEE Transactions on Industrial Electronics,* vol. 62, no. 5, pp. 3072-3080, 2015.

[111] K. Atallah and D. Howe, "Calculation of the rotational power loss in electrical steel laminations from measured H and B," *IEEE Transactions on Magnetics,* vol. 29, no. 6, pp. 3547-3549, 1993.

[112] Q. Yu and D. Gerling, "Analytical Modeling of a Canned Switched Reluctance Machine With Multilayer Structure," *IEEE Transactions on Magnetics,* vol. 49, no. 9, pp. 5069-5082, 2013.

[113] D. M. Ionel, M. Popescu, M. I. McGilp, T. J. E. Miller, S. J. Dellinger, and R. J. Heideman, "Computation of Core Losses in Electrical Machines Using Improved Models for Laminated Steel," *IEEE Transactions on Industry Applications,* vol. 43, no. 6, pp. 1554-1564, 2007.

[114] R. Rocca, F. G. Capponi, S. Papadopoulos, G. D. Donato, M. Rashed, and M. Galea, "Optimal Advance Angle for Torque Maximisation in High-Speed, Single-Pulse Operated, Switched Reluctance Machines," in *2019 IEEE International Electric Machines & Drives Conference (IEMDC)*, 2019, pp. 80-85.

[115] G. B. Arfken and H. J. Weber, "Mathematical Methods for Physicists," vol. 1, E. A. Press, Ed. Orlando, FL: Elsevier 2005, pp. 321-327.

[116] J. Corda and J. M. Stephenson, "Analytical estimation of the minimum and maximum inductances of a double salient motor," presented at the International Conference on Stepping Motors and Systems, University of Leeds, 1979.

[117] C. Ming, K. T. Chau, C. C. Chan, E. Zhou, and X. Huang, "Nonlinear varying-network magnetic circuit analysis for doubly salient permanent-magnet motors," *IEEE Transactions on Magnetics,* vol. 36, no. 1, pp. 339-348, 2000.

[118] M. Takemoto, A. Chiba, H. Akagi, and T. Fukao, "Torque and Suspension Force in a Bearingless Switched Reluctance Motor," *Electrical Engineering in Japan,* vol. Vol. 157, no. 2, pp. 72-82, 2006.

[119] C. D. Jones and L. F. Smith, "Optimum Arrangement of Rectangular Fins on Horizontal Surfaces for Free-Convection Heat Transfer," *Journal of Heat Transfer,* vol. 92, no. 1, pp. 6-10, 1970.

[120] D. A. Howey, P. R. N. Childs, and A. S. Holmes, "Air-Gap Convection in Rotating Electrical Machines," *IEEE Transactions on Industrial Electronics,* vol. 59, no. 3, pp. 1367-1375, 2012.

[121] A. Boglietti and A. Cavagnino, "Analysis of the Endwinding Cooling Effects in TEFC Induction Motors," *IEEE Transactions on Industry Applications,* vol. 43, no. 5, pp. 1214-1222, 2007.

[122] A. Boglietti, E. Carpaneto, M. Cossale, S. Vaschetto, M. Popescu, and D. A. Staton, "Stator Winding Thermal Conductivity Evaluation: An Industrial Production Assessment," *IEEE Transactions on Industry Applications,* vol. 52, no. 5, pp. 3893-3900, 2016.

[123] M. Ehsani, Y. Gao, and A. Emadi, "Modern Electric, Hybrid Electric, and Fuel Cell Vehicles: Fundamentals, Theory, and Design, Second Edition," Boca Raton, Florida, USA: CRC Press, Taylor & Francis Group, 2010, p. 534.

[124] I. Boldea, L. Tutelea, and C. I. Pitic, "PM-assisted reluctance synchronous motor/generator (PM-RSM) for mild hybrid vehicles: electromagnetic design," *IEEE Transactions on Industry Applications,* vol. 40, no. 2, pp. 492-498, 2004.

[125] A. Fatemi *et al.*, "Design of an Electric Machine for a 48-V Mild Hybrid Vehicle," in *2018 IEEE Energy Conversion Congress and Exposition (ECCE)*, 2018, pp. 2278-2285.

[126] D. Winterborne, M. Shiref, S. Snow, and V. Pickert, "TC48: A low-cost 48 V integrated drive for mild hybrid electric vehicles," *The Journal of Engineering,* vol. 2019, no. 17, pp. 4590-4594, 2019.

[127] Available and Online. *https://cogent-power.com/downloads*.

[128] R. Rocca, "Optimal Design of a Switched Reluctance Starter Generator for Short-Mid range Aircraft Applications " Master Degree, Electrical and Electronic Engineering, The University of Nottingham, Nottingham, 2015.

[129] T. A. Lipo, W. Liu, and Z. Du, "Comparison of AC Motors to an Ideal Machine Part II-Non-Sinusoidal AC Machines," in *2019 IEEE International Electric Machines & Drives Conference (IEMDC)*, San Diego, CA, 2019, pp. 1810-1817.

[130] A. Pavan, S. N, R. K. R, N. C. Lenin, and S. R, "Thermal Investigation of a Switched Reluctance Motor," *International Journal of Electrical Engineering,* vol. 8, no. 2, pp. 115-121, 2015.